



University of Zagreb
FACULTY OF ELECTRICAL ENGINEERING AND COMPUTING

Branimir Ivšić

**TEXTILE ANTENNAS FOR BODY-CENTRIC
COMMUNICATION SYSTEMS**

DOCTORAL THESIS

Zagreb, 2013



University of Zagreb
FACULTY OF ELECTRICAL ENGINEERING AND COMPUTING

Branimir Ivšić

TEXTILE ANTENNAS FOR BODY-CENTRIC COMMUNICATION SYSTEMS

DOCTORAL THESIS

Supervisor: Professor Davor Bonefačić, PhD

Zagreb, 2013



Sveučilište u Zagrebu
FAKULTET ELEKTROTEHNIKE I RAČUNARSTVA

Branimir Ivšić

**TEKSTILNE ANTENE ZA KOMUNIKACIJSKE
SUSTAVE NA LJUDSKOM TIJELU**

DOKTORSKI RAD

Mentor: prof. dr. sc. Davor Bonefačić

Zagreb, 2013.

This doctoral thesis was obtained at University of Zagreb, Faculty of Electrical Engineering and Computing, Department of Wireless Communications

Doctoral supervisor: Professor Davor Bonefačić, PhD

Doctoral thesis has: 241 pages

Doctoral thesis No.:

ABOUT THE SUPERVISOR

Davor Bonefačić was born in Zagreb in 1968. He received Dipl.Ing., Mr.Sc. and Dr.Sc. degrees in electrical engineering from the University of Zagreb, Faculty of Electrical Engineering and Computing (FER), Zagreb, Croatia, in 1993, 1996 and 2000, respectively.

Since March 1993 he has been with the Department of Wireless Communications at FER. In 1996 he was a visiting researcher at the Third University of Rome, Rome, Italy. In June 2010 he was promoted to Full Professor. He led one and participated in 3 scientific projects financed by the Ministry of Science, Education and Sports of the Republic of Croatia and participated in 4 COST projects financed by the EU. Currently he is participating in two research projects, "Multifunctional antennas in communication and radar systems" and "Meteorological observation and data assimilation methods", financed by the Ministry of Science, Education and Sports of the Republic of Croatia and one COST Action: IC1102 "VISTA - Action on Versatile, Integrated, and Signal-aware Technologies for Antennas within the ICT Domain". He is member of the WG for small antennas within the EurAAP (European Association on Antennas and Propagation). He published one book chapter and more than 85 scientific papers in journals and conference proceedings in the area of small, active and integrated antennas, applications of metamaterials in antennas, and radar systems. He is a co-author of one university textbook and more than 35 professional and technical papers, studies and evaluations.

Prof. Bonefačić is a member of the Croatian Academy of Engineering (HATZ) and a member of IEEE, KoREMA and Elmar societies. He participated in 12 organizing or program committees of international conferences of which four times he served as committee or conference chair or co-chair. He is member of the editorial board of one scientific journal and he serves as a reviewer for various international journals and conferences. In 1993 he received the Award of the Rector of the University of Zagreb and the bronze plaque "J. Lončar" from FER. He received the silver plaque "J. Lončar" from FER for outstanding master thesis in 1996. In 2009 he received the "R. Podhorsky" award from the Croatian Academy of Engineering (HATZ) for excellence in scientific and professional achievements.

O MENTORU

Davor Bonefačić rođen je u Zagrebu 1968. godine. Diplomirao je, magistrirao i doktorirao u polju elektrotehnike na Sveučilištu u Zagrebu Fakultetu elektrotehnike i računarstva (FER), 1993., 1996., odnosno 2000. godine.

Od ožujka 1993. godine radi na Zavodu za radiokomunikacije FER-a. Godine 1996. bio je gostujući istraživač na Università degli Studi di Roma Tre, Rim, Italija. U lipnju 2010. godine izabran je u zvanje redovitog profesora. Vodio je jedan te sudjelovao na još tri znanstvena projekta Ministarstva znanosti, obrazovanja i športa Republike Hrvatske te četiri projekta COST Europske Unije. Trenutačno sudjeluje na istraživačkim projektima: "Višefunkcijske antene u komunikacijskim i radarskim sustavima" i "Metode motrenja i asimilacije meteoroloških podataka" koji financira Ministarstvo znanosti, obrazovanja i športa Republike Hrvatske te na projektu COST IC1102: "VISTA - Action on Versatile, Integrated, and Signal-aware Technologies for Antennas within the ICT Domain". Član je radne skupine za male antene u sklopu EurAAP (European Association on Antennas and Propagation). Objavio je jedno poglavlje u znanstvenoj knjizi i više od 85 radova u časopisima i zbornicima konferencija u području malih, aktivnih i integriranih antena, primjeni metamaterijala u antenama te radarskih sustava. Koautor je jednog sveučilišnog priručnika i više od 35 stručnih radova, studija i elaborata.

Prof. Bonefačić je član Akademije tehničkih znanosti Hrvatske (HATZ) te stručnih udruga IEEE, KoREMA i Elmar. Sudjelovao je u 12 međunarodnih programskih odbora znanstvenih konferencija od čega je četiri puta bio predsjednik ili su-predsjednik odbora ili konferencije, član je jednog uredničkog odbora inozemnog znanstvenog časopisa te sudjeluje kao recenzent u većem broju inozemnih i domaćih časopisa i konferencija. Godine 1993. nagrađen je nagradom Rektora Sveučilišta u Zagrebu i brončanom plaketom "J. Lončar" FER-a. Srebrnu plaketu "J. Lončar" FER-a za posebno istaknuti magistarski rad dobio je 1996. godine. Godine 2009. nagrađen je godišnjom nagradom "R. Podhorsky" Akademije tehničkih znanosti Hrvatske za osobito vrijedno znanstveno i stručno dostignuće.

PREFACE

“The important thing is not to stop questioning.”

(A. Einstein)

This PhD thesis is the result of my six years of research carried out at the Department of Wireless Communications at the University of Zagreb, Faculty of Electrical Engineering and Computing. During that period I had the opportunity to work in a creative atmosphere of the Department and to learn many skills in the field of antennas and general electromagnetics, as well as to discover the outstanding beauty of this field, both in the theoretical and practical sense.

First and foremost, I would like to thank my doctoral supervisor, prof. Davor Bonefačić for strong support and encouragement during the period of writing my PhD thesis. I thank him for providing the support and guidelines for work and continuously seeing the bigger picture in the research, while at the same time inciting me to come up with my own ideas.

Furthermore, I acknowledge the contribution of other members of the antenna group at our Department – in particular prof. Juraj Bartolić, prof. Zvonimir Šipuš and prof. Silvio Hrabar. Along with my supervisor, during my years spent at the Department, I also had plenty of valuable and helpful discussions with each of them, from which I learned a lot about the way of thinking and approaching problems within the scientific area of antennas and electromagnetics. Thus, I felt as a part of a true team, which I appreciate a lot. Many of the results of those discussions are implemented throughout my thesis.

With the help from Department and especially prof. Bartolić I also had the opportunity to take part in research at EPFL, Lausanne – with prof. Anja Skrivervik and Mr. Jovanče Trajković, with whom I have established a nice cooperation. My credits also go to prof. Željko Penava (from the University of Zagreb, Faculty of Textile Technology) for providing the needed textile materials and practical ideas on how to implement the textile into antennas, i.e. how to join the two fields of research.

I would like to say a large “thank you” to Mr. Damir Petričević for technical support in manufacturing of the antennas proposed in the thesis, as well as graduate students from FER which were involved in project and helped me with measurements – namely Z.

Sriča, I. Bubalo, J. Bešlić, A. Kuštra, G. Golemac, M. Katalenić, and the legendary Mr. I. Vujica. I also acknowledge my sister's friend Eva for having time for proofreading my thesis and improving my English.

More informally, I would like to emphasize my office mates Mr. Komljenović, Mr. Dumić, Mr. Muštra, Mr. Najman as well as the joined mates, such as Mr. Zaluški, Mr. Muha and Ms. Bačić. I feel I was really lucky to have such great people from my generation in my direct environment with whom I had countless coffees and specific discussions about PhD-related topics – exchanging ideas, doubts, problems etc. I also appreciate their technical help (sharing computer memory, helping with measurements and acquiring equipment such as buckets) and understanding, especially in the stressful period of meeting the thesis deadline. Here, I also acknowledge the older research assistants from neighbouring offices who were willing to share parts of their experience with me, and the assistant who encouraged me to improve the mathematical part of the thesis. Moreover, I acknowledge other members of Department staff as well, who, although not explicitly listed, were also helpful, at least unconsciously.

Outside the Department, I would like to give credits to many of my friends and colleagues who were with me from the period I was a graduate student or even before, and who backed me to finish my thesis. Here, I stress Madam Tihana who was always somewhere here, who showed interest in my work during plenty of weekend nights out, and whose corporative spirit I found inspiring and beneficial to keep in mind.

Last, but by no means the least, my endless “thank you” goes to my family – my mother, father, brother Trpimir, sister Dubravka, niece Magdalena and others. They provided me with everyday advice and logistical support I needed – well, I think they know that already. Still, I would like to thank my mother for her direct help with embroidering of the textile on the antennas, and helping me with acquiring the chemicals needed for obtaining the phantom.

After all, I regard my thesis as a nice accomplishment, but also as a responsibility and obligation towards society in general. I hope that during my later work I will keep that in mind and find the way to fulfill this responsibility, this thesis being only the beginning.

SUMMARY

The development of personal body-centric communication systems is an important part of the new generation of wireless communication systems, and one of the recent challenges of communication science and technology. An inevitable part of any such system are antennas, which are required to ensure the wireless transfer of the signal, either within or outside the body, depending on the application. This doctoral thesis deals with the design of small wearable antennas and studying their performance in the body-centric environment by focusing on the specific characteristics of such an environment compared to free space. Several antenna prototypes were realized, and their performance was tested on the body of a human volunteer, as well as on a liquid muscle-equivalent phantom. The influence of bending and moisture in the textile substrate was researched. It was found that bending in the E -plane and low moisture content has a significant influence on the antenna characteristics. The body-centric environment is modelled analytically by calculating Green's function in the spectral domain for a circular cylinder, and modelling the propagation around the torso using creeping waves. In the next stage, conductive threads and yarns were researched and utilized to make the conductive part of the antenna. A conductive mesh embroidered into some conventional fabric was found to be a simple method enabling both the desired conductivity, and the adequate properties of clothes to be retained. The use of a metallic button was found to be suitable for feeding, both from the aesthetical and functional points of view. Based on those findings, a general strategy for the realization of wearable antennas is proposed, and a full-textile prototype PIFA antenna has been designed, and shown to operate properly.

Keywords: body-centric communications, wearable textile antennas, conductive textiles, creeping waves, on-body propagation, off-body propagation, human body phantoms, PIFA antenna, influence of antenna bending, influence of moisture in textile substrate

STRUKTURIRANI SAŽETAK

Tekstilne antene za komunikacijske sustave na ljudskom tijelu

Osobni komunikacijski sustavi na ljudskom tijelu dio su nove generacije radijskih komunikacijskih sustava čiji je razvoj jedan od izazova današnje komunikacijske znanosti i tehnologije, a primjenu nalaze u mnogim područjima života – medicini, industriji, vojsci pa i zabavi. U ovoj doktorskoj disertaciji posebna je pozornost posvećena antenama koje su neizostavni dio takvih komunikacijskih sustava, te su istraživani posebni uvjeti propagacije elektromagnetskog vala u blizini ljudskog tijela, s ciljem pronalaska prikladnih antena koje bi se nosile na odjeći a osigurale bi pouzdan prijenos radijskog signala s površine ljudskog tijela, uz površinu tijela ili u tijelo, ovisno o konačnoj primjeni. Zbog karaktera komunikacijskih sustava na ljudskom tijelu kao dodatni zahtjev na antene postavlja se njihova estetska prihvatljivost i nenametljivost te niska cijena, ali i postojanost u realnim uvjetima okoline u kojoj su namijenjene za rad (prije svega otpornost na mehanička naprezanja i utjecaj vremenskih prilika).

U prvom poglavlju (*1. Introduction*) sažeto je prikazana motivacija i ciljevi rada, te je razrađen sadržaj rada. U drugom poglavlju (*2. An overview of body-centric communication systems*) dan je pregled današnjih znanstvenih i industrijskih trendova u istraživanju radijskih sustava na ljudskom tijelu zajedno s mogućim primjenama. Poseban naglasak je bio na dosadašnjem razvoju antena te uočenim tehnološkim problemima, čime je dana perspektiva istraživanja provedenog u doktorskoj disertaciji.

Treće je poglavlje (*3. Electromagnetic modelling of the human body*) posvećeno elektromagnetskim svojstvima ljudskog tijela koje je potrebno poznavati kako bi se mogao izraditi prikladan računalni ili laboratorijski model ljudskog tijela (fantom) te istraživati utjecaj antene i elektromagnetskih valova na ljudsko tijelo ali i utjecaj ljudskog tijela na antenu i radijski sustav. Uz odgovarajuću teorijsku pozadinu i pregled suvremenih metoda izrade fantoma, posebno je obrazložen izbor te opisana izrada i istraživanje osobina tekućeg fantoma koji se koristio u doktorskom radu.

U četvrtom je poglavlju (*4. Interaction between the antenna and the human body*) razrađivana problematika smanjivanja dimenzija antene koja predstavlja dodatni izazov u projektiranju antena u nižim frekvencijskim područjima kao što je UHF. Primjenom

metoda smanjivanja antena projektirana je i izvedena tekstilna antena u frekvencijskom području UHF. Predložena antena ima prorez u vodljivoj ravnini što povećava međudjelovanje antene i ljudskog tijela. Razvijen je i opisan jednostavni model međudjelovanja antene i ljudskog tijela za slučaj proreza u vodljivoj ravnini, te su opisana preliminarna mjerenja na izrađenom prototipu antene.

U petom poglavlju (*5. Propagation aspects for on-body channels and communications*) razmatrana je propagacija elektromagnetskog vala uz površinu ljudskog tijela kao i radijska veza dviju antena na tijelu. Podrobno je izložena teorija površinskih i puzajućih valova te je proračunom Greenove funkcije za beskonačni cilindar modelirano okruženje ljudskoga tijela. Analitički model uspoređen je s računalnim simulacijama te mjerenjima na tekućem fantomu i dobrovoljcu. Također su prikazani rezultati eksperimentalnog ispitivanja radijske veze na tijelu za različite položaje odašiljačke i prijemne antene na tijelu koje miruje i tijelu koje se kreće.

U šestom poglavlju (*6. Practical issues in the antenna design for body-centric communication systems*) razrađivani su praktični aspekti izrade tekstilnih antena. Predložena je metoda za ispitivanje elektromagnetskih svojstava komercijalnih tekstilnih materijala te opisana izrada i karakterizacija nekoliko prototipova tekstilnih antena za frekvencijska područja UHF i ISM 2.4. Sustavno su ispitivani utjecaj savijanja i vlage u tekstilnom supstratu na parametre antene, te je pokazano kako savijanje u E -ravnini i male količine vlage imaju znatan utjecaj na parametre antene.

U nastavku je istraživana upotreba vodljivih tekstilnih vlakana kojima bi se izradili vodljivi dijelovi antene. Pokazalo se kako je tekstilna mreža ušivena u neku postojeću tkaninu jednostavan postupak kojim je moguće ostvariti ravnotežu između željene vodljivosti i dobrih svojstava same odjeće. Nadalje, pokazano je kako je uporaba metalnog gumba za povezivanje antene s elektroničkim sklopovima dobar kompromis s estetskog i funkcionalnog gledišta. Na temelju istraživanja dane su opće smjernice za izradu tekstilnih antena te je u skladu s njima izrađen i karakteriziran prototip potpune tekstilne antene tipa PIFA. Pokazalo se kako je izrađena antena funkcionalna.

Na kraju doktorskog rada najvažnija postignuća i doprinosi izneseni su u zaključku, dok su u tri dodatka detaljnije razrađeni teorijski koncepti vezani uz rad – sferni harmonici, teorija površinskih valova kao i matematički aparat za analizu površinskih valovoda.

Ključne riječi: komunikacije u prisutnosti ljudskog tijela, tekstilne antene, vodljivi tekstili, puzajući valovi, propagacija duž ljudskog tijela, propagacija izvan ljudskog tijela, modeli ljudskog tijela, PIFA antena, utjecaj savijanja na antenu, utjecaj vlage u tekstilnom supstratu

CONTENTS

1. INTRODUCTION	1
2. AN OVERVIEW OF BODY-CENTRIC COMMUNICATION SYSTEMS	5
2.1. Wearable computers	6
2.2. Military communication systems	10
2.3. Medical sensing equipment	15
2.3.1. <i>Bioimplantable antennas</i>	19
2.4. Trends in the development of antennas for off-body and on-body communications	23
2.4.1. <i>Propagation mechanisms</i>	24
2.4.2. <i>Controlling surface waves</i>	26
2.4.3. <i>The frontiers in the frequency ranges</i>	30
2.5. Design aspects for wearable textile antennas	36
2.5.1. <i>Dielectric textile substrates</i>	39
2.5.2. <i>Conductive textiles</i>	41
3. ELECTROMAGNETIC MODELLING OF THE HUMAN BODY	47
3.1. Complex permittivity and conductivity	49
3.2. Dispersion models for electric permittivity	53
3.2.1. <i>Resonant model (Lorentz)</i>	53
3.2.2. <i>Relaxation models (Debye and Cole-Cole)</i>	55
3.2.3. <i>Electrical model of the human body</i>	56
3.3. Human body phantoms.....	60
3.4. Development of a liquid phantom for ISM 2.4 GHz.....	63
3.4.1. <i>Characterization of the wideband planar monocone antenna with the use of the phantom</i>	66
3.4.2. <i>Comments on the stability of the phantom with regard to aging</i>	70
4. INTERACTION BETWEEN THE ANTENNA AND THE HUMAN BODY	73
4.1. Fundamental limitations of the antennas	74
4.1.1. <i>Spherical modes of free space</i>	75
4.1.2. <i>The Chu approach</i>	77
4.1.3. <i>Field approach to the derivation of Q</i>	80
4.2. The proposed PIFA for 400 MHz.....	81
4.2.1. <i>Further analysis of the PIFA</i>	85
4.2.2. <i>Symmetric PIFA</i>	87
4.3. Modelling the interaction between the PIFA antenna and the human body	91
4.3.1. <i>PIFA without the slot</i>	91

4.3.2.	<i>Evaluating the impedance of the slot</i>	93
4.4.	Measurements on the prototype.....	98
5.	PROPAGATION ASPECTS FOR ON-BODY CHANNELS AND COMMUNICATIONS	101
5.1.	Planar surfaces.....	102
5.2.	Wavenumbers of surface waves.....	107
5.2.1.	<i>Lossy dielectric</i>	107
5.2.2.	<i>Conductive surfaces</i>	108
5.3.	Waves in cylindrical structures.....	110
5.3.1.	<i>Convergence issues. Watson transformation</i>	113
5.3.2.	<i>Green's function for cylindrical structures</i>	114
5.3.3.	<i>Searching for the creeping wave pole</i>	116
5.4.	Calculation of the creeping wave pole.....	118
5.5.	Measurements around the human body torso.....	120
5.5.1.	<i>Measurements on the human body phantom</i>	122
5.6.	Other on-body propagation measurements.....	124
6.	PRACTICAL ISSUES IN THE ANTENNA DESIGN FOR BODY-CENTRIC COMMUNICATION SYSTEMS	129
6.1.	Measuring the permittivity of textile materials.....	130
6.2.	Prototype of the wearable UHF 400 antenna and the influence of bending.....	136
6.2.1.	<i>Measurements on the prototype</i>	139
6.2.2.	<i>Antenna bending</i>	142
6.2.3.	<i>Antenna in the presence of the human body</i>	144
6.2.4.	<i>Remarks on the UHF antenna</i>	145
6.3.	Prototypes of the quarter-wavelength antenna for the ISM 2.4 band and a phenomenological evaluation of the influence of moisture.....	147
6.3.1.	<i>Improving the antenna design for the ISM 2.4 band</i>	151
6.4.	Design and characterization of the textile microstrip antenna for the ISM 2.4 band.....	153
6.4.1.	<i>The influence of the body</i>	154
6.4.2.	<i>The influence of bending</i>	156
6.4.3.	<i>The influence of the environmental conditions</i>	159
6.4.4.	<i>Antenna under extreme conditions - freezing</i>	162
6.4.5.	<i>Comments on the antenna placement on the body</i>	164
6.5.	Full-textile antennas.....	166
6.5.1.	<i>The preliminary measurements on the textile samples</i>	166
6.5.2.	<i>Creating the conductive mesh</i>	170
6.5.3.	<i>Realizations of PIFA antennas using embroidered conductive textile mesh</i>	173

6.5.4. <i>Effect of the conductive yarn</i>	176
6.5.5. <i>The feeding issue</i>	178
6.6. A practical strategy for the wearable antenna design	180
6.6.1. <i>Comments on the current density and the effective length of yarn</i>	186
6.6.2. <i>Characterization of the full-textile PIFA antenna</i>	188
7. CONCLUSION	195
APPENDIX A. SPHERICAL HARMONICS	199
Vector eigenvectors	199
Expansion in spherical coordinates.....	202
APPENDIX B. SURFACE WAVE - PROTOTYPE SOLUTION	207
Plane wave incidence – parallel polarization.....	207
Equivalent scheme – plane wave incidence.....	209
APPENDIX C. EQUIVALENT SCHEMES OF THE SURFACE	
WAVEGUIDING STRUCTURES	213
Surface impedance.....	213
Dielectric slab.....	215
Surface waves in the wave spectrum	219
REFERENCES	223
ABOUT THE AUTHOR	235
AUTHOR’S PUBLICATIONS	237
O AUTORU	241

1. INTRODUCTION

Body-centric systems refer to communication systems which include communication in the presence of the human body. They can be considered as a continuation of the trend started by the development of mobile phones, while their possible applications range from military communication systems to medical telemetry or commercial use. The antenna is a necessary part of any body-centric device, so its design needs to be modified to conform to the specific demands and characteristics of the body-centric environment. This thesis deals with the design of small planar antennas, suitable to be worn on the body, and thereby used in body-centric communication systems. The main concerns of the thesis are:

- the properties of textile substrates used for the design of wearable antennas
- the specific characteristics of the body-centric environment compared to free space
- the use of conductive threads for the manufacturing of conductive parts of antennas, which would suitably replace the conventional conductive materials
- a strategy for the design of wearable textile antennas

The thesis begins with a comprehensive and up-to-date overview of relevant literature and research directions in body-centric communication systems, putting the main goals of the research into broader perspective. A review of present and future applications is given, followed by current trends in antenna design for body-centric applications. Emphasis is put on the demands on antennas for off-body and on-body applications, and, finally, some design issues regarding textile antennas are summarized.

In the course of the thesis, several antenna prototypes in the UHF (around 400 MHz) and ISM (around 2.4 GHz) bands have been designed, and used to evaluate different aspects of the body-centric environment. The former band is suitable for medium distance communications (e.g. military or rescue-service applications); however, the size of the antenna is the main challenge due to the large wavelength. The latter band, on the other hand, enables the design of antennas with better radiation characteristics (due to lower demands on size reduction); however, it is only suitable for communication over shorter distances due to higher losses.

A professional CAD program, CST Microwave Studio, was used to design the antennas, optimize their dimensions and performance, and calculate electromagnetic fields and currents when needed. The relevant results were verified by measurements performed using the Rohde&Schwartz ZVA 40 vector network analyzer. For evaluating the antenna performance in the vicinity of the human body, measurements were performed partly on the volunteer, and

partly on a physical phantom manufactured using water solutions of salts and ethers which mimic the electric properties of the human body.

The theoretical investigation of the interaction of the antenna with the human body was performed using numerical calculations and an analytical model. The PIFA antenna was designed with the slot in the ground plane, and it was shown that the coupling of the antenna and the body through the slot is significant when the radiating part of the antenna (i.e. the patch) is placed over the slot. Such coupling can reduce the radiation efficiency down to only -17 dB, so the position of such a slot needs to be controlled and avoided for off-body and on-body communications. In order to gain clearer insight into the features of the PIFA antenna and the slot in the ground plane, an equivalent circuit was derived, explaining the increase in the antenna resonant frequency when the antenna is placed on the body. An analytical model is obtained for propagation around the torso, estimating the path loss which needs to be taken into account in the design of on-body communication systems.

On-body and off-body communications were also investigated in the real environment. For on-body communications, two antennas were placed on the body of a volunteer, and for off-body communications, one antenna was put on the body and another (a calibrated UWB horn) was in the room, acting as a base station. In that way, a simple communication system consisting only of a transmitter and a receiver was obtained, and the transmission parameter of the system was measured for various relative positions of the antennas. This research reflects similar research in literature, whereas the main goal here was to obtain insight into the communication channel from the viewpoint of the antenna engineer (i.e. space and surface waves), and to estimate the limitations of analytical modelling in the realistic environment.

The antennas have also been exposed to mechanical deformations such as bending, and extreme environmental conditions such as applying water (which simulates rain) and freezing. For these cases changes of bandwidth, input impedance and gain were measured. It was found that bending in the E -plane is more critical for the antenna properties than bending in the H -plane, and the strategy suggested was to extend the bandwidth of the original antenna so as to enable it to cope with the shift in the resonant frequency when bent. Furthermore, it was found that choice of the position of the antenna on the body also affects antenna characteristics, so it was suggested that the antenna should be placed on the parts of body which reduce the probability of bending or other deformations. It was also found that moisture in the textile substrate has a strong influence on the antenna properties, even for low water content in the textile substrate.

In the final stage, the use of conductive textiles was investigated. To make the antennas flexible, as well as a true part of clothes, the use of conductive textiles for making the conductive parts of the antennas is advised, if possible. The conductive textiles were created using two methods – weaving and embroidering, while the latter was found to perform better in terms of simplicity of manufacturing, controlability of the conductive thread densities, as well as in terms of fully becoming a part of clothes. After obtaining the most suitable conductive textile material, the prototype of a full-textile PIFA antenna was designed and shown to operate properly. The design of the full-textile PIFA can also be generalized to a more general strategy for the design of wearable antennas. This strategy is based on the experience obtained and issues observed in the design of wearable antennas throughout the thesis, together with the insight gained into the coupling between antennas and the human body, properties of textile substrates and conductive textile realizations.

2. AN OVERVIEW OF BODY-CENTRIC COMMUNICATION SYSTEMS

The development of the mobile phone in 1980s marked a new era in electronics, as various personal wireless communication devices started to become a part of everyday life, and their use has been growing ever since. Such progress was conditioned by advances in the technology of electronic component fabrication, which enabled the size of such components to be reduced, making devices convenient for the user. Since antennas are necessary parts of any wireless device, techniques for reducing their size have consequently emerged in order to conform to the demands of modern communication systems. Unlike with electronic components, the antenna miniaturization is a virtue of compromise between volume, bandwidth and efficiency, due to fundamental physical constraints (the antenna size needs to be comparable to the wavelength). Furthermore, advances in embedded software and digital signal processing have enabled modern personal devices to acquire many functions, such as voice and data transfer, as well as positioning and entertainment. Along with this trend, advances have also occurred in the area of implantable sensors for medical telemetry, as well as in the development of communication systems for specialized occupations (military teams, firefighters, emergency rescue teams...) [1, 2].

The term *body-centric system* refers to a personal communication system which consists of body-worn devices which communicate with the environment (“off-body”), mutually (“on-body”) and, possibly, with medical implants (“in-body”). Such a system can be seen as a convergence of wireless and wired networks with consumer electronics, computer technology and communications [1].

In this chapter we outline the state of the art in the area of body-centric communication systems, with regard to the possible applications and current trends in the related technology. The communication and antenna aspects are emphasised, and concepts from literature regarding operation in various frequency ranges, from below 1 MHz to around 60 GHz, are reviewed. We also describe the concepts and visions from consumer electronics that have paved the way to the current scientific activities in the area of body-centric systems, thus putting them into broader perspective. Finally, we review the practical issues regarding the design of wearable antennas, such as common properties of materials for dielectric substrates, and address the design of conductive threads as the critical point in the final design of the antenna.

2.1. Wearable computers

As early as in 1993, the vision of so-called *wearable computing* was proposed at the Massachusetts Institute of Technology (MIT) [3, 4] as the next step in the development of personal electronic devices, while the first concrete steps towards its realization were taken in the late 1990s and the early years of the 21st century. Such a concept consisted of unifying the functions of various personal devices of that time (mobile phone, personal digital assistant-PDA, pager, laptop, electronic translator, medical sensors, etc.) into one interface that would provide portability during operation, while at the same time not requiring much conscious attention. The philosophy of wearable computers was inspired by the concept of the *cyborg* (a man-computer symbiosis) from the popular literature in the 1960s [5]. The main principles of wearable computers can be summarized as in [4, 5]:

- usability at any time and any place, not just at the desk
- constant access to information services
- augmenting human perception and reality and mediating interaction between the user and the environment
- awareness of the environment and adapting interaction modalities based on the user's context
- user interface which allows for the focusing of the user's attention and presenting information in an unobtrusive, context-dependent manner

In Fig. 2.1, two prototypes of wearable computer are shown. The left prototype was produced in 1994 by the Matias Corporation, and consists of a small display worn on one forearm and a half-QWERTY keyboard (which can be used for one-hand typing) on the other forearm. This concept was later commercialized by IBM, Panasonic, Nokia and other developers, but only a few achieved any considerable market success.

On the right picture, one version of the prototype of the wearable computer built by the University of South Australia in 2003 [4, 6] is shown. This computer features the technique of so-called *augmented reality*, which superposes computer-generated images and data over the user's view of the physical world by using a see-through head-mounted display (HMD), which eventually overlays the wearer's actual vision of reality with additional virtual information. The augmented reality technique can therefore be seen as a convenient and unobtrusive way of interaction between a computer and the user, which enhances their vision of the physical world [4].

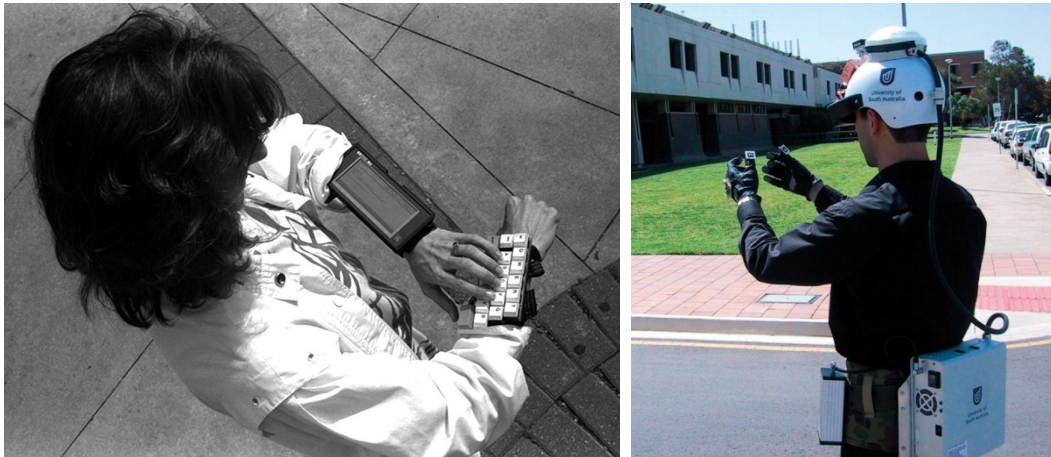


Figure 2.1 Prototypes of wearable computers [4]

In Fig. 2.2, the wearable wrist-worn computer proposed in 2007 by Eurotech is shown. This device is intended primarily for emergency, security and logistics applications. It supports several communication protocols, and contains GPS, audio and video sensors [7]. To date, several other wearable computers have been manufactured; however they share similar characteristics as the examples described here.



Figure 2.2 Wrist-worn wearable computer, Zypad WL100, developed in 2007 [4, 7]

Another idea present from the beginnings of wearable computers is to use everyday clothes, and to integrate as much electronics as possible into them, which leads to the concept of so-called *e-textile* or *smart clothing*. Such a concept has given rise to research looking for new textile materials that would support integration of various electronic components, while maintaining the primary function of clothing (Fig. 2.3). The ultimate goal is to implement the whole computer, its communication system, peripheral sensors (on-body and in-body) and power supply into clothes and accessories such as shoes, rings, glasses etc. [4, 8]. In that way,

the wearable computer would become a practical everyday device that would indeed enhance the user's way of life, and change the way computers are used today.

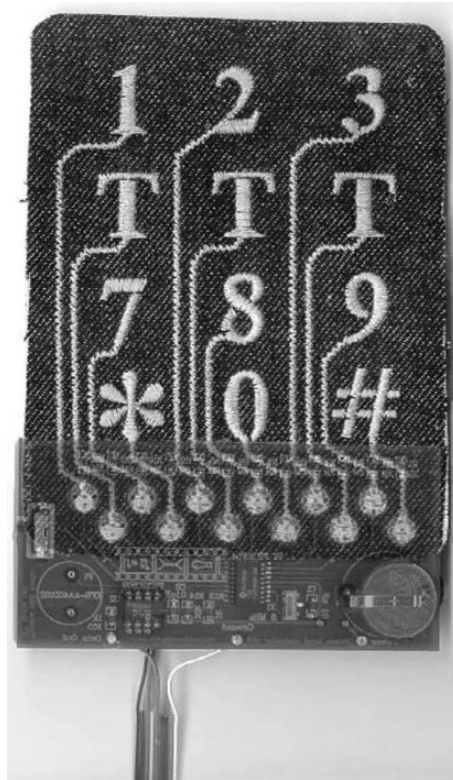


Figure 2.3 Keyboard embroidered into a jacket using smart textile [5]

Although the miniaturization of electronic components, as well as the development of microprocessor hardware and software, have made a huge variety of applications possible, one of the main challenges for wearable computers is the power supply. The enhanced functionality and additions of peripherals to wearable computers require large amounts of power, and the distribution of power becomes more complicated. If the battery life is too short, then the wearable computer is impractical for use. Larger batteries, on the other hand, make the computer too bulky, while the use of exotic batteries (e.g. Plutonium 238) suffers from political and environmental issues. The proposed solutions are wireless charging through inductive coupling with a charger set in the environment, converting mechanical energy such as the energy created by pressing a keyboard or the energy of walking, using solar panels integrated into clothes etc. Such solutions are, however, yet to be realized [5].

Another challenge is the interaction between the user and the computer. Interaction using a wrist-mounted keyboard (as shown in Fig. 2.1) or a hand-held trackball can still be deemed rather impractical (as it requires a lot of attention from the user), so the solution is to equip the wearable computer with sensors placed on-body, which would eventually replace manual

information entry by context awareness (location, activities, environment), and combine it with communications using voice and hand gestures [4, 8]. In addition, the head-mounted display (HMD) and augmented reality which were originally envisioned as the most suitable and unobtrusive form of communication are too expensive for mass production, so research has been redirected into hand-held displays as the currently dominant, yet less ambitious, form of display [8]. For instance, the wrist-worn computer shown in Fig. 2.2 clearly reflects this trend.

In parallel to the developments in the area of wearable computers, recent years have seen the emergence of smart phones as mainstream consumer devices, since they provide a broad range of sensors and a capability for a more than sufficient amount of data transfer for an average user. Although smart phones do not exactly follow the principles of wearable computing, they are widely accepted, and more feasible with regard to the present state of technology, thus presenting a fair compromise between user demand, power supply, price, and production capabilities. It could, therefore, be argued that the vision of full-scale wearable computers is still a rather futuristic one, too ambitious at this time and not adopted by the general public at the moment. Here we note that some research in the area of wearable computers is still going on for specific professions, such as military or rescue teams, which require powerful and portable computing and communications in various environments [4, 8].

Nevertheless, some elements of this vision, such as integrating and interconnecting various sensors and clothes, providing personal networking access (e.g. Bluetooth, Wi-Fi, etc.), extending the functionality of the smartphone using carry-on peripherals (e.g. Bluetooth headset), are still being extensively researched, with the goal of achieving a degree of integration between the user and the environment. This is what is meant by the term *body-centric communication systems* in today's sense.

Two examples of commercial peripheral on-body sensor systems are given in Fig. 2.4. The left system consists of a sensor embedded in shoes, which communicates with a handheld device and sends data and statistics about how fast the user is walking or running, how many calories are spent, what distance is passed etc. [9]. The right system is worn on the triceps, and consists of several sensors that collect data about temperature, skin conductivity, calories spent, heat flux, number of steps taken while walking, etc. It can serve as an auxiliary tool for physicians – by monitoring the lifestyle data of the patient using this sensor for some time, could, for example, help prevent and treat some chronic diseases [10].



Figure 2.4 Examples of commercial on-body sensors. Left: Nike+iPod musical shoes [9]; right: BodyMedia SenseWear system [10]

2.2. Military communication systems

Alongside the trends in communication systems for the general public and research in wearable computers, communication between soldiers on the field is one of the primary needs for military teams, since having knowledge about the action on the ground and the position of other soldiers and military units, while at the same time being connected to the headquarters, clearly improves the effectiveness of the team (Fig. 2.5). In addition, some future scenarios include the implementation of sensors for monitoring the physiological condition of soldiers, so the action can, if needed, quickly be modified from the operating centre with regard to the situation on the field [11]. Hence, establishing a stable, fast and reliable communication system that allows for the transfer of large quantities of information is of great interest for the military. Such a communication network needs to be independent, since military teams often operate in environments where no other communication systems are present (forests, caverns, mountains, deserts, canyons etc.), while the transferred data needs to be safe from interception from e.g. hostile units.

Modern communication protocols are principally able to provide fast and secure data transfer for most cases, so the challenge that remains is the development of various sensors and the improvement of the quantity and quality of information they send and process. The sensors themselves are, nevertheless, quite convenient for placement on the body or integration into clothes, since the electronic components they contain are nowadays miniaturized enough so as not to require much space.



Figure 2.5 Typical battlefield scenario [11]

Apart from the development of sensors, another major challenge is the connectivity – the transfer of data among soldiers, military units and operation centres is performed wirelessly, i.e. antennas are needed as a mediator between sensors and free space. Thus, the issue on the hardware level is to build antennas which can support large data transfer over short and medium distances (usually up to a few hundred meters), are durable under different weather and environmental conditions, and can be integrated into the uniform (typically in the helmet or suit) so that they do not impose any constraints on soldiers' activities. Similar communication issues also arise for various emergency rescue teams, or even space and astronaut teams, so they are considered together here, while the proposed antenna solutions are applicable and modifiable to meet the specific demands of each team.

In general, large wavelengths exhibit smaller path losses, so for off-body communications over a medium distance, VHF and UHF frequency ranges were researched first, since in these bands electromagnetic waves are able to penetrate through heavy weather, foliage, concrete buildings etc., while the dimensions of the antenna, compared to the human body, are still suitable for trying to conform the antenna to the body [12]. Several proposed antenna designs have been reported for frequencies from around 100 to 400 MHz [12–18]. These antennas are mainly of large dimensions, small gain (due to losses in the body), and support relatively low data rates; hence the motivation to explore higher frequency ranges for use when possible. In addition, these antennas are typically ultra-wideband (bandwidth>20%), but intended for operation in a narrower sub-band (contained in the total bandwidth of the antenna), so the influence of the body does not cause detuning of the antenna in the desired band [13].

In Fig. 2.6, the possibility of the placement of the UHF antenna in a military vest is shown. The particular antenna was produced by introducing modifications to an asymmetric flared

dipole antenna, and operates in the range $225 \div 400$ MHz [14, 15]. The idea is to imprint the antennas onto the bulletproof ceramic plates which are incorporated into the vest, which is a practical solution, not obtrusive to the soldier, while at the same time isolating the antenna from direct contact with the body, thereby somewhat improving radiation efficiency. Furthermore, since the bulletproof ceramic substrate possesses the electrical permittivity of around 10, the reduction of the antenna size is also possible.

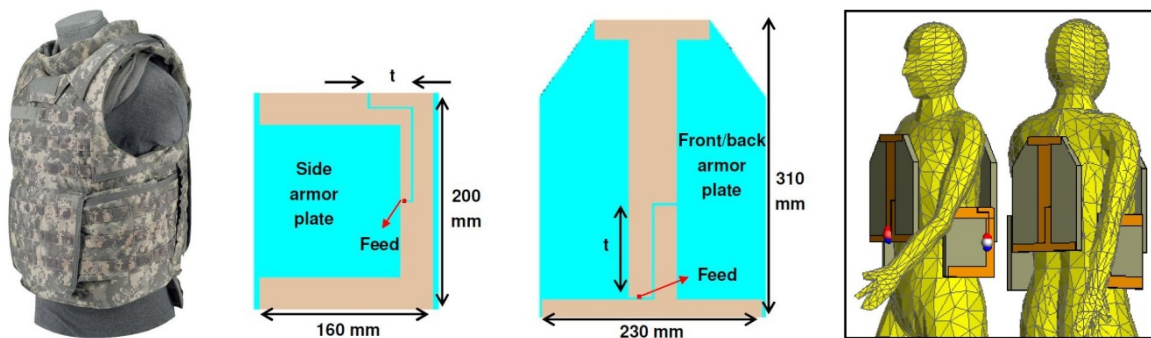


Figure 2.6 Typical military vest and placement of the antennas on the bulletproof armor plates contained in the vest [14]

In Fig. 2.7, another example of a vest-mounted antenna is given. This antenna is a component of the so-called Combat Wear Integration (COMWIN) concept [16], and is intended for radio frequencies and portable radios, while exhibiting suitable impedance coverage ($VSWR < 3$) in the range of $30 \div 500$ MHz. Here, the idea is to construct the entire vest using a thin, canvas-based conductive textile material (“Electron”), except for the small gap that separates the upper and lower half of the antenna and extends around the torso. The copper tape (as seen in Fig. 2.7) is used only to enable the soldering of the coaxial cable that feeds the gap from the back side. Therefore, this antenna is basically a horizontal slot antenna conformed to a vertical cylinder (i.e. body) of finite height. Wideband impedance coverage was obtained by optimizing the width and shape of the slot [16].

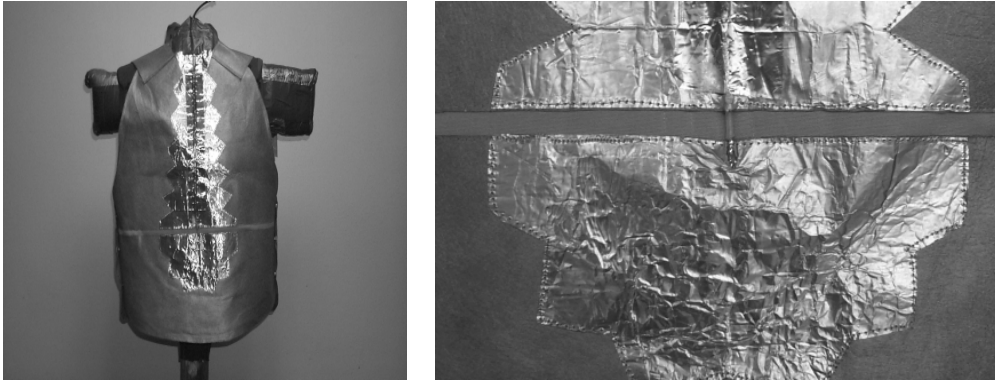


Figure 2.7 UWB antenna for portable radios [16]

As an example of an antenna for the ISM 2.4 (2.4÷2.48 GHz) band, a circularly polarized antenna originally made for protective clothing for fire-fighters (however, it can be simply modified for other military or rescue teams) is shown in Fig. 2.8 [19, 20]. This antenna is merely a rectangular patch on a foam substrate with truncated corners and a diagonal feeding which excites both TM_{10} and TM_{01} modes. In addition, since the resonant frequencies of the two excited modes are slightly shifted (due to the difference in patch length and width), operation in the relative bandwidth of around 10% is obtained, which enables comfortable bandwidth for operation, and reduces the possible detuning when placed on the body. The circular polarization and placement of several antennas on the clothes further give rise to polarization and radiation pattern diversity, which can mitigate the effect of fading by multipath, which occurs in the real environment. To prevent the antenna from being damaged by extreme environmental conditions such as fire and water, the antenna was integrated in the fire-fighters' protective jacket beneath the fireproof outer layer and the waterproof layer, as suggested in the right picture in Fig. 2.8 [20]. The same circularly polarized antenna was successfully rescaled to cover the GPS-L1 band (around 1.575 GHz) in [21], so the positioning and navigation of fire-fighters (or members of a rescue team) can be obtained using the same antenna concept as another possible functionality.

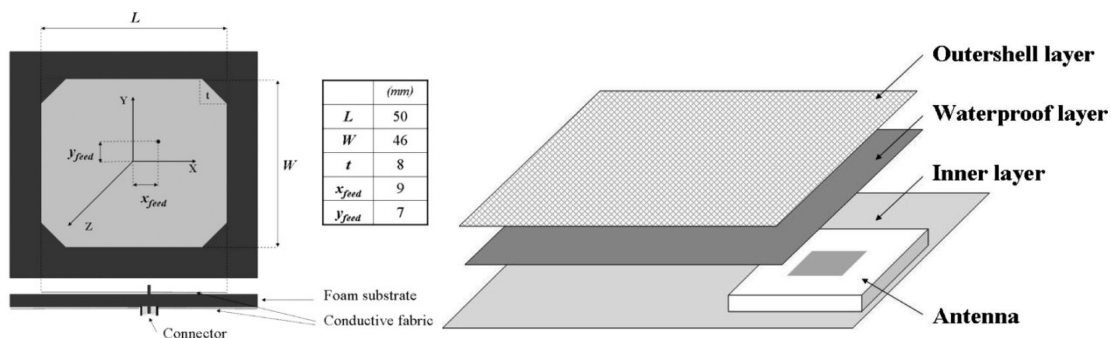


Figure 2.8 Circularly polarized antenna for fire-fighters and rescue teams [19, 20]

Body-centric systems are also being researched for space applications, since their application can be useful, e.g., for the future Lunar and Martian outposts planned by NASA and several other space agencies around the world. The typical link between the astronaut and the operation system is obtained using voice over internet protocol (VoIP), coupled with standard high-definition video of the astronaut and the surrounding environment. In addition, biotelemetry data, tracking, navigation and mobile computing are also expected to be used in the next generation of astronaut suits, which means that large data rates are required. Therefore, the design of light-weight antennas which provide enough bandwidth for large data rates, and are electronically reconfigurable when changing the antenna platform, is being extensively researched for space applications [22, 23].

In Fig. 2.9, some solutions for space applications are summarized. In the upper left picture, the equiangular spiral antenna which operates in the range of 2÷4 GHz is shown, while in the upper middle picture, the 8-element antenna array is shown. Such an array could be, for example, mounted as an access point on a habitat wall in Lunar or Martian posts, or used as a body-worn platform [23]. In the upper right picture, the antenna called “complementary 8-element” is shown, while the integration of six antennas of this kind into the so-called EVA-extravehicular activity suit for astronauts is shown on the bottom. This antenna exhibits acceptable ultra-wideband impedance matching for the 2.1÷10 GHz range, while multiple antennas integrated into the suit enable radiation pattern diversity. In addition, although antennas are linearly polarized (since circular polarization in UWB systems would require additional complex electronics), multiple antennas are placed in a way that also enables polarization diversity using the antenna system beamformer. The conductive part is made of an e-textile called “Nora” (with a declared resistance of 0.03 Ω /sq [23]), which exhibits a similar performance to conventional conductive materials. The use of e-textile enables direct integration with the suit’s textile layers, which presents another flexibility compared to the metal plates formerly used in suits (their use was restricted only to the rigid portions of the suit).

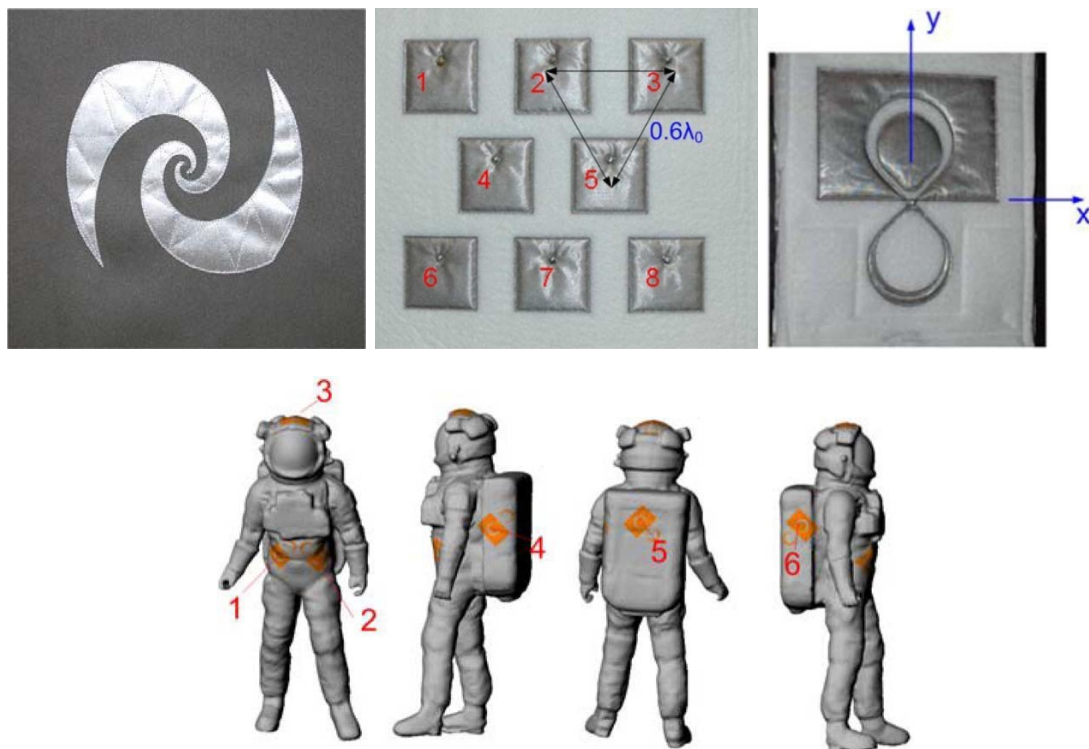


Figure 2.9 Antennas and antenna arrays for space applications and examples of their placement on the astronaut suit [22, 23]

2.3. Medical sensing equipment

The idea of remote patient monitoring has a history starting from the beginning of the 20th century (1906), when electrocardiography (EKG) was first introduced. In addition, pacemakers and cochlea implants are other examples of well-established and widely used implants in the body which have improved life quality of many people. The miniaturization of electronic components, submicron electronics, nanotechnology and microelectromechanical systems (MEMS) have also led to the construction of microscopic implantable sensors and drug release devices, as well as mobile robots that could treat various conditions and monitor the patient's status from a distance. Therefore, the need for a reliable communication link between implanted devices and external monitoring devices has consequently emerged, which has given rise to the concept of *in-body* communications [1].

In Table 2.1, the most common body data measured using various implantable sensors are summarized, and the required bandwidth for remote patient monitoring is also illustrated. These data are collected by the sensor in the body, and transmitted to the base using, e.g., a data controller placed on the body which collects and resends sensor data (data could also be sent to a handheld monitoring device or even directly to the base station).

Table 2.1 Common signal parameters in patient monitoring [1]

Signal	Typical amplitude	Clinical resolution	Bits/Sample	Typical sample rate (Hz)	Data rate (kb/s)
Body temperature	30°C ÷ 45°C	0.1°C	8	0.01	≈0
Fluid output	0 ÷ 1000 mL/h	1 mL/h	10	0.1	≈0
Fluid intake	0 ÷ 100 drops/min	1 drop/min	8	1	≈0
Respiration	12 ÷ 40 breaths/min	1 breath/min	8	0.01	≈0
Oxygen saturation (S _p O ₂)	70% ÷ 100%	1 %	8 ÷ 10	100	1
Blood pressure	Systolic: 0 ÷ 250 mm Hg Diastolic: 0 ÷ 200 mm Hg	1 mm Hg	9	120	1
EKG	1 mV p-p	10 μV	8 ÷ 12	250	9
EEG	10 ÷ 100 μV p-p	1 μV	12	200	153.6

The earlier versions of human body sensors were inductively coupled (i.e. via near field) with a controlling device outside the body, as principally shown in Fig. 2.10. In the same figure, communication with a pacemaker is shown. The small coil is implemented in the pacemaker, while a larger external coil is placed on the chest of the patient, thereby establishing an inductive link. The carrier frequency ranges from 9 to 315 kHz with a data rate of up to 512 Kb/s [1]. In addition to this example, several other inductive in-body links have been reported, with the carrier frequency ranging from 1 to around 100 MHz, and with the typical antennas being based on loops, coils, wound spirals of various shapes, etc [1].

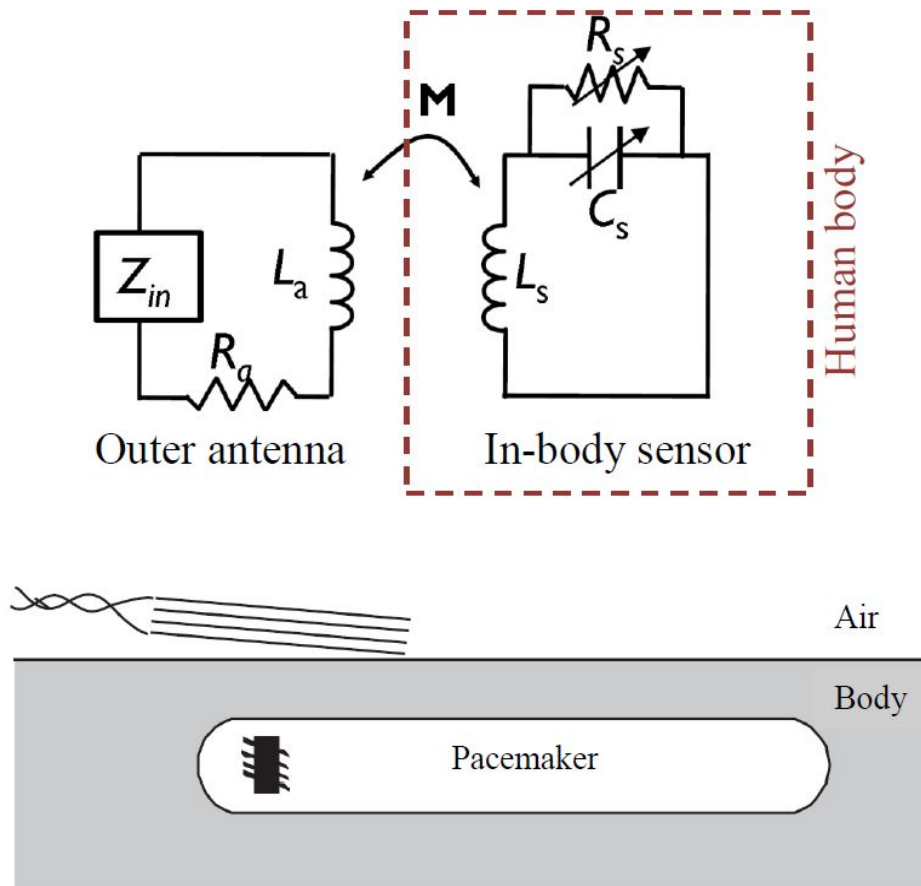


Figure 2.10 Principle scheme of in-body sensor operation and communication with a pacemaker [1]

The main drawbacks of inductive coupled communication systems are the low bandwidth (and, hence, low data rates), and the range of communication restricted to only a few centimetres from the body (due to poor radiation efficiency). Also, the inter-coil positioning needed to get a reliable link is rather sensitive, adding to the complexity of such a system. To overcome these limitations, modern research in implantable sensors and communications is oriented towards establishing a radiofrequency (RF) link between implants and outer devices [1, 24].

Since 1999, several standards for biotelemetry and communication with body implants have appeared, while the most important one is called MICS (Medical Implants Communication System), which extends from 402 to 405 MHz. This standard is currently regulated by the United States Federal Communications Commission (FCC) and the European Radio Communications Committee (ERC). It allows for 10 channels of 300 kHz of bandwidth, and sets the maximum effective isotropic radiated power to -16 dBm to avoid interference with the collocated Meteorological Aids Service band [24, 25]. This standard possesses the

advantage of being available worldwide, providing high data-rate transmissions, acceptably propagating through human tissues, and lending itself to small antennas [24]. It also requires transmitters in the implanted device to transmit the signal only when commanded to do so by an external controller (except for the so-called “medical implant event” – an emergency situation vital for the safety of a patient), and to use frequency agility techniques to avoid narrow-band interference by selecting a channel with the lowest ambient noise. As for other standards, in the US there is also the Wireless Medical Telemetry Service (WMTS), used, e.g. for transmitting video images through sensors with integrated cameras, and occupying three bands - 608÷614 MHz, 1395÷1400 MHz and 1427÷1432 MHz [25]. Finally, the ISM (Industrial, Scientific, Medicinal) band (2.4÷2.48 GHz) can be used for sending data to an implant; however, it does not allow for sending data from the implants, and is shared with other computer equipment services (Bluetooth, Wi-Fi) that use the same band, which can make communication difficult in some cases [1]. The ISM band can still be used for wirelessly powering the implants, i.e. sending a “wake-up” sequence, similar to the principle used in RFID [26, 27].

Using an RF link, the on-body controlling unit or handheld device (Fig. 2.11) can collect data from the implanted sensors, and send them further using existing communication protocols. Therefore, by establishing the radiofrequency link between in-body implants and external monitoring devices, the patient can stay at home while still being remotely connected to the emergency team in a hospital, which monitors his status, thus improving healthcare in general.

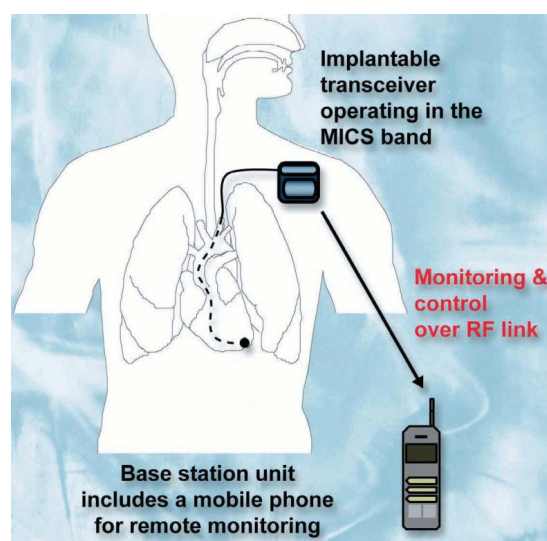


Figure 2.11 Principle of an implantable MICS transceiver [25]

2.3.1. Bioimplantable antennas

A critical point in RF-linked implantable communication systems is to design a suitable antenna. The antennas and propagation systems for medical applications share similar characteristics to other body-centric applications; however, the transmitted power is much lower, while antennas are electrically small, which leads to a generally poor radiation efficiency. In addition, the human body is a hostile environment for radiofrequency propagation, due to conductive losses which it introduces. Moreover, since the human body is conductive, placing conductive parts of an antenna in direct contact with body tissue would short-circuit the antenna. The implanted antennas also need to be biocompatible, which means that the materials used for the antenna must not be detrimental to the user's health, and the implant should not be rejected by the body. All in all, the design of a proper bio-implantable antenna is a challenging task due to the many demands in a realistic scenario. To avoid the problem of antenna-tissue contact, and, at the same time, to preserve biocompatibility, the conductive portion of the antenna is usually covered by a superstrate, or the bio-implantable antenna structure insulated using a thin layer of low-loss biocompatible clothing [24]. The summary of biocompatible materials used for antennas for medical implants, together with their electric properties in the MICS band, is given in Table 2.2.

Table 2.2 Biocompatible materials for implantable antennas [24, 29]

Material	ϵ_r	$\tan \delta_e$
Teflon	2.1	0.001
MACOR [®]	6.1	0.005
Ceramic alumina	9.4	0.006
zirconia	29	≈ 0
PEEK (Polyether ether ketone)	3.2	0.01
Silastic MDX-4210	3.3	≈ 0
Rogers RO3210	10.2	0.003

Patch antennas with various modifications are receiving considerable attention as a good candidate for bio-implantable antennas, due to their flexibility in design, shape and conformability, which allows for the relatively easy miniaturization and integration into the structure of a biomedical sensor [24]. A typical example of a bio-implantable antenna is given in Fig. 2.12 [28, 29]. This particular antenna is a dual-resonant meandered patch, made on the

Rogers RO3210 substrate (the superstrate of the same material was also added to protect the metallic part of the patch from the body), and designed to send data collected by the body sensor in the MICS band, while being powered by the “wake-up” signal from the outside source in the ISM 2.4 band, thereby being able to remain in the sleep mode when not in use, which reduces energy consumption. The final antenna design was obtained using the particle swarm optimization algorithm, and is intended for skin implants for glucose monitoring applications [28, 29].

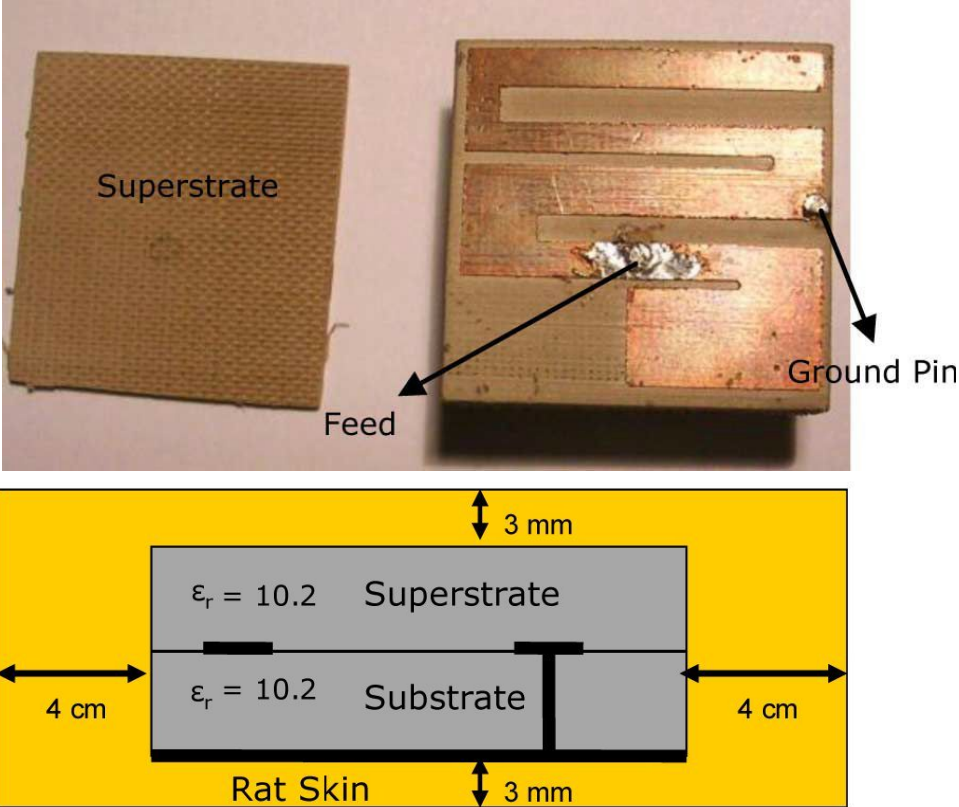


Figure 2.12 Prototype of a dual-band bio-implantable antenna and the scheme of its implementation into rat skin [28, 29]

To research the characteristics of the antenna in the supposed environment, skin-mimicking phantoms have been produced both for the MICS and the ISM band, and the measurements were first performed on the phantom and on real skin tissue samples taken from rats, with simulated and measured results generally matching [28]. To further evaluate such a testing procedure, and investigate the influence of live tissue on the antenna properties, in [29], the *in-vivo* testing of the antennas by implementing them into the skin of live rats (which emulated an environment as realistic as possible) was performed (Fig. 2.13). Here, some

discrepancies in the antenna performance were observed between the simulated and measured results (although the antenna appeared to work properly in the MICS/ISM band). These discrepancies possibly arise due to the air gap and interstitial fluid between the antenna and the skin, internal body temperature, variation of tissue electrical parameters due to the age of rats etc. This example outlines the challenges and difficulties in designing an implantable antenna. It needs to be tested in the surrounding space in which it is supposed to operate, yet the realistic environment is difficult to model due to many contributing factors. Therefore, *in-vivo* testing is a vital step for assessing the performance of the antenna designed using conventional strategies. It provides feedback for the designer for further modifications of the first design, in order to obtain the final product [29].

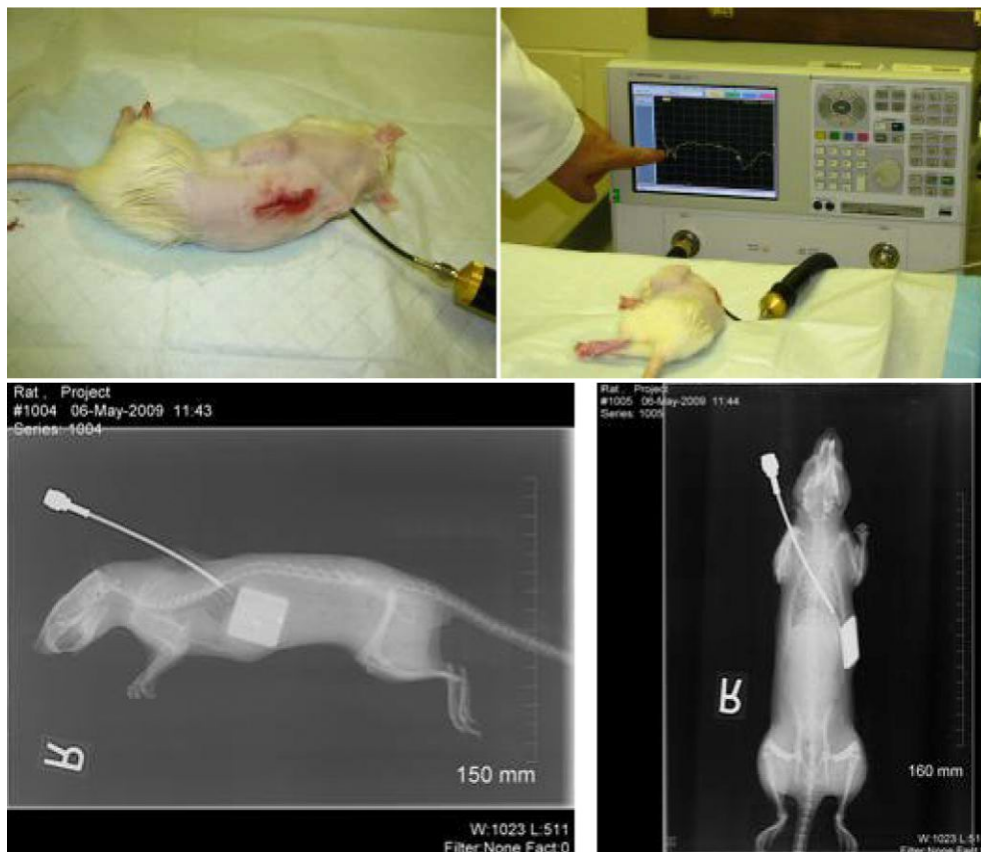


Figure 2.13 The antenna implanted into rat skin – setup and X-ray image [29]

In [30 – 32], the design of a multilayered implantable spiral antenna was described in detail, and some general procedure steps and issues in practical antenna design were outlined. The final antenna operates in the MICS/ISM band, and is shown in Fig. 2.14. Note that a bio-implantable antenna typically possesses low gain (of the order of -20 dBi and even down to -30 dBi, especially in the MICS band, where the antenna is electrically smaller [30]), which

means that it radiates poorly, and the improvement of the antenna gain is generally a challenge. Nevertheless, it is still suitable for personal area network communication for up to 10 m in the MICS and 5 m in the ISM band using some already available transceivers such as Zarlink [31]. The design procedure can be outlined as follows [31, 32]:

- choose an initial antenna type depending on the available volume, required bandwidth and electronics to be used
- perform an initial design in free space using, e.g. classical antenna miniaturization techniques (although this is an unrealistic scenario, such a procedure speeds up the simulations and gives the rough antenna design)
- add the surrounding medium (i.e. a numerical body phantom and biocompatible material coating) into the simulations and tune the initial design; if necessary, gradually add complexity to the phantom and retune the antenna again
- design the first prototype and characterize its performance on the physical phantom and *in-vivo* if possible
- modify the prototype to address the issue of the real environment, influence of the actual feeding method and other practical issues

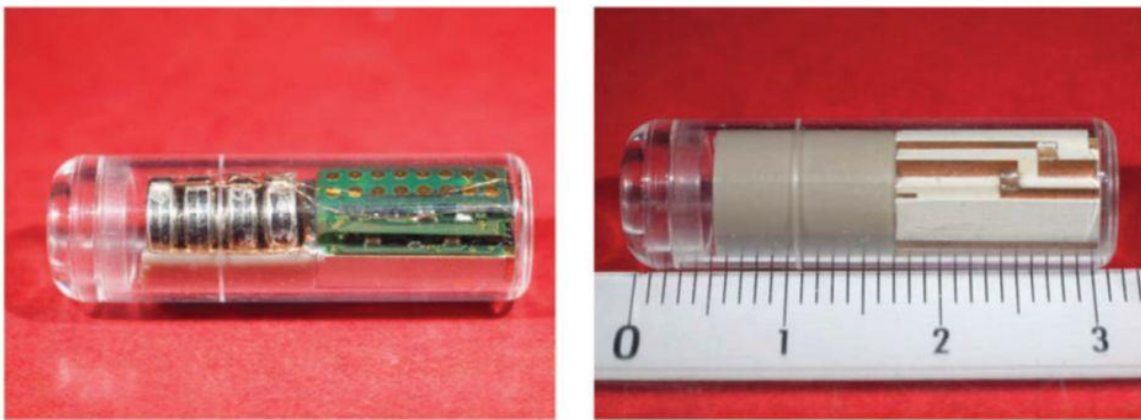


Figure 2.14 Multilayered spiral antenna with implant and circuitry [32]

The mentioned design procedure shows some additional steps which need to be taken when designing an antenna for application in the human body, compared to a general antenna design where the surrounding medium is free space. The presence of a lossy and inhomogeneous medium such as the human body extends the simulation time (when the simulation is performed in a realistic scenario), and adds some more uncertainty to the antenna design since, in that case, the antenna performance cannot be observed by itself, but only together with the body. Therefore, the idea is to perform the design process in a few

steps, being aware that each particular step is intermediate, and knowing what one wants to achieve by taking that particular step (i.e. the idea is to control one variable at a time). Basically, one starts from a rough and simple design, while complexity (in terms of refining the surrounding body model) needs to be added gradually, and the initial design retuned over and over to match the added complexity. Although this may appear tedious, in the end, it is less time-consuming than proceeding immediately from scratch to the final scenario [32]. We also note that the abovementioned guidelines for antenna design are quite general, and in addition to the design of bio-implantable antennas, they can be useful for the design of antennas for other applications that include the human body as a significant participant in the communication and wave propagation process.

2.4. Trends in the development of antennas for off-body and on-body communications

In previous subchapters we have shown some typical scenarios where body-centric systems can be applied, and provided an overview of the typical issues which arise from each application. Since wireless communication among body-worn devices is almost by definition required for their operation, and the antenna is a crucial part of any wireless device, the development of suitable antennas and antenna systems is an important part of modern communication and antenna science, regardless of the final application of devices. In section 2.3, some critical points were outlined for the design of bio-implantable antennas for *in-body* communications (i.e. communications between the implant and a body-worn device or base station), where communication needs to take place through the body, a rather hostile medium due to losses it introduces. Another concern is the influence of the antennas and electromagnetic waves on human safety, which leads to the demand for proper insulation of the antenna (and the implantable sensor) from the organs of the body, and establishing communication systems which operate properly with generally low transmitted powers. Since implants are intended to be worn on-body for a long time, powering issues arise as well (especially where there is large data transmission, which consumes a lot of battery power). Although there are some methods to recharge the implant battery noninvasively (e.g. by inductive charging), the most feasible idea is to extend the battery life by using the implant only when needed, which gives rise to dual-band communication protocols such as MICS/ISM [24]. All these issues add another layer of complexity to the antenna design, compared to the design in free space, so compromises are needed.

2.4.1. Propagation mechanisms

As for *on-body* and *off-body* communications, many of the techniques and principles from the design of bio-implantable antennas are applicable here. However, unlike with communications with medical implants (where electromagnetic waves propagate inside the body), any radiation into the human body is, in fact, an unwanted effect here. These two aspects of body-centric communications are based on the radiation and propagation of electromagnetic waves outside, but still in the vicinity of the human body, which acts as a scatterer in the antenna near-field, significantly affecting the antenna radiation properties. The difference between *on-* and *off-body* communications is in the dominating mechanism of electromagnetic wave propagation (Fig. 2.15).

For the case of *off-body* communications, the communication takes place between body-worn devices and base units or mobile devices placed at some distance from the body. The communication is realized by space waves. Note that, compared to the case of an antenna in free space, in the realistic environment, beside the presence of the human body, one needs to consider multiple reflections, scattering, absorption and diffraction of the transmitted signal due to objects placed in the environment (and the body itself), which leads to multipath propagation and fading. Therefore, off-body communications are modelled using statistic methods for channel modelling.

On-body communications take place between two devices located on the body (e.g. communication between various components of body-worn equipment such as sensors, headsets, wearable computers, etc.). Here, the communication is realized by waves that are guided across the plain portion of the surface of the body as surface waves, or around the curvature of the body as creeping waves (Fig. 2.15). Since the body is a lossy medium, a part of the waves is absorbed by the body, adding to path loss, as well as to the undesired radiation into the human body. On-body communications can be roughly modelled using a deterministic approach [33, 34], by approximating the body with some canonical electromagnetic structure established in literature, and expanding the relevant field equations accompanied by the boundary conditions. However, in reality, the human body shape is not invariant (due to walking, lying, sitting, standing or even breathing), so when designing an on-body link, one also needs to consider its behaviour and stability in realistic scenarios.

In addition to the radiofrequency communication mechanisms described above, there have also been reports of communication systems which use the human body as a transmission

channel [36, 37]. These systems use the VHF band (10 MHz and below), where wave penetration into the human body is significant (e.g. at 10 MHz the penetration depth into muscle tissue is ≈ 20 cm [38]). Instead of antennas, communication among the devices is here obtained using transmitting and receiving electrodes which basically generate and receive volume currents through the human body (Fig. 2.16). Those devices can serve for transmitting an ID code, electronic money, exchanging personal information etc. Such a variation of on-body communications is also labelled *intra-body* communications, and is popular mainly in Japan and Korea [37, 39]. An example of an intra-body system is given in Fig. 2.17.

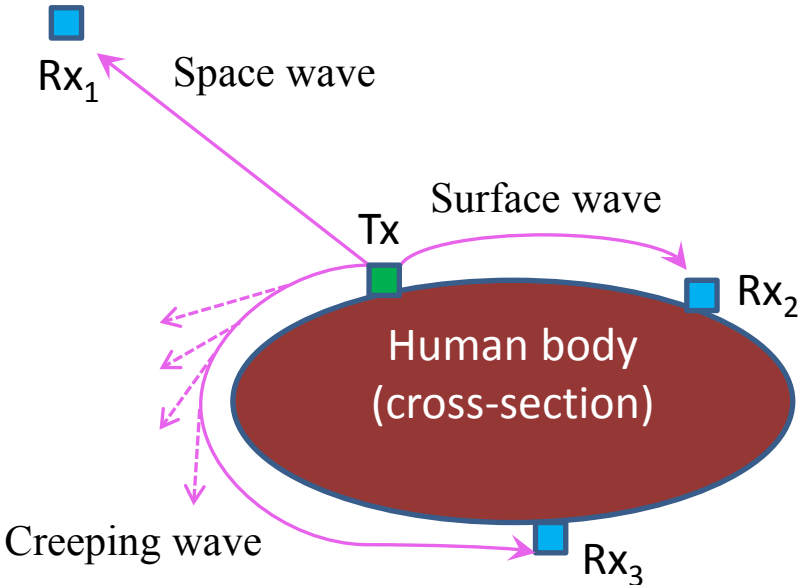


Figure 2.15 Propagation mechanisms for on-body and off-body communications

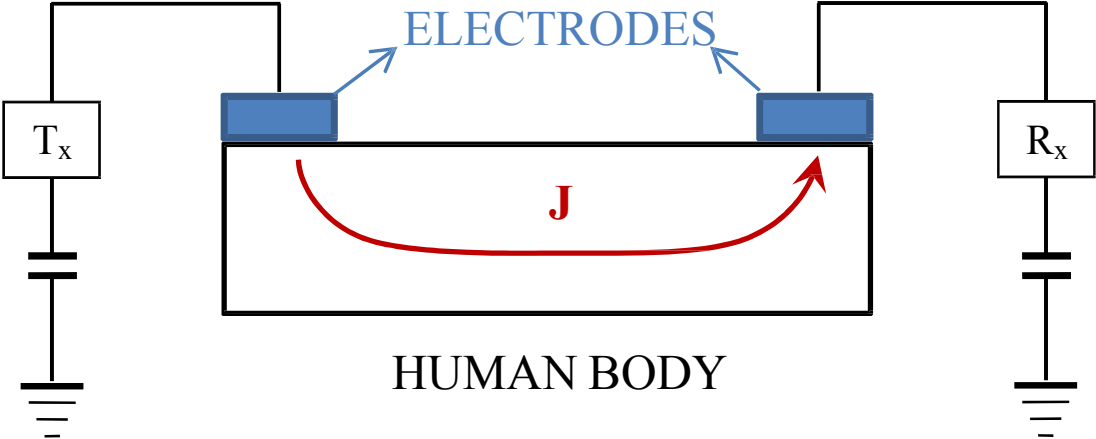


Figure 2.16 Principle scheme of an intra-body communication system [39]

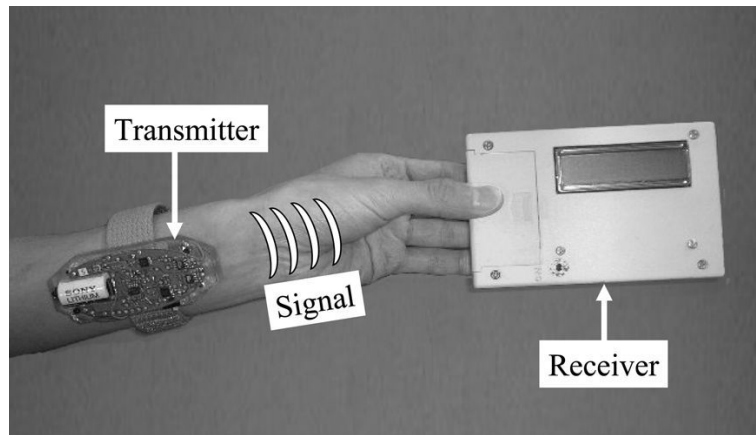


Figure 2.17 Transmission system using the human body as a channel [37]

2.4.2. Controlling surface waves

At higher frequencies (e.g. ISM 2.4 GHz), surface and creeping waves along the body are more pronounced and propagate together with space waves. For off-body communications, surface waves can spoil the radiation pattern of the antenna, and reduce its efficiency (since the power in surface waves is considered as lost in this case). So, for this case, equipping the antenna with artificial surfaces in its vicinity in order to control and prevent surface waves has been studied in literature [40 – 43]. In addition, the same surfaces are used to prevent radiation into the human body, i.e. to reduce the influence of the human body presence, typically for antennas without a ground plane. The considered surfaces belong to a class of electromagnetic bandgap (EBG) structures which typically consist of an element (i.e. the unit cell) periodically repeated in one to three dimensions, depending on the desired application. Those unit cells can be made of metals or dielectrics (or a combination of those) and can acquire various shapes and sizes which are tailored to obtain certain electromagnetic properties (at a specific frequency range) which cannot be found in natural materials. More details about the classification and possible uses of EBG and other artificial periodic structures are given, e.g. in [44, 45], while it needs to be noted that the most classic example of an EBG structure are the so-called EBG mushrooms [46], which are in principle periodic arrays of patches placed over a ground plane, each patch connected to the ground plane using a via hole.

For low profile antennas generating space waves, the common application of periodic electromagnetic structures is to tailor them to act as a high impedance surface, i.e. as an artificial magnetic conductor (AMC) in the specified frequency range [46]. The obtained composite surface can be placed as a ground plane below the patch, thus preventing back-

radiation and generation of surface waves by the planar antenna. When applied to the body-worn antenna, this also reduces radiation towards the body. In Fig. 2.18, two examples of wearable antennas integrated with EBG structures are shown. The left structure is a slot antenna placed over an EBG structure, which enabled impedance matching in the desired frequency range (around 2.8 GHz), as well as improved radiation efficiency in the presence of the human body from around 16% to up to 76% [41]. In the right picture, a dual band coplanar antenna (intended for ISM 2.4 and ISM 5.8 GHz) is shown [42]. The integrated EBG structure consists of 3×3 unit cells (each unit cell is a concentric patch), and the gain improved by 6 dB compared to the antenna alone, when the antenna was placed on the body. Furthermore, by using an EBG structure, back radiation was reduced in free space by at least 12 dB, which led to a reduction in SAR values by more than 95% when the antenna was placed on the body [42].

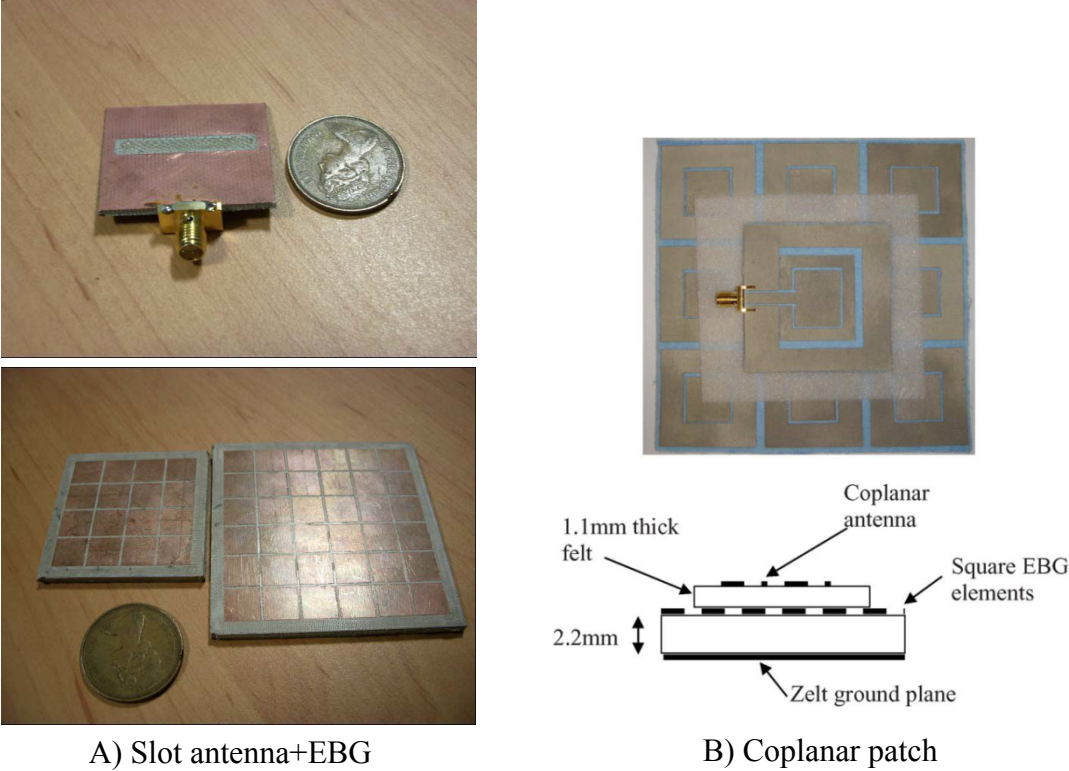


Figure 2.18 Examples of planar antennas equipped with EBG structures [41, 42]

In both examples in Fig. 2.18, the EBG structures were planar patches over a solid ground plane (i.e. variation of mushrooms [46] without via-holes), which makes them somewhat more convenient to build and implement into the human body, although still adding more layers to the overall radiating structure. Despite the added complexity, both EBG structures

proved to be effective in suppressing surface waves, reducing SAR rates and improving broadside gain.

Unlike for the antennas for off-body communications described above, surface waves are the fundamental mechanism for on-body communications, which means that one needs to direct the maximum radiation tangential to the surface of the body, thus maximizing the surface wave portion of radiation and increasing coupling (S_{21}) with other antennas placed on the body. Such an antenna should in principle have a similar radiation pattern as a monopole placed vertically over the body [47, 48]. In reality, a portion of communication is still obtained via propagating waves that are reflected or diffracted from the near objects, so the antenna coupling can be better in realistic multipath environments; however, multipath makes propagation modelling more complex. The antenna proposed in [47] is a microstrip antenna (called “HMMPA” - higher mode microstrip patch antenna) which operates in a higher order TM_{21} mode, and has exhibited fair results when compared to monopole and microstrip structures. However, the structure is somewhat difficult to build and place in the human body due to the grounding posts placed between the patch and the ground plane.

In [48], a surface-wave Yagi antenna is proposed. Such an antenna is flat-profiled, and can be used for integration with a sticking plaster type sensor. In [49], the concept of tailoring EBG structures to obtain the opposite effect from the usual use, i.e. to enhance surface waves instead of suppressing them, was proposed. Such a surface wave antenna is intended for use in the ISM 2.4 band, and is placed between the periodic array and the ground plane (i.e. inside the artificial surface), as illustrated in Fig. 2.19. The idea is to use the fact that input-match frequency band of the antenna provided with the EBG does not necessarily coincide with surface wave suppression band gap of the EBG, so the EBG was optimized for impedance match at ISM 2.4 GHz, and surface wave suppression in the ISM 5.8 GHz band (the latter enabled the possibility of off-body use in that band). The simulation results showed that the path loss was only around 4 dB larger (when the antennas were placed on the opposite side of the body) compared to the $\lambda/4$ monopole.

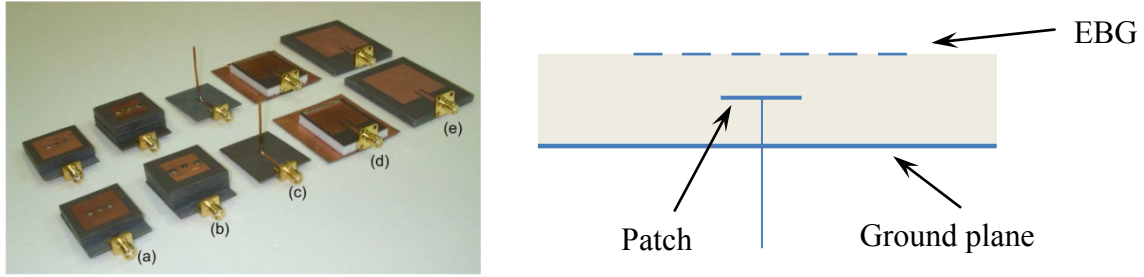


Figure 2.19 Left: Several prototypes of HMMPA, monopoles and microstrip on-body antennas [47]; Right: Scheme of a patch immersed in an EBG ground plane for surface wave excitation [49]

In [50, 51], a reconfigurable on/off-body communication system was developed. It consists of an aperture-fed antenna and two striplines, one of which is used for feeding the aperture (“off-body mode”), and another one to obtain transmission, as in a regular transmission line (“on-body mode”). The switching between the two modes of operation is provided by using two PIN diodes [51]. The outline of the structure is given in Fig. 2.20. In the upper picture, the switchable stripline layer is given, while in the lower picture, the prototype is shown. Although providing overall good performance for both types of communications, the structure contains three layers of dielectric and a full-length transmission line, which makes it rather bulky, while the on-body mode is not actually a wireless one. Therefore, it can be used primarily when additional stability for the on-body communication link is required [51].

The properties of the communication channel can be determined or modelled analytically for some idealized cases; however, an experimental evaluation is usually performed to test the antenna in real conditions. For that purpose, a simple on-body or off-body communication system is typically designed (consisting only of a transmitter and a receiver), and the time variation of the transmission parameter (S_{21}) is measured in various realistic circumstances (e.g. static body, mobile body, various positions of antennas on the body, indoors, outdoors etc.). Finally, the channel response is determined using statistical methods, and the placement of the antenna on the body is chosen depending on the desired properties of a particular application [1]. Recent research in body-centric communication systems is also focused on antenna arrays for multiple signal reception (so-called *MIMO systems*), in order to mitigate the effects of multipath propagation, and increase the channel capacity while maintaining the same bandwidth [52]. Here, various antennas are placed on the body; however, (unlike on-body propagation) mutual coupling in off-body MIMO applications needs to be reduced (each antenna needs to act independently), so the use of EBG structures can be considered for such applications as well.

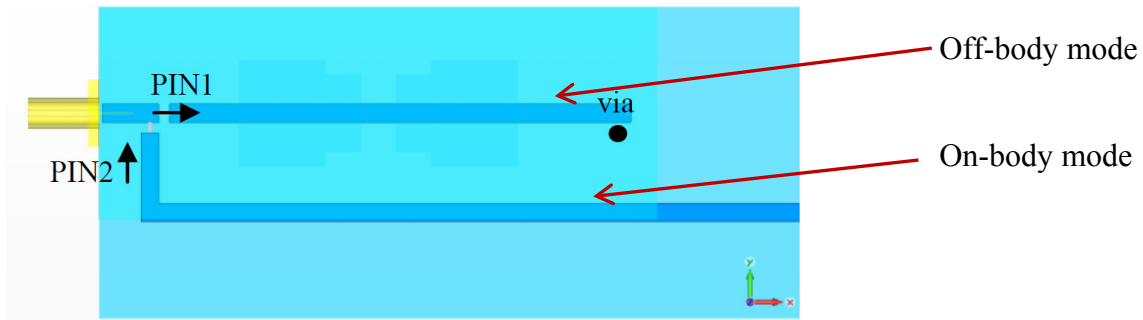


Figure 2.20 Reconfigurable on/off-body communication system [51]

2.4.3. *The frontiers in the frequency ranges*

At the present time, body-centric communication systems mostly use various frequency bands between 400 MHz and 3 GHz (e.g. UHF, MICS, ISM 2.4). The interest is, however, growing for higher frequency ranges which enable higher data transfer rates and smaller sizes of the antennas. Since the early years of the 21st century, ultra-wideband (UWB) technology has attracted much attention due to its data rate capabilities and immunity to fading (since the bandwidth is wide enough to prevent its occurrence in the whole band simultaneously). The common definition of an ultra-wideband (UWB) system is a system operating within the absolute bandwidth of 500 MHz and more, or a relative bandwidth of at least 25% [53]. In 2002, the U.S. Federal Communications Commission (FCC) allocated the frequency band from 3.1÷10.6 GHz for unlicensed commercial use, with strict requirements to avoid interference with other systems, which marked the beginning of the interest in the use and development of UWB systems for commercial use. According to the FCC standard, the maximum allowed spectral power density in these systems is -41.3 dBm/MHz. This roughly corresponds to the maximum total power of 0.5 mW, while the obtained data rates are usually around 100 MB/s. This is deemed suitable for short-range applications in radar sensing (e.g. locating of buried objects), locating and communications, as well as in military systems (since for UWB systems, it is virtually impossible to intersect signal without prior knowledge about

the parameters of the system), or medical imaging [53 – 55]. The used signals can be in the frequency domain (such as for parallel frequency coding - OFDM); however, due to the wide spectrum, the use of short, pulsed signals is being extensively considered (e.g. in the pulsed radio system). This has given rise to additional time-domain characterization of the designed antennas in terms of impulse response, ringing (additional resonances in the antenna which generally lower the data rate), dispersion (which influences the pulse width) and signal correlation (pulse fidelity) with regard to different directions (i.e. pulse is not radiated equally in all directions, unlike in conventional narrowband antennas). In principle, modern ultra-wideband antennas are obtained using several principal methods and their combinations [53], while some more details about them can be found in [54]:

- *Travelling wave antennas*. Smooth transition from the transmission line to free space – e.g. Vivaldi antennas
- *Frequency-independent antennas*. Antennas whose shape is independent from physical scaling (i.e. shape variation in angular direction only) – e.g. biconical antennas
- *Self-complementary antennas*. The metal part can be replaced by a dielectric, and vice versa, while the antenna structure is unchanged – e.g. logarithmic spiral
- *Multi-resonant antennas*. Multiple resonating structures at different frequencies forming a wideband response together – e.g. log-periodic antenna
- *Electrically small antennas*. The idea is to use small antennas below resonance to obtain “equally bad” matching and gain in a broad frequency range (and then to apply the matching network) – e.g. monocone antenna

In [55], a reduced size ultra-wideband antenna which excites the E -field normal to the surface of the body (thus being able to support surface waves) was proposed, intended for use in on-body communications (Fig. 2.21). Although its total height was reduced to around 1 cm, the antenna exhibited satisfactory performance in terms of matching in the whole UWB range (but with a radiation efficiency of only 19% to 40%), while the SAR values remained within the regulatory standards, which was confirmed by measurements on wideband phantoms (this was expected due to low overall power). Further research of the time-domain behaviour of the same antenna, however, revealed a significant pulse distortion, which means that only non-coherent modulation procedures (e.g. on-off keying, pulse-position modulation) can be used when the antenna is used for pulsed communications [56].

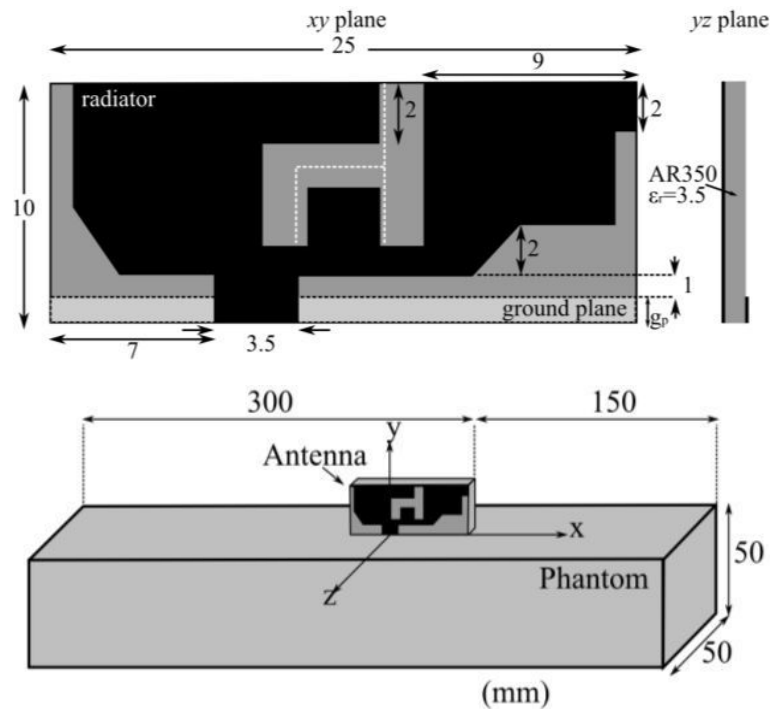


Figure 2.21 Compact UWB antenna and its placement on the phantom [55, 56]

Some more research concerning UWB implementation in body-centric systems is presented in [57], where two UWB antennas were compared with regard to their performance on the body, both in frequency and time domain. The antennas in question are the PICA (planar inverted cone antenna) and the coplanar waveguide (CPW) tapered slot, as shown in Fig. 2.22. Both antennas exhibited excellent impedance matching in the whole UWB range (both in free space and when placed on the body), and omnidirectional radiation in the azimuthal plane for the case of free space, while the front to back ratio increased by up to 30 dB when the antenna was placed on the body. As for the analysis in the time domain, the pulse fidelity factor of the impulse response compared to the one at 0° (when the antennas were facing each other) was measured in different directions and positions on the body, and the average values were 86% and 88% for the CPW and PICA antenna respectively, which makes them both suitable for implementation on the body and use in pulsed radio systems [57]. From the examples presented, it can be seen that the UWB technology, thanks to its robustness against detuning when placed on-body, and its high data rate capabilities and low power (hence low SAR), is an interesting and promising choice for body-worn systems. Nevertheless, improvements in the accompanying communication protocols, which could handle pulses in the time domain, are yet to be seen, as well as widespread commercial and medical applications.

PICA antenna



CPW tapered slot antenna

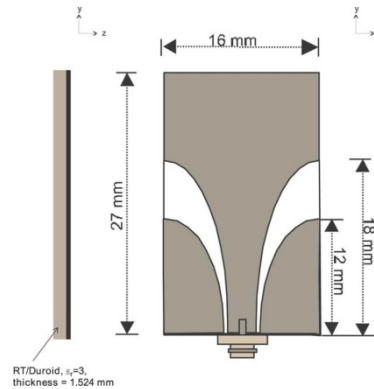


Figure 2.22 Examples of UWB antennas – PICA and CPW tapered slot [57]

Apart from the UWB range (3.1 ÷ 10.6 GHz), there is also an emerging interest in millimetre-wave bands such as 60 GHz (in the unlicensed range 57 ÷ 64 GHz), due to the possible miniaturization of antennas, lower interference with other devices and possibilities for obtaining high data rates (up to 5 Gb/s) [58, 59]. Moving the body-centric systems towards higher frequencies has its economic value as well, since the lower frequency bands are already occupied by many other devices (GSM, UMTS...), which also makes them rather expensive to use when higher data rates are needed (and the unlicensed bands are too narrow). The small physical dimensions of the antennas in the mm-wave range ($\lambda \approx 5$ mm) eliminate virtually any concern about compromise regarding size reduction and the antenna performance, giving rise (at least in principle) to the design of high-gain antennas and phased antenna arrays with satisfactory bandwidth, by which the typical problems with the communication channel in that range (fading due to multipath and high attenuation due to the path loss and oxygen absorption) can be reduced. Another problem in the mm-wave off-body communications is the strong shadowing of the body (non line-of-sight conditions, since the body is electrically large in those frequencies), which leads to significant fading; but, again, this could be overcome by using switched antennas placed on various positions on the body or in the environment [48]. The envisaged use of mm-wave communications is mainly for short-range communications (i.e. in the range of the personal area network, up to around 10 m), and applications such as soldier-to-soldier short range communication, kiosk downloading, or simple wireless communication, positioning or sensing [59] have been reported. The high channel losses in the 60 GHz band nevertheless possess the advantage of ensuring secure communication and data transfer, which is highly difficult to intercept from a larger distance, which fulfils one of the paramount requirements for the military, but also general body-centric

communication systems. Moreover, for on-body communications, the probability of co-channel interference between adjacent on-body networks is reduced, thus allowing the collocation of a larger number of users within a certain area [60].

In Fig. 2.23, two examples of textile antennas for use in the mm-band are given. The left picture shows the Yagi-Uda antenna with an end-fire pattern, while in the right picture, an antenna array consisting of four elements is shown. These antennas are characterized in [58 – 60], with regard to their performance in free space and on the human body phantom (matching and gain), and the textile materials used. For radiative parts, copper foil (glued to the textile and then cut with a laser) was used, since it was found that conductive textiles require high cutting accuracy for a patterned patch in the mm-wave range, which affects the reproducibility of the process (the conductive textile could, however, still be used for a ground plane).

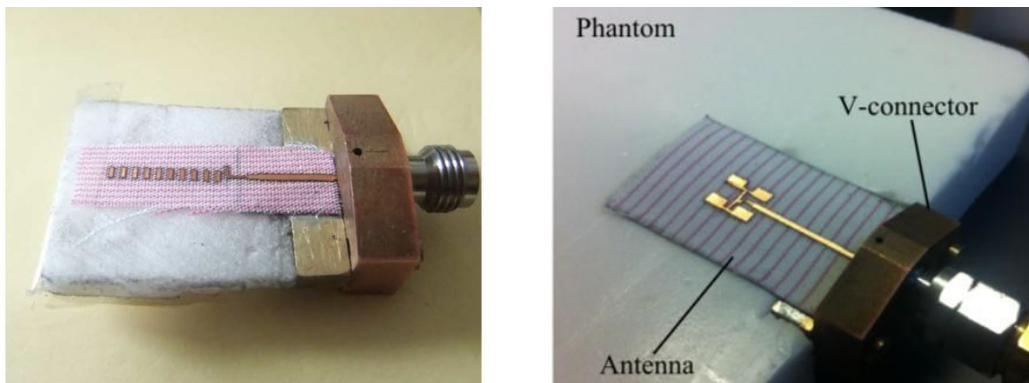


Figure 2.23 Left: Textile Yagi-Uda antenna for mm-wave on-body applications [59]; Right: Textile antenna array for mm-wave off-body applications [60]

In addition, due to the demands of high fabrication accuracy which arise due to the small wavelength of operation, it is recommended [59] to use only conventional textiles (e.g. cotton) for the antenna substrates in order to facilitate the commercial manufacturing process. It was found that the presence of the human body reduces radiation efficiency down to 48 % when the antenna is placed directly on the body (i.e. the phantom); however, when the antenna was placed only around 5 mm from the body, the efficiency and gain were comparable to free space which means that the antenna is adequate for mounting on clothes, which provides exactly those few millimetres needed to enhance the antenna efficiency and reduce the SAR [58].

To make a link budget, the communication channel for the mm-wave range can be modelled statistically from a large number of measurements [61]; however, there are also reports of

deterministic channel models using ray-tracing methods (i.e. geometric optics combined with UTD – Uniform Theory of Diffraction) [62]. The principle of ray tracing is to launch a bunch of rays from the transmit antenna over a selected spatial angle, and to track each of the rays until it either illuminates the area of interest, or the power of the ray falls below a preselected threshold level. Note that as the observed frequency of the carrier increases, its accuracy improves, since geometric optic approximations are made for the infinite frequency. Using ray tracing combined with animation software, in [62] highly realistic simulations of typical combat scenarios, both indoors and outdoors (Fig. 2.24), were performed, thus obtaining the angular spread of the signal and the power delay profile (PDP), which was used for channel characterization.

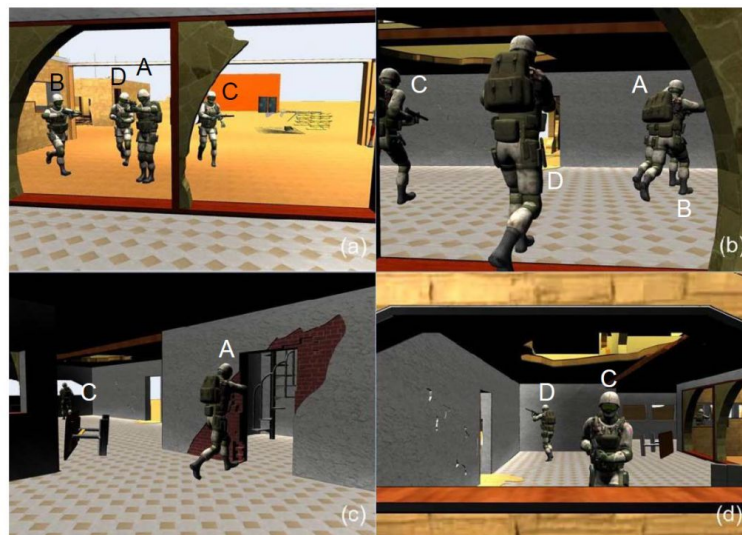


Figure 2.24 Sample of key frames of animated simulation for modelling of the communication channel among soldiers at mm-wave frequencies - the military team enters the building [62]

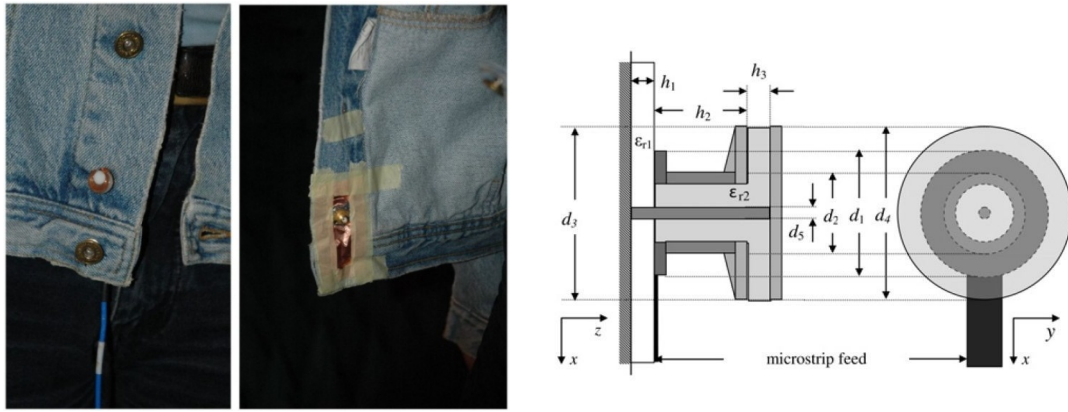
The example mentioned also outlines a more general need for improvements in conventional computer-aided design software, since, for body-centric communication systems, body motion needs to be taken into account for an accurate characterization of the antenna performance and the communication channel. Another instance of combining electromagnetic simulation software and body motion is described in [63], where the FDTD method for field analysis was used in conjunction with the animation movie, where data about the geometry of each frame were given. Note that, unlike [62], the created moving phantom in [63] is more suitable for the ISM band, since the required number of FDTD cells in the mm-wave band would make the simulation computationally intractable.

In [64, 65], a review of other work related to communication in millimetre waves, as well to the next generation of communication systems, is provided. Apart from the design of antennas, another challenge is the generation of a good-quality and stable carrier, since the common microwave oscillators, as well as avalanche diode oscillators (IMPATT), cannot be adequately used due to the relatively large phase noise levels in the mm-wave range. Therefore, the generation of signal using photonic techniques (e.g. photo-mixing, laser pulse techniques, quantum cascade lasers etc.) has emerged in recent years as a potential solution [64].

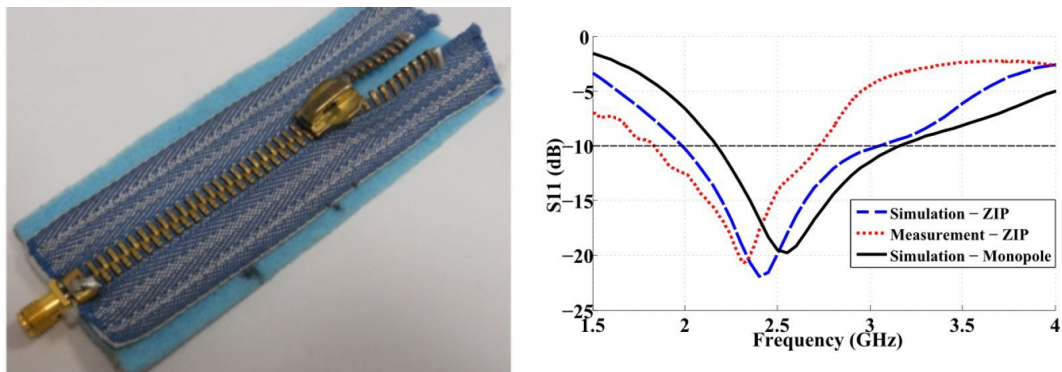
Apart from the 60 GHz band, several other bands ranging from 70 to 90 GHz have recently been allocated by the Federal Communication Commission, which could be exploited for communications over larger distances, due to the absence of atmospheric attenuation in these ranges, leading to a myriad of new possible applications of body-centric systems and beyond (ship-to-ship communications, broadband satellite communications, communication between unmanned vehicles, etc.). The mm-wave technology, similar to the UWB technology, is being actively researched today for implementation in the next generation of communication systems, while some practical commercial solutions and global standardization are expected to occur in the near future [64, 65].

2.5. Design aspects for wearable textile antennas

The presence of the human body as a living organism which performs a variety of daily activities in different environments adds new features to the antenna design, compared to the conventional ones commonly discussed in antenna literature (e.g. antenna in free space for static base stations). Thus, in order to design antennas to work properly in the vicinity of human body, one needs to consider in detail the antenna radiation mechanism, its fundamental constraints, and the electrical properties of the human body. Apart from the need for size reduction and maintaining satisfactory technical characteristics, the antennas in question need to be lightweight, reasonably priced, aesthetically acceptable, robust and suitable for maintenance and integration with clothes. Ideally, the user should not be constantly aware of their presence any more than he is aware of the presence of some other clothing item. Thus, from the beginning of research into body-centric communications, the idea has been to exploit parts of clothes to function as the antenna, which has led to planar or low profile antennas as the natural choice. The conventional wearable antennas are consequently planar dipoles, monopoles or microstrip antennas (usually with some modifications) [35].



(a) Button antenna



(b) Zip antenna

Figure 2.25 Use of conductive parts of clothes as antennas [66 – 68]

In Fig. 2.25, two examples of possible integration of the antenna into clothes are shown [66 – 68]. The antennas are monopoles, and are primarily intended for operation in the ISM 2.4 band, e.g. for Wi-Fi applications, although there are possibilities for extension of operation into the ISM 5.8 band (5.725÷5.875 GHz). The idea in both designs is to use parts of clothes which are made of metal (in particular, jeans buttons and zip openings), so that the antenna is properly camouflaged and easy to implement. Both monopoles possess a ground plane which directs the main portion of the radiation away from the body, which is an advantage in terms of reducing energy dissipation in the undesired direction, as well as insulating the antenna from the body.

The more common approach to antenna design for body-centric applications is, however, to implement planar antennas into clothes, i.e. to use the textile as a substrate. Such an approach has prompted extensive research into the dielectric properties of textiles used in clothes, as well as research into conductive textiles which could be used for the conductive parts of the antenna. The interaction between wearable antennas and textile materials is threefold, each

aspect being a specific issue which needs to be considered in the wearable antenna design [69]:

- i. Use of clothing as a carrier for antennas
- ii. Use of clothes or fabric as the dielectric part of the antenna (e.g. substrate)
- iii. Design of the conductive parts of the antenna using conductive textiles



Top and bottom view

Antenna on the user's back

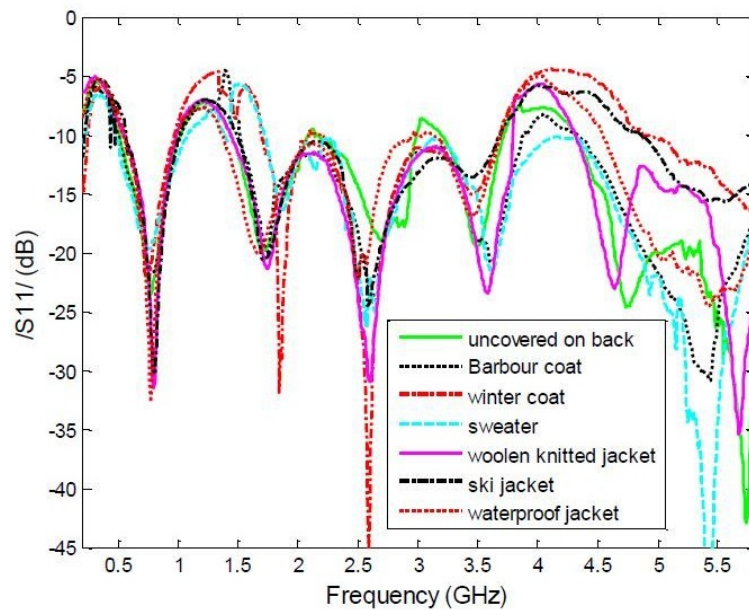


Figure 2.26 The dual band antenna and the effect of covering it with various garments [70]

Regarding the first issue, in [70], a dual band textile antenna that covers a wide range of usual frequency bands, ranging from digital television to wireless communications (GSM, ISM, WiMAX, UMTS-LTE), was proposed. Among other issues, the influence of clothing onto the antenna performance was investigated by putting the antenna on the user's back, and then placing a number of usual garments (coats, sweaters, jackets) used in various daily activities onto the wearer. It was found that the effect of covering the antenna was only marginal, even

for heavy and thick garments such as ski jackets, as illustrated in Fig. 2.26. On the other hand, the radiation efficiency when the antenna was placed directly on the body fell even below 10% for some frequency ranges it is supposed to cover. As a remedy to such low efficiency, backing the antenna with an EBG structure and a felt substrate was investigated, and it was found that by using a felt substrate as a simple solution, it is possible to recover radiation efficiency to around 40 % in the upper bands, and 90% in the lower band [70]. This outlines the need to isolate the antenna from the influence of the body by either placing it at a larger distance from the body, or backing with the proper ground plane or artificial surfaces such as EBG.

2.5.1. Dielectric textile substrates

The second issue in the design of wearable antennas is the choice of a proper textile substrate which could act as a part of the antenna. In Table 2.3, the electric properties of textile materials that could be used as antenna substrates are summarized (popular names for textiles have been used, as commonly found in antenna literature). Note that these properties can somewhat vary depending on the manufacturer, so, in literature, some differences in the stated electric properties can be observed. In addition, electric properties slightly vary with frequency due to dispersion and with temperature and climate conditions (e.g. relative humidity of the air) [71], but they can be used as a guideline for antenna design. As can be seen, most materials generally have a low relative permittivity and losses, which, nevertheless, affect the resonant frequency and the bandwidth of the antenna, so their effect on the antenna performance cannot be neglected in the final and precise antenna design. The two main categories of clothing textiles are natural and synthetic fibers. The latter are made of various polymers, and are usually named after the trademark of the manufacturer [1]. The commonly used synthetic substrates are fleece, Cordura[®], Vellux[®], synthetic felt, lycra etc., while from natural substrates, jeans, cotton, silk, wool and other materials used in daily clothes can be typically used [1, 72].

In the real environment (i.e. when worn on the body), the antenna is subject to mechanical deformations such as stretching and bending, so, in order to make the antenna characteristics stable, one should ideally choose a material which does not deform easily (such as e.g. upholstery fabric, which is a multilayer composition of polyacryl and polyester). The use of inelastic fabric is, however, often impractical, and can result in uncomfortable clothes, so compromises are needed [1]. With the goal of assessing the antenna properties in the

environment where it is intended to be used, the influence of the antenna bending onto the antenna performance attracted considerable attention in literature (e.g. [74–78]). For instance, in [74], different synthetic textile materials were explored for a circularly polarized GPS antenna, and it was found that synthetic textile such as Cordura[®] exhibits a fair compromise between flexibility and maintaining its mechanical shape i.e. keeping the antenna characteristics stable for GPS applications (Fig. 2.27).

Table 2.3 Electric properties of textile substrates at microwave frequencies [1, 61, 72, 73]

Material	Relative permittivity	Loss tangent
Felt	1.1÷1.38	0.023
Woollen felt	1.45	0.02
Polyamide mesh	1.14	≈0
Fleece (nonwoven fabric)	1.1÷1.17	0.0035
Closed-cell foam	1.52	0.012
Polyethylene foam	1.05	0.0001
Silk	1.75	0.012
Tweed	1.69	0.0084
Panama	2.12	0.018
Moleskin	1.45	0.05
Cordura [®]	1.9	0.0098
Nomex [®]	1.18	0.004
Cotton	1.6	0.04
100% polyester	1.9	0.0045
Quartzel [®] fabric	1.95	0.0004
Cordura/lycra [®]	1.5	0.0093
Jeans textile	1.7	0.025
Acrylic textile	2.6	N. A.

In addition, in [75, 76], it was found that bending in the *E*-plane has the dominant effect on the antenna performance in terms of input-matching and impedance bandwidth, since it changes the current path. Some more complex deformations, such as crumpling, have been shown to reduce the overall radiation efficiency, which was for some types of crumpling more than 4 times lower compared to the best value [77]. Thus, when designing a body-worn antenna, one needs to evaluate the stability of its characteristics with regard to mechanical

deformations, and the bending of the antenna has been established as a standard test, considered to simulate the real conditions well enough. Apart from the influence of mechanical deformations, the final choice of the textile substrate (and the placement of the antenna on the body) is also determined by the desired application, price, material characteristics in supposed environmental and climate conditions [11, 71], material durability, aesthetic properties etc.



Figure 2.27 Left: GPS antenna with different textile substrates (upholstery fabric, Cordura[®], 2-layer upholstery fabric) [1, 74]; Right: Typical measurement setup for antenna bending [75]

2.5.2. Conductive textiles

The third, and the most challenging, issue in the wearable antenna design is to design its conductive part in a way that it is suitable to be worn on clothes. To make the antenna prototype, the use of copper tape for conductive parts is flexible and realistic enough for laboratory testing; so the antenna concepts proposed in scientific papers are often copper-based (e.g. [1]). However, in the real world, the antenna needs to be integrated into clothes, and should share the same characteristics as everyday clothes – to be comfortable, unobtrusive, aesthetically appealing, washable, drapable (elastic in all directions [79]) etc. Such demands clearly give rise to the need for embroidering the conductive threads (or fabrics) into the clothes, thereby making the antenna a truly integral part of clothes. Although the use of metallic threads in clothing dates back to ancient times, when it was used for protective armour and decoration [73], and can theoretically be used for electrical functions, the focus of research in the textile industry is nowadays shifted towards producing conductive threads that would meet all of the abovementioned requirements for regular clothes (i.e. the conductive thread ultimately needs to be considered as a full textile as much as, for example, cotton thread is). Such a concept is also commonly called *Smart textile* or electro-textile (*E-textile*). There are three principle ways to create conductive fibers [73]:

- the filling of fibers with carbon or metal particles
- the coating (plating) of fibers with conductive polymers or metal
- the use of fibers that are entirely made of conductive materials

To reduce the price and keep other good properties of textile, the conductive fibers are usually mixed with nonconductive ones, hence obtaining conductive thread and fabric. Nevertheless, in the electric terms, conductive textiles are considerably different from e.g. copper plate (which is, of course, approximated with PEC), which adds another layer of complexity to the wearable antenna design. The issues with conductive threads that need to be addressed in the design of E-textiles for antenna applications are [69]:

- the distance between conductive fibers, which limits the highest usable frequency (since the structure can become non-homogeneous for smaller wavelengths). In addition, a sparse grid cannot support all the possible currents close to the antenna excitation point
- non-metallic fibers possess finite conductivity (usually of the order of magnitude down to 10^4 S/m [79, 80]), which causes losses in the antenna
- for some textiles, there is a preferred direction of current flow depending on the direction of conductive fibers, i.e. the textiles exhibit anisotropic electromagnetic properties
- non connected interlaced conductive threads, which appear irregularly throughout the textile due to oxidized surfaces
- fibers filled with carbon or metal particles can be electrically inhomogeneous if the manufacturing process is not perfect, which leads to high demands on manufacture

The commonly used conductive fabrics in the antenna design and their electric properties are illustrated in Table 2.4. Note that the conductivity is expressed via so-called sheet resistance, in Ohm per square. This is in fact the inverse of conductivity divided by substrate thickness, and is used as a figure of merit for expressing the conductive properties of textile [81]. For convenience, in Table 2.4, the conductivity of fabrics is calculated as well. The general demand on conductive threads is to ensure sheet resistance of less than $1 \Omega/\text{sq}$, which, for 0.1 mm thick fabric, corresponds to $\sigma \approx 10^4$ S/m [79]. It can be seen that some commercially available fabrics [81] well exceed this limit, and could be up to the order of magnitude of 10^6 S/m, which is only one order of magnitude less than copper ($\sigma_{\text{Cu}}=5.81 \cdot 10^7$ S/m). Therefore, the use of conductive fabrics available today shows potential for replacing the real conductor on technical grounds, the downside still being the price and availability of the conductive material. When designing a full-textile antenna for wearable applications, the finite

conductivity (which reduces radiation efficiency and gain) of the used material needs to be taken into account.

Table 2.4 Electric properties of conductive textile fabrics at microwave frequencies [72, 81]

Material	Thickness [mm]	Sheet resistance [Ω/sq]	Conductivity [S/m]
Nora Ni-Cu-Ag plated woven	0.15	0.02	$3.3 \cdot 10^5$
Nora Nylon	0.13	0.009	$0.85 \cdot 10^6$
FlecTron	0.15	0.1	$0.66 \cdot 10^5$
Zelt	0.06	0.01	$1.66 \cdot 10^6$

In Fig. 2.28, the prototype of a UHF spiral antenna with the conductive part made using several different techniques is shown. The antenna itself was designed for wideband coverage in the UHF and VHF bands (100 MHz ÷ 1 GHz), and is intended for off-body communications [18]. Of the three considered methods, conducting nylon exhibited the best RF performance (in terms of radiation efficiency and gain) when applied in the antenna, while conducting thread was the worst due to the finite conductivity of the threads. Apart from the mentioned ones, several other methods were also considered (copper-coated fabric, liquid crystal polymer, phosphor-bronze mesh, etc.); however, the three methods mentioned were found to be more practical for wearing on the clothes [18]. It was also noted that in non-metallic conductive threads, the feeding cannot be soldered to antenna, but conductive epoxy, considered a less durable and firm method than soldering, needs to be used instead. Thus, the connection of the antenna feeding onto conductive textiles can be a matter of concern, especially when robust antenna solutions are required [18].

The most appealing method for obtaining a conductive textile thread is to use metal-coated (plated) polymer filaments, since in that way the flexibility, drapability and other properties of common textiles are best preserved compared to other methods, while conductivity, although lower than in fully conductive threads, can still be deemed suitable for applications in electric circuitry and antennas. There is a number of commercially available threads (yarns) with trade names (e.g. X-static[®], Agposs[®], Shieldex[®], Aracon[®], AmberStrandTM etc.), which vary in coating thickness, conductivity, material type and number of base polyester filaments [83]. For instance, some threads contain high-performance polymers as the base filament, such as Kevlar[®] or Zylon[®] that can be directly soldered, which is clearly an advantage.



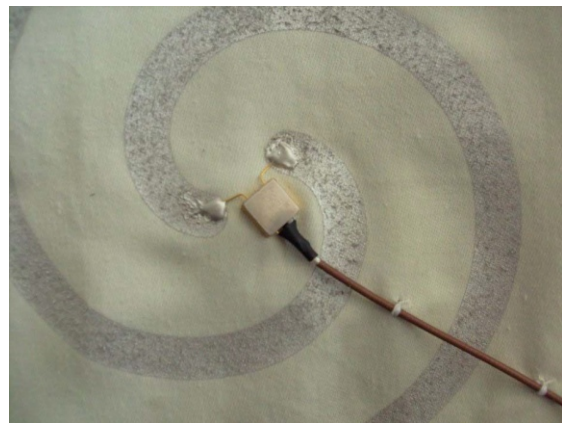
A) Prototype



B) Conducting nylon



C) Embroidered conductive thread



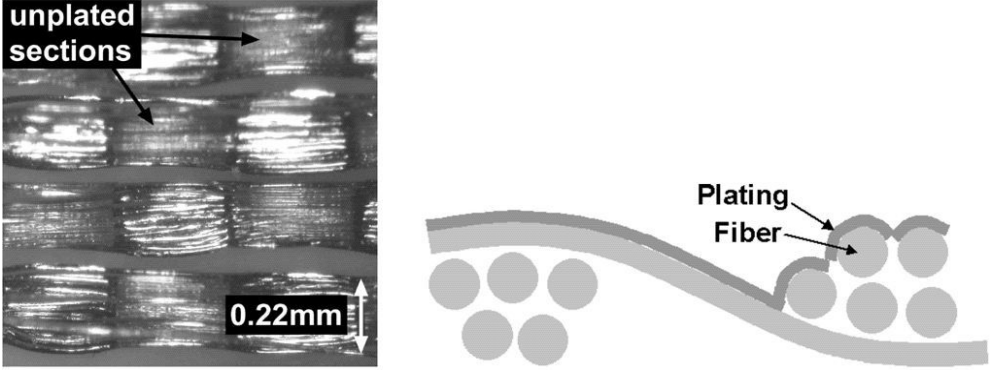
D) Conductive paint

Figure 2.28 Spiral UHF antenna made from several conducting materials [18, 82]

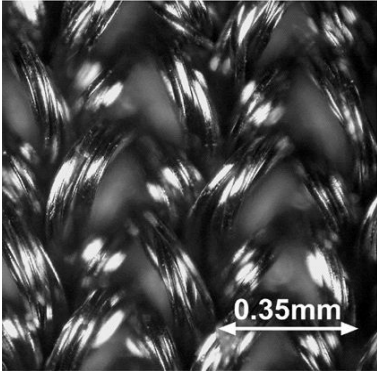
The conductive fabric which can be used for antennas is obtained by incorporating conductive threads by means of weaving or knitting. In knitted fabrics, the threads meander through and create interlocked loops, while in the woven fabric, the threads are straight in two orthogonal directions, i.e. in directions of warp and weft [73]. Apart from the properties of the threads, the textile texture (i.e. the method of fabric production) also has an effect on the efficiency of the textile as an electro-conductive material, and how well it can approximate the homogeneous copper (PEC) plate. In [79], the three different conductive textile fabric textures are compared, as shown in Fig. 2.29.

When the plating process was applied, portions of fibers at the intersection remained unplated after weaving, which results in fibers that are not continuously conductive, but the current needs to “jump” from one fiber to another (i.e. from warp to weft and vice versa) at crossing

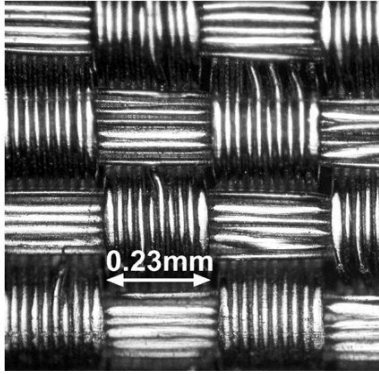
points, leading to a sheet resistance of around 5 Ω /sq. Thus, structures that are plated after weaving are not suitable for antenna applications due to high resistance [79].



A) Nickel-plated woven and its cross-section (plated after weaving)



B) Silver-plated knitted



C) Nickel-plated woven (plated before weaving)

Figure 2.29 Different conductive textile textures [79]

For the case of knitted fabric, a sheet resistance of 1 Ω /sq was measured, which is within the usual requirements for textile conductivity in the antenna design, while the best performance (0.02 Ω /sq) was exhibited for woven fabric that was plated before weaving. A possible explanation for higher sheet resistance of knitted fabric is that conductivity is not uniform, since the current flows both through threads, and interconnections across threads, the latter exhibiting higher losses (i.e. resistance) [73]. In addition, for knitted fabric, the resistance was shown to exhibit inhomogeneous behaviour when the fabric was exposed to bending, again due to the cell-like structure of knitted material, which is an undesirable effect for most applications [79].

Note that the abovementioned example is given for fabrics entirely made of conductive materials. As already stated, in many applications, conductive threads are mixed with

nonconductive threads (due to the price and retention of other properties of classical textiles), which can have an additional detrimental effect on the conductive textile performance. A simple method for the characterization of various conductive textiles is proposed in [69]. For that purpose, a wideband PICA antenna was made, and its conductive part was replaced by various conductive fabrics (parallel graphite threads, polymerized textile, mixtures of polyester and steel in two ratios), and compared to the performance of copper mesh and copper tape (Fig 2.30). It was found that the radiation efficiency varied in the range of more than 10 dB for various textiles, and, as a general rule, it was established that conductive threads need to ensure current flow around the edges of the antenna and beneath the patch, since this is the area where most currents reside [69]. Although mixing conductive and nonconductive threads can result in effective sheet conductivity lower than the ones stated in Table 2.4, by gaining knowledge about the current flow in the antenna, it is possible to reduce the amount of conductive threads, while retaining a suitable textile fabric which, among other benefits, can result in commercially appealing solutions. Therefore, designing a proper conductive textile is a challenge which requires knowledge both in antenna and textile design, and is thus attractive for further research.

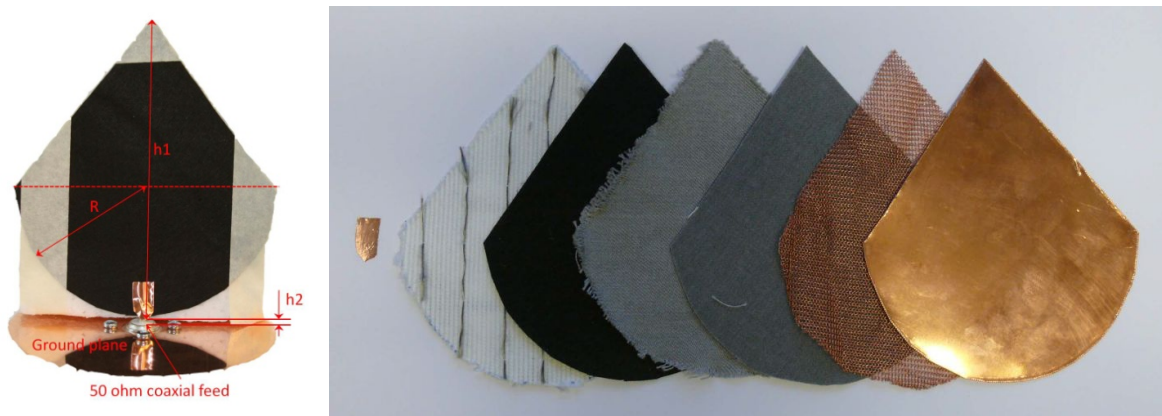


Figure 2.30 PICA antenna for wideband characterization of conductive textiles and some samples of conductive fabrics [69]

3. ELECTROMAGNETIC MODELLING OF THE HUMAN BODY

For the design of an antenna for body-centric communication systems, one needs to evaluate the interaction between the antenna and the human body. There are two principal points of view as regards such interaction [39, 84]:

- the exposure of the human body tissue to the radiation
- the reduction of the antenna radiation efficiency due to losses

Regarding the human body exposure, since the advent of the mobile phone and other wireless communication devices, as well as medical implant devices, their use has been accompanied by health concerns about possible adverse effects of their effect on the human body (in particular, brain tumors), prompting various international epidemiological studies. Although the most comprehensive epidemiological study up to date, published in 2010 [85], did not find conclusive evidence about increased tumor risk due to microwave radiation exposure, the EM radiation vs. health debate is still alive; both in the medical community and the popular media (see e.g. [86]). The exposure of the human body is usually expressed in terms of the specific absorption rate (SAR), which accounts for the power absorbed in tissue [W/kg] and is defined as:

$$SAR = \frac{d}{dt} \left(\frac{dW}{dm} \right), \quad (3.1)$$

where W is the energy absorbed in tissue, m is the mass of a tissue and t is the time.

Another definition, derived from (3.1), is most widely used in electrical engineering since it relates SAR values to electric fields:

$$SAR = \frac{\sigma |E|^2}{\rho} \quad (3.2)$$

where σ is the conductivity of the body, E the amplitude of the electric field in the media concerned (human tissue) and ρ the mass density of the absorbing media.

The acceptable SAR values are prescribed by various national and international regulatory agencies [87]. The two typical limits for mobile systems in the GSM band are 1.6 W/kg averaged over 1g of tissue (United States) and 2 W/kg averaged over 10 g of tissue (European Union) [1].

For body-centric communications, at higher frequencies (UWB and mm-wave), the use of higher SAR values, from 2 to 4 W/kg, has however also been reported as relevant at times [55, 88]. Apart from SAR, radiation in the human body can also be expressed in terms of power density (i.e. the power absorbed by tissue), incident power density – IPD (the power radiated by the source), or the rate of increase in body temperature [58].

On the other hand, the power absorbed by the human body can be considered lost from the point of view of the antenna, thus reducing the antenna radiation efficiency (i.e. the ratio of radiated and applied power) and gain. For in-body communications, the radiation efficiency of the antenna can be even below 1% [31], while for on-body and off-body communications, radiation efficiency typically ranges from 10% when the antenna is not isolated from the body, to around 40% and more, depending on the type of the antenna and its isolation from the body (e.g. [70]). Additionally, the presence of the human body in the antenna near field can significantly alter its input matching and bandwidth, as will be elaborated in Chapter 4.

It is thus necessary to use a human body model in computer simulations and laboratory tests in order to observe the actual behaviour of the designed body-centric antenna when placed in the environment in which it is supposed to operate, and modify the initial antenna design accordingly. In this chapter, we review the electromagnetic properties of materials in order to build an electromagnetic model of the human body. In that way, the human body as a material, as well as propagation in the presence of the human body, can be put into perspective with the existing electromagnetic theory, while only stressing the particular properties of the human body as a medium. It should be noted that, in electromagnetic terms, the human body is classified as an inhomogeneous lossy media of arbitrary (irregular) shape, which is (apart from the anisotropy) a rather general medium, i.e. the human body is neither a good conductor, nor a good dielectric. Additionally, at frequencies of the GSM band and higher, the dimensions of the human body are several wavelengths in extent, which means that diffraction and scattering from the body need to be taken into account when studying on-body and off-body propagation (using e.g. geometrical and uniform theory of diffraction) in that range. This means that a complete representation of the human body is a challenging task from the electromagnetic and numerical viewpoints. Some of the numerical issues will be illustrated in Chapter 5, where the model for on-body propagation will be derived.

In this chapter we are primarily interested in the physical realization of media which possess the same electromagnetic properties as the human body. Such a model serves as a phantom for evaluating the interaction between antennas and the human body. Due to the complexity of

the model, a number of approximations need to be taken to simplify the geometry and reduce the quantity of material produced. Nevertheless, the dominant effect of the human body on the antenna properties can usually be represented with fair accuracy using suitable approximations for the observed application. For instance, when studying on-body and off-body propagation the inhomogeneity of the body rarely needs to be taken into account since most fields reside in muscles and skin (which possess similar EM properties), due to losses and penetration depth.

3.1. Complex permittivity and conductivity

The dielectric permittivity, ϵ , is a quantity which represents the response of the material to the applied electric field. In the presence of the applied electric field (in the first case, assumed static), the positive and negative bound charges in the atom interact with the field by perturbing the centre of electron orbitals, and thus shifting charges within the atom [89, 90] from the equilibrium position, which creates the so-called *dipole moment* (polar molecules with a permanent dipole moment are considered later). The dipoles which emerge are macroscopically described in terms of the polarization vector \mathbf{P} , as suggested at the atomic level in Fig. 3.1. In linear, time-invariant homogeneous dielectrics, the polarization vector is proportional to the applied electric field, hence we write:

$$\mathbf{P} = \epsilon_0 \chi \mathbf{E}, \tag{3.3}$$

where ϵ_0 is the dielectric permittivity of vacuum, included in the expression for convenience. The coefficient χ is called the media *susceptibility*. The susceptibility is in general a tensor, since in general materials the dipoles are not necessarily aligned with the applied electric field, due to e.g. some other forces in the material (such as forces in a crystal lattice). These materials are called anisotropic materials. Nevertheless, many usual materials are isotropic, and χ is a scalar quantity which leads to a linear connection between the electric field and polarization vector.

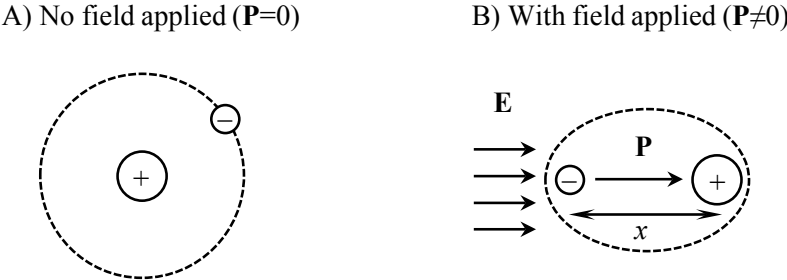


Figure 3.1 The polarization at the atom level

According to Maxwell's equations, free charge in a specific volume is calculated by integrating the electric displacement vector \mathbf{D} over a surface enclosing that volume. The same vector is also associated with radiation (via displacement current $\partial\mathbf{D}/\partial t$). The polarization vector contributes to the displacement vector as:

$$\mathbf{D}(\mathbf{r}) = \varepsilon_0 \mathbf{E}(\mathbf{r}) + \mathbf{P}(\mathbf{r}), \quad (3.4)$$

where it is stressed that all the vectors are functions of the position vector \mathbf{r} .

After inserting (3.3), the expression for electric displacement can be rewritten as:

$$\mathbf{D}(\mathbf{r}) = \varepsilon_0 (1 + \chi) \mathbf{E}(\mathbf{r}) = \varepsilon_0 \varepsilon_r \mathbf{E}(\mathbf{r}) = \varepsilon \mathbf{E}(\mathbf{r}), \quad (3.5)$$

where ε_r is the relative permittivity and ε the total permittivity of the medium.

When the applied fields are time-varying, in real media there is a time lag between the change in the field and change in polarization, since the charges in media possess inherent inertia and internal losses. This means that the response is time-dependent, and that atoms in dielectrics can store, release and dissipate the energy of the applied field. For time-varying fields, the constitutive relation (3.5) may be written as a convolution integral [91]:

$$\mathbf{d}(\mathbf{r}, t) = \varepsilon_0 \mathbf{e}(\mathbf{r}, t) + \varepsilon_0 \int_{-\infty}^t \chi(t - \tau) \mathbf{e}(\mathbf{r}, \tau) d\tau, \quad (3.6)$$

where lowercase letters are used for the respective fields in order to stress the general time dependence. Note that in the time domain, the susceptibility is actually the impulse response of the material to the applied electric field.

The arbitrary time dependence of the fields is typically treated using the Fourier transform, by which it is represented as an integral sum of sinusoidal fields. In the frequency domain, the convolution integral from (3.6) becomes a product (as in a static case). Therefore, at some frequency ω we can write:

$$\mathbf{D}(\mathbf{r}, \omega) = \varepsilon_0 \mathbf{E}(\mathbf{r}, \omega) + \varepsilon_0 \chi(\omega) \mathbf{E}(\mathbf{r}, \omega) = \varepsilon_0 \tilde{\varepsilon}_r(\omega) \mathbf{E}(\mathbf{r}, \omega) = \tilde{\varepsilon}(\omega) \mathbf{E}(\mathbf{r}, \omega). \quad (3.7)$$

Of course, the same results would have been obtained if the sinusoidal time dependence (phasor approach) was assumed and inserted directly in (3.6). Due to the properties of the Fourier transform and the causality requirements [91], the permittivity in the frequency domain becomes a complex function of frequency:

$$\tilde{\varepsilon}(\omega) = \varepsilon'(\omega) - j\varepsilon''(\omega). \quad (3.8)$$

The frequency dependency of the permittivity (due to the time lag between applied field and material response) is called *dispersion*.

Apart from the dipoles, which are associated with the charges that are moving only within an atom, in a material there are also the so-called *free electrons*, which are not bound into the atom and can move within the whole material. When the electric field is applied, the free electrons move across the material with the drift velocity \mathbf{v} , which is proportional to the applied field:

$$\mathbf{v} = \mu_e \mathbf{E}, \quad (3.9)$$

where constant of proportionality μ_e is called *electron mobility*. The current density \mathbf{J} is given by multiplying velocity with the volume electron density ρ as [89]:

$$\mathbf{J} = \rho \mathbf{v} = \rho \mu_e \mathbf{E} = \sigma \mathbf{E}. \quad (3.10)$$

The quantity σ is called the *conductivity*, and represents the property of the material to produce an electric current as a response to the applied electric field. The inverse quantity $1/\sigma$ is the *resistivity* of the media. Therefore, eq. (3.10) is an electromagnetic analogue to Ohm's law [89]. In general, conductivity can also be a complex and frequency-dependent value; however, at microwave frequencies it can be assumed constant. For anisotropic media, the conductivity is also a tensor [91].

The Maxwell's curl equation for the magnetic field is given in the frequency (phasor) domain as:

$$\nabla \times \mathbf{H} = \mathbf{J} + j\omega \mathbf{D} = \sigma \mathbf{E} + j\omega \epsilon \mathbf{E}, \quad (3.11)$$

which can be rewritten using (3.8), as:

$$\nabla \times \mathbf{H} = j\omega \left(\epsilon' - j \frac{\omega \epsilon'' + \sigma}{\omega} \right) \mathbf{E} = j\omega \left(\epsilon_0 \epsilon_r - j \frac{\sigma_e}{\omega} \right) \mathbf{E} = j\omega \tilde{\epsilon}_e \mathbf{E}, \quad (3.12)$$

where $\sigma_e = \omega \epsilon'' + \sigma$ is the effective conductivity of the medium, and ϵ' is replaced with $\epsilon_0 \epsilon_r$. Note that in macroscopic terms, it is impossible to make a distinction between $\omega \epsilon''$ and σ [88], so the distinction between these two terms is often ignored in practice.

The conductivity (and hence also ϵ'' , which enters the equation in the same way) represents losses for electromagnetic waves, since a portion of the wave energy resides in the conducting current. With complex permittivity, the wavenumber (propagation coefficient) of plane electromagnetic waves in unbounded media also becomes complex and is given as:

$$k = \sqrt{\omega^2 \mu \tilde{\epsilon}_e} = \sqrt{\omega^2 \mu \epsilon_0 \epsilon_r - j \omega \mu \sigma_e} = \beta - j \alpha, \quad (3.13)$$

which leads to spatial dependence of the field moving in e.g. z -direction according to factor:

$$e^{-jkz} = e^{-j\beta z} e^{-\alpha z}, \quad (3.14)$$

from which the exponential decay in the direction of propagation is obvious.

The commonly used forms for effective complex permittivity are:

$$\tilde{\epsilon}_e = \epsilon' - j\epsilon'' - j\frac{\sigma}{\omega} = \epsilon_0 \epsilon_r - j\frac{\sigma_e}{\omega} \quad (3.15)$$

and

$$\tilde{\epsilon}_e = \epsilon_0 \epsilon_r \left(1 - j \frac{\sigma_e}{\omega \epsilon_0 \epsilon_r} \right) = \epsilon_0 \epsilon_r (1 - j \tan \delta_e), \quad (3.16)$$

where $\tan \delta_e$ is the so-called loss tangent (as suggested in Fig. 3.2). The frequency dependence of ϵ_r , σ_e and $\tan \delta_e$ in (3.12)-(3.16) is, of course, presumed (and omitted for clarity).

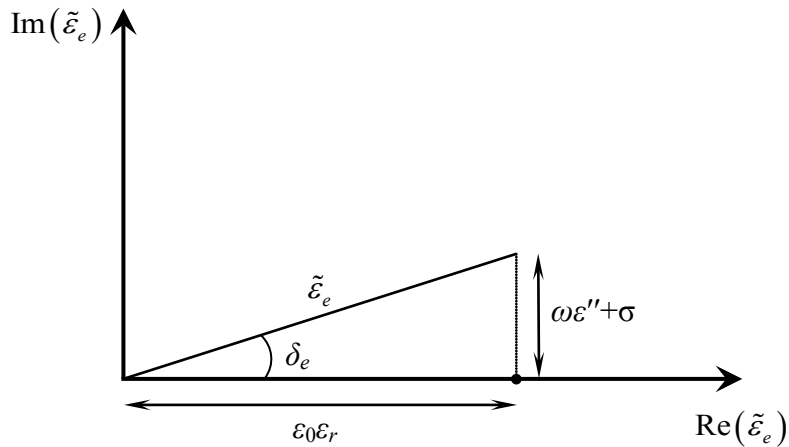


Figure 3.2 Effective complex permittivity

Another commonly used quantity is the so-called *penetration depth*, δ . It is the distance by which the field amplitude is e^{-1} times smaller than the field at some reference point (e.g. the surface of the lossy media). It is found from (3.14) as:

$$e^{-\alpha z} = e^{-1}, \text{ i.e.}$$

$$z = \delta = \frac{1}{\alpha}. \quad (3.17)$$

The most widely recognized expression for δ is obtained from the case of a good conductor [89]:

$$\delta = \sqrt{\frac{2}{\omega\mu\sigma_e}}. \quad (3.18)$$

Similar observations can be made for magnetic properties of materials; however, since the human body does not possess magnetic properties, they are not discussed here [88]. Thus, the macroscopic electromagnetic properties of the human body can be fully described in terms of effective complex permittivity. The real part of complex permittivity represents the response of the bound electrons in the atom to the applied field, while the imaginary part represents losses that arise either due to conductivity (σ) or the time lag between the applied field and material response (ϵ''). Therefore, there are three common ways to express losses, via either:

- a) effective conductivity (σ_e) – often termed only *conductivity* for simplicity
- b) loss tangent ($\tan \delta_e$)
- c) penetration depth (δ).

3.2. Dispersion models for electric permittivity

3.2.1. Resonant model (Lorentz)

The classical simple model, typically used to model a dielectric response to the applied electric field $\mathbf{e}(t)$, is to recognize that the displacement of the electron orbitals from the equilibrium position by an amount x (Fig. 3.1) produces a restoring (elastic) force, and that there is an inherent inertial force (due to Newton's 2nd law). In addition, it is reasonable to assume that there is some energy loss (damping) due to interaction with other particles or radiation. Therefore, the dielectric stores, releases and dissipates energy of the applied field, which leads to modelling with an equation analogous to the harmonic oscillator or parallel RLC circuit [89, 91]:

$$m \frac{\partial^2 \mathbf{x}(t)}{\partial t^2} + \gamma \frac{\partial \mathbf{x}(t)}{\partial t} + k_s \mathbf{x}(t) = q \cdot \mathbf{e}(t), \quad (3.19)$$

where m is the electron mass, γ the damping coefficient and k_s represents the spring constant that accounts for elastic force. The displacement $\mathbf{x}(t)$ is written in vector notation, and is assumed to point in the same direction as the applied field (i.e. from negative to positive charge, as in Fig. 3.1). The factor $q \cdot \mathbf{e}(t)$ is the exciting Lorentz force that is exhibited on a

dipole charge q due to the applied field. If we take the equation in the frequency (or phasor) domain, the solution is:

$$\mathbf{X}(\omega) = \frac{\frac{q}{m} \mathbf{E}(\omega)}{(\omega^2 - \omega_0^2) + j\omega \left(\frac{\gamma}{m} \right)}, \quad (3.20)$$

where $\omega_0^2 = k_s/m$ is recognized as the resonant frequency of an undamped system.

The dipole moment of a single atom is given by:

$$\mathbf{P}_i(\omega) = q \cdot \mathbf{X}(\omega). \quad (3.21)$$

Polarization is defined as the volume average of dipole moments contained in a volume, which for sinusoidal time-dependence leads to [89]:

$$\mathbf{P}(\omega) = N_e \mathbf{P}_i(\omega) = N_e q \mathbf{X}(\omega), \quad (3.22)$$

where N_e is the number of dipoles in a unit volume (all the dipole moments are assumed to be equal). By combining (3.22), (3.20) and (3.5), the permittivity is obtained as:

$$\tilde{\epsilon}(\omega) = \epsilon_0 + \frac{\frac{N_e q^2}{m}}{(\omega^2 - \omega_0^2) + j\omega \left(\frac{\gamma}{m} \right)}. \quad (3.23)$$

This is called the Lorentz single-resonant model for electric permittivity. The frequency characteristics of real and imaginary parts of permittivity are given in Fig. 3.3. Near the resonant frequency ω_0 , the imaginary part exhibits a large amplitude which accounts for the energy absorption in the material. In general, there are several resonant frequencies arising due to various mechanisms of polarization, and the permittivity near all of the resonant frequencies can be represented using this model, while the total permittivity is then obtained as a sum of contributions from each polarization mechanism [89].

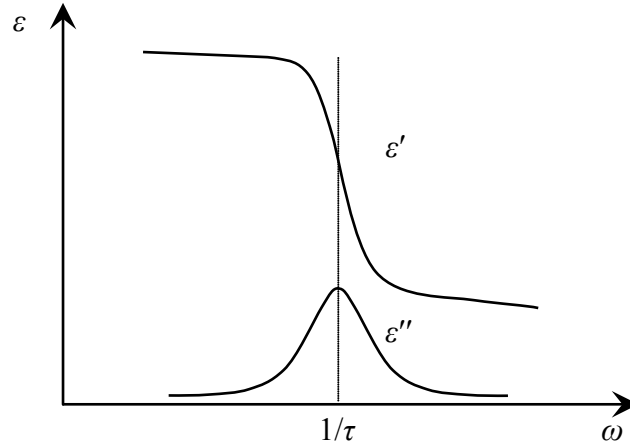


Figure 3.3 Lorentz frequency characteristics of complex permittivity

3.2.2. Relaxation models (Debye and Cole-Cole)

For solids and polar liquids such as water (i.e. molecules with a permanent dipole moment, which is nonzero even when no field is applied), the more suitable model is to replace the resonance effect by relaxation. The polar molecule can be viewed as tending to rotate due to the applied field and experiencing collisions with other particles which prevent them from accelerating. This means that the damping coefficient γ in (3.19) dominates over the acceleration term $\partial^2 \mathbf{x} / \partial t^2$, so the latter can be neglected, which leads to:

$$\gamma \frac{\partial \mathbf{x}(t)}{\partial t} + k_s \mathbf{x}(t) = q \cdot \mathbf{e}(t), \quad (3.24)$$

which has a homogeneous solution of the form:

$$\mathbf{x}(t) = \mathbf{x}_0 e^{-\frac{k_s t}{\gamma}} = \mathbf{x}_0 e^{-\frac{t}{\tau}}, \quad (3.25)$$

where $\tau = \gamma / k_s$ is called the *Debye relaxation time*.

The solution to the inhomogeneous equation in the frequency domain is given as:

$$\mathbf{X}(\omega) = \frac{q \cdot \mathbf{E}(\omega)}{j\omega\gamma + k_s}. \quad (3.26)$$

This, after some manipulations, leads to the permittivity of the form:

$$\tilde{\epsilon}(\omega) = \epsilon_0 + \frac{\frac{N_e q^2}{m}}{\frac{k_s}{m} + j\omega \left(\frac{\gamma}{m} \right)} = \epsilon_0 + \frac{\frac{N_e q^2}{m\omega_0^2}}{1 + j\omega\tau}. \quad (3.27)$$

Based on the relaxation spectrum (3.27), Debye proposed a more general form of the dispersion equation [91]:

$$\tilde{\epsilon}(\omega) = \epsilon_{\infty} + \frac{\epsilon_s - \epsilon_{\infty}}{1 + j\omega\tau} \quad (3.28)$$

where ϵ_s is the real static value of permittivity, and ϵ_{∞} is the real part of permittivity when $\omega \rightarrow \infty$ (in practice it is taken at optical frequencies). As seen from Fig. 3.4, the real part of permittivity decreases with frequency, while the absorption in material (large imaginary part) occurs around $\omega\tau=1$. The Debye equation is used for many materials to approximate permittivity at the microwave frequency range [89].

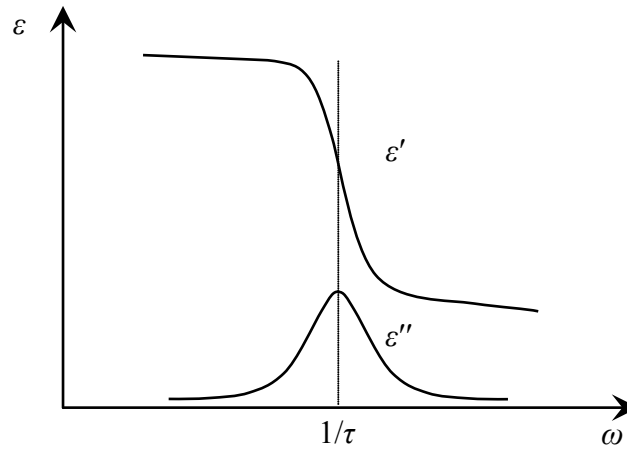


Figure 3.4 Debye frequency characteristics of complex permittivity

For a more accurate representation of permittivity of polar liquids other than water, there is a generalization of the Debye equation (3.28), which adds another degree of freedom α :

$$\tilde{\epsilon}(\omega) = \epsilon_{\infty} + \frac{\epsilon_s - \epsilon_{\infty}}{1 + (j\omega\tau)^{1-\alpha}} \quad (3.29)$$

This is called the *Cole-Cole equation*. The nonzero parameter α tends to broaden the relaxation spectrum and results from a spread of relaxation times centred around τ . For water, the parameter α is only 0.02, which means that the Debye model is sufficient in that case; however, for other liquids (such as oil), the parameter α can be much higher [91].

3.2.3. Electrical model of the human body

The Cole-Cole equation (3.29) can be even more refined by using more relaxation times that take into account different mechanisms of polarization, each of which possesses its own relaxation time, corresponding static permittivity and parameter α in the denominator. The

permittivity is then obtained by summing up contributions from each mechanism. For human body modelling, four relaxation times are commonly used in literature, called the *4-Cole-Cole model*. By using that model, and by taking into account the conductivity σ that arises due to free electrons in body tissue, the dispersion equation suitable for broadband modelling of the effective complex permittivity of human body is given as [1]:

$$\tilde{\epsilon}_e(\omega) = \epsilon_\infty + \sum_{m=1}^4 \frac{\epsilon_{s,m} - \epsilon_\infty}{1 + (j\omega\tau_m)^{1-\alpha_m}} - j \frac{\sigma}{\omega}. \quad (3.30)$$

The respective parameters τ_m , α_m , $\Delta\epsilon_m = \epsilon_{s,m} - \epsilon_\infty$ can be used to calculate electric parameters of the human body at a given frequency, while a comprehensive list of their values (and calculated respective electric parameters) for many organs and tissues can be found e.g. in [92], which is the result of several precise measurement campaigns taken in 1990s. This list is thus commonly taken today as a theoretical reference [88]. To illustrate the matter, in Table 3.1, the electric properties of some human body tissues are summarized at the frequency of 2.45 GHz [92]. For convenience, the losses are expressed in all three common ways – via conductivity, loss tangent and penetration depth.

Table 3.1 Electric properties of some body tissues at $f=2.45$ GHz

Tissue name	ϵ_r	σ [S/m]	$\tan \delta_e$	δ [cm]
Blood	58.264	2.545	0.320	1.612
Blood vessel	42.531	1.435	0.248	2.430
Body fluid	68.208	2.478	0.267	1.785
Bone - cancellous	18.548	0.805	0.318	2.875
Bone - cortical	11.381	0.394	0.254	4.578
Bone - marrow	5.297	0.095	0.132	12.884
Brain- grey matter	48.911	1.808	0.271	2.072
Brain – white matter	36.167	1.215	0.246	2.647
Breast fat	5.147	0.137	0.195	8.830
Fat	5.280	0.105	0.145	11.702
Muscle	52.729	1.739	0.242	2.233
Nerve	30.145	1.089	0.265	2.701
Skin - dry	38.007	1.464	0.283	2.257
Skin - wet	42.853	1.592	0.273	2.203

It can be noted from Table 3.1 that, in principle, there are two types of tissues. In the first group there are tissues with high water content (e.g. muscle or skin) that exhibit high permittivity and losses, while the second group consists of tissues with low water content (e.g. fat or bone). Hence, it can be said that the water content (including dissolved salt) in tissues is the most decisive parameter for the electric properties of the body, since water itself possesses high relative permittivity (around 81), while the presence of salt in water (which is the case in human body tissues) determines the losses in human body tissues.

When designing a body-centric antenna for a specified frequency range, the influence of the human body on its properties needs to be investigated, since this is the environment where the antenna is supposed to operate properly. Thus, in accordance with (3.30), the frequency dispersion of tissue parameters needs to be taken into account by calculating the actual parameters at the desired frequency range. In Figs. 3.5 – 3.7, the frequency dependence of permittivity, conductivity and penetration depth is shown for three typical tissues. It can be seen that, at microwave frequencies, the dry tissues (represented by fat) exhibit losses and permittivity around an order of magnitude lower than wet tissues (represented by muscle and skin), as also illustrated in Table 3.2 for exemplary frequencies in UHF and ISM frequency range.

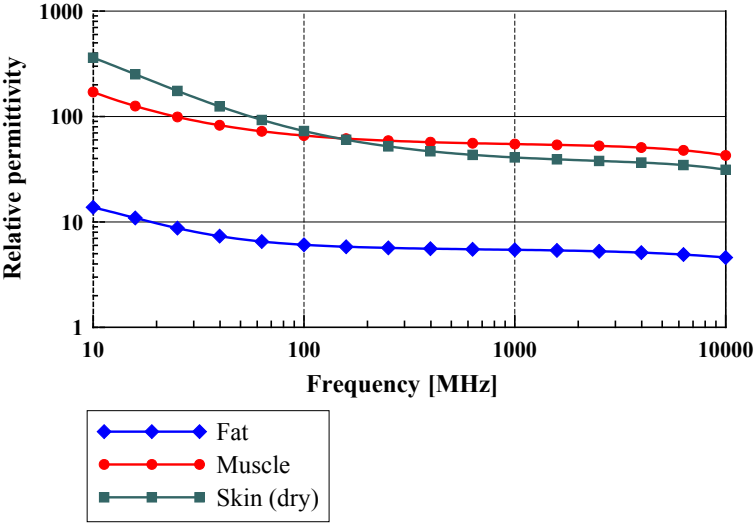


Figure 3.5 Frequency dependency of relative permittivity for representative human body tissues

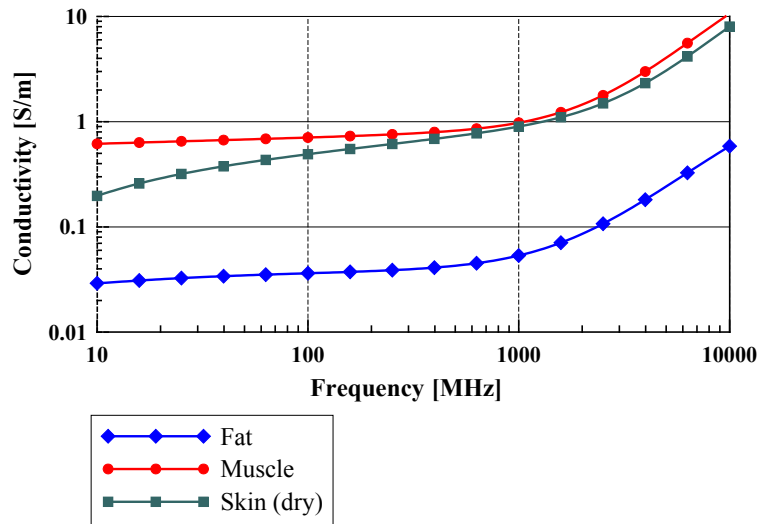


Figure 3.6 Frequency dependency of conductivity for representative human body tissues

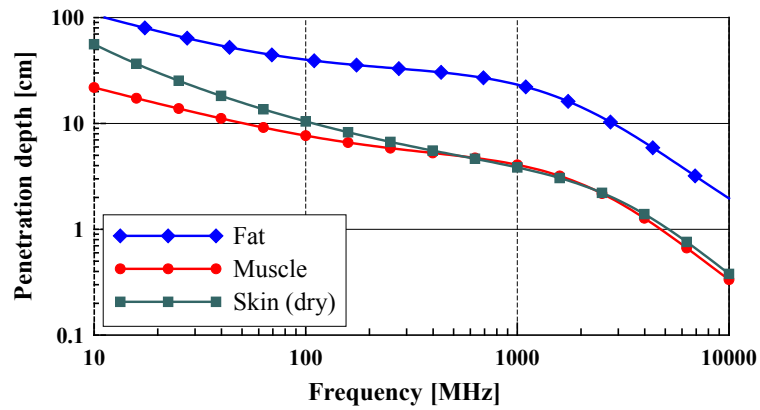


Figure 3.7 Frequency dependency of penetration depth for representative human body tissues

Table 3.2 Electrical parameters of representative human body tissues at UHF and ISM 2.4 frequency range

	UHF ($f=400$ MHz)	ISM 2.4 ($f=2.45$ GHz)
SKIN	$\epsilon_r=46.787$	$\epsilon_r=38.007$
	$\sigma=0.7$ S/m	$\sigma=1.46$ S/m
	$\delta=5.53$ cm	$\delta=2.26$ cm
MUSCLE	$\epsilon_r=57.129$	$\epsilon_r=52.729$
	$\sigma=0.8$ S/m	$\sigma=1.74$ S/m
	$\delta=5.26$ cm	$\delta=2.23$ cm
FAT	$\epsilon_r=5.58$	$\epsilon_r=5.28$
	$\sigma=0.04$ S/m	$\sigma=0.1$ S/m
	$\delta=30.9$ cm	$\delta=11.7$ cm

Moreover, when modelling the body behaviour for on-body and off-body communications, it should be noted that penetration depth at microwave frequencies (as shown in Fig. 3.7) is of the order of a few centimetres, meaning that the major influence of the human body onto the antenna properties in that case is primarily determined by the properties of skin and muscle (since these tissues are closest to the antenna and the field penetrates there the most). Additional influence is exhibited by the layer of fat and, for the case of the human head, by bones and brain matter. Hence, to build a reliable model of the human body for on-body and off-body communications at microwave frequencies, one actually needs to consider the properties of only a few tissues. Of course, when studying in-body propagation or performing precise SAR measurements, the modelling demands are made somewhat more stringent by the inhomogeneity of the body, which needs to be taken into account by modelling internal organs as well; however, even in that case, some approximations and simplifications are often made [88].

3.3. Human body phantoms

Apart from affecting the properties of antennas and EM wave propagation, the human body as a living organism needs to be protected from potentially negative health effects of electromagnetic radiation. Hence, there are ethical concerns regarding the use of living bodies for examining the interaction between the antenna and the human body, while the design needs to be made in a way to reduce any undesired radiation into the human body when possible. On the other hand, when designing an antenna for body-centric communication systems, it is crucial to test the performance of the antenna in the vicinity of the human body, since the presence of a high-permittivity lossy dielectric possibly affects the antenna near field, hence generally resulting in the detuning of the antenna resonant frequency and reducing radiation efficiency. The off-body propagation channel is also affected by the presence of the human body, since it acts as a strong scatterer, adding to the path loss. Thus, there is an interest to approximate the human body with a model which would enable the evaluation of the antenna properties in the vicinity of human body, while the tests on a living human body can be performed afterwards (i.e. once the antenna was shown to conform to standards of exposure), when needed. Therefore, human body models (so-called “phantoms”) are extensively used in the research of body-centric communication systems. The term *phantom* in literature refers both to numerical and experimental (physical) models of the human body [39, 84].

Another advantage in using a phantom lies in ensuring the reproducibility of laboratory measurements or numerical simulations, since measurements on the body add some more uncertainty due to changes of body positions and shape during measurements (e.g. measuring the radiation pattern on the human body requires the subject to stand still on a rotating plate for a while, which is, at best, difficult to obtain [42]), as well as the variation of body electric properties from human to human, and even their daily variations.

There are plenty of *numerical phantoms* which are used with various degrees of precision. In theoretical analyses, the canonical shapes (planar, cylindrical or spherical) or their combinations – (one-layered or multi-layered) are used, since they provide adequate approximation of the interaction between the antenna and the human body, while taking up reasonable amounts of computer memory. In addition, the increases of computer power have also allowed for the development of inhomogeneous phantoms, containing even full organs created from volume elements (“voxels”) to which different permittivities and conductivities are assigned [1, 84, 88], while the radiation properties of the antenna are determined using common numerical approaches (FDTD, UTD, MoM, FEM etc.).

For even more precision in computer modelling of the propagation channel in the presence of the human body, recent developments in computer electromagnetic software [62, 63] take into account body motion in the real environment by combining animation software with numerical algorithms (as already described in section 2.4.3). In that way, a highly accurate simulation tool for modelling the communication channel is obtained, which is suitable for e.g. military applications, where reliable signal coverage (and thus precise modelling) is strongly required for operation on the field.

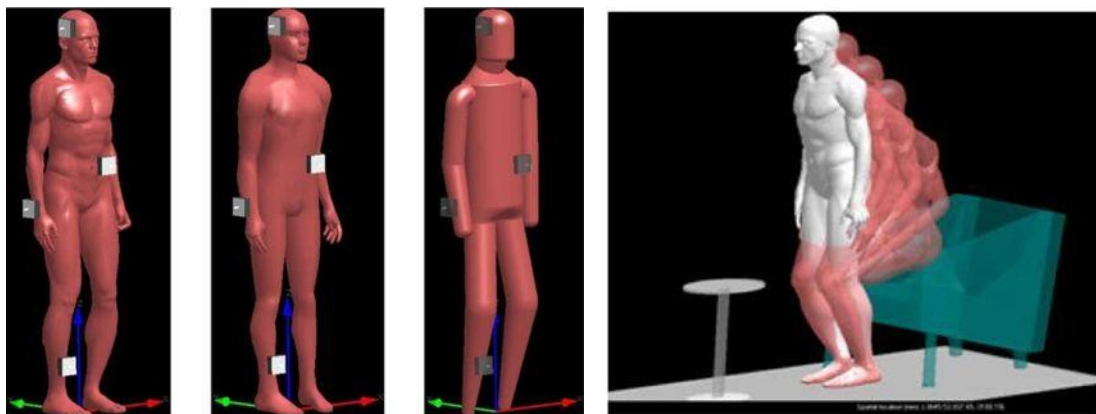


Figure 3.8 Numerical phantoms of various levels of complexity and frames of simulated body movement [63]

Physical phantoms can, in theory, range from a homogeneous approximation of a body part (e.g. muscle, skin, brain tissue etc.) to full-scale models which take virtually every part of the human body into account (unlike numerical phantoms, the use of phantoms with body inhomogeneity taken into account by more than 3 layers is rare in the field of antennas [24]). The oldest and simplest phantoms are homogeneous liquids (typically contained in low-permittivity bottles or containers), which are basically water solutions of various substances designed to mimic the dielectric properties of the human body. Typically, salt (NaCl) is used to control the conductivity, while sugar (at lower frequencies) or some more advanced chemicals (at higher frequencies), such as diethylene glycol monobutyl ether (DGBE), diacetin, polyethylene glycol mono phenyl (Triton X-100) etc., are exploited to control the permittivity. The chemicals used for phantoms are otherwise used industrially for manufacturing of detergents or in the cosmetic industry as an ingredient of e.g. hair colours [93]. The mixtures are obtained in various ratios to obtain the sought electromagnetic properties in the desired frequency range, while several recipes are available in literature [94, 95].

For more precise measurements, especially when the outer shell of the liquid phantom container poses a problem (e.g. for determining SAR on the surface), semisolid (self-shaping, gel) and solid phantoms are available. The common ingredients for a semisolid phantom (apart from water and NaCl) are polyethylene powder (for controlling permittivity), agar (for obtaining self-shaping gel properties), TX-151 (solidifying powder – used for increasing the viscosity) and Sodium dehydroacetate (as a preservative) [84, 96]. Semisolid phantoms can also be made to mimic the human body properties in a broad frequency range [96]. For solid phantoms, microwave ceramic powder, graphite powder, and bonding resin are used, and mixed at a high temperature and pressure [97]. Although solid phantoms are the only phantoms whose electric and mechanical properties do not vary over time, their manufacturing process is rather complicated. Therefore their use is not widespread [84].

As already mentioned, only few tissues are actually relevant for modelling on-body or off-body communications, so for the antenna measurements, the most commonly used phantoms are homogeneous liquids (contained in a shell) and self-shaping gels that vary in the substances used for their manufacture and the tissue they represent (usually muscle, skin or brain tissue). In [24], there are also reports of a three-layered phantom (muscle-fat-skin), which approximates the inhomogeneity of the body. The phantoms also vary in shape, which of course depends on the container used (in the case of liquid phantoms), and can range from

a simple box to the full body in various positions (Fig. 3.9), similar to the shapes of numerical phantoms. The common shapes of the physical phantoms and their possible uses are listed as follows [88]:

- *The rectangular box.* Adequate for measuring input reflection coefficient or gain when the antenna is on the body surface.
- *The cylindrical box.* Used as a refinement of the rectangular box e.g. for measuring the non-line-of-sight propagation on body surfaces. Also recommended as a standard by ETSI (European Telecommunications Standard Institute) [88].
- *The spherical shell.* Used for modelling the human head for internal SAR measurements, or as an approximation for in-body communication measurements.
- *Full-body shape.* Used for precise measurements of SAR, in-body propagation, scattering from the human body etc.



Figure 3.9 Left: Commercial phantom torso shell to be filled with liquid [98] . Right: Solid phantom head [39]

3.4. Development of a liquid phantom for ISM 2.4 GHz

Following the previous discussions, for the purpose of our measurements, a homogeneous liquid phantom was found to be suitable to confidently estimate the influence of the body on the antenna performance, and to serve as a proper standard for the human body. After examining the literature and the obtainable chemicals, a tissue-equivalent phantom according to recipe proposed in [94] was chosen. In Table 3.3, the liquids used for the phantom are listed, together with their mass fraction. To make one kilogram of the phantom, the required mass (calculated from mass fraction) of liquid substances was converted to volume (by

dividing with liquid density) in order to be put in the mixing cylinder, while a technical balance with the resolution of 0.01g was used for evaluating the salt content.

After mixing the ingredients, the parameters of the phantom were measured using a dielectric coaxial probe. The procedure required calibration of the probe by using open end, short circuit and water (Fig. 3.11). By using the measured complex input coefficients during the calibration, and by knowing the water temperature, it is possible to extract the sought electric properties of the phantom. The method is described in more detail in [101].

Table 3.3 The substances used in the manufacturing of the phantom

Ingredient	Manufacturer	Mass fraction [%]	Density [g/cm ³]	Quantity in 1 kg of phantom
H ₂ O - deionized	-	71.89%	1	0.719 L
DGBE	Acros Organics	7.99%	0.95	0.076 L
Triton X-100	Packard Instrument Co.	19.97 %	1.07	0.213 L
NaCl	Kemika	0.15%	(2.165)	1.5 g



Figure 3.10 The chemicals and equipment used in the manufacturing of the phantom. From left to the right: deionized water, DGBE, Triton X-100, NaCl; mixing cylinder, technical balance

The phantom was actually obtained in two stages – in the first stage, 1 kg of phantom was obtained (that proved suitable for the characterization of antennas in the ISM 2.4 band), while

in the second stage, two additional kilograms of the phantom were manufactured using the same procedure as described above, and mixed with the first one. The comparison between the measured electric parameters of the phantom obtained in that way with the theoretical (reference) values from [92] is given in Figs. 3.12 and 3.13. In Table 3.4, the obtained results are summarized for the frequency of 2.45 GHz (the central frequency of the ISM 2.4 band where the phantom is supposed to operate). It can be seen that the measured values are close to the targeted ones within a margin of around 3% and 5.5% for relative permittivity and conductivity, respectively. Moreover, from Figs. 3.12 and 3.13, it can also be seen that the obtained phantom covers an even larger frequency range around the required one (ISM 2.4), with a rather small deviation from the theoretical values from [92]. Here, one needs to note that the electric parameters of the body are subject-specific to some extent, also even varying with time for the same person [96], so in that respect, the observed deviation from the theoretical values can be deemed acceptable. Therefore, the obtained phantom is adequate for representing human (muscle) tissue in measurements of on-body and off-body propagation.

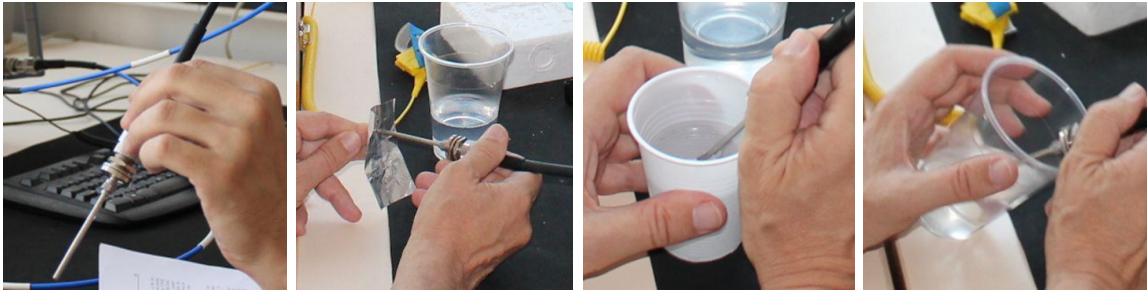


Figure 3.11 Calibration of the dielectric probe and measuring the phantom electric parameters (from left to the right – open, short, water; phantom)

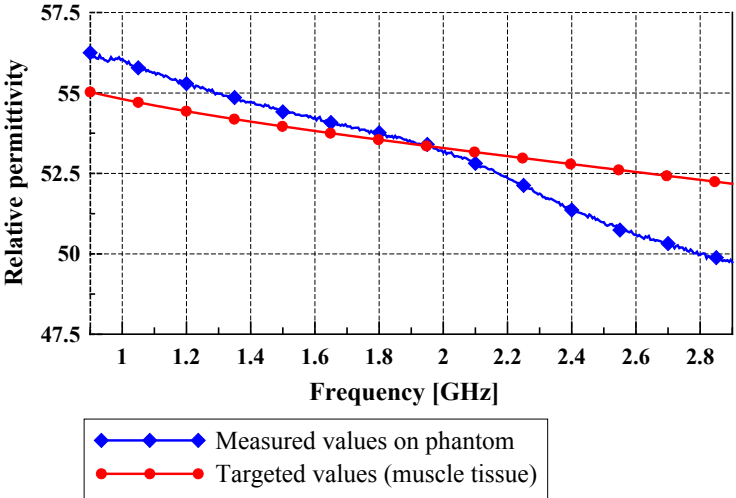


Figure 3.12 Frequency characteristics of the realized phantom permittivity

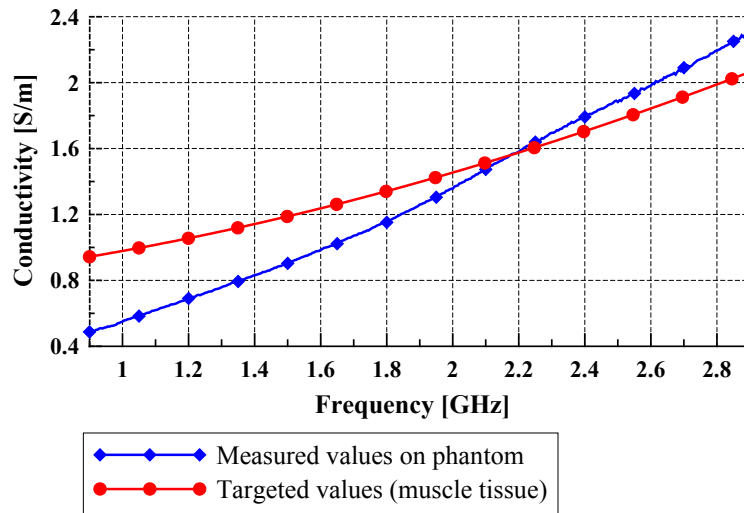


Figure 3.13 Frequency characteristics of the realized phantom conductivity

Table 3.4 Comparison of the targeted and measured electric properties for the muscle phantom for $f=2.45$ GHz

	ϵ_r	σ [S/m]
Measured on the phantom	52.729	1.739
Targeted value (muscle)	51.139	1.842

3.4.1. Characterization of the wideband planar monocone antenna with the use of the phantom

The obtained phantom was used for the laboratory characterization of the performance of various antenna realizations in the vicinity of the human body. Here, we describe the design of a wideband planar monocone antenna, and compare its properties in free space and on the human body phantom.

The use of wideband antennas was considered in our research as a way of alleviating the influence of the human body onto the antenna performance – namely, the idea is to “allow” the human body to alter the resonant frequency of the antenna by some amount; however, if the antenna possesses a larger bandwidth than required, its input matching could remain stable in the actual frequency band (in particular, the ISM 2.4 band was considered). Using the commercial CST Microwave Studio [99] software, we have designed a planar monocone antenna for operation around the ISM 2.4 band and optimized its dimensions with the goal of achieving the relative bandwidth in free space of at least 20%. The scheme of the antenna is

given in Fig. 3.14, together with its relevant dimensions in millimetres after optimization. The actual realization was obtained by applying copper tape on the fleece substrate (Fig. 3.15).

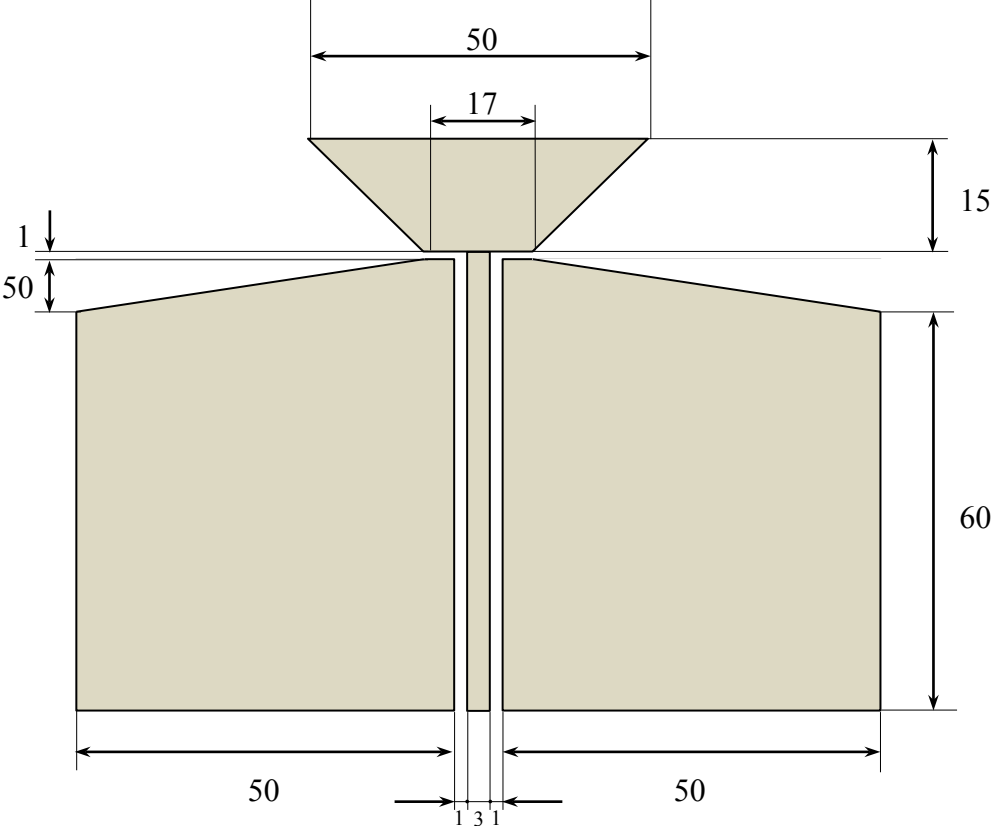


Figure 3.14 The wideband antenna for measurements on the phantom (dimensions in millimetres)

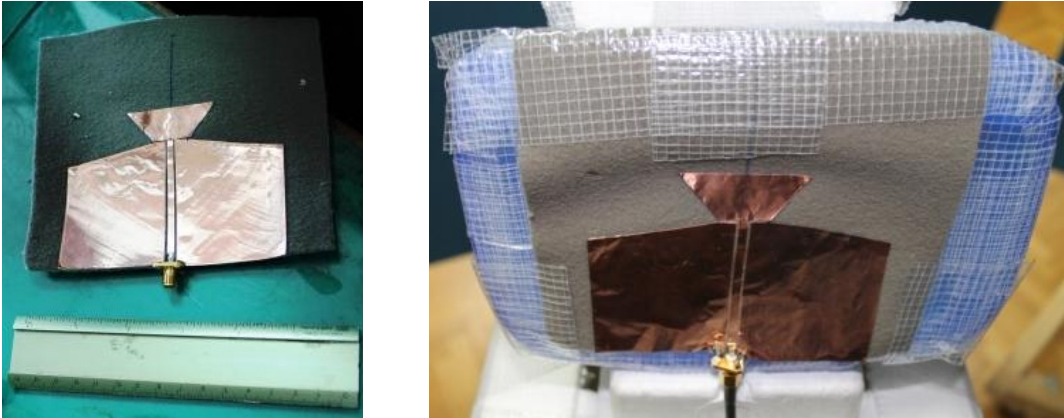


Figure 3.15 The proposed wideband antenna in free space (left) and mounted on the box containing the muscle-equivalent liquid (i.e. the phantom)

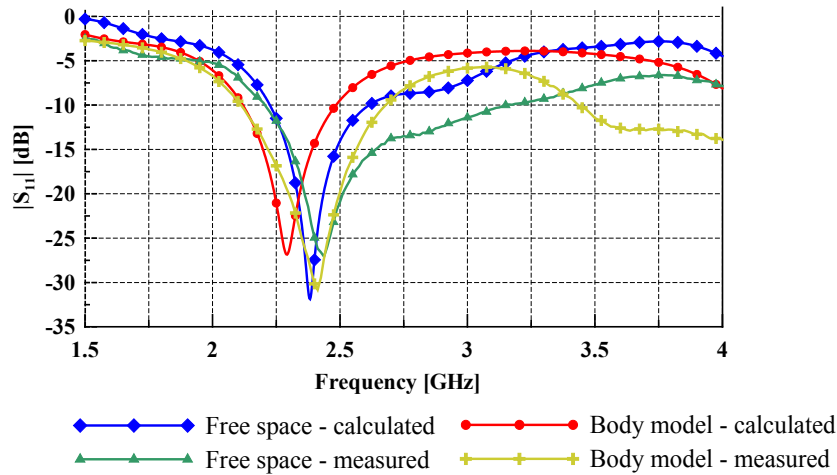


Figure 3.16 Calculated and measured magnitudes of the input reflection coefficient

In Fig. 3.16, a comparison between calculated and measured magnitudes of the input reflection coefficient is given for the cases of the antenna in free space and on the body model. A brick of dimensions $15 \times 15 \times 5$ cm filled with the predefined material from CST Microwave Studio, which has $\epsilon_r = 52.65$, $\sigma = 1.78$ S/m (which closely corresponds to muscle tissue at 2.45 GHz [92]), was chosen as the numerical phantom in the simulations. The R&S ZVA 40 vector network analyser was used for measurements.

It can be seen that the measured values in free space correspond very well with the calculated ones, while some minor discrepancies have been observed for the case of the human body, presumably due to the slight differences in the electric parameters of the numerical and physical phantom, and due to the influence of the layer of the plastic box in which the phantom was contained, which had not been taken into account in numerical simulations. Nevertheless, the obtained phantom can be said to represent the human body with good accuracy, while the antenna, due to its wide bandwidth, possessed adequate impedance matching in the desired ISM 2.4. band for all considered cases. We also note that, unlike the free space case, there are more ways to express what the antenna in the presence of the human body means (on the real human body there is also the influence of clothing layers, as well as a variation of electric parameters from human to human), so the use of a phantom as a model of the human body provides a laboratory tool for reproducible measurements and characterization of the antenna (any systematic influence such as the layer of plastic shell of the container can be eventually controlled), at least for the lifetime of the phantom (as already mentioned, liquid phantoms are exposed to evaporation, and thus suffer from changes in electric parameters over longer periods).

In Fig. 3.17, the measured co-polarization radiation patterns at the frequency of 2.4 GHz are given, for the antenna in free space and the antenna mounted on the phantom. It can be seen that back radiation was reduced by around 15÷20 dB when the human body phantom is present. In Table 3.5, a comparison of simulated (in CST Microwave Studio) and measured gain of the antenna at a frequency of 2.4 GHz is given for the antenna in free space and the antenna placed on the body phantom. Gain is measured using a calibrated horn antenna in the direction of maximum radiation (around -30° in the E -plane). It can be seen that, in the presence of the human body, the calculated and measured gain is reduced by 3.7 and 6.37 dB, respectively, meaning that a discrepancy between the calculated and measured results is observed. However, this confirms that in the presence of the human body, a portion of radiated power is absorbed in the body, leading to reduced radiation efficiency and gain. In addition, gain was simulated for the case when the antenna is placed 5 mm away from the phantom (which corresponds to a layer of clothes between the antenna and the human body). For that case, gain was recovered (and the directivity increased), which suggests that the influence of the body can be reduced by placing the antenna on the outer part of clothes (some more investigation of this effect will be given in section 6.4.1).

It also needs to be noted that the proposed antenna possesses a bandwidth larger than 20%; however, the radiated power when placed on the body model is considerably reduced (as can be seen in the radiation patterns and comparison of gain), which leads to lower radiation efficiency and increased radiation into the human body due to the absence of the ground plane. The proposed concept illustrates the benefits of using wideband antennas for body-centric communications, while it can also show potential for improvement by placing e.g. an EBG structure below the antenna to obtain isolation from the human body and enhanced radiation away from it. The use of a phantom facilitated the measuring of the radiation pattern in the presence of the human body, while also being a reproducible way of representing the interaction between the antenna and the human body.

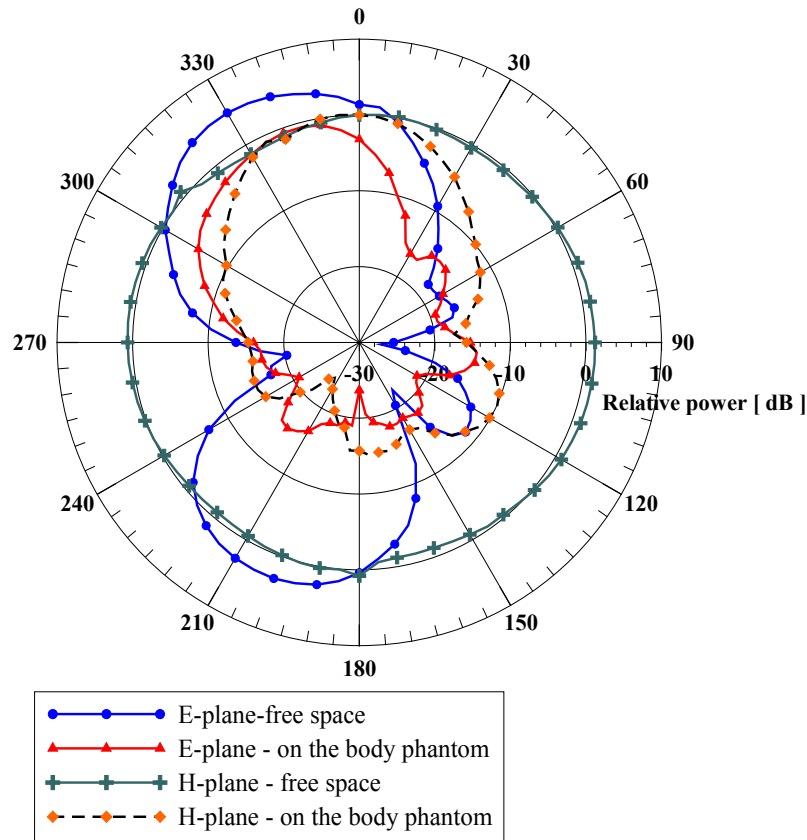


Figure 3.17 Measured co-polarization radiation patterns in free space and on the body phantom ($f=2.4$ GHz)

Table 3.5 Measured and simulated gain at maximum direction (-30° in E -plane) at $f=2.4$ GHz

	Free space	On the phantom	5 mm from the phantom
Measured	4.73 dBi	-1.64 dBi	-
Simulated	3.4 dBi	-0.3 dBi	4.8

3.4.2. Comments on the stability of the phantom with regard to aging

To put the phantom in a timeline with other research, it needs to be noted that the process of manufacturing the phantom was actually repeated twice, six months apart, due to the requirements of a larger quantity of phantom for further research (in particular, for the research of on-body propagation which will be described in Chapter 5). This has provided us with an opportunity to check the reproducibility of the recipe for the phantom, as well as to check the constancy of the phantom parameters.

After mixing the first portion of the phantom and performing measurements on the wideband antenna, the phantom was stored in a firmly closed plastic box. After six months, the phantom

required thorough stirring to recover its properties, which it did pretty well. Another portion of 2 kg of phantom was produced using the same procedure as described above. In Figs. 3.18 and 3.19, the comparison between the electric parameters of both portions of the phantom is given, together with their mixture.

In addition, the properties of the first portion of the phantom have been compared in its original state (i.e. the first use) and after a few months (before being mixed with the second portion), which is also shown in Figs. 3.18 and 3.19. The small rise in conductivity and drop in permittivity after aging can be ascribed to some water evaporation which occurred during the period of six months. Nevertheless, the new electric properties can still be considered to differ from the targeted values within the acceptable values, so the first portion is still suitable for further use and mixing with another portion.

The results also confirm that acceptable accuracy and reproducibility around the theoretical values in the desired frequency range (ISM 2.4 GHz) were obtained for all the considered cases, and that the body phantom represents the muscle tissue properly, thereby being suitable for on-body and off-body antenna and communication channel characterization. Although the first portion of the phantom retained its properties after six months, this should not last for an even longer period. The obtained phantom still suffers from water evaporation over time, which can, at best, only be slowed down by storing the phantom in firmly closed bottles or containers after usage.

The final comment regarding the manufacturing of the phantom is that the particular recipe we used for the phantom was actually (according to [94]) supposed to target the properties of the head tissue, having the permittivity of around 40 (middle value between skull, white and grey tissue, which is used for SAR measurements on the human head). Therefore, it came as quite of a surprise when the obtained phantom was shown to mimic the properties of the muscle tissue. This did not have a major role in our research (since investigations in the area of body-centric communications are widely performed using both versions of the phantom and several others), but, it is worth noting. Moreover, we note that the investigation of the chemicals that could be used for modelling the human body, apart from the ones we used, can be another topic of research by itself.

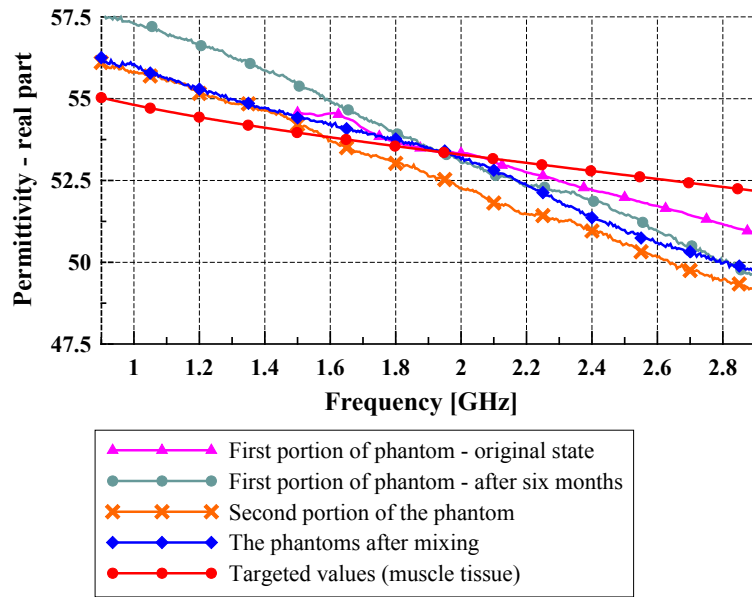


Figure 3.18 The permittivity of the phantom – analysis of stability and reproducibility

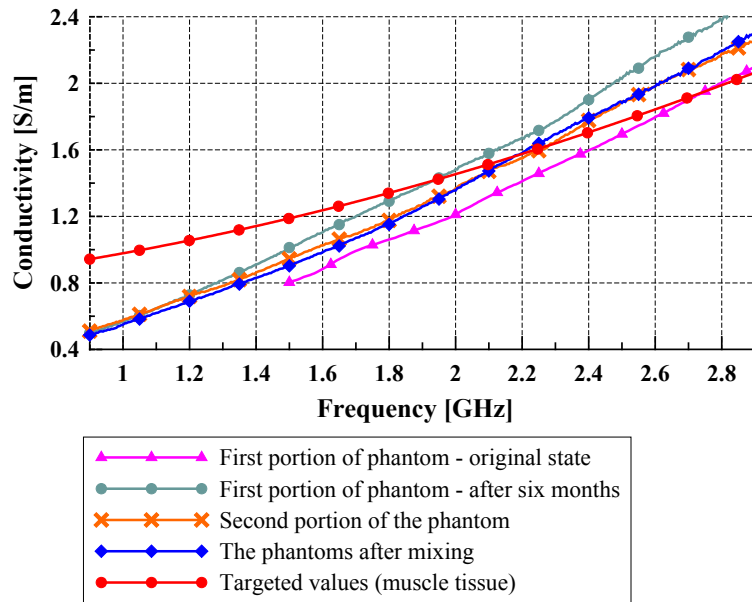


Figure 3.19 The conductivity of the phantom – analysis of stability and reproducibility

4. INTERACTION BETWEEN THE ANTENNA AND THE HUMAN BODY

Planar antennas are good candidates for use in body-centric communications, particularly for on-body and off-body communications, since they are usually low-profile and can be made conformable to the human body. Before addressing the practical issues (choice of material, real-environment conditions, durability etc.) we study some critical points in the antenna design, and constraints on the antenna size, followed by observations on the coupling between the antenna and the human body. Based on the fundamental derivation of the radiated field from the antenna, it will be shown that the miniaturization of the antenna is an art of compromise between volume, efficiency and bandwidth. In Fig. 4.1 the antenna size reduction principle is briefly illustrated. A detailed review of methods for antenna size reduction is given in [2, 24]. A part of this chapter was published by the author of the thesis in [102] , while small antennas were also studied by the author in [103, 104].

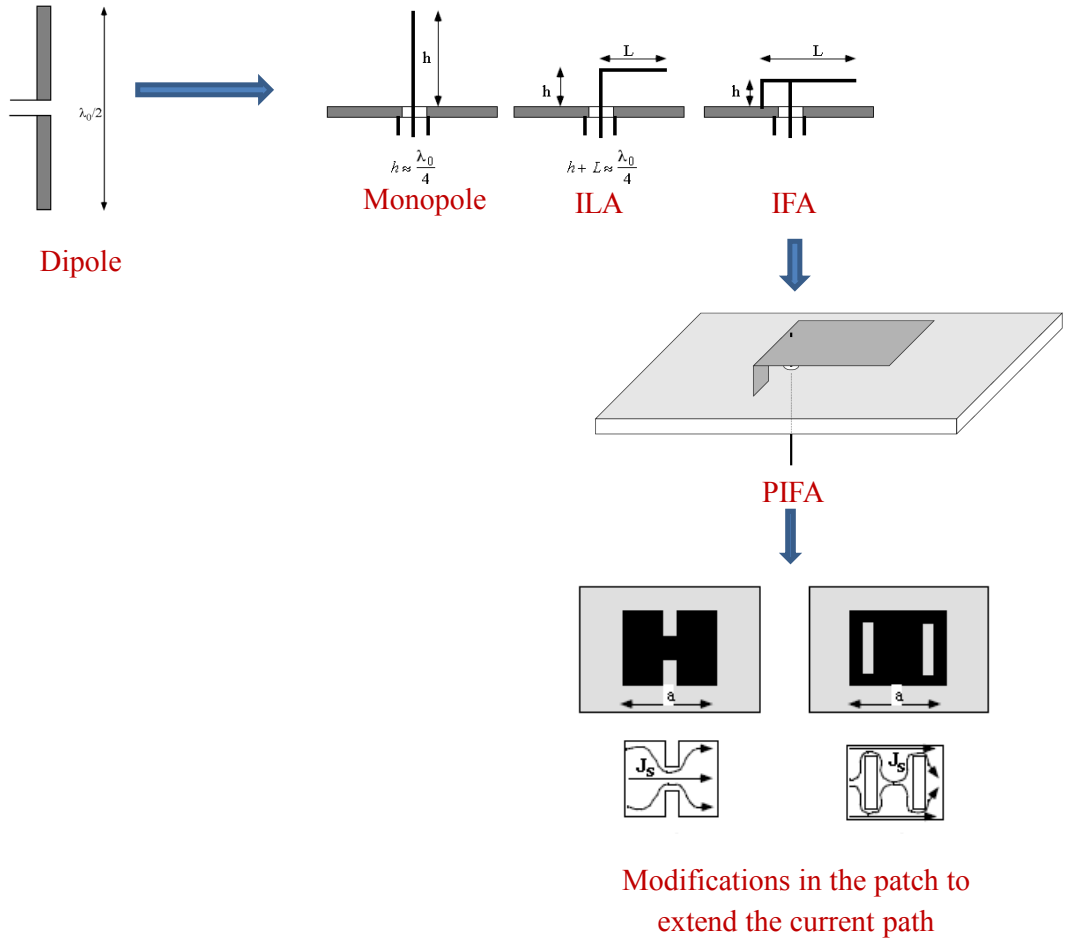


Figure 4.1 Illustration of the antenna size reduction principle [2]

4.1. Fundamental limitations of the antennas

One of the critical challenges in the antenna design is to design a small antenna which could conform to modern miniaturized electronic devices. Unlike electronic devices, the size of which is merely determined by the technology of fabrication, the antenna size should be comparable to its wavelength [2] in order to obtain good radiation properties. Therefore, non-miniaturized small antennas (in terms of their physical dimensions) can be produced only to operate in higher frequencies, while for lower frequencies, a compromise between volume, bandwidth and efficiency needs to be made.

An electrically small antenna can be defined as an antenna that could be enclosed within a sphere of a radius equal to $\lambda/2\pi$ (a so-called *radiansphere*), where λ is the operating wavelength in free space [105]. The maximum theoretical bandwidth of small antennas has been researched by many authors, and the interest in it is renewed in modern days, with the emergence of demands for reducing the size of antennas.

In order to characterize the antenna bandwidth, we use the quality factor Q , which comes from circuit theory and is defined as 2π times a ratio of time-averaged stored energy and energy dissipated in one period T of oscillations (P_{dis} represents the dissipated power):

$$Q = 2\pi \frac{W_{stored}}{W_{dis}} = 2\pi \frac{W_{stored}}{P_{dis} \cdot T} = \omega \frac{W_{stored}}{P_{dis}} \quad (4.1)$$

For antennas, stored energy consists of the electric (e) and the magnetic (m) part. In resonance these two are equal, so we can write $W_{stored} = 2W_e = 2W_m$. This can be also regarded to be approximately valid near resonance, where the antenna is supposed to operate. As for dissipated power, it is dissipated either due to losses in the antenna structure (metal and dielectric), or due to radiation (the latter is usually larger, and thus often assumed to be the only loss mechanism).

By introducing the quality factor Q , and by modelling the antenna with an RLC circuit near resonance, one gets the relationship between half-power bandwidth and Q (valid for $Q \gg 1$, which certainly is the case for small antennas):

$$\frac{\Delta f}{f_c} = \frac{1}{Q} \quad (4.2)$$

where Δf is the difference between upper and lower frequency, where dissipated power falls by half, and f_c is the central (resonant) frequency. Note that, strictly speaking, the exact

relationship between the Q -factor and the antenna bandwidth does not exist, since antenna modelling using an RLC circuit is only an approximation [106]. Nevertheless, the relationship (4.2) is widely accepted in engineering, so determining the antenna bandwidth is simply reduced to evaluating the antenna Q -factor.

There are two main approaches to the derivation of the antenna bandwidth - one approach is based on deriving the equivalent network (Chu approach), while the other one (Collin-Rotschild; McLean) is based on field analysis. In addition, there are some other approaches which can be considered merely as a refinement of the two mentioned. Both network and field approaches yield similar results, especially for lower order modes [106]. Here, we provide a detailed derivation of the Chu equivalent scheme, which has been recognized by many authors as a classic and intuitive approach that illustrates the issues of antenna limitations well, and visualises free space in terms of an equivalent electric scheme.

4.1.1. Spherical modes of free space

The basis for evaluating the stored and radiated energy in both approaches is to expand the electric and magnetic fields in an infinite volume (which represents free space) in spherical transverse vector eigenfunctions, i.e. spherical harmonics (the detailed derivation is given in Appendix A). The antenna is enclosed within the sphere of a diameter of $2a$, where a is the antenna maximum dimension, and the fields outside the sphere are evaluated. In the region external to the sphere $r > a$ (we assume the case of free space, where wavenumber is $k = k_0$ and constitutive parameters are equal to ϵ_0 and μ_0). The expansion is of the form:

$$\begin{aligned} \mathbf{E} &= \sum_{m,n} (a_{mn} \mathbf{M}_{mn}^{TE} + b_{mn} \mathbf{N}_{mn}^{TM}) = \mathbf{E}^{TE} + \mathbf{E}^{TM}, \\ \mathbf{H} &= -\frac{k_0}{j\omega\mu_0} \sum_{m,n} (a_{mn} \mathbf{N}_{mn}^{TE} + b_{mn} \mathbf{M}_{mn}^{TM}) = \mathbf{H}^{TE} + \mathbf{H}^{TM}, \end{aligned} \quad (4.3)$$

where the linearly independent vector eigenvectors \mathbf{M} and \mathbf{N} are derived using scalar functions ψ which are the solutions for the Helmholtz equation in spherical coordinates. The general form of the term in (m,n) of \mathbf{M} , \mathbf{N} and ψ , for both TM and TE case is:

$$\begin{aligned} \mathbf{M}_{mn} &= \nabla \times (\psi_{mn} \cdot \mathbf{r}), \\ \mathbf{N}_{mn} &= \frac{1}{k_0} (\nabla \times \nabla \times (\psi_{mn} \cdot \mathbf{r})), \end{aligned}$$

$$\psi_{mn} = h_n^{(2)}(k_0 r) \cdot P_n^m(\cos \theta) \cdot e^{-jm\varphi}, \quad (4.4)$$

where $h_n^{(2)}(k_0 r)$ is the spherical Hankel function of the second kind and the n -th order, $P_n^m(\cos \theta)$ are associated Legendre polynomials of degree n and order m , while $\mathbf{r} = r\hat{\mathbf{r}}$ is the radial position vector.

Note that, in fact, the fields in (4.3) are given as a linear combination of two mutually dual cases (modes) – transverse electric (TE) and transverse magnetic (TM), where “transverse” in this case means with respect to radial coordinate r . The “generating” functions ψ^{TM} and ψ^{TE} are of the same form as in (4.4), and differ only up to some multiplicative constant which depends on the boundary conditions. With the analysis performed as above, the view of free space as a spherical waveguide naturally arises, and the TM and TE spherical modes are often considered as modes of free space [108].

Since TE and TM modes are duals of each other, they each provide the same quality factor Q for the same double index mn . In addition, the ratio of stored and radiated electromagnetic energy is independent of the azimuthal index m . Therefore, we can restrict observations to TM_{0n} modes (without loss of generality), where \mathbf{M} and \mathbf{N} functions for some arbitrary n are explicitly calculated using vector identities, and the expression for the associated Legendre equation is calculated as [89, 107]:

$$\begin{aligned} \mathbf{M}_{0n}^{TM} &= \nabla \times (\psi_{0n}^{TM} \cdot r\hat{\mathbf{r}}) = M_{0n}^\varphi \hat{\boldsymbol{\phi}}, \\ \mathbf{N}_{0n}^{TM} &= \frac{1}{k_0} (\nabla \times \mathbf{M}_{0n}) = N_{0n}^r \hat{\mathbf{r}} + N_{0n}^\theta \hat{\boldsymbol{\theta}}, \end{aligned} \quad (4.5)$$

where:

$$\begin{aligned} M_{0n}^\varphi &= h_n^{(2)}(k_0 r) \cdot \frac{dP_n(\cos \theta)}{d\theta}, \\ N_{0n}^r &= \frac{1}{k_0 r \sin \theta} h_n^{(2)}(k_0 r) \cdot \frac{d}{d\theta} \left(\sin \theta \frac{dP_n(\cos \theta)}{d\theta} \right) = -\frac{1}{k_0 r} h_n^{(2)}(k_0 r) n(n+1) P_n(\cos \theta), \\ N_{0n}^\theta &= -\frac{1}{k_0 r} \frac{d}{dr} (r h_n^{(2)}(k_0 r)) \frac{dP_n(\cos \theta)}{d\theta}. \end{aligned}$$

The amplitudes of the electric and magnetic fields in TM_{0n} mode are finally obtained after some manipulations as [105]:

$$\begin{aligned}
H_\varphi &= -\frac{k_0}{j\omega\mu_0} b_{0n} M_{0n}^\varphi = \frac{b_{0n}}{j\omega\mu_0} \frac{\sin\theta}{r} \frac{dP_n(\cos\theta)}{d(\cos\theta)} \left[k_0 r h_n^{(2)}(k_0 r) \right] \\
E_r &= b_{0n} N_{0n}^r = -b_{0n} \frac{n(n+1)}{(k_0 r)^2} P_n(\cos\theta) \left[k_0 r h_n^{(2)}(k_0 r) \right] \\
E_\theta &= b_{0n} N_{0n}^\theta = b_{0n} \frac{\sin\theta}{k_0 r} \frac{dP_n(\cos\theta)}{d(\cos\theta)} \frac{d \left[k_0 r h_n^{(2)}(k_0 r) \right]}{d(k_0 r)} \quad (4.6)
\end{aligned}$$

4.1.2. The Chu approach

Using the expressions (4.6), the normalized wave impedance in the radial direction of the n -th mode is calculated, after some manipulations, for $r=a$ as:

$$Z_{w,0n} = \frac{E_\theta}{H_\varphi} = \frac{j\eta_0}{k_0 a} + \frac{j\eta_0}{h_n^{(2)}(k_0 a)} \frac{dh_n^{(2)}(k_0 a)}{d(k_0 a)}, \quad (4.7)$$

where $\eta_0 = \sqrt{\mu_0 / \epsilon_0}$ is the wave impedance of free space.

To obtain the equivalent circuit, the idea is to expand the wave impedance (4.7) into a network of alternating series capacitors and shunt inductors, which is terminated with the characteristic impedance of free space η_0 , as given in Fig. 4.2. This is analogous to the Cauer LC -network realization [106].

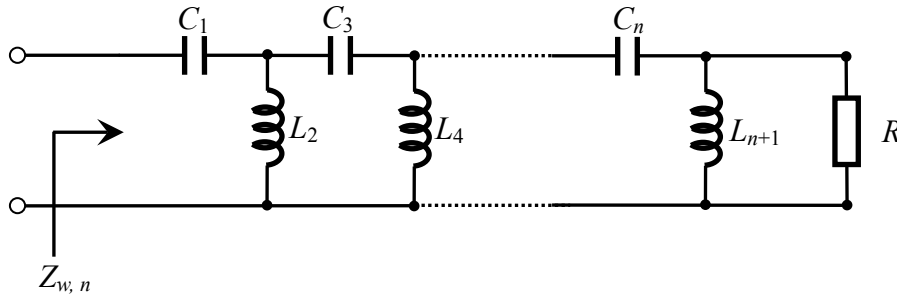


Figure 4.2 Chu ladder network

The input impedance for the network in Fig. 4.2 is given for an odd n as:

$$Z_{w,0n} = \frac{1}{j\omega C_1} + \frac{1}{\frac{1}{j\omega L_2} + \frac{1}{\frac{1}{j\omega C_3} + \frac{1}{j\omega L_4} + \dots + \frac{1}{\frac{1}{j\omega C_n} + \frac{1}{j\omega L_{n+1}} + R}}}. \quad (4.8)$$

To obtain the values of the elements of the network, the following recursive formulations valid for spherical Bessel and Hankel functions need to be used [105, 107]:

$$h_n^{(2)}(k_0 r) = \frac{2n-1}{k_0 r} h_{n-1}^{(2)}(k_0 r) - h_{n-2}^{(2)}(k_0 r), \quad (4.9)$$

$$\frac{dh_n^{(2)}(k_0 r)}{d(k_0 r)} = h_{n-1}^{(2)}(k_0 r) - \frac{n+1}{k_0 r} h_n^{(2)}(k_0 r), \quad (4.10)$$

$$\frac{h_1^{(2)}(k_0 r)}{h_0^{(2)}(k_0 r)} = j + \frac{1}{k_0 r}. \quad (4.11)$$

Using (4.10) for $r=a$, the expression for the wave impedance (4.7) is readily rewritten as:

$$\frac{Z_{w,0n}}{\eta_0} = \frac{n}{jk_0 a} + \frac{1}{\frac{h_n^{(2)}(k_0 a)}{jh_{n-1}^{(2)}(k_0 a)}},$$

which is finally expanded using (4.9) as:

$$\frac{Z_{w,0n}}{\eta_0} = \frac{n}{jk_0 a} + \frac{1}{\frac{2n-1}{jk_0 a} + \frac{1}{\frac{2n-3}{jk_0 a} + \frac{1}{\frac{2n-5}{jk_0 a} + \dots + \frac{1}{\frac{3}{jk_0 a} + \frac{1}{\frac{1}{jk_0 a} + 1}}}}}. \quad (4.12)$$

By multiplying (4.12) with η_0 , and by comparison with (4.8), the elements of the ladder network are readily obtained as [106]:

$$\begin{aligned}
 C_1 &= \frac{\varepsilon a}{n}, \\
 L_2 &= \frac{\mu_0 a}{2n-1}, \\
 C_3 &= \frac{\varepsilon a}{2n-3}, \\
 L_4 &= \frac{\mu_0 a}{2n-5},
 \end{aligned} \tag{4.13}$$

etc. The final resistance R is equal to η_0 .

Now, we pay particular attention to the lowest order (dominant) mode, TM_{01} . This is the linearly polarized mode which is excited e.g. by a short dipole antenna [106]. The equivalent electric scheme is given in Fig 4.3.

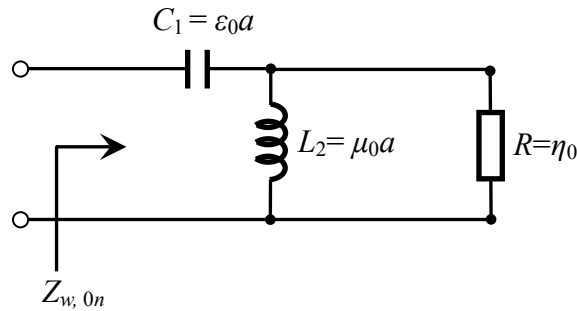


Figure 4.3 Equivalent circuit for TM_{01} mode

Using classical circuit analysis, the stored electric energy and dissipated power can be calculated, which finally leads to the Q -factor of the TM_{01} mode:

$$Q_{01} = \omega \frac{2W_e}{P_{rad}} = \frac{1}{k_0 a} + \frac{1}{(k_0 a)^3}. \tag{4.14}$$

In a similar manner, the Q -factors for higher order modes are derived, and follow as [105]:

$$\begin{aligned}
 Q_{02} &= \frac{3}{k_0 a} + \frac{6}{(k_0 a)^3} + \frac{18}{(k_0 a)^5}, \\
 Q_{03} &= \frac{6}{k_0 a} + \frac{21}{(k_0 a)^3} + \frac{135}{(k_0 a)^5} + \frac{675}{(k_0 a)^7},
 \end{aligned} \tag{4.15}$$

etc. For $n > 3$, the calculation of the Q -factor via equivalent schemes becomes cumbersome, so in these cases, the original ladder network is further approximated by a simple RLC network [106]. Note also that this is only the theoretical lowest limit for Q – in practical antenna realizations, the Q -factor is even higher.

Note that Q rapidly grows as soon as the parameter $k_0 a$ (which represents the antenna electrical length) becomes smaller than 1. Therefore, an antenna which is electrically small exhibits a large Q -factor. From eq. (4.2) it follows that such an antenna is inherently narrow-band.

4.1.3. Field approach to the derivation of Q

To complete the discussion about fundamental limitations of the antenna, we provide a brief overview of another common method of evaluation of the antenna Q , which is based on field analysis [105]. Again, the antenna is enclosed by a sphere of a diameter of $2a$, where a is the largest antenna dimension. The procedure is outlined for a short dipole antenna (which excites only the TM_{01} mode), where the field amplitudes E_θ and E_r are given by expanding (4.6) and calculating the spherical Hankel function and the associated Legendre polynomial of the order $n=1$ [106, 107]:

$$h_1^{(2)}(k_0 r) = \frac{e^{-jk_0 r}}{k_0 r} \left(-1 + \frac{j}{k_0 r} \right),$$

$$P_1(\cos \theta) = \cos \theta,$$

$$E_r = 2b_{01} \cos \theta e^{-jk_0 r} \left(\frac{1}{(k_0 r)^2} - \frac{j}{(k_0 r)^3} \right),$$

$$E_\theta = b_{01} \sin \theta e^{-jk_0 r} \left(\frac{j}{k_0 r} + \frac{1}{(k_0 r)^2} - \frac{j}{(k_0 r)^3} \right). \quad (4.16)$$

Note that, from [106], $b_{01} = \frac{Il}{4\pi} k_0^2 \eta_0$; l is the dipole length, and I is the current (assumed constant).

The derivation of the Q -factor proceeds as follows:

i) Calculate the total energy density outside the sphere containing the antenna

$$w_e^{tot} = \frac{1}{2} \epsilon_0 \mathbf{E} \cdot \mathbf{E}^* = \frac{1}{2} \epsilon_0 (E_\theta^2 + E_r^2). \quad (4.17)$$

ii) Calculate the radiated energy density in the far field:

$$w_e^{rad} = \frac{1}{2} \epsilon_0 E_{\theta,rad}^2, \quad (4.18)$$

where $E_{\theta,rad}$ is the term in $1/r$ in (4.16), which is the only non-negligible term contributing to the radiation [89].

iii) Obtain the non-radiated (stored) energy density and energy outside the sphere of a radius of a as a difference between the total and radiated energy

$$w_e^{nr} = w_e^{tot} - w_e^{rad},$$

$$W_e^{nr} = \int_0^{2\pi} \int_0^\pi \int_a^\infty w_e^{nr} \sin \theta dr d\theta d\varphi. \quad (4.19)$$

iv) Calculate the radiated power by integrating the Poynting vector over a sphere of a large radius

$$P_{rad} = \int_0^{2\pi} \int_0^\pi E_\theta H_\varphi^* r^2 \sin \theta dr d\theta d\varphi. \quad (4.20)$$

v) Use the definition of Q in (4.14) to obtain

$$Q_{01} = \omega \frac{2W_e}{P_{rad}} = \frac{1}{k_0 a} + \frac{1}{(k_0 a)^3}.$$

The result for the first mode is same as in the Chu approach by equivalent network. Generally, for lower order modes, both approaches yield the same results for Q [105, 106].

4.2. The proposed PIFA for 400 MHz

At this stage of research, our focus was on body-centric communications in the UHF range (in particular, around 400 MHz), with the goal of designing a wearable textile antenna for that range. Such an antenna is in principle intended for medium-range off-body communications (up to a few hundred meters), which could be useful e.g. for rescue and military teams. Much of this section has been published by author of the thesis in [102].

Using the commercial software CST Microwave Studio, the antenna based on a PIFA concept (which is commonly exploited in GSM communications) was designed and optimized for

operation around 400 MHz in free space. 4 mm-thick nonwoven fabric (i.e. fleece, of relative permittivity of 1.1 [76]) was assumed to be the substrate, which is quite thin in terms of the wavelength in the UHF frequency range. The proposed antenna consists of the ground plane with a slot, a slotted patch and a shorting wall (S.W.), as shown on Fig. 4.4. The design itself was inspired by the antenna proposed in [109], where the slots were introduced to extend the current path and make the antenna appear longer. This is one of the standard methods in the antenna size reduction [2].

In the first considered case, the patch was placed along one edge of the ground plane, i.e. asymmetrically (the position of the patch above ground plane was examined later). The slot in the ground plane was placed at a distance of 80 mm from the shorting wall, beneath the patch, while the feeding point in free space was placed at a 49.5 mm distance from the shorting wall. The dimensions of the antenna components for the first considered case are summarized in Fig. 4.5 and Table 4.1.

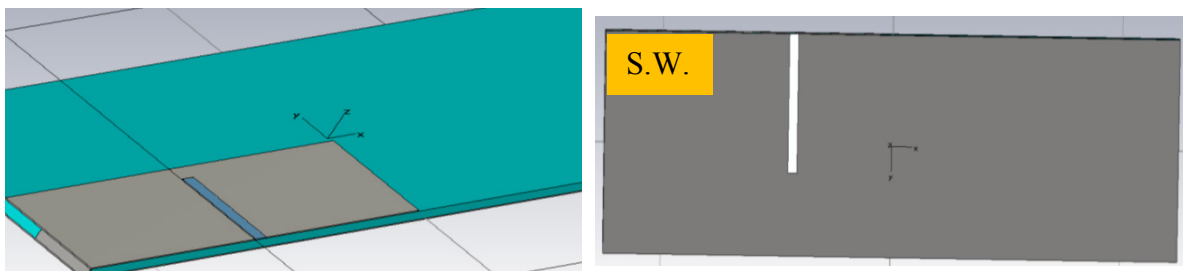


Figure 4.4 The proposed PIFA – top and bottom view

When placed on the body model, the resonant frequency shifted upwards by 21% (i.e. to around 500 MHz), as shown in Fig. 4.6 (the feeding point was altered to obtain better impedance matching for this case, as shown in Table 4.1.). Such unexpected up-shift in frequency was confirmed by simultaneous simulations in Ansoft HFSS. In addition, as qualitatively shown in Figs. 4.7 and 4.8, most of the field on the ground plane for the case with the body was concentrated mostly around the patch region (i.e. part of the ground plane further from the patch had very low magnitudes), suggesting that the antenna in the presence of the body appears to be electrically shorter. Furthermore, the part of the ground plane placed further away from the patch appears redundant in terms of surface currents and fields, suggesting that some further reduction in the size of the ground plane is possible in the presence of the human body. Also, we note that an apparent magnitude of the reflection coefficient larger than that for some frequencies (out of resonance) arises due to numerical instability, i.e. a lower number of cells was used to speed up the simulation process. This was

confirmed by a raising number of cells. As the resonant frequency of various cases is looked for at this point, it is of no great importance in this stage of research.

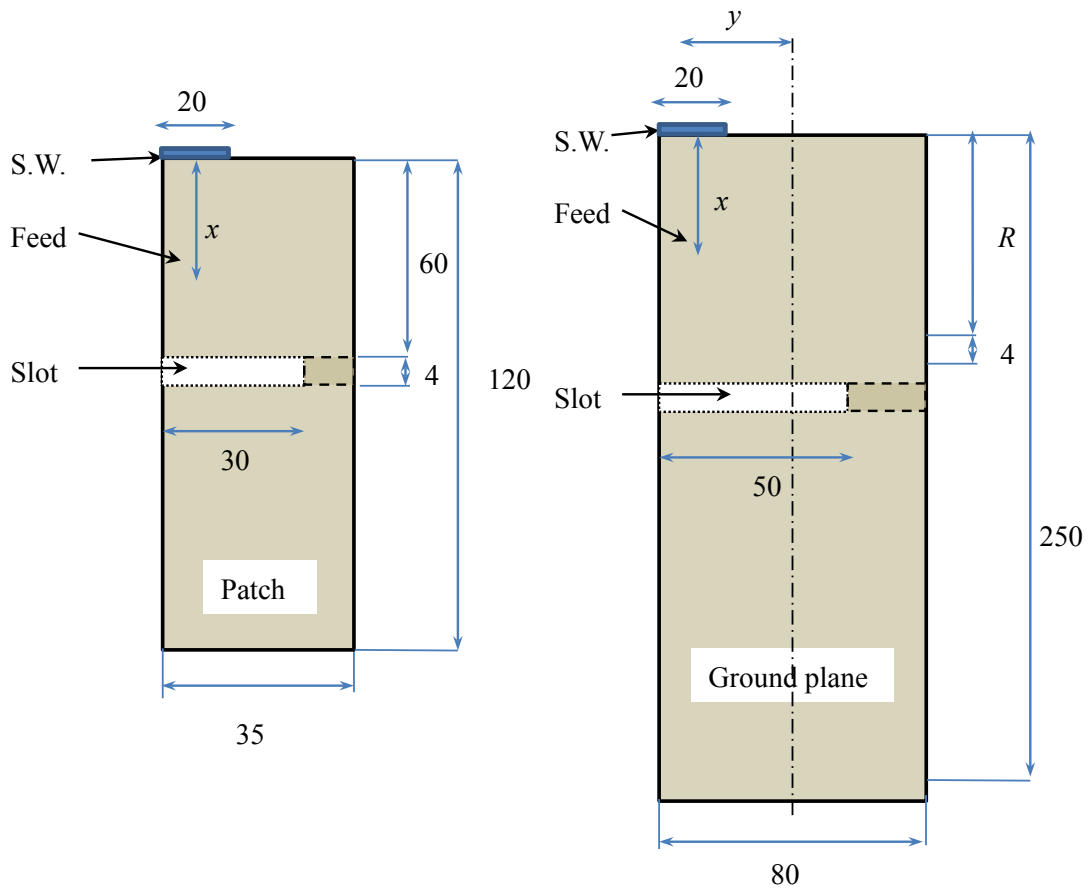


Figure 4.5 Sketch of the proposed PIFA – ground plane and patch are given separately

Table 4.1 Dimensions of proposed PIFA for the UHF 400 band in [mm]

Ground plane size	250 × 80
Patch length	120
Patch width	35
Shorting wall (S.W.) length	20
Ground plane slot length	50
Ground plane slot position (R)	80
Patch slot length	30
Slot width	4
Feeding distance from the S.W. (x) – free space	49.5
Feeding distance from the S.W. (x) – with body	30
Feeding distance from ground plane symmetrical (y)	30

As shown in Table 4.2, radiation efficiency in the presence of the body model plummeted to -17 dB, leading to a gain of around -13 dBi. Such low values of radiation efficiency are not unusual in the relevant literature on body centric systems (as described in Chapter 2), and this means that there is a significant influence of the body on the antenna performance for the case of the PIFA antenna with the slot in the ground plane. The use of such an antenna for off-body communications (which is its primary intention) is, however, not recommended in the form described above, since most radiation resides inside the human body via the slot in the ground plane, instead of radiating into outer space.

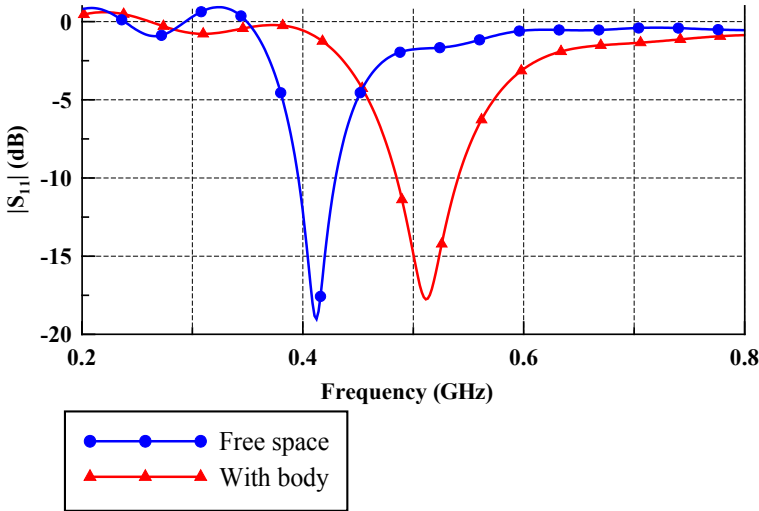


Figure 4.6 Input reflection coefficient vs. frequency for proposed antenna

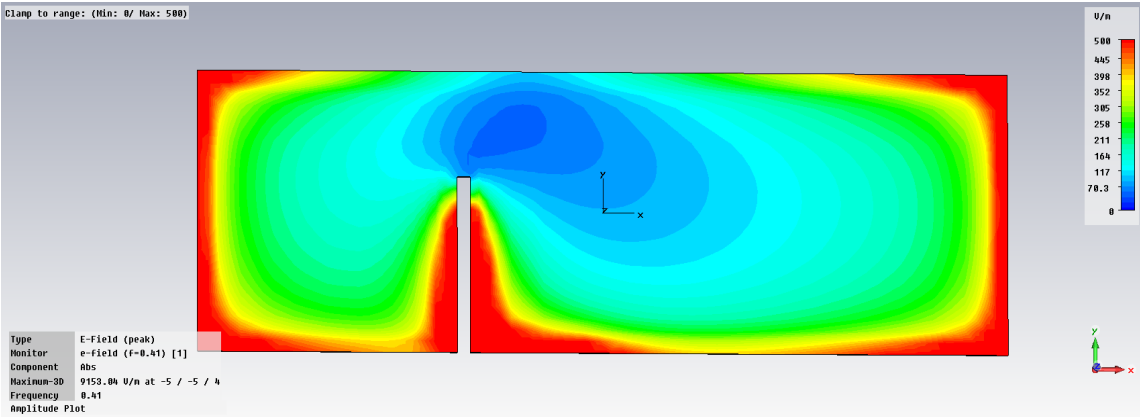


Figure 4.7 Magnitude of the electric field on the ground plane in free space (scale from 0- blue to 500 V/m-red)

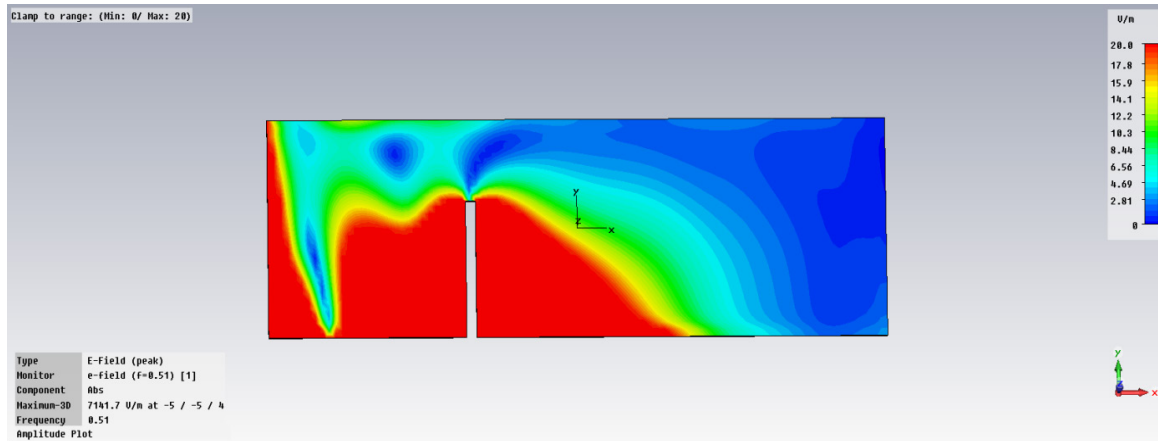


Figure 4.8 Magnitude of the electric field on the ground plane with the body model (Scale from 0- blue to 20 V/m - red)

Table 4.2 Calculated radiation efficiency and gain of the analyzed PIFA antenna

	Free space	With body
Rad. efficiency	-0.201	-16.88 dB
Gain	2.489	- 12.66 dBi

4.2.1. Further analysis of the PIFA

A. Position of the slot in the ground plane

When the slot was removed from the ground plane, resonant frequency was around 500 MHz for both the free space case and the case with the body model. Furthermore, radiation efficiency with the body model was 10 dB higher (although the bandwidth was reduced). This means the slot in the ground plane interacts with the antenna near field and alters its radiation properties, as well as largely contributing to the coupling with the body (apart from diffraction from the finite ground plane).

In subsequent simulations, sweeping of the length and position of the slot in the ground plane was performed in order to investigate the influence of the slot on the antenna performance. As expected, by increasing the length of the slot in free space, the resonant frequency was lowered. When the body model was present, the influence of the slot length on the resonant frequency and matching bandwidth was less pronounced.

The position of the slot also influences the resonant frequency and matching in free space, as shown in Fig. 4.9. The resonant frequency is lower when the slot is placed closer to the shorting wall, which means a stronger influence is exerted there. Also, the feeding point is

changed, i.e. a mismatch occurs for the cases when the slot in the ground plane is close to the shorting wall ($R=20$ and 40 mm, as described in Fig. 4.5). When placed on the body (Fig. 4.10), the effect of the slot again generally diminishes; however, stronger influences were observed for the cases when the slot is placed between the shorting wall and the feeding point ($R=20$ and 40 mm), suggesting that some additional resonances occur. Still, it needs to be noted here that different results for the two respective slot distances were obtained in another CAD program (HFSS), i.e. no resonances, nor irregularities were observed. By looking at the current density distribution in CST, no additional resonance could have been observed, so this needs further explanation.

The influence of the patch position on the ground plane was also investigated. By moving the patch away from the edge of the ground plane, it was found that it is possible to improve the radiation efficiency by up to around 7 dB. The effect was observed even when the patch was moved closer to the other edge, meaning that the improvement in efficiency in fact occurs by leaving a part of ground plane slot open. This suggests that the patch and the ground plane form a capacitor through which, when a slot is placed, the antenna near field couples more with the body, thereby reducing radiation efficiency. The more the slot was uncovered, the more such coupling was reduced. The relevant results are summarized in Table 4.3.

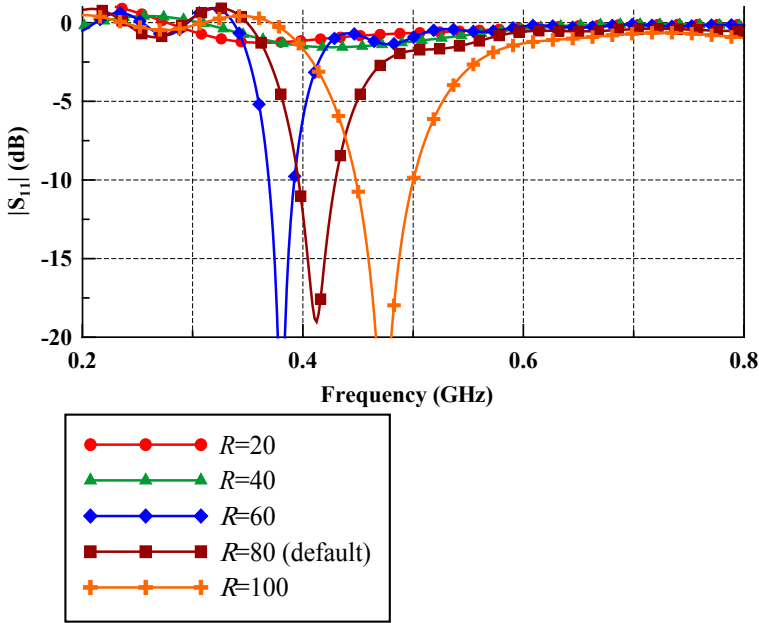


Figure 4.9 Input reflection coefficient for various distances R between the ground plane slot and the shorting wall – free space

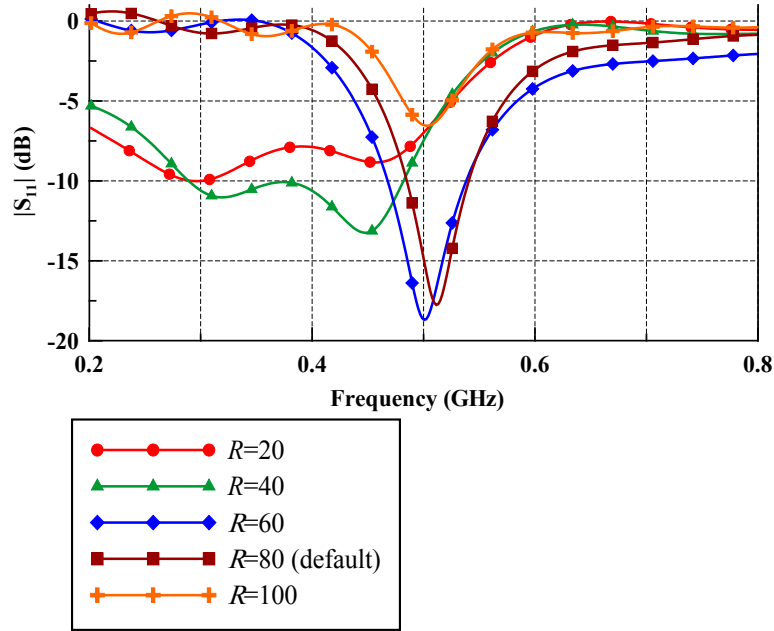


Figure 4.10 Input reflection coefficient for various distances R between the ground plane slot and the shorting wall – the case with the body model

Table 4.3 Influence of the patch position on PIFA parameters

Distance from the edge [mm]	Rad. efficiency [dB]	Resonant frequency [GHz]	BW [%]
0 (default)	-16.98	0.511	10.78
10	-15.95	0.504	7.2
20	-13.15	0.484	3.54
30	-10.18	0.487	2.1

4.2.2. Symmetric PIFA

As an illustration, we consider the case where the patch was moved to the middle of the ground plane along the ground plane width, i.e. placed symmetrically (Fig. 4.11). For this case, the patch distance from the edge was 22.5 mm. The radiation efficiency was around -12 dB, which is an improvement of 5 dB compared to the PIFA placed along the edge of the ground plane. On the other hand, the observed frequency up-shift (compared to free space) was only around 2%. Therefore, when a part of the slot in the ground plane is open, the effect of the slot in the ground plane on the resonant frequency is considerably lower, as described before.

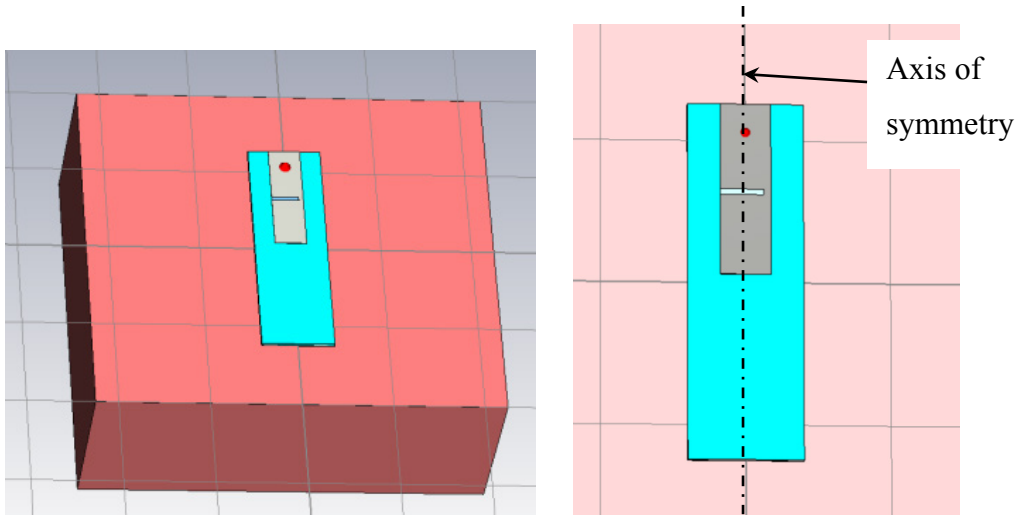


Figure 4.11 PIFA with the symmetrically placed patch on the body - illustration

For the case of the symmetrically placed patch, the influence of the slot (in the ground plane and in the patch, respectively) on the antenna performance was separately analyzed in some more detail. In Table 4.4, the positions of the feeding point are summarized for each observed case. It can be seen that, when body is present, better matching is obtained with the feeding point somewhat closer to the shorting wall. The influence of each slot on the antenna matching bandwidth and resonant frequency is shown in Table 4.5, while the radiation efficiency and gain for the considered cases are summarized in Table 4.6.

By analyzing the results, it can be observed that the presence of the slot in the ground plane contributes to the radiation bandwidth and couples with the body, causing the already observed up-shift in resonant frequency. On the other hand, the slot in the patch merely lowers the resonant frequency (both in free space and with body model) making the antenna appear electrically larger, and has no significant effect on the coupling with body.

Table 4.4 Distance between the feeding point and the plane of shorting wall in [mm]

	In free space	With body
No slots	10	8
Only ground plane slot	25	20
Only patch slot	15	10
Both slots	30	20

Table 4.5 Influence of each respective slot in the PIFA on resonant frequency and bandwidth

	f_r - free space	f_r - with body	BW-free space	BW-with body
No slots	0.551 GHz	0.549 GHz	2.18 %	1.27 %
Only ground plane slot	0.531 GHz	0.549 GHz	6.59 %	8.62%
Only patch slot	0.486 GHz	0.484 GHz	2.67 %	1.03 %
Both slots	0.475 GHz	0.484 GHz	5.68 %	3.72 %

Table 4.6 Calculated radiation efficiency and gain for the considered cases

	Rad. efficiency [dB]	Gain [dBi]
No slots	-5.551	-0.859
Only ground plane slot	-11.55	-6.889
Only patch slot	-7.085	-3.019
Both slots	-12.27	-8.231

To illustrate the coupling of the antenna with the human body, in Fig. 4.12, the power flow in the E -plane is depicted. It can be seen that the coupling occurs through the slot and through the edge of the ground plane where the shorting wall is present. We attempted to reduce the latter coupling mechanism by adding some more ground plane behind the shorting wall (i.e. effectively translating the patch and the slot in the x -direction), which is shown in Fig. 4.13. Although it is obvious that, for the case of the added ground plane behind the shorting wall, there is only coupling through the slot, virtually no improvement in radiation efficiency has been obtained for this case, which means that the coupling of the antenna with the body through the edge of ground plane produces a minor effect compared to the coupling through ground plane.

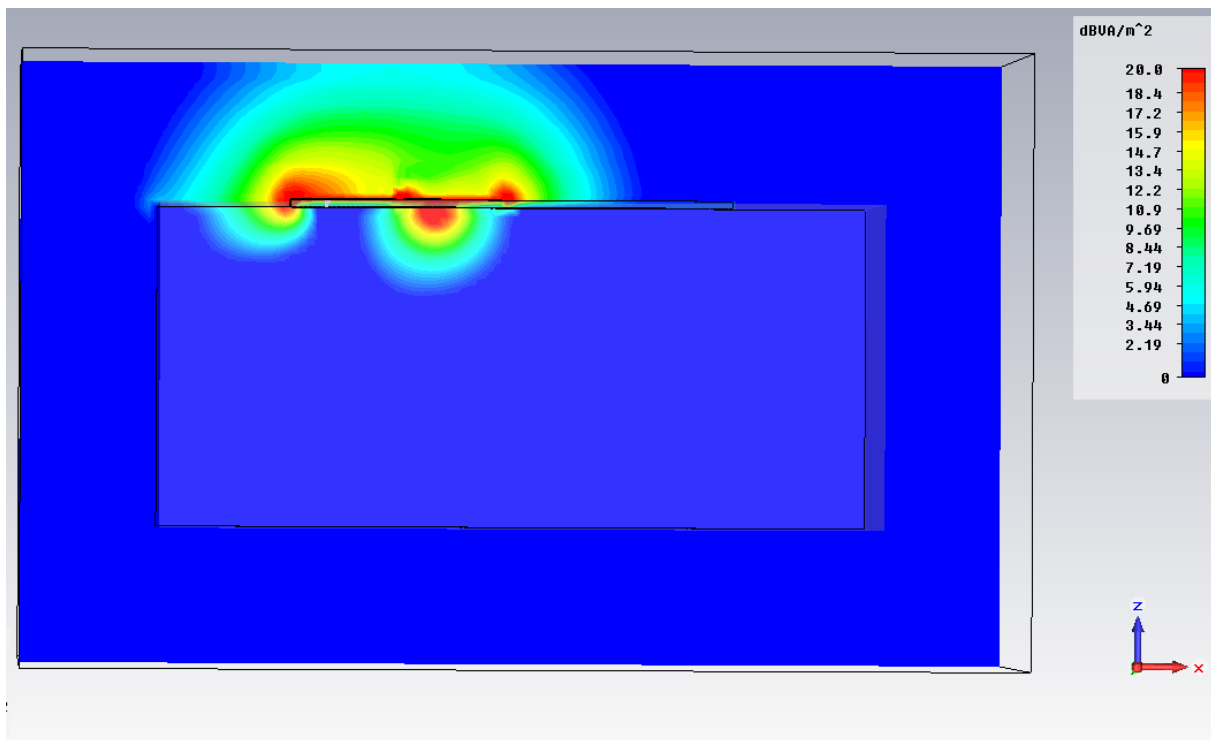


Figure 4.12 Power flow in the E -plane – symmetric patch

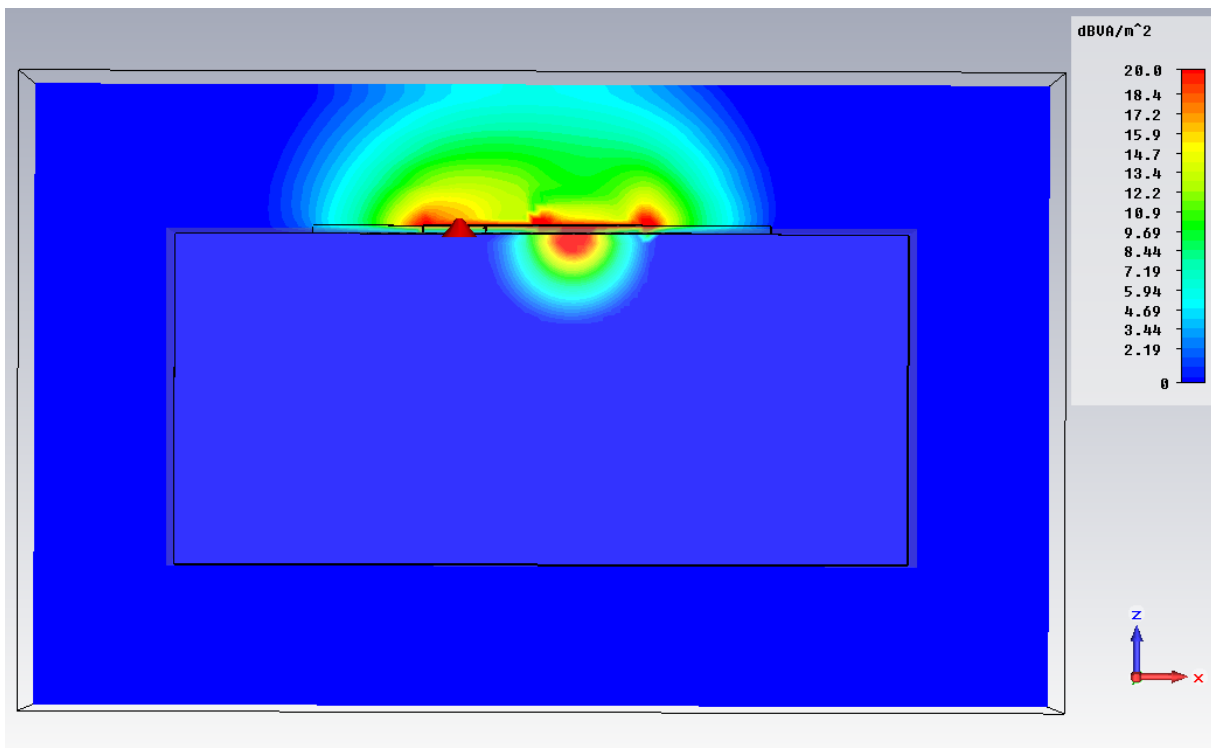


Figure 4.13 Power flow in the E -plane for symmetric patch; translated in the x -direction

4.3. Modelling the interaction between the PIFA antenna and the human body

The previous analysis gives rise to the question of why the resonant frequency for the proposed PIFA shifts upwards when the antenna is placed on the body, which is unexpected in the sense that the presence of a high permittivity media (i.e. human body) is supposed to actually decrease it. Thus, the presence of the slot in the near field suggests there is a more complex coupling mechanism between the antenna and the human body than a simple assumption of the presence of high permittivity media. To model such coupling in electrical terms, the PIFA antenna is first modelled as a resonant RLC circuit, while, in continuation, the slot impedance is investigated. To simplify the procedure, and focus only on the influence of the slot, we have investigated the PIFA antenna without the additional slot in the patch (which was found only to extend the current path), and with the shorting wall extending over the full length of the PIFA antenna. In that way, we approximate the PIFA antenna with a $\lambda/4$ microstrip antenna.

4.3.1. PIFA without the slot

In the first case, we derive the model for the PIFA in free space without the slot in the ground plane. Furthermore, the antenna is placed symmetrically, i.e. in the middle of the ground plane, while it was found that placing the antenna on the edge does not significantly affect the model. The considered case is given in Fig. 4.14, while the ground plane and patch dimensions are retained as in Table 4.1. The feeding point was found to be 12 mm from the plane of the shorting wall, while the resonant frequency in this case is 0.577 GHz.

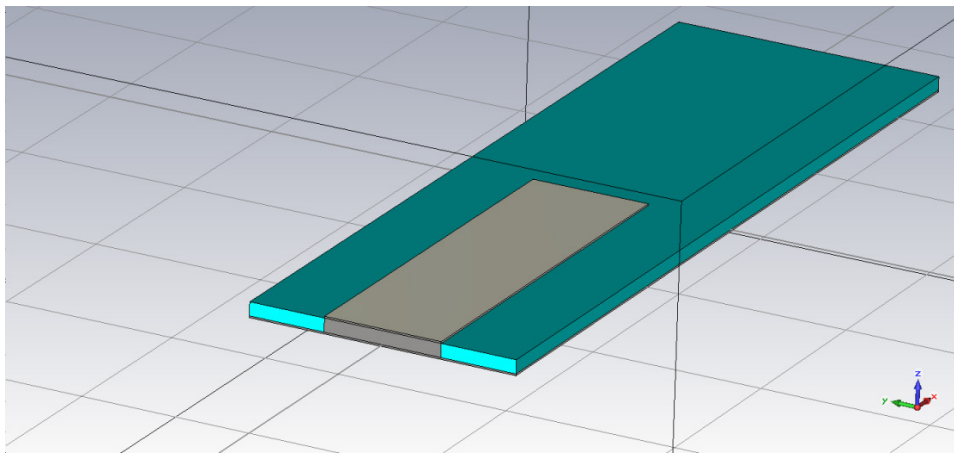


Figure 4.14 The considered antenna used for building the equivalent model

In Fig. 4.15, the assumed transmission line model for such a PIFA antenna is given, based on [110]. The shorting wall was assumed as a short circuit, while the radiating slot was modelled as the parallel of slot capacitance and radiation resistance (admittance formulation is used for convenience). The inductance of the feeding was neglected. To check the validity of this model for the considered PIFA antenna, we have calculated the parameters of the radiating slot based on known input impedance and the placement of the feeding point.

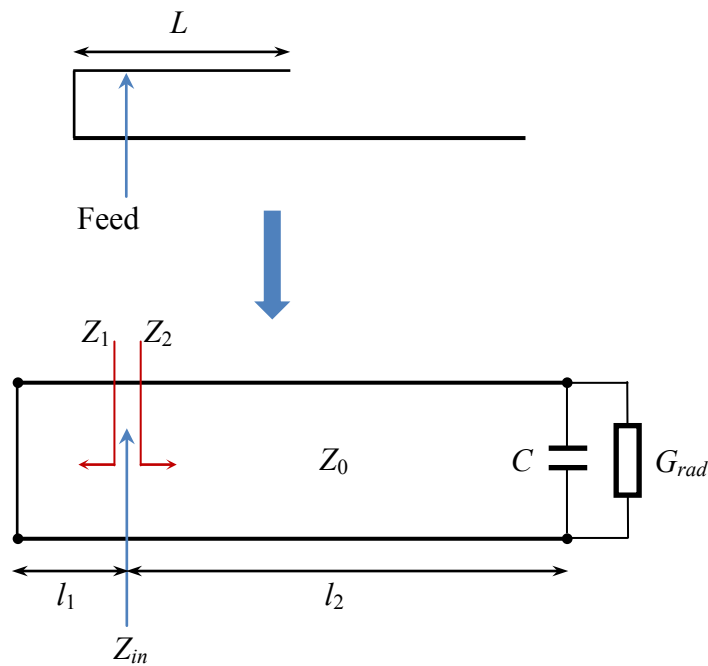


Figure 4.15 Model for PIFA without slot

The obtained input impedance at resonance (from CST Microwave Studio) is:

i) $Z_{in}=43.824+j6 \Omega$

This is parallel to the impedances Z_1 and Z_2 seen at the feeding point on the left (short circuit) and right (open end) side. Now, from the short circuit (zero impedance) representing the shorting wall, and knowing the distance of the feeding (denoted l_1 in Fig. 4.15), we obtain the impedance Z_1 using transmission line equations [111]:

ii) $Z_1=j*Z_0*\tan(k*l_1) =j*4.5287$

The impedance Z_2 follows from $Z_{in}= Z_1 \parallel Z_2$ as:

iii) $Z_2=0.4675-j*4.4544$

Using transmission line equations [111] with known distance to the open end l_2 , the impedance of the radiating slot is calculated as:

$$\text{iv) } Z_{\text{rad}}=113.96 - j*455.55,$$

which leads to the admittance of the radiating slot as:

$$\text{v) } Y_{\text{rad}}= 0.0005+j*0.0021$$

The admittance of the radiating slot, obtained by the analysis of the PIFA using transmission line equations, is checked by the empirical formulas, by which the admittance of the radiating slot is calculated from the slot geometry [112]:

$$G_{\text{rad}} = \frac{1}{R_{\text{rad}}} = \frac{W}{120\lambda_0} \left(1 - \frac{1}{24} (k_0 h)^2 \right) \quad (4.21)$$

$$B_2 = \omega C = \frac{W}{120\lambda_0} \left(1 - 0.636 \ln (k_0 h)^2 \right) \quad (4.22)$$

where W is the patch width and h the patch height, and k_0 and λ_0 are the wavenumber and wavelength at the considered frequency (0.577 GHz). Using the expressions (4.21) and (4.22), the following value for the admittance of the radiating slot is obtained:

$$\text{vi) } Y_{\text{rad}}= 0.00056+j*0.0016$$

Comparing the two values (v and vi), it can be seen they are basically similar (the slight discrepancy presumably arises due to inductance of the feeding which was not taken into account). This means that the supposed model of the PIFA is applicable for analysis.

4.3.2. Evaluating the impedance of the slot

The presence of the slot in the ground plane was investigated by creating a section of the microstrip line of the same width and height as in the considered antenna. The ground plane width was extended to 12 cm, and the slot was placed at the same distance from port 1 as in Table 4.1. The simulation setup is shown in Fig. 4.16. Four cases are considered (SH is the relative coordinate with respect to the symetral):

- patch not covering the slot (SH =17.5)
- half of patch covering the slot (SH=0)
- the whole patch covering the slot up to the edge (SH=-17.5)
- whole patch deeply over the slot (SH=-27.5)

In Figs. 4.17 and 4.18, the polar plot of the input impedance is given in the frequency range from 0.2 to 1.2 GHz for the considered cases (magnitude is given in dB, for convenience). In Fig. 4.17, the slot is placed in free space, and it can be seen that, when the patch is placed

deeply above the slot, impedance turns out to be inductive. When the slot is placed over the muscle-equivalent body model (as in section 4.2), the impedance in the considered frequency range is slightly capacitive.

The inductive character of the slot in free space is expected if the slot was assumed as a parallel *RLC* circuit, since the slot is below resonance at the considered frequency range [112]. The real component of impedance corresponds to the radiation resistance of the slot. The equivalent scheme of the PIFA antenna with the slot in the ground plane in free space is given accordingly in Fig. 4.19.

On the other hand, the slightly capacitive character of slot impedance can be explained by increased added parallel capacitance, which comes from the increased permittivity of the human body. In that way, the inductive character of the slot is compensated by parallel capacitance, which, when it comes into a series with the capacitive impedance of the open end (calculated in section 4.3.1), reduces the total capacitance of the circuit and raises the resonant frequency.

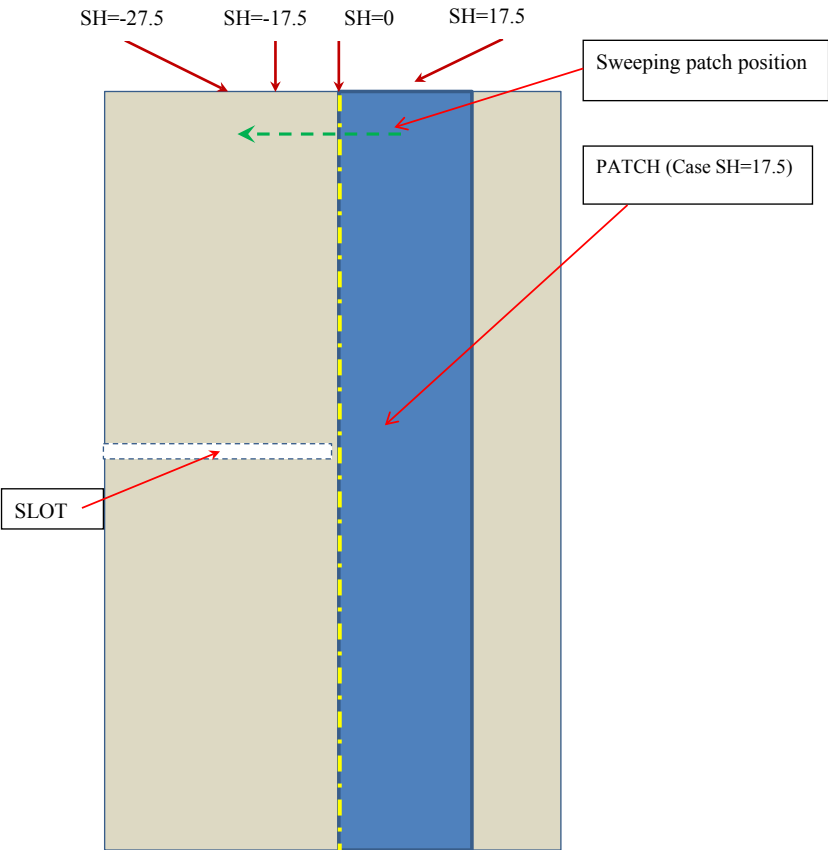


Figure 4.16 Simulation setup for evaluating the impedance character of the slot

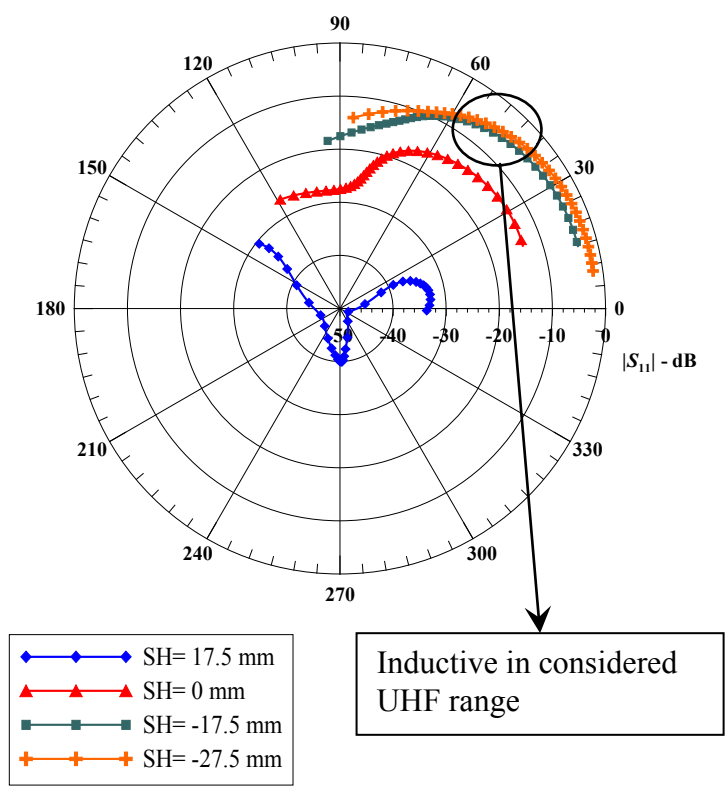


Figure 4.17 Polar plot of input reflection coefficient for the considered cases in Fig. 4.16 – slot in free space (start frequency: 0.2 GHz, stop: 1.2 GHz; marker step: 0.23 GHz)

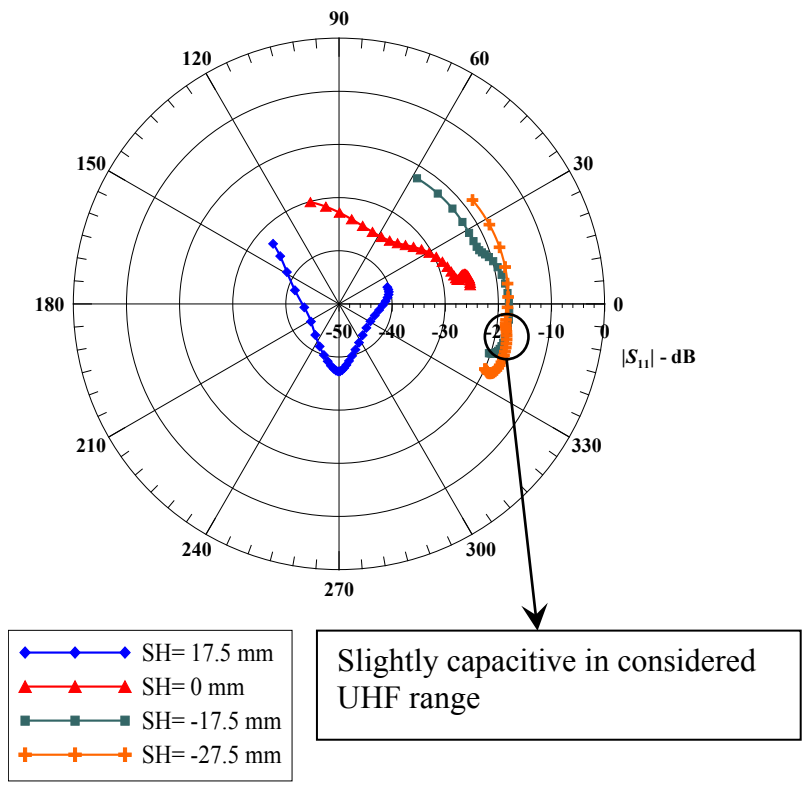


Figure 4.18 Polar plot of input reflection coefficient for the considered cases in Fig. 4.16 – slot on the body model (start frequency: 0.2 GHz, stop: 1.2 GHz; marker step: 0.23 GHz)

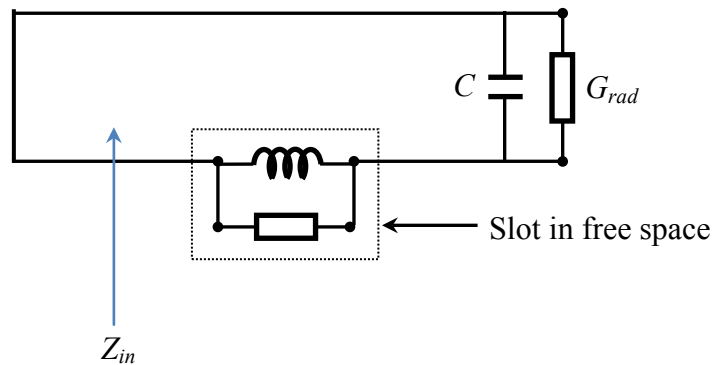


Figure 4.19 PIFA with the slot in the ground plane in free space – equivalent scheme

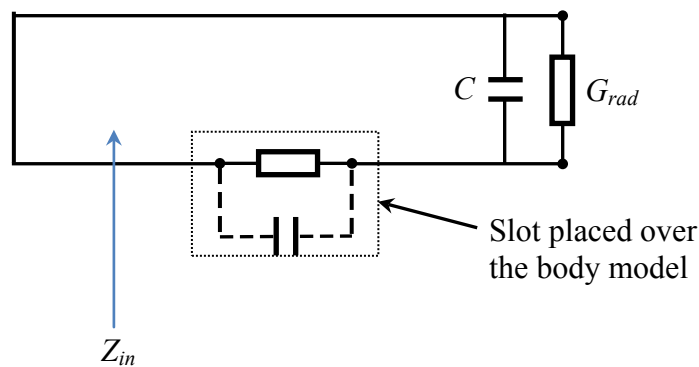


Figure 4.20 PIFA with the slot in the ground plane on a body model – equivalent scheme

To check the proposed model, we have performed simulations in CST Microwave Studio for the PIFA antenna with the ground plane slot in free space (dimensions are given in Table 4.1 the differences being the absence of the slot in the patch and the extension of the shorting wall over the full length), and on the body model (as in section 4.2). The feeding points for the two cases were optimized at 50 mm from the plane of the shorting wall in free space, and 30 mm in the case of the body model.

In the next simulations, the slot in the PIFA in free space was filled with 50 parallel impedances (to act as a homogeneous impedance in the slot), and their value was varied in order to obtain a similar response of input reflection coefficient as in the case with the human body model (the feeding point was placed to the value optimized for the slot above the human body model, as well). Note that each impedance is a parallel RC-circuit by itself. Using such optimization, we have effectively replaced the human body model with RC circuits in the model. The parameters of a single RC-circuit are given in Table 4.7, while the obtained results (magnitude of input reflection coefficient) are given in Fig. 4.22. It can be seen that it is possible to obtain similar performance to the PIFA antenna on the body (and raise the

resonant frequency compared to the case of free space) by using parallel resistors and capacitors, which is in accordance with the proposed model.

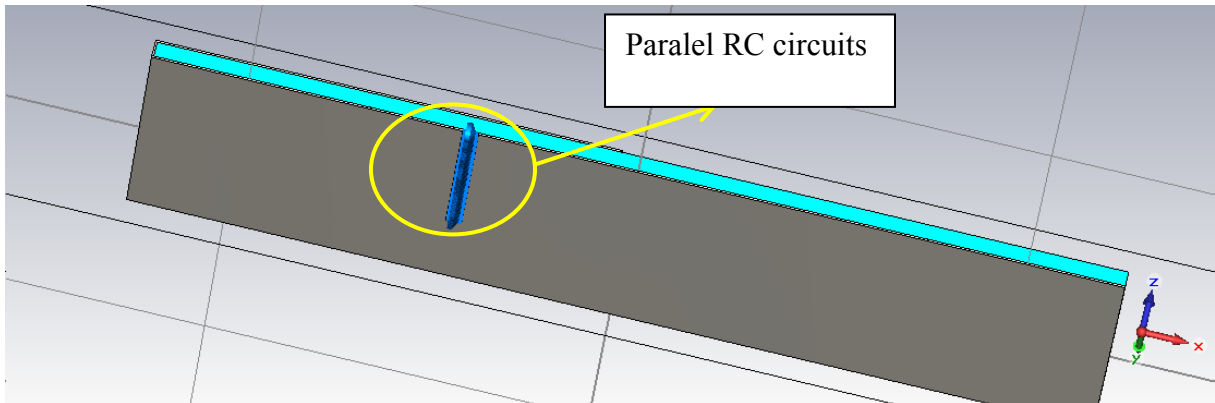


Figure 4.21 PIFA antenna in free space with paralel RC circuits in the slot

Table 4.7 Parameters of single RC-circuit representing the human body model

R [Ω]	300
C [pF]	0.1

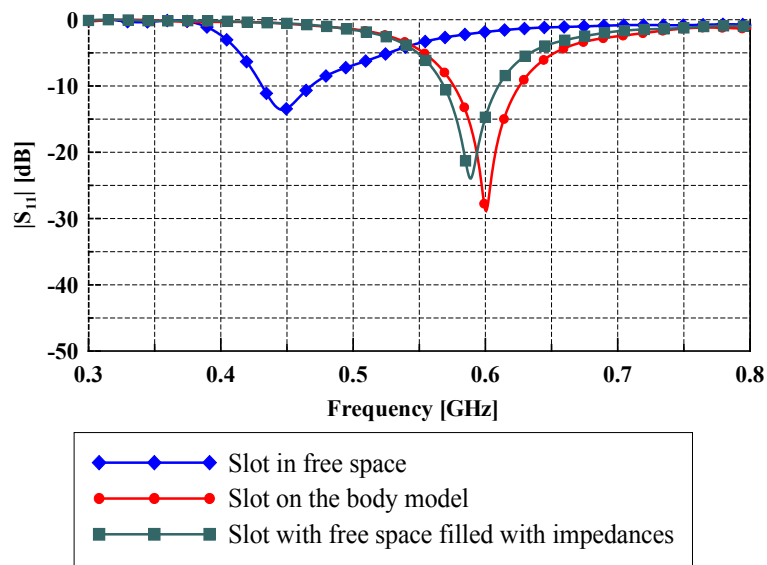


Figure 4.22 Calculated magnitudes of input reflection coefficient for three cases of the PIFA antenna with the slot in the ground plane.

4.4. Measurements on the prototype

Finally, according to the dimensions given in Table 4.1, the prototype of the PIFA antenna was obtained, and its performance was measured in free space and on the body of a human volunteer. The results are given in Figs. 4.24 and 4.25, respectively. While good matching between simulated and measured results is obtained in free space, for the case with the human body, the observed shift in frequency is less pronounced.

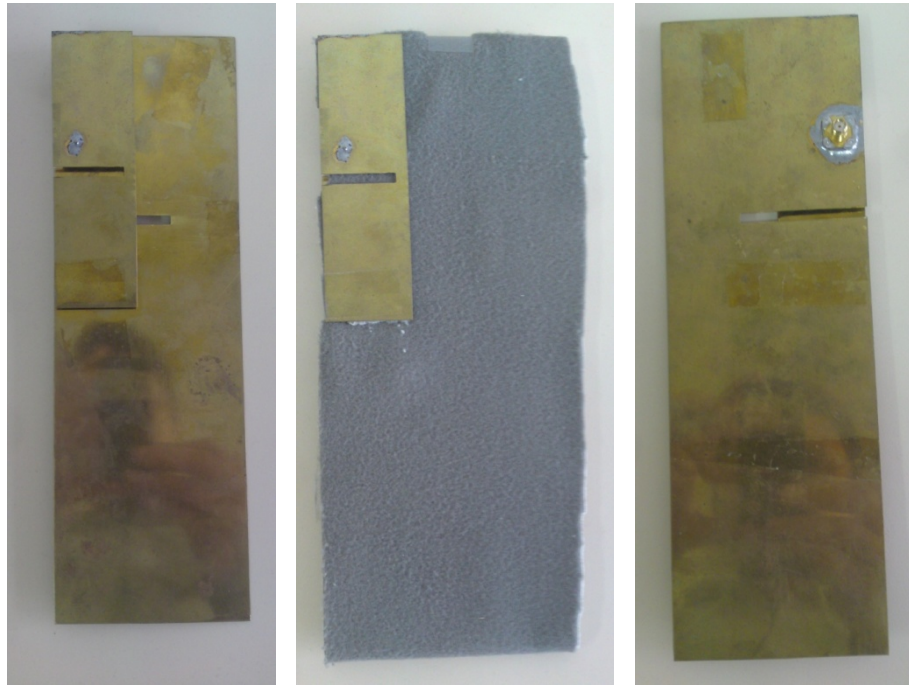


Figure 4.23 Prototypes of the PIFA antenna. From left to the right: air substrate; fleece substrate; bottom view

In addition, the use of microstrip feeding instead of a coaxial one from the bottom (as in simulations) was also considered. The antenna fed using a microstrip line is shown in Fig. 4.26, while the relevant results are given in Fig. 4.27. The simulation in this case was also performed for the PIFA antenna placed 5 mm away from the body (instead of right on the body, as in previous simulations), which is closer to the realistic case (layer of clothes). For such a case, the simulated up-shift in resonant frequency is less pronounced, and is in accordance with the measurements, thereby explaining them. This suggests that the influence of the human body on the antenna properties can be reduced when the antenna is placed on the outer part of the clothes. This observation will be further exploited in Chapter 6.

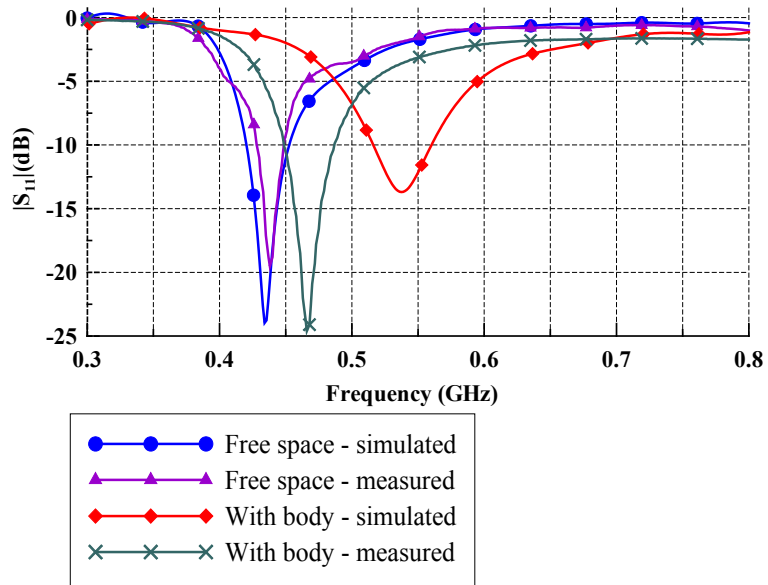


Figure 4.24 Measurements on the prototype –air substrate

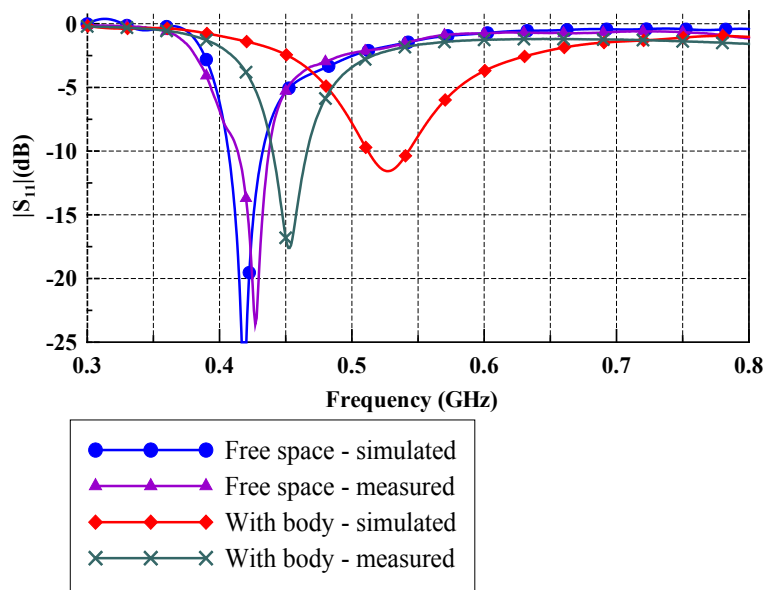


Figure 4.25 Measurements on the prototype – fleece substrate



Figure 4.26 Prototypes of PIFA antenna with microstrip feeding

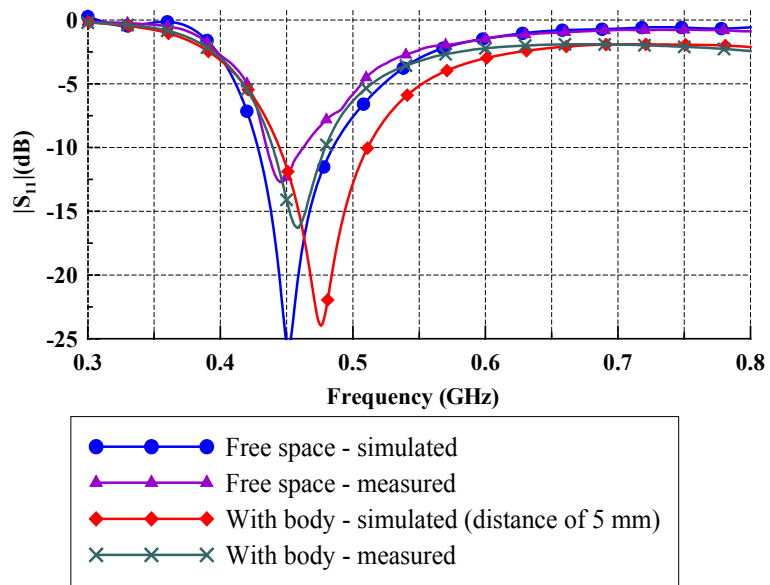


Figure 4.27 Measurements on the prototype – microstrip excitation and air substrate. Simulations were performed for the antenna placed 5 mm away from the body.

5. PROPAGATION ASPECTS FOR ON-BODY CHANNELS AND COMMUNICATIONS

As shown in the previous chapter, the presence of the human body affects the radiation properties of the antenna, which leads to the need to characterize the human body in electromagnetic terms, as well as model the propagation in the presence of the human body. For communication between two devices located on the human body, the surface of the body takes the role of the transmission channel, and the dominating propagation mechanisms are surface waves and creeping waves (Fig. 2.15). On-body links are considered more power effective than off-body ones, where the signal is less deterministic due to scattering, multipath etc. On-body propagation has attracted considerable interest in literature recently [33, 34, 113], with the principal goal of optimizing positions of antennas on the body, which could provide a reliable link in various circumstances so the requirements of on-body transceivers can be specified by the knowledge of the path loss. The positions on the body also need to be chosen in a way that they are not obtrusive, and do not affect other activities of the user.

In the first part of this chapter, we provide a brief review of the relevant terminology concerning surface waves. The discussion is accompanied by Appendices B and C, where some more detailed derivations of the basic principles concerning surface waves are given. It will be shown that surface waves can occur either across the boundary with lossy media (metal or dielectric), or across inhomogeneous surfaces such as dielectric slab and artificial composite surfaces (EBG, corrugated soft/hard surfaces, metamaterials, etc. [44]). The latter surfaces are being extensively researched in the design of antenna and communication systems since they are capable of controlling the propagation of the surface wave at some specified frequency and direction, and are thus suitable for application e.g. in filters or for enhancing the antenna radiation characteristics (see section 2.4). Optical fibers are also an example of surface waveguides.

In the context of on-body communications, the human body as a channel (i.e. surface waveguide) needs to be characterized. Since the human body is a lossy medium, a part of the waves guided along the surface is always lost in it, contributing to path loss and increased power absorption in the body. Moreover, the human body is large in comparison to the wavelength, which means that methods of geometrical optics and diffraction should be used for the analytical characterization, while the exact characterization is done numerically (due to the body shape irregularity).

From the engineering point of view, the human body is arguably not the best choice for a surface waveguide, so transmitting and receiving systems need to be capable of coping with the path loss the human body introduces. The most critical point in on-body communication with the largest path loss are the waves that flow (“creep”) around the curved surface of the body in non line-of-sight (NLOS) conditions, so, in the second part of this chapter, we model the propagation around a curved lossy cylinder (which represents the human body torso). The performance of the numerical model has also been evaluated by measurements, both on the human body of the volunteer and on a phantom, which is accordingly described. Finally, it needs to be noted that, in reality, on-body propagation is also accompanied by reflected, diffracted and scattered waves from the environment, which leads to multipath propagation, and limits the extent of theoretical modelling for the commonly used frequencies such as ISM 2.4. However, multipath can in fact enhance on-body communication, so analytical modeling is still valid as a worst case scenario. For higher frequencies, such as 60 GHz, the analytical modelling will turn out to be more accurate [113]. In the final part of the chapter, we shall thus address some of the uncertainties which arise when antennas are placed on a real body, and characterize (using measurements) a few typical on-body links with respect to their actual performance in realistic environments.

5.1. Planar surfaces

Apart from the classic free-space plane waves obtained by Maxwell equations, in structures that contain boundaries there is another class of waves which are guided across the interface between two surfaces. To illustrate the various kinds of waves that can be guided due to the presence of a surface, as a simplest case we consider a plane interface between air and a lossless dielectric placed at $x=0$ (Fig. 5.1). We assume that the dielectric extends to infinity, so that two regions (homogeneous in x) are actually present and divided by the interface plane ($x=0$).

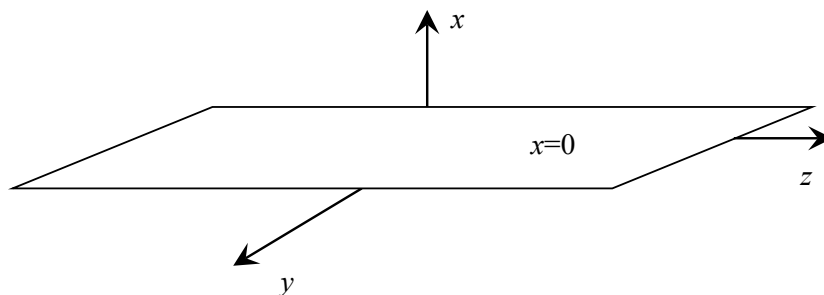


Figure 5.1 Plane interface between air and dielectric

With such a choice of regions the problem is reduced to 2D due to continuous translation symmetry (homogeneity) of the structure in the transversal plane, which means that the y - and z - axes could be chosen as such that there is no field variation in the y -direction (i.e. $\partial/\partial y=0$) [114, 115]. It follows that a wave function u (which represents e.g. the electric or magnetic field component) satisfies the 2D homogeneous Helmholtz equation:

$$\left(\frac{\delta^2}{\delta x^2} + \frac{\delta^2}{\delta z^2} + k^2 \right) u(x, z) = 0. \quad (5.1)$$

Using the method of separation of variables, the general solution can be written in the form:

$$u(x, z) = A \cdot e^{-jk_x x} e^{-jk_z z}, \quad (5.2)$$

where k_x and k_z are wavenumbers (propagation coefficients) in the x - and z - directions, respectively; and A is a complex constant. The wavenumbers in the air region also satisfy the relation:

$$k_x^2 + k_z^2 = k_0^2 = \frac{\omega^2}{c^2}, \quad (5.3)$$

where k_0 is the wavenumber of free space. The frequency is determined from (5.3) as:

$$\omega = c \cdot k_0 = \sqrt{k_x^2 + k_z^2}, \quad (5.4)$$

where c is the velocity of light and k_0 is the wavenumber in free space. For any given real value of k_z , we can find the value of k_x as:

$$k_x = \sqrt{\left(\frac{\omega}{c} \right)^2 - k_z^2}. \quad (5.5)$$

When $k_z < \omega/c$, the waves in the air are of the form of planar waves which travel at the speed of light (i.e. “fast waves”). However, for $k_z > \omega/c$, one gets an imaginary $k_x = -j\alpha_x$, meaning that the wave exponentially attenuates in the air according to the factor $e^{-\alpha_x x}$ ($\alpha_x > 0$), and the only direction of actual propagation is the transverse one (in z -direction), i.e. the wave is guided (“trapped”) along the surface. Also, the phase velocity of such $v_p = \omega/k_z$ is smaller than the speed of light, so surface waves are also regarded as slow waves. In Fig. 5.2, the positions of fast waves and surface (slow) waves are given on the ω - k_z diagram (so-called dispersion diagram [115]):

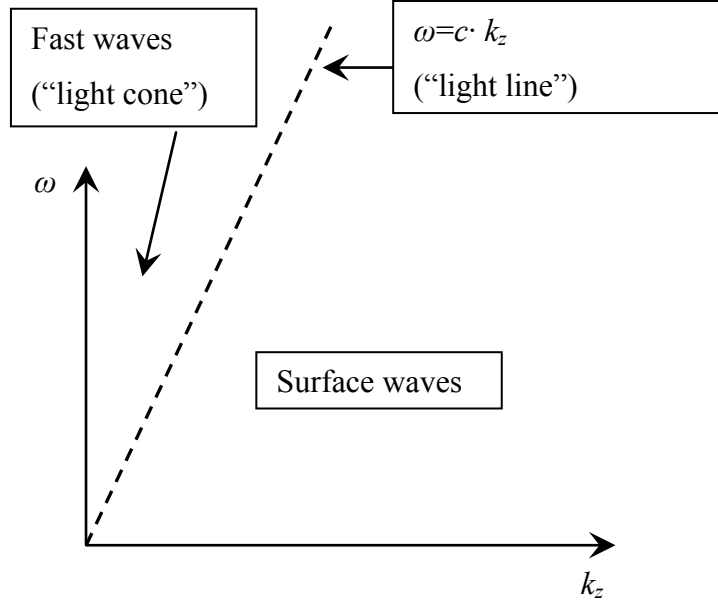


Figure 5.2 General dispersion diagram [115]

The considered waves are also called *trapped surface waves* and they are the main guiding mechanism of many structures like optical fibers, artificial dielectrics, dielectric coatings on metal surfaces etc. [114], hence this term is often interchanged with the term “surface waves”.

To find other types of waves which exist along the surface, we note that k_x and k_z could both be complex. In addition, when the considered medium is lossy (i.e. contains conductivity), the wavenumber k of the medium also becomes complex (the imaginary part represents losses):

$$k = k' - jk'' \tag{5.6}$$

We thus write k_x and k_z as:

$$\begin{aligned} k_x &= \beta_x - j\alpha_x, \\ k_z &= \beta_z - j\alpha_z, \end{aligned} \tag{5.7}$$

Now we rewrite (5.2) as:

$$u(x, z) = A \cdot e^{-j\beta_x x} e^{-j\beta_z z} \cdot e^{-\alpha_x x} e^{-\alpha_z z} = A \cdot e^{-j\boldsymbol{\beta} \cdot \mathbf{r}} \cdot e^{-\boldsymbol{\alpha} \cdot \mathbf{r}} \tag{5.8}$$

It is obvious that β is associated with the change in phase, while α denotes the rate of attenuation in the respective (x - or z -) direction. In (5.8), we have also introduced the vector form of the expression, where $\boldsymbol{\beta} = \beta_x \hat{\mathbf{x}} + \beta_z \hat{\mathbf{z}}$ and $\boldsymbol{\alpha} = \alpha_x \hat{\mathbf{x}} + \alpha_z \hat{\mathbf{z}}$ are the phase and attenuation vectors, respectively. In addition, $\mathbf{r} = x\hat{\mathbf{x}} + z\hat{\mathbf{z}}$ is the position vector.

We now put the expressions (5.6) and (5.7) into (5.2), and after equating real and imaginary components, we obtain:

$$\beta_x^2 - \alpha_x^2 + \beta_z^2 - \alpha_z^2 = k'^2,$$

$$\alpha_x \beta_x + \alpha_z \beta_z = k''^2. \quad (5.9)$$

With these expressions obtained, we have an insight into the constant amplitude and constant phase planes which are defined as $\alpha \mathbf{r} = \text{const.}$ and $\beta \mathbf{r} = \text{const.}$, respectively. From (5.9) it is obvious that:

$$\alpha \beta = \alpha_x \beta_x + \alpha_z \beta_z = k''^2, \quad (5.10)$$

which means that the constant amplitude and constant phase do not coincide for waves along the boundary, i.e. the amplitude and phase change in different directions. For lossless media such as air the imaginary part of k is zero, which means (5.10) that the constant amplitude and constant phase plane are perpendicular, as shown in Fig. 5.3. In lossy dielectrics, the angle between α and β is still near 90° , since the losses are usually small. On the other hand, in conductors (when the conductivity is large) the direction of α and β is almost the same [89]. Such general waves in which the planes of constant amplitude and phase do not coincide are referred to as *non-uniform plane waves* [89] or *complex waves* [114].

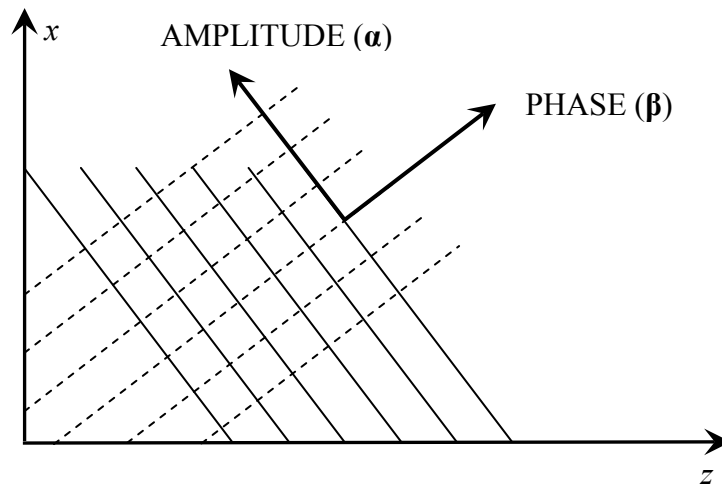


Figure 5.3 Constant amplitude and constant phase planes for non-uniform planar waves in the air [114]

Now, depending on the sign of components of vectors α and β , we can characterize various types of waves in the air which can travel along the surface in the $+z$ -direction (i.e. when

$\beta_z > 0$). The types of complex waves are summarized in Table 5.1, with respect to attenuation in the x - and z - directions, and propagation in the $\pm x$ -direction.

Table 5.1 Complex waves in air [114]

Case	α_x	β_x	α_z	β_z	Name of the wave
A	0	+	0	+	Fast wave
B	+	+	-	+	Backward leaky wave
C	+	0	0	+	Trapped surface wave (“slow wave”)
D	+	-	+	+	Zenneck surface wave
E	0	-	0	+	Plane-wave incidence
F	-	-	-	+	(no particular name)
G	-	0	0	+	Untrapped surface wave
H	-	+	+	+	Forward leaky wave

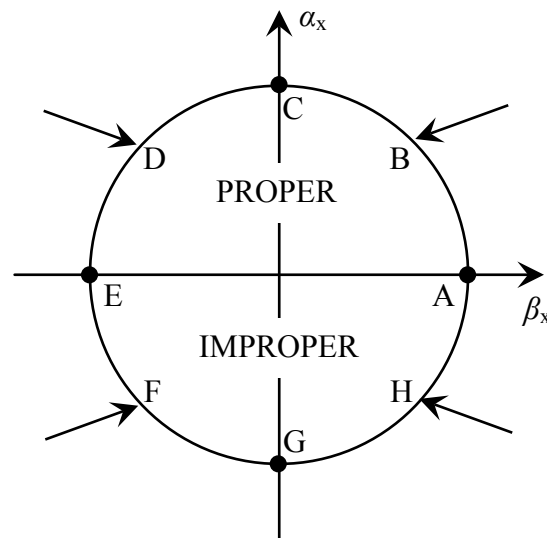


Figure 5.4 Proper and improper waves in the complex k_x plane for the cases from Table 5.1

In Fig. 5.4, all the mentioned cases are shown in the complex k_x plane, on a circle $|k_x| = \text{const}$. The waves in the lower part of the plane ($\alpha_x < 0$) are also termed *improper* waves, since their amplitude increases in the $+x$ - direction, which violates the radiation condition. However, it can be shown that, under certain conditions, the improper waves still can exist locally, i.e. within a portion of space [114]. Zenneck waves and trapped surface waves are both considered as surface waves with very similar characteristics. They are both guided across the surface, the only difference being that Zenneck waves possess attenuation in the z -direction. However, the existence and the actual excitation of Zenneck waves (apart from the theoretical

one) is sort of a long-lasting problem in the field of electromagnetics concerning wave propagation around the Earth [116, 117], but it is relevant for on-body communication as well [113].

5.2. Wavenumbers of surface waves

In Appendix B, the prototype solution for surface waves is derived by observing the oblique incidence of the TM_z polarized wave onto the lossless dielectric, and searching for Brewster's angle of the total transmission (where no standing wave would exist in the air). The associated wavenumbers for Brewster's angle, when applied to lossy surfaces (dielectric or metal) assumed homogeneous in the normal direction, give rise to surface waves which exponentially decay away from the surface (i.e. Zenneck waves), and which correspond with the complex angles of incidence. Here, we summarize the expressions for the sought wavenumbers of lossy dielectrics and metals of finite conductivity, which are relevant for modeling the surface of the human body in electric terms.

5.2.1. Lossy dielectric

The lossy dielectric is characterized by complex permittivity, which leads to a complex wavenumber k_d as well. The extension of the previous analysis to the plane wave incidence on lossy surfaces is straightforward. The lossy dielectric is characterized by complex relative permittivity (as in section 3.1):

$$\varepsilon_r = \varepsilon_r' - j\varepsilon_r'' \quad (5.11)$$

From (B.22), it can be concluded that total transmission occurs for the following wavenumbers in the x - and z - direction (the coordinate system in question is given in Fig. 5.1):

$$k_x = -k_0 \frac{1}{\sqrt{\varepsilon_r + 1}}, k_z = k_0 \frac{\sqrt{\varepsilon_r}}{\sqrt{\varepsilon_r + 1}} \dots x > 0,$$

$$k_{x1} = -k_0 \frac{\varepsilon_r}{\sqrt{\varepsilon_r + 1}}, k_{z1} = k_z \dots x < 0. \quad (5.12)$$

When the permittivity is complex and $\varepsilon_r'' \ll \varepsilon_r'$, the wavenumbers in the x - and z - direction are obtained from (5.11) and (5.12) after some rearranging and using binomial expansion [46, 90], and we get to the following expressions:

$$\begin{aligned}
k_x &= -k_0 \frac{1}{\sqrt{\varepsilon_r' - j\varepsilon_r'' + 1}} \approx -k_0 \frac{1}{\sqrt{\varepsilon_r' + 1}} - j \frac{k_0 \varepsilon_r''}{2(\varepsilon_r' + 1)^{\frac{3}{2}}} = \beta_x - j\alpha_x, \\
k_{x1} &= -k_0 \frac{\varepsilon_r' - j\varepsilon_r''}{\sqrt{\varepsilon_r' - j\varepsilon_r'' + 1}} \approx -k_0 \frac{\varepsilon_r'}{\sqrt{\varepsilon_r' + 1}} + jk_0 \frac{\varepsilon_r''(\varepsilon_r' + 2)}{(\varepsilon_r' + 1)^{\frac{3}{2}}} = \beta_{x1} - j\alpha_{x1}, \\
k_z = k_{z1} &= k_0 \sqrt{\frac{\varepsilon_r' - j\varepsilon_r''}{\varepsilon_r' - j\varepsilon_r'' + 1}} \approx k_0 \sqrt{\frac{\varepsilon_r'}{\varepsilon_r' + 1}} - jk_0 \frac{\varepsilon_r''}{2\varepsilon_r'(\varepsilon_r' + 1)^{\frac{3}{2}}} = \beta_z - j\alpha_z.
\end{aligned} \tag{5.13}$$

Waves in the air are proportional to $e^{-jk_x x} e^{-jk_z z}$, which means that attenuation occurs both in the x - and z - direction. This wave is said to be trapped on the surface, while at the same time exhibiting attenuation in the direction of propagation. Historically, the surface wave on the lossy dielectric was used to model radio propagation around the Earth since the early 20th century. It is also called the Zenneck wave [90, 114], as mentioned in Table 5.1, and it differs from trapped surface waves (Table 5.1) only over attenuation in the z -direction, which arises due to power absorption in the surface. In terms of Brewster's angle (0), we note that by introducing losses in the surface material, we have moved away from the picture of incident plane waves totally transmitted through the media, so here we rather consider specific wave configuration where no standing wave is present, while fields in the two regions are interrelated through boundary conditions. In other words, the Brewster's angle has become complex, which leads to a complex angle of incidence. which corresponds to non-uniform plane wave in the air [89, 90]. Such a case occurs for some specific wavenumbers (5.12), which need to be found for each configuration.

5.2.2. Conductive surfaces

In surfaces with high conductivity ($\sigma \gg \omega \varepsilon_0$), such as metals, the relative permittivity is given as:

$$\varepsilon_r = 1 - j \frac{\sigma}{\omega \varepsilon_0} \approx -j \frac{\sigma}{\omega \varepsilon_0}. \tag{5.14}$$

For typical metals (such as copper), conductivity is of the order of 10^7 S/m. By inserting this expression in (5.12) one obtains wavenumbers for surface waves along the metal surface [46]:

$$k_x = -k_0 \frac{1}{\sqrt{-j \frac{\sigma}{\omega \varepsilon_0} + 1}} \approx -k_0 \sqrt{\frac{\omega \varepsilon_0}{2\sigma}} (1 + j) = \beta_x - j\alpha_x,$$

$$k_{x1} = -k_0 \frac{-j \frac{\sigma}{\omega \epsilon_0}}{\sqrt{-j \frac{\sigma}{\omega \epsilon_0} + 1}} \approx -k_0 \sqrt{\frac{\sigma}{2\omega \epsilon_0}} (1-j) = \beta_{x1} - j\alpha_{x1},$$

$$k_z = k_{z1} = k_0 \sqrt{\frac{-j \frac{\sigma}{\omega \epsilon_0}}{-j \frac{\sigma}{\omega \epsilon_0} + 1}} \approx k_0 \left(1 - j \frac{\omega \epsilon_0}{2\sigma}\right) = \beta_z - j\alpha_z. \quad (5.15)$$

From (5.15), it is obvious that the fields travel across the metal surface with very small attenuation in the z -direction. From the vertical wavenumber in metal (k_{x1}), and the field decay proportional to factor $e^{-\alpha_{x1}x}$ the penetration (skin) depth can be calculated as:

$$k_0 \sqrt{\frac{\sigma}{2\omega \epsilon_0}} x = 1, \text{ i.e.}$$

$$x = \delta = \frac{2}{\omega \mu \sigma}. \quad (5.16)$$

This is the depth at which the field magnitude in metal falls to $1/e$. In metals, it is typically of the order 10^{-6} m at microwave frequencies, meaning that the fields penetrate into the metal at only a very small depth [46]. Wave impedance in metal (also surface impedance) is given as:

$$Z_s = Z_{w1} = \sqrt{\frac{\omega \mu}{2\sigma}} (1+j) \cos \theta_t \approx \sqrt{\frac{\omega \mu}{2\sigma}} (1+j) = \frac{1+j}{\sigma \delta}, \quad (5.17)$$

since, from Snell's law:

$$\cos \theta_t = \sqrt{1 - \sin^2 \theta_t} = \sqrt{1 - \frac{k_0^2}{k_1^2} \sin^2 \theta_t} \approx 1. \quad (5.18)$$

where $|k_1| \gg |k_0|$ is the wavenumber in metal. This means that the surface impedance of the metal is independent of the incident angle. Note also that the transmitted angle θ_t is in fact complex, which is characteristic for conductive surfaces [89, 90].

In Appendix C it was asserted that the surface reactance for lossy dielectrics and metals that occur in nature is generally rather low, meaning that the wave is loosely bound to the surfaces and extends in the air, thereby being of limited usability in the practical waveguiding systems [90], since such systems would have large dimensions (especially at lower frequencies) to “collect” the energy transmitted by the wave. In contrast to single lossy surfaces, in the same

appendix some principles of modern surface waveguiding structures (dielectric slab or rod; artificial composite surfaces such as EBG etc.) are formulated. In accordance to those considerations, the human body as a surface waveguide can be considered as a rather hostile medium with large attenuation, even for such low distances as a body-to-body link.

In [118], the possibility of on-body communication via surface (Zenneck) waves was investigated and compared with the measured results. It was shown that the surface waves from the discrete portion of the wave spectrum (as given in Appendix C) are rather unlikely to contribute to on-body communication in the existing solutions. A more general form of surface waves was suggested as more accurate, and a better candidate for the description of propagation - *Norton waves*, which do not necessary contain the surface wave discrete portion of the spectrum, and which decay more rapidly than the assumed Zenneck waves (Norton waves are obtained using geometrical optics as a diffracted field when both source and receiver are placed exactly on the ground [117]). Therefore, the issue of on-body propagation can also, in some sense, be seen as a continuation of the search for the practical realization of Zenneck waves, which has lasted for more than a century [117].

5.3. Waves in cylindrical structures

We turn our attention to the cylindrical structures which can serve to model the propagation around the body torso, and thus extend the discussion about surface waves onto cylindrical structures accordingly. Propagation around the torso can be considered as the worst case scenario in terms of path loss, since non line-of-sight (NLOS) conditions appear, and the wave going around the curved surfaces suffers from exponential attenuation due to radiation of the portion of wave into outer space, even if the cylinder is lossless [114]. The circular cylinder is a canonical structure for which the wave equation can be solved analytically, and is a good model for approximating many realistic objects in radiation and scattering problems. Thus, we approximate the human body torso as a circular cylindrical structure containing a lossy dielectric, and analytically model the propagation around the torso. The geometry of the considered cylindrical structure is given in Fig. 5.5. The cylindrical coordinate system (r, φ, z) is used. The scalar Helmholtz equation for a wave function u takes the following form in cylindrical coordinates:

$$\nabla^2 u + k^2 u = \frac{\partial^2 u}{\partial r^2} + \frac{1}{r} \frac{\partial u}{\partial r} + \frac{1}{r^2} \frac{\partial^2 u}{\partial \varphi^2} + \frac{\partial^2 u}{\partial z^2} + k^2 u = 0, \quad (5.19)$$

where k is the wavenumber of the medium.

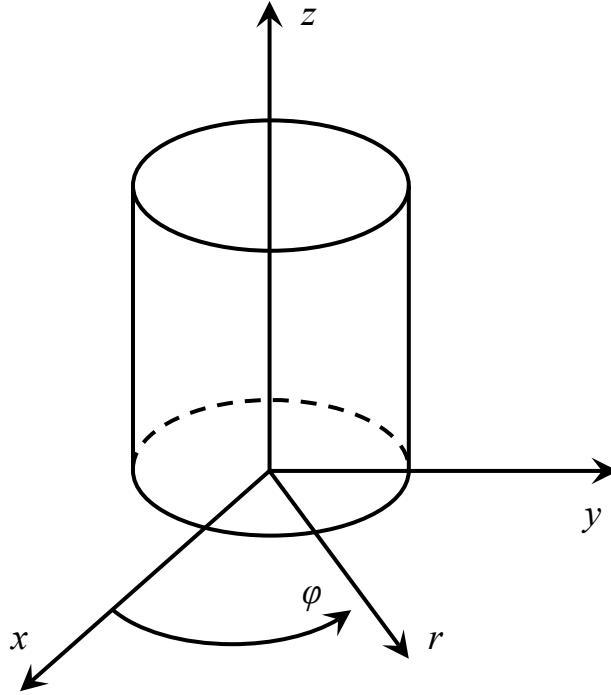


Figure 5.5 The coordinate system for analyzing cylindrical structures

The solution proceeds by the separation of variables, as in [119]. We assume that the wave function u can be written as a product of three functions, each function being of one respective r -, φ - and z - coordinate:

$$u(r, \varphi, z) = f(r) \cdot g(\varphi) \cdot h(z). \quad (5.20)$$

Now, this form can be inserted into (5.19), and after some rewriting three separate equations can be obtained [120]. To summarize the principle, we note that the continuous translational symmetry [115] can be assumed along the z -axis (the cylinder usually extends in the z -direction for many wavelengths), so the dependence in that direction can be written as:

$$h(z) = e^{-jk_z z}. \quad (5.21)$$

Next, we note that, in the angular (φ -) direction, the solution must be periodic with the period of 2π . Therefore, we can expand the angular dependence in the Fourier series in φ -, i.e. a series of the form $e^{-jm\varphi}$, where m is integer. For an integer m , the fundamental solution is given as:

$$g(\varphi) = e^{-jm\varphi}. \quad (5.22)$$

With these assumptions, the scalar wave function $u(r, \varphi, z)$ can be represented as $f(r)e^{-jm\varphi}e^{-jk_z z}$, which reduces (5.19) to:

$$\frac{\partial^2 f}{\partial r^2} + \frac{1}{r} \frac{\partial f}{\partial r} + \left(k_r^2 - \frac{m^2}{r^2} \right) f = 0, \quad (5.23)$$

where $k_r^2 = k^2 - k_z^2$. The equation (5.23) is recognized as Bessel differential equation of the order m , the solution to which may be chosen among Bessel functions of the first and second kind and/or Hankel functions of the first and second kind, denoted respectively as [108]:

$$f(r) \sim J_m(k_r r), Y_m(k_r r), H_m^{(1)}(k_r r), H_m^{(2)}(k_r r). \quad (5.24)$$

All the mentioned functions are linearly independent, and a linear combination of any two can in principle be picked as the solution [120]. In general, Bessel functions are suitable for representing standing waves, and Hankel functions for travelling waves. Furthermore, the outward travelling wave (in the $+r$ -direction) usually conforms to the physical reality, so the function $H_m^{(2)}$ is preferred, since it represents the outward traveling wave. On the other hand, the function Y_m possesses singularity at zero, so it is rarely used. Therefore, the most flexible of the possible linear combinations is [120]:

$$f(r) = C_1 J_m(k_r r) + C_2 H_m^{(2)}(k_r r). \quad (5.25)$$

The wave function is finally written as:

$$u(r, \varphi, z) = \left[C_1 J_m(k_r r) + C_2 H_m^{(2)}(k_r r) \right] \cdot e^{-jm\varphi} e^{-jk_z z}. \quad (5.26)$$

This is the elementary solution. The total solution for a particular excitation is given as a Fourier sum of the elementary solutions in the φ -direction, and at the same time as a Fourier integral in the z -direction (due to continuous spectrum of k_z), typically written as [122]:

$$u_{total}(r, \varphi, z) = \frac{1}{(4\pi)^2} \sum_m \int_{k_z} \tilde{U}(r, m, k_z) \cdot e^{-jm\varphi} e^{-jk_z z}, \quad (5.27)$$

where

$$\tilde{U}(r, m, k_z) = C_1 J_m(k_r r) + C_2 H_m^{(2)}(k_r r) = C_1 J_m\left(\sqrt{k^2 - k_z^2} r\right) + C_2 H_m^{(2)}\left(\sqrt{k^2 - k_z^2} r\right). \quad (5.28)$$

The factor $(4\pi)^{-2}$ in the equation (5.27) arises as a result of the definition of the Fourier series and the integral. The equation (5.28) is actually the expression for the wave function in the spectral domain, which is commonly used for solving excitation problems, i.e. solving inhomogeneous wave equations.

5.3.1. Convergence issues. Watson transformation.

For cylindrical structures, the main issue is to evaluate the Fourier series in φ . Although the above-described procedure of obtaining the total field is straightforward to comprehend, in reality, when performing it numerically, this infinite summation must be truncated and made finite. This immediately gives rise to the question of how many terms in φ - one needs to take to reasonably approximate the required function. To ensure accuracy around 2%, one usually needs to take terms of the order of at least $2ka$, where a is the radius of the cylinder [116]. For large cylinders, this means many terms need to be taken into account, which slows down the computation process. In addition, evaluating Bessel and Hankel functions of a large order makes such a task even more time-consuming. Therefore, it is desirable to resort to alternative representations with faster convergence characteristics.

One of the techniques which has been successfully used since the early 20th century (when one of the central practical problems in radio was propagation over the Earth which has an extremely large radius) is the so-called Watson transformation, which is based on transforming the Fourier sum into a complex integral representation and then using the art of changing the contour of integration. The technique is applicable both to spherical and cylindrical problems [114, 116]. The basis for the Watson transformation is the integral of the form:

$$I = \int_{C_1+C_2} \frac{f(v)}{\sin v\pi} dv, \quad (5.29)$$

where the curves C_1 and C_2 are chosen in a way to enclose the m poles of I (i.e. nulls of $\sin v\pi$, which are real integers), as given in Fig. 5.6.

The contours C_1 and C_2 enclose $2m+1$ poles. By letting $m \rightarrow \infty$ and evaluating the integral in terms of residuums at poles v_m , we obtain:

$$I = 2\pi j \sum_m \text{Res}(v_m) = 2\pi j \sum_m \left. \frac{f(v)}{\frac{\partial}{\partial v} \sin v\pi} \right|_{v=v_m} = 2j \sum_m f(m)e^{-jm\pi}, \quad (5.30)$$

where residue $\text{Res}(v_m)$ is defined for expressions of the form $N(v)/D(v)$ as [114]:

$$\text{Res}(v_m) = \lim_{v \rightarrow v_m} (v - v_m) \frac{N(v)}{D(v)} = \frac{N(v_m)}{D'(v_m)}. \quad (5.31)$$

From (5.30), it is apparent that the Fourier series can be represented as:

$$\sum_m f(m)e^{-jm\pi} = \frac{1}{2j} \int_{C_1+C_2} \frac{f(v)}{\sin v\pi} dv. \quad (5.32)$$

By transforming the sum into an integral, it is possible to alter the contour of integration and obtain a fast converging series, as it will be shown on the concrete example.

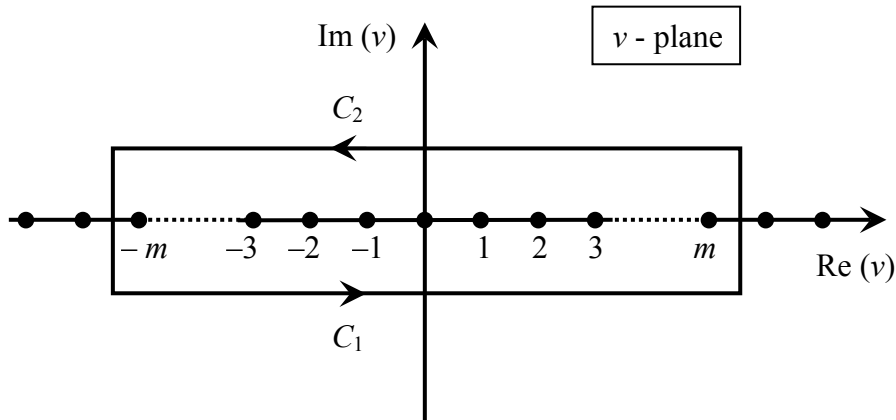


Figure 5.6 Contour of integration for integral I which encloses m poles [114]

5.3.2. Green's function for cylindrical structures

We consider the z -directed current line source placed at the edge of a dielectric circular cylinder of the radius a . Furthermore, we focus on the waves which propagate normally to the cylinder axis, thereby neglecting z -dependence, and thereby reducing the problem to 2D (this is equivalent to considering the infinite line source excitation [89]). We also formulate the problem in the spectral domain, which makes manipulations more convenient. With such excitation, the z -component of the magnetic field (H_z) is zero, which suggests TM_z waves occur. The typical procedure in such a case is to derive the scalar wave equation for the z -directed electric field and simply obtain other field components using Maxwell's equations [122] (alternatively, one could derive fields from vector potential \mathbf{A}_z [89]). The analyzed configuration is given in Fig. 5.7.

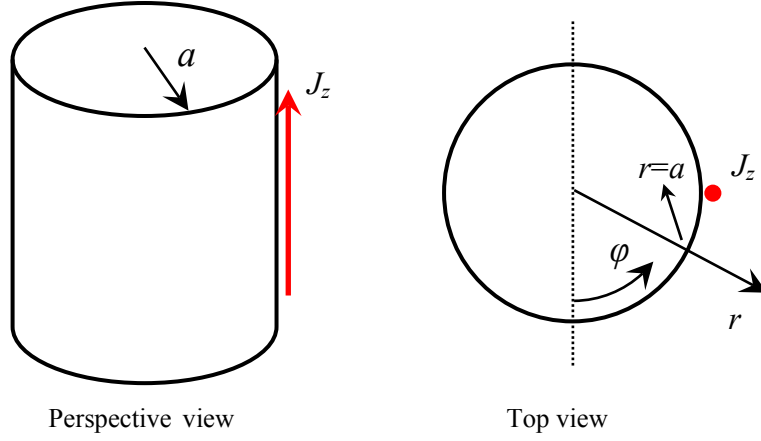


Figure 5.7 The sketch of the considered structure

According to (5.25) and the fact that we expect standing waves inside the cylinder and outward traveling waves outside the cylinder, we choose to write the fields in each region as:

A) Inside the cylinder ($r < a$):

$$\tilde{E}_z(r, m) = A J_m(k_r^+ r) = \tilde{E}_z^+, \quad (5.33)$$

B) Outside the cylinder ($r > a$):

$$\tilde{E}_z(r, m) = B H_m^{(2)}(k_r^- r) = \tilde{E}_z^-. \quad (5.34)$$

The constants A and B need to be determined using boundary conditions at the air-cylinder interface ($r = a$). The boundary conditions are the continuity of the tangential (E_z) electric field component and the jump in the tangential magnetic field component (H_ϕ) by the amount of current density J_z , which is, in spectral domain, given as [122]:

$$A) \tilde{E}_z^+ = \tilde{E}_z^-,$$

$$B) \tilde{H}_\phi^+ - \tilde{H}_\phi^- = \tilde{J}_z.$$

The angular magnetic field H_ϕ is obtained using Maxwell's equations as:

$$\tilde{H}_\phi = \frac{1}{j\omega\mu} \frac{\partial \tilde{E}_z}{\partial r}. \quad (5.35)$$

From these boundary conditions, the coefficients A and B are interrelated as:

$$B = A \frac{J_m(k_r^+ a)}{H_m^{(2)}(k_r^- a)}, \quad (5.36)$$

$$\frac{A}{j\omega\mu}k_r^+J'_m(k_r^+a) - \frac{B}{j\omega\mu}k_r^-H_m^{(2)'}(k_r^-a) = \tilde{J}_z. \quad (5.37)$$

By solving this system of equations, we get expressions for A and B as:

$$A = \frac{j\omega\mu H_m^{(2)}(k_r^-a)}{\left(k_r^+J'_m(k_r^+a)H_m^{(2)}(k_r^-a) - k_r^-J_m(k_r^+a)H_m^{(2)'}(k_r^-a)\right)} \cdot \tilde{J}_z \quad (5.38)$$

and

$$B = \frac{j\omega\mu J_m(k_r^+a)}{\left(k_r^+J'_m(k_r^+a)H_m^{(2)}(k_r^-a) - k_r^-J_m(k_r^+a)H_m^{(2)'}(k_r^-a)\right)} \cdot \tilde{J}_z. \quad (5.39)$$

Finally, we write Green's function:

A) Inside the cylinder

$$\tilde{E}_z^+(r, m) = \frac{j\omega\mu H_m^{(2)}(k_r^-a) \cdot J_m(k_r^+r)}{k_r^+J'_m(k_r^+a)H_m^{(2)}(k_r^-a) - k_r^-J_m(k_r^+a)H_m^{(2)'}(k_r^-a)} \cdot \tilde{J}_z. \quad (5.40)$$

B) Outside the cylinder (air side)

$$\tilde{E}_z^-(r, m) = \frac{j\omega\mu J_m(k_r^+a)H_m^{(2)}(k_r^-r)}{k_r^+J'_m(k_r^+a)H_m^{(2)}(k_r^-a) - k_r^-J_m(k_r^+a)H_m^{(2)'}(k_r^-a)} \cdot \tilde{J}_z. \quad (5.41)$$

The field in the spatial domain is given as a series in the angular (φ -) direction, in accordance with (5.27):

$$E_z(r, \varphi) = \sum_{m=-\infty}^{\infty} \tilde{E}_z(r, m) \cdot e^{-jm\varphi}. \quad (5.42)$$

5.3.3. Searching for the creeping wave pole

In accordance with (5.29), we transform the summation into an integral:

$$\sum_{m=-\infty}^{\infty} \tilde{E}_z(r, m) \cdot e^{-jm\varphi} = \frac{1}{2j} \int_{C_1+C_2} \frac{\tilde{E}_z(r, \nu) e^{-j\nu(\varphi-\pi)}}{\sin \nu\pi} d\nu, \quad (5.43)$$

where C_1+C_2 is the contour of integration, as given in Fig. 5.6.

Having obtained the integral representation, it is possible to change the contour of the integration in a way to enclose the poles of $\tilde{E}_z(r, \nu)$ instead of the poles of the integrand ($\sin \nu\pi$), and subsequently evaluate the integral. The new contours C_1' and C_2' are shown in Fig. 5.8.

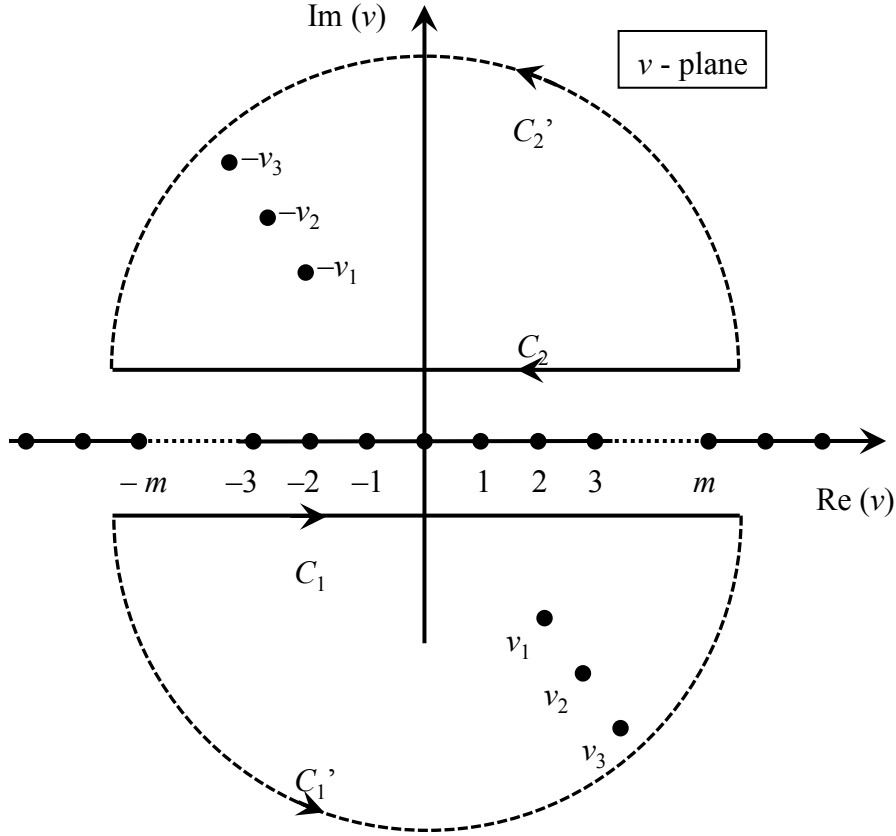


Figure 5.8 Contours of integration for residue series [114]

It turns out that the integral is given in terms of residues at poles of the electric field instead of residues of $\sin v\pi$.

$$\frac{1}{2j} \int_{C_1+C_1'+C_2+C_2'} \frac{\tilde{E}_z(r, v) e^{-jv(\varphi-\pi)}}{\sin v\pi} dv = -\pi \sum_m \text{Res}(v_m) - \pi \sum_m \text{Res}(-v_m). \quad (5.44)$$

If the electric field in (5.41) is written as a fraction $N(v)/D(v)$, using the residue sum, we obtain the more convenient form of the summation [114]:

$$\sum_{m=-\infty}^{\infty} \tilde{E}_z(r, m) \cdot e^{-jm\varphi} = \sum_{m=1}^{\infty} \frac{N^+(v_m)}{\left(\frac{\partial D}{\partial v}\right)\Big|_{v=v_m}} e^{-jv_m\varphi} + \sum_{m=1}^{\infty} \frac{N^-(v_m)}{\left(\frac{\partial D}{\partial v}\right)\Big|_{v=v_m}} e^{-jv_m(2\pi-\varphi)}, \quad (5.45)$$

where $N^\pm(v_m) = \frac{-\pi N(v_m) e^{\pm jv_m\pi}}{\sin v_m\pi}$.

The poles v_m are obtained by finding nulls in the denominator $D(v)$ in (5.41):

$$D(\nu_m) = k_r^+ J'_{\nu_m}(k_r^+ a) H_{\nu_m}^{(2)}(k_r^- a) - k_r^- J_{\nu_m}(k_r^+ a) H_{\nu_m}^{(2)'}(k_r^- a) = 0. \quad (5.46)$$

Taking a closer look into (5.45), it is obvious that the electric field can be interpreted as a linear combination of waves which travel in $+\varphi$ and $-\varphi$ direction, with the propagation coefficient $\pm\nu_m$. In addition, since ν_m is complex, its imaginary part contributes to exponential attenuation along the cylinder surface. Physically, the attenuation occurs due to radiation. The waves that travel around the cylinder in the angular direction are called *creeping waves*.

For small cylinders, one can observe a standing wave pattern around the cylinder, due to interference of waves in the opposite directions. On the other hand, for large cylinders, waves travel around the cylinder and attenuate due to radiation along the curvature (the interference is negligible for large cylinders since most of wave energy is already radiated when the waves “meet”). In terms of ν_m , the series converge faster than the original Fourier series (5.42), and usually only a few terms are needed to accurately represent the electric field [114, 116].

5.4. Calculation of the creeping wave pole

To summarize the previous discussions, we note that to obtain the creeping wave poles ν_m one needs to find the nulls of (5.46), while the general creeping wave solution for the electric field is of the form:

$$A_1 e^{-j\nu_m \varphi} + A_2 e^{+j\nu_m \varphi}, \quad (5.47)$$

where A_1 and A_2 are amplitudes of the electric field in both azimuthal directions $\pm\varphi$, and are basically equal (since a circular cylinder is axially symmetric), while the exact expression is given in eq. (5.45). For our investigations, the assumption of unit amplitude is found suitable, since they can be normalized to the actual values obtained by a particular antenna, while the slope of the total field amplitude along the curved surface (produced by the imaginary part of ν_m , as well as by interactions of waves in two azimuthal directions) is relevant for the sought estimation of the path loss.

The poles are obtained numerically, using the commercial software MATLAB R2009b, for which the routine for evaluating the Bessel/Hankel functions of the complex order was written by using the so-called Olver’s approximation [107, 123], where Bessel and Hankel functions are approximated with the Airy functions and derivatives Ai and Ai' (already implemented in MATLAB). The suitable approximations are listed as follows:

$$H_\nu^{(1)}(z) \approx 2 \cdot e^{-j\frac{\pi}{3}} \cdot \gamma(\nu, z) \cdot \frac{Ai(e^{j\frac{2\pi}{3}} \nu^{\frac{2}{3}} \xi)}{\nu^{\frac{1}{3}}}, \quad (5.48)$$

$$H_\nu^{(1)'}(z) \approx 4 \cdot e^{j\frac{2\pi}{3}} \cdot \frac{1}{\gamma(\nu, z)} \cdot \frac{e^{j\frac{2\pi}{3}} Ai'(e^{j\frac{2\pi}{3}} \nu^{\frac{2}{3}} \xi)}{\nu^{\frac{2}{3}}}, \quad (5.49)$$

where $H_\nu^{(1)}(z)$ and $H_\nu^{(1)'}(z)$ is the Hankel function of the first kind of the (complex) order ν , while the parameters γ and ξ are given as:

$$\xi = \left(\frac{3}{2}\rho\right)^{\frac{2}{3}}; \quad \gamma = \left(\frac{4\xi}{1-(z/\nu)^2}\right)^{\frac{1}{4}}; \quad \rho = \ln\left(1 + \sqrt{1-(z/\nu)^2}\right) - \ln(z/\nu) - \sqrt{1-(z/\nu)^2}.$$

The Hankel function of the second kind is obtained by changing the sign of j in each term in (5.48) and (5.49), while the Bessel functions and derivatives follow as:

$$J_\nu(z) \approx \frac{H_\nu^{(1)}(z) + H_\nu^{(2)}(z)}{2},$$

$$J_\nu'(z) \approx \frac{H_\nu^{(1)'}(z) + H_\nu^{(2)'}(z)}{2}. \quad (5.50)$$

The sought creeping wave poles lie in the fourth quadrant of the complex plane (to conform to the physical reality of attenuation in the direction of propagation), which is already suggested in Fig. 5.8. Now the task is reduced to creating a complex array and drawing the inverse of the denominator (5.46) of the Green's function (i.e. $1/D(\nu)$), from which the complex poles follow readily by mere inspection.

Table 5.2 Parameters of the circular cylinder used to model the human body torso

Cylinder radius	14 cm
Relative permittivity	52.729
Conductivity	1.739 S/m

The parameters of the cylinder in question, by which we simulate the average human body torso at the ISM 2.4 band, were taken as described in Table 5.2. In Fig. 5.9, the contour plot of the function $1/D(\nu)$ is given in the fourth quadrant of the complex plane, for the cylinder in question at the frequency of 2.45 GHz (which is the central frequency of the ISM band).

The complex order ν is normalized to the electrical length of a cylinder ($k_0 a$) in free space for convenience. Since such a summation is a fast converging one, the first term (i.e. the one with smallest negative imaginary part) could be deemed sufficient to represent the most contributing portion of the creeping wave. Therefore, from Fig. 5.9, one readily obtains the value of the most contributing pole at the observed frequency:

$$\nu_m = (1.245 - j 0.439) \cdot k_0 \cdot a = 9.583 - j 3.379.$$

The electric field in the creeping wave follows via (5.47), with the assumption of the amplitude and normalization to the corresponding length of the arc associated with an angle φ :

$$E = e^{-\frac{j\nu_m l}{a}} + e^{-\frac{j\nu_m (2 \cdot a \cdot \pi - l)}{a}}. \tag{5.51}$$

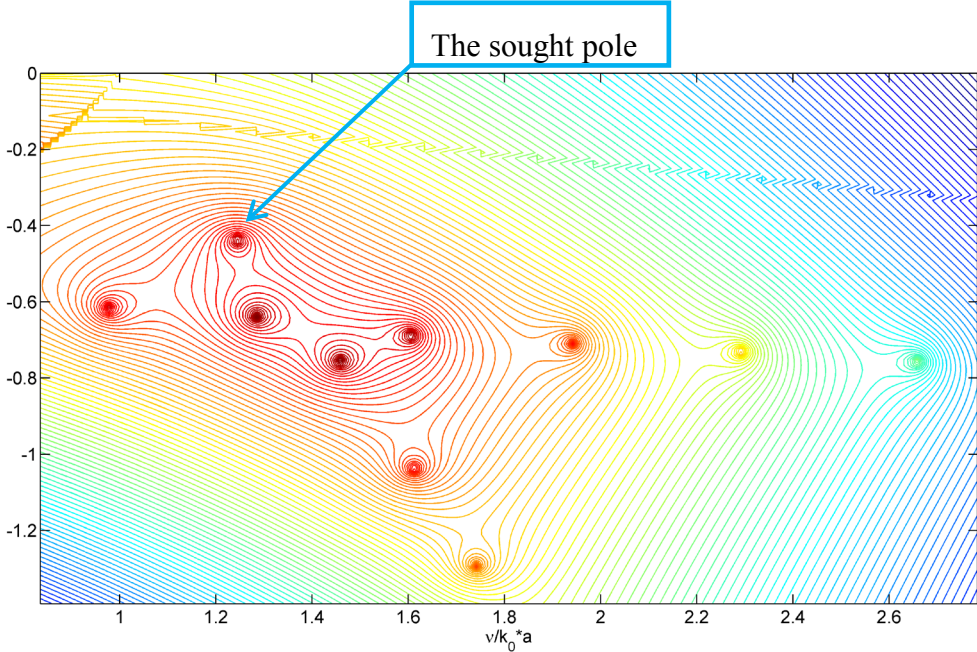


Figure 5.9 The complex plane with poles of the Green’s function of the electric field

5.5. Measurements around the human body torso

The most critical issue in the propagation around the torso is when the receiving antenna comes to the shadow region of the transmitting antenna, which leads to exponential attenuation. The supposed dominating propagation mechanism around the body torso is the so-called creeping wave, which flows around the curved surface and exponentially attenuates due to radiation. Two prototypes of PIFA antenna for the ISM 2.4 band were used for the

measurements (the design and characterization of these antennas is given in section 6.3.1). Much of this section has been published by the author of the thesis in [124].

The measurements of the antenna coupling have been taken in 21 points (4 cm distance) around the body torso (Fig. 5.10), while the whole process has been repeated three times due to the sensibility of the measurement, especially in the shadow region, where the signal was reduced to the level of the outside interference.

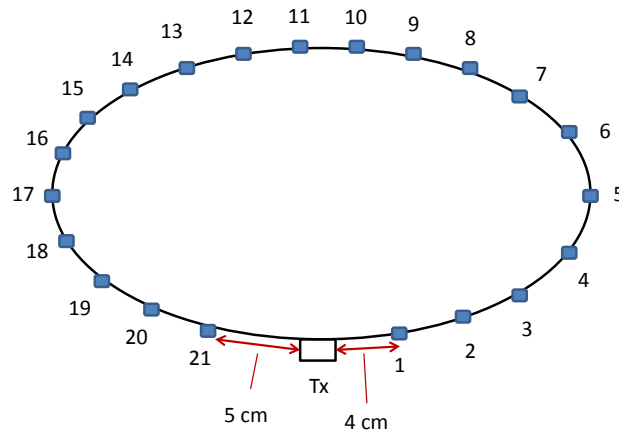


Figure 5.10 Measurement of propagation around the torso

To approximate the measured results, the cylinder radius was taken as 14 cm (which closely corresponds to the circumference of the body). Using Olver’s representation for Bessel and Hankel functions of the complex order [123], the propagation coefficient of the creeping wave was calculated as $\nu_m=1.245-j\cdot0.439$, while the electric field was written as in (5.51).

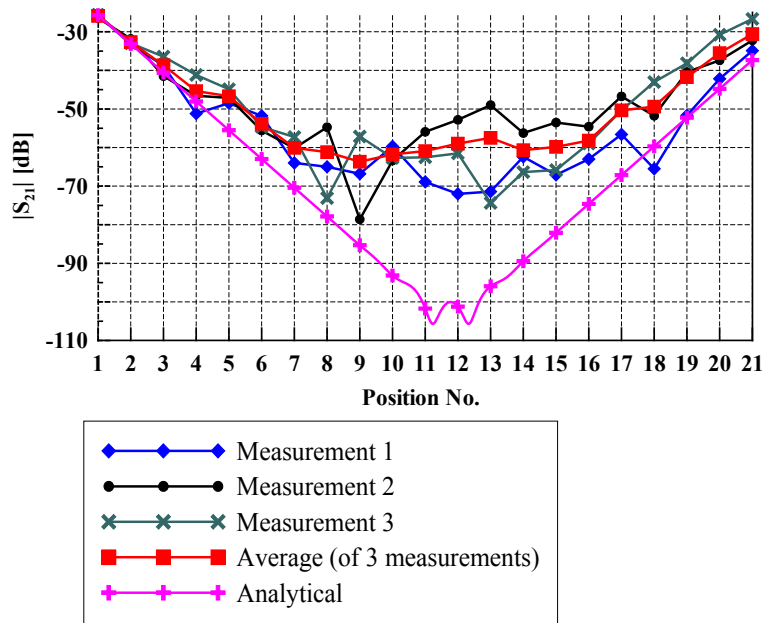


Figure 5.11 Propagation around the human body torso

In Fig. 5.11, the comparison between measured and analytical results is given. The slope in transition to the shadow region (positions 1 to 4) is basically similar both for measured and calculated results (around 140 dB/m); however, in the shadow region, the signal was reduced to the level of the outside interference, meaning that the model could not be confirmed for this region. This presumably occurs due to the finite height of the cylinder (i.e. the body) in reality.

5.5.1. Measurements on the human body phantom

To evaluate the limitations of the model of propagation around the torso, we have repeated measurements on the human body phantom placed in a cylindrical bucket. Using the human body phantom instead of a volunteer adds some more regularity to the measurements (better control of electrical parameters, possibility of using an exactly cylindrical structure, absence of side-effects such as moving of the subject, breathing etc.). The bucket radius in question is 12.5 cm, which is comparable to the radius of the human body used for the model (14 cm). A smaller water-filled bucket of a radius of 10 cm and height of 17 cm was placed in the bucket. In that way, the cylindrical, 2.5 cm thick shell was created and subsequently filled with tissue-equivalent liquid (phantom). Such a procedure was performed as there was a limited quantity of the phantom available. To add some additional shadowing, two more buckets (height 33 cm, radius 12.5 cm) were filled with water and placed below and above the bucket containing the phantom (as in upper left picture in Fig. 5.12). Simulations were performed in CST Microwave Studio for the two respective heights of the considered cylindrical shell – 17 cm and 97 cm (bottom and upper right picture in Fig. 5.12, respectively).

The measured results of propagation around the bucket are given in Fig. 5.13 together with the comparison with the corresponding analytical model and simulations for the shell height of 17 cm. It can be seen that better correspondence with measured results was obtained using simulations in CST (which have taken into account the finite height of the cylinder). In Fig. 5.14, the simulated results for the larger cylinder height (97 cm) are given and compared to the measured results and simulations for the cylinder height of 17 cm. The simulations were performed only for the first half of the cylinder to reduce simulation time due to the large demands on computer memory (the other half can be reconstructed by symmetry). With larger cylinder height, the slope more similar to the one of the analytical model was observed rather deeply across the shadow region (only when the antennas were placed on almost the opposite sides of cylinder did the slope flatten, and the fall in magnitude was still smaller than in the analytical model).

The observed results suggest that, in propagation around the torso, the finite height of the human body plays a role, and that the waves in the vertical direction (i.e. z -direction, as denoted in Fig. 5.7) also diffract onto the shadow side of the human body and add to the creeping waves, thereby reducing the path loss compared to the case of the infinite cylinder, where creeping waves are the only mechanism of propagation into the shadow region. In reality, as stated in [47], a portion of on-body communication is still obtained via propagating waves, which are reflected or diffracted from the nearby objects. These multipath waves add to the creeping waves and waves diffracted due to finite body height, making the on-body propagation modelling even more complex. Therefore, the model of propagation using creeping waves can be considered principally as a worst-case scenario when designing some on-body communication system, while other mentioned propagation mechanisms would generally reduce the path loss when antennas are placed in non-line-of-sight, and enhance the communication.

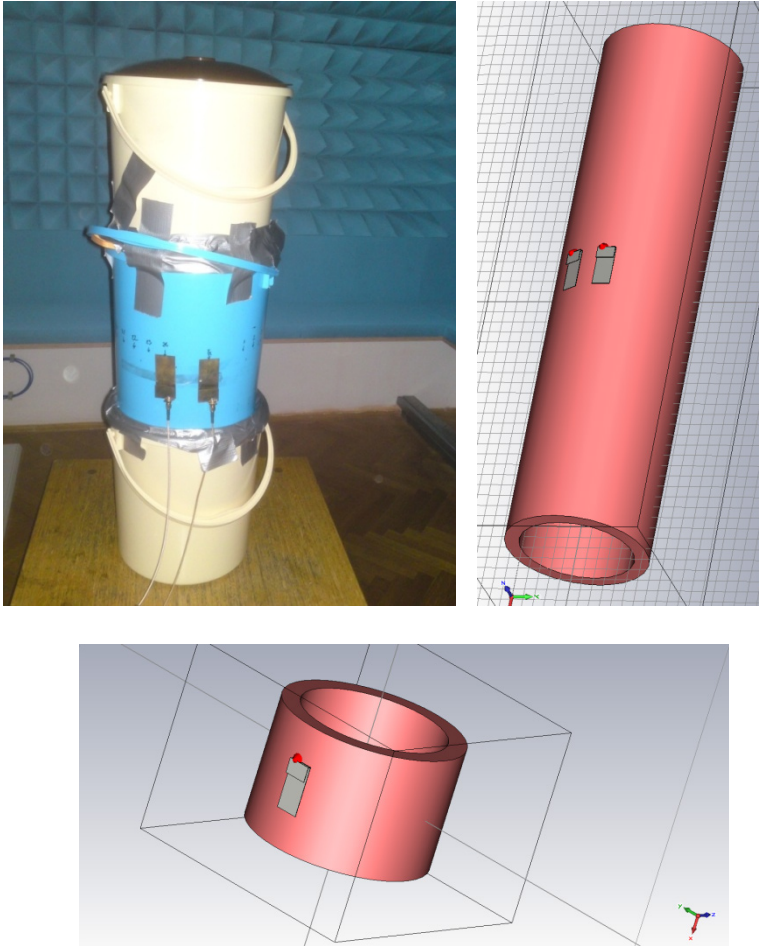


Figure 5.12 Measurement setup and simulation setups for two cylinder heights

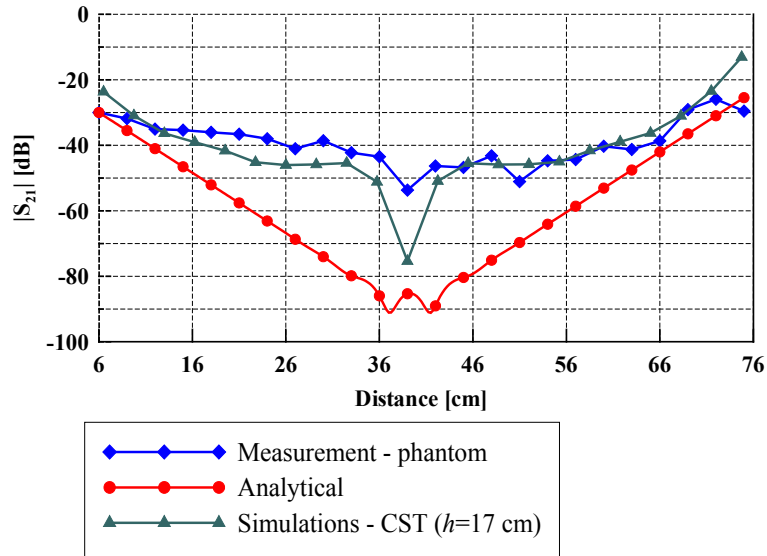


Figure 5.13 Propagation around the phantom - comparison

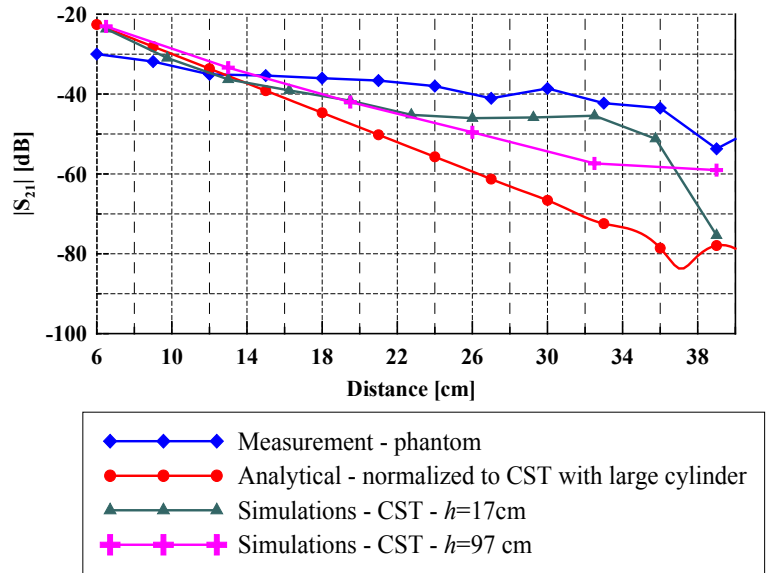


Figure 5.14 Comparison of simulations for the two cases of cylinder heights

5.6. Other on-body propagation measurements

Apart from measurements of propagation along the human body torso which served to isolate the creeping wave portion of the wave spectrum, some other practical on-body measurements were performed in order to evaluate the behavior of the on-body wireless link in real circumstances. The antennas were mounted on the body of the volunteer and, using the R&S ZVA 40 vector network analyser, the coupling (S_{21}) between the antennas was measured for various circumstances and positions in order to investigate the wireless link between two antennas placed on the body. The measurements are related to those presented in [1]; however,

the aim here was to find suitable positions of the antennas on the body which would serve as a basis for modelling the channel from the antenna viewpoint. The typical setup is given in Fig. 5.15, while the measured and simulated results for the vertical link are presented in Fig. 5.16 as a representative of surface wave attenuation (in this case estimated around 32 dB/m). The measured results correspond well with the simulated ones; however, a larger discrepancy was observed for lower signal values (i.e. larger distances between antennas), since the signal was reduced to the level of the outside interference. Much of this section has been published by the author of the thesis in [124].

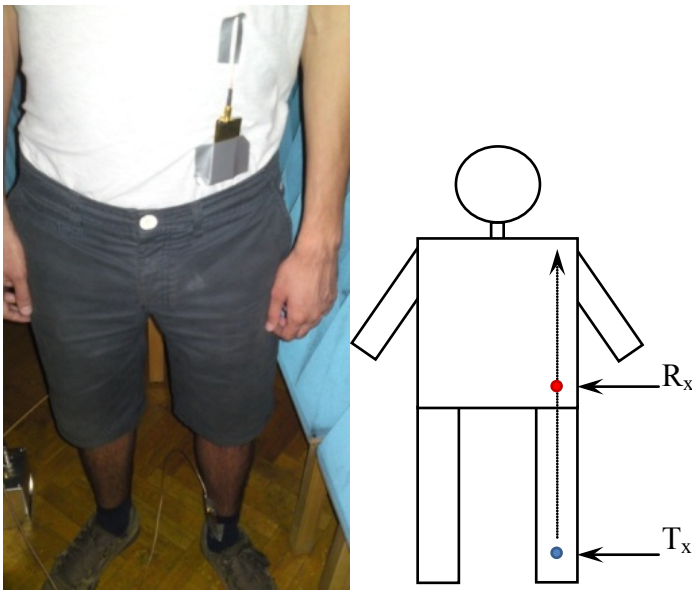


Figure 5.15 Measuring the vertical link (Tx-fixed, Rx-moving)

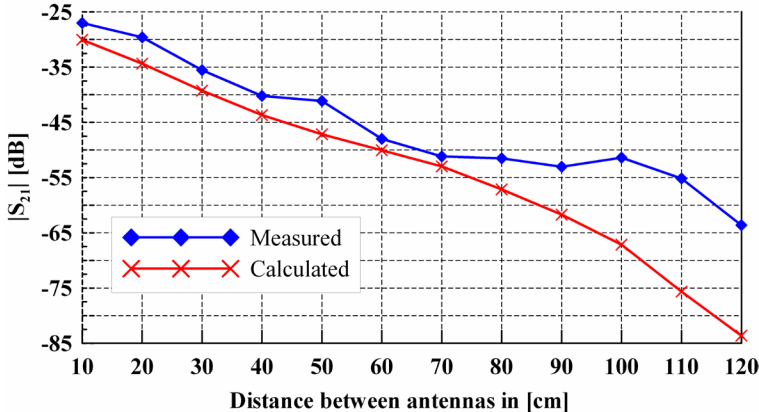


Figure 5.16 Signal decrease with distance along the body



Figure 5.17 The analyzed on-body links. From left to the right: Shoulder-belt; wrist-belt; head-belt

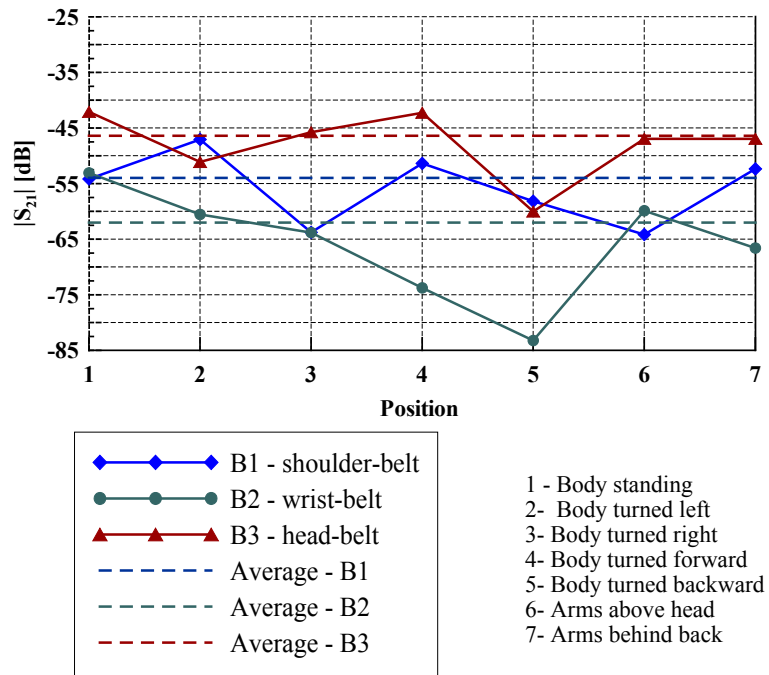


Figure 5.18 Measured on-body links variations with regard to body position

In Fig. 5.17 three typical on-body links are shown, which are further analyzed in various real-environment circumstances such as changes of the body position and shape, and moving. The measured magnitudes of transmission coefficient S_{21} (together with the comparison with the average magnitude) of the considered links with regard to changes of body position are presented Fig. 5.18. These situations are expected to occur when the antennas are mounted onto a real user. The link between the wrist and the belt exhibited largest variations around the average, since their relative positions are most prone to changes with body positions. On the

other hand, the link between the head and the belt was mostly stable, except for the case when the body was turned backward and therefore acted partly as a shadow between the antennas.

In Figs. 5.19 and 5.20, the same on-body links were analyzed when the human subject was walking in the anechoic chamber and in the room, respectively. The measured link between the shoulder and the belt exhibited the smallest variations with time around the average in the anechoic chamber; however, when walking in the room (i.e. in the real environment) the link between the head and the belt again turned to be the most stable one. Nevertheless, for practical reasons, one would still choose the link between the shoulder and the belt as more suitable for use.

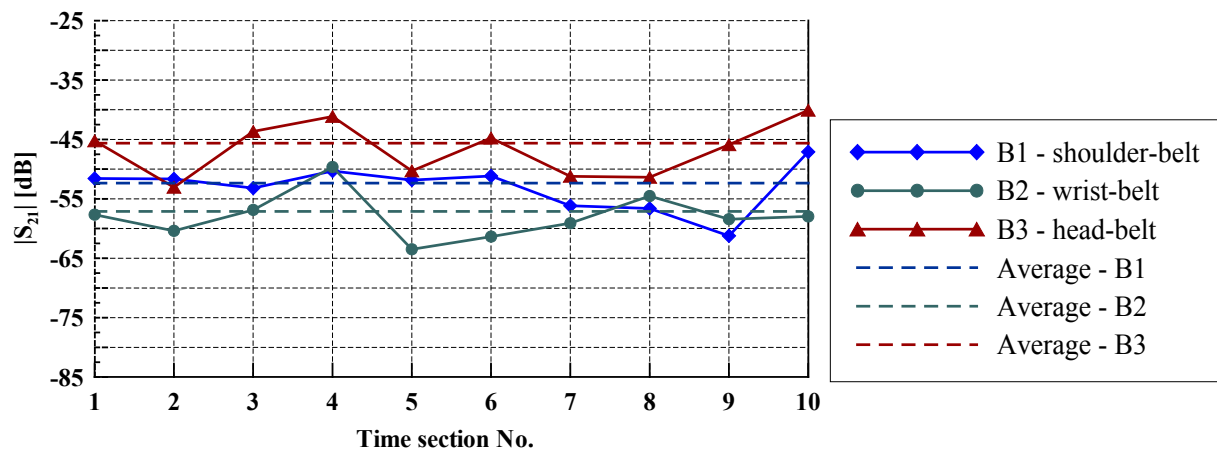


Figure 5.19 Measured time variation of the three typical on-body links with regard to human walking in anechoic chamber

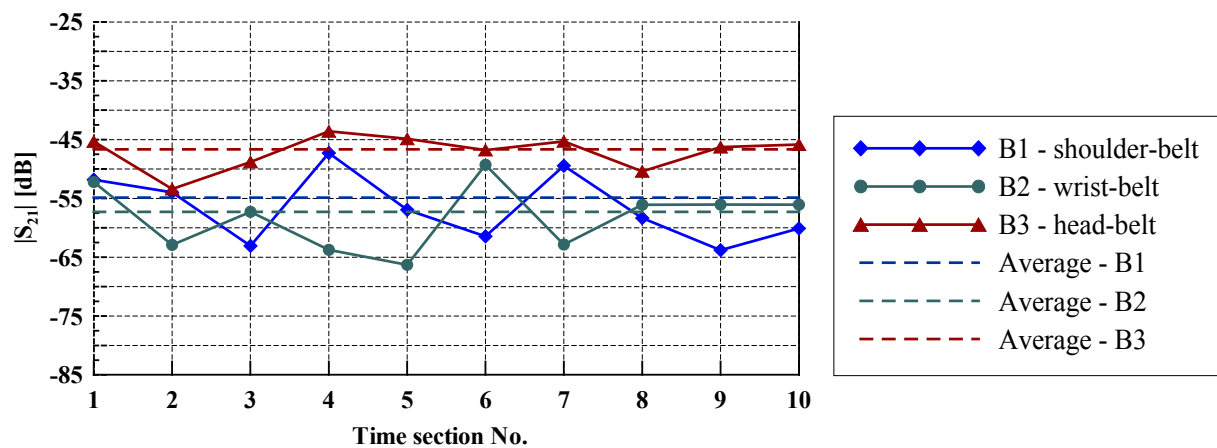


Figure 5.20 Measured time variation of the three typical on-body links with regard to human walking in the room

6. PRACTICAL ISSUES IN THE ANTENNA DESIGN FOR BODY-CENTRIC COMMUNICATION SYSTEMS

In this chapter, we are focused primarily on the process of the antenna design and the procedure of obtaining and optimizing the antenna performance, starting from the canonical $\lambda/2$ microstrip antenna, to the full-textile antenna. Therefore, several prototypes in both the UHF 400 and ISM 2.4 frequency bands have been manufactured, and practical issues that arise from the use of the antenna in real environment are addressed using a cut-and-try process (of course, respecting issues already observed in the relevant literature). To make a proper wearable antenna, the natural choice is to first design a prototype antenna using conventional materials and in the conventional environment (i.e. free space), and then get to the final design for the desired application (i.e. a full-textile antenna suitable to be worn on the body). A gradual progress towards the final design (i.e. adding more realistic factors to the antenna) also provides for a better understanding of the influences and possible practical problems at each step, thereby serving as a guideline for future design. Although the chronological order of the antenna design process was generally kept to in this chapter, three antenna designs have already been presented in previous chapters, since they served for studying the physical model of the human body, as well as the analytical models for interaction between the antenna and the human body. These issues have gained considerable attention and provided useful data for aiding progress in the antenna design and understanding of the radiation in the vicinity of the human body. Those antenna designs and the experience taken from them are only outlined here in the context of progress in the design of the antennas themselves. Major issues affecting the antenna performance which need to be explored in the antenna design for body-centric systems are influenced by:

- The textile substrate
- The real human body
- Mechanical deformations
- Environmental and climate conditions
- Conductive textiles

Thus, a simple measurement method for evaluating the permittivity of the dielectric textile substrate is proposed and described in the first section of the chapter. In the following sections, the antenna prototypes which served for measuring various conditions from the real environment are described, both in the UHF 400 and ISM 2.4 bands. It can be seen that the

measurement methods were also gradually refined, taking more factors into consideration. Moreover, in line with the experience gained at a specific step, each new design tried to solve the issues of the previous step, neglecting some influences which were found marginal. The antennas in the first part of the chapter were made using conventional conductive materials (copper plate and copper tape) which were found acceptable for laboratory tests used for evaluating the effects of bending and moisture.

After developing the prototypes that exhibited fair performance on the body, the next part of the chapter describes the transition to full-textile antennas, where the conductive part is made of textile. The issue of designing conductive textiles is left as the last step since suitable prototypes had already been obtained by that time, and their behaviour in the vicinity of the human body studied. Therefore, the performances of antennas made of conductive textiles are compared to the prototypes, while the challenges of designing proper conductive textile are outlined. In the final section, a full-textile antenna for the ISM 2.4 band is proposed. Based on the experience gained in the design and characterization of antenna prototypes and textile materials, an outline is presented describing the design of such an antenna and the solutions to the surrounding issues, in order to serve as a practical strategy for the design of wearable antennas.

6.1. Measuring the permittivity of textile materials

To measure the dielectric properties of textile materials, a coaxially-fed $\lambda/2$ microstrip antenna was designed using the commercial software CST Microwave Studio [99]. Such an antenna is intended to resonate at 2.5 MHz when in the air, while the resonant frequency is expected to decrease in the presence of the textile substrate. Since the chosen antenna is a canonical one, it could be used as a benchmark for other investigations of the interaction of the antenna with the human body. In addition, the size of the half-wavelength microstrip antenna in the considered frequency bandwidth (near ISM 2.4 GHz) could even be deemed acceptable by itself, while the presence of a ground plane reduces its effect on the human body. The final dimensions of the antenna are summarized in Table 6.1.

After optimizing the parameters in CST, the prototype was manufactured (Fig. 6.1), and its characteristics were checked by measurements (using the R&S ZVA 40 vector network analyser). The feeding point was first calculated by simulations at 11 mm from the radiating edge, and then shifted by 2 mm (i.e. to the distance of 13 mm) to improve the measured bandwidth and matching, and to get closer to the results of the first simulations which used a

discrete port. The simulation procedure was then refined by using real coaxial feeding (waveguide port), while the reference plane (short circuit) was shifted to conform to the antenna ground plane both in simulations and measurements. In Figs. 6.2 and 6.3, the input reflection coefficient for the two respective positions of the feeding point x (11 mm and 13 mm) of the designed antenna on an air substrate is given, together with the comparison with the refined simulation procedure. The results for both cases show very good agreement, both in amplitude and phase, which means that the obtained computer model is suitable for further calculations and analysis. Furthermore, the obtained antenna is fully calibrated and controllable, and it is suitable for precise measurements of dielectric properties of the inserted textile materials.

Table 6.1 Dimensions of the $\lambda/2$ microstrip antenna for the ISM 2.4 band intended for measuring the permittivity of textile materials

Parameter	Dimensions [mm]
Length (L)	52
Width (W)	62.5
Substrate height (h)	4
Ground plane dimensions	125 x 125
Feeding point distance from the radiating edge (x)	13

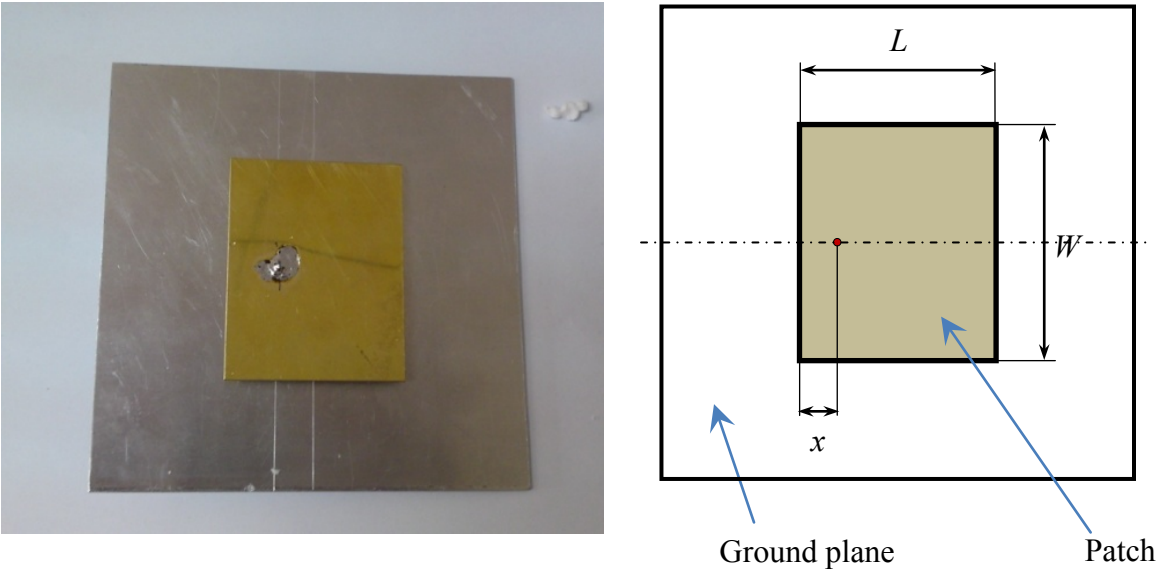


Figure 6.1 Prototype of the half-wavelength microstrip antenna intended for measuring the permittivity of textile materials

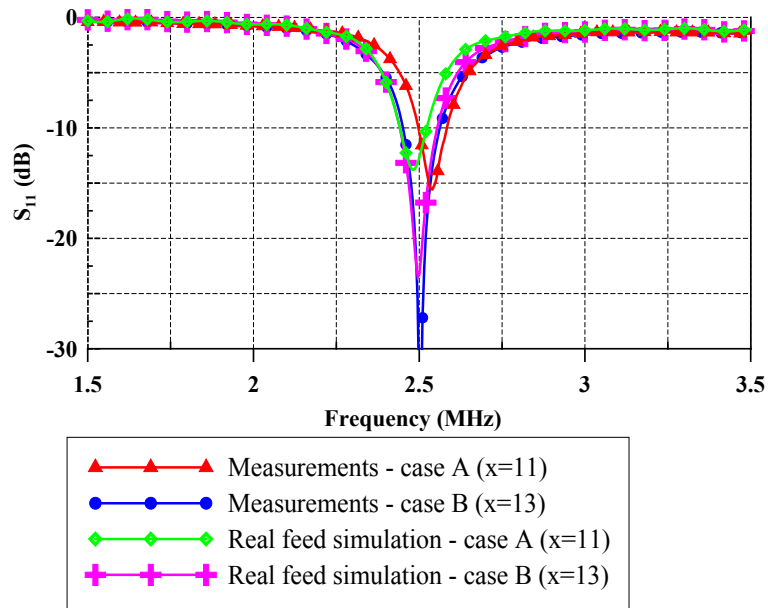


Figure 6.2 Magnitude of the input reflection coefficient of the simulated and measured antennas vs. frequency

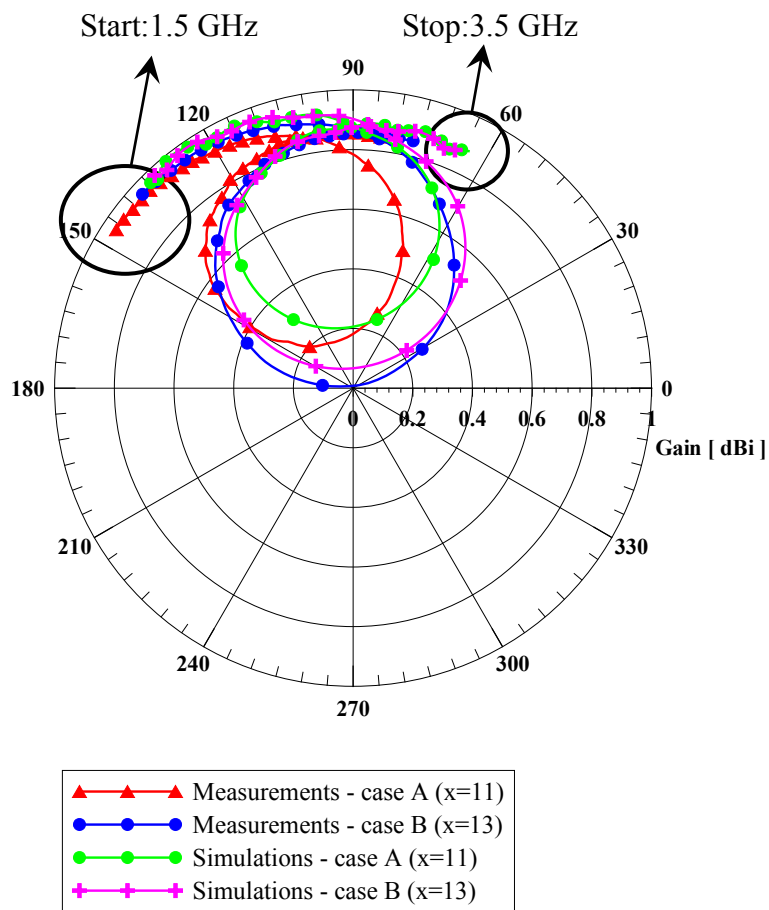


Figure 6.3 Polar plot of the input reflection coefficient for the two feeding point positions - $x = 11$ mm and 13 mm (referent impedance: 50Ω , marker step: 0.06 GHz)

The permittivity of the textile material is intended to be measured by inserting a textile sample as the substrate and observing the shift in resonant frequency, which is first demonstrated by simulations for the theoretical, 4 mm thick nonwoven fabric material with the permittivity of 1.1 (i.e. fleece [76]), as illustrated in Fig. 6.4.

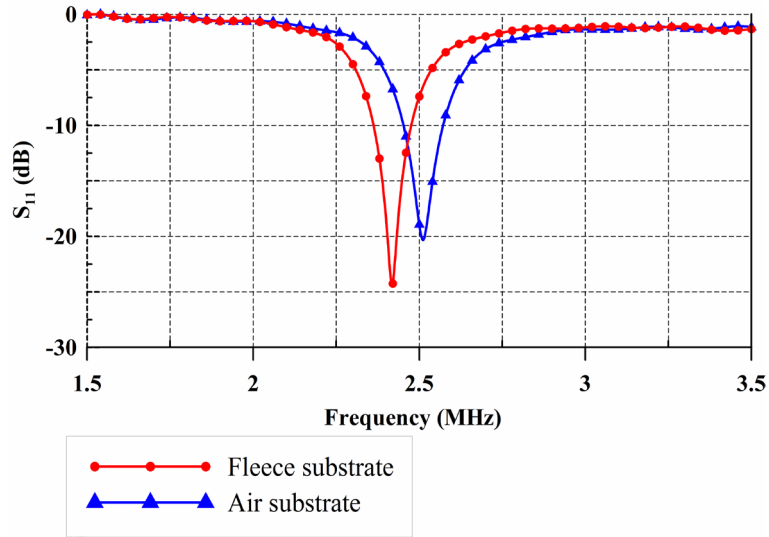


Figure 6.4 Calculated magnitude of the input reflection coefficients with and without the presence of the fleece substrate

Using the microstrip patch antenna (Fig. 6.1), the permittivity of three commercially available materials (fleece, wool and denim) was measured (Fig. 6.5). The materials were inserted as the antenna substrates one at the time (for wool and denim, two and four layers of material needed to be used, respectively, to obtain the required substrate height of 4 mm), and the shift in resonant frequency was observed for each case.

The effective permittivity (ϵ_{eff}) was calculated using the following expression:

$$L_{resonant} \propto \frac{c}{f_1} = \frac{c}{f_2 \sqrt{\epsilon_{eff}}}, \text{ i.e.}$$

$$\epsilon_{eff} = \left(\frac{f_1}{f_2} \right)^2 \quad (6.1)$$

where $L_{resonant}$ is the resonant length (proportional to wavelength) which depends on the geometry of the antenna, while f_1 and f_2 are the associated resonant frequencies on the air and material substrate, respectively. Since for the microstrip antenna $W \gg h$, the effective permittivity can be considered close enough to the relative permittivity of the textile substrate as well [112].

In Figs. 6.6 and 6.7, the measured results for the inserted textile substrates are given. It can be seen that the resonant frequency has somewhat shifted downwards, due to the influence of the textile substrate. Using the measured resonant frequency, the effective permittivity of the textile materials was calculated from (6.1). The results are given in Table 6.2. It can be seen that the measured permittivities are relatively low, but still affecting the radiation properties of the antennas. In addition, the measured values of the permittivity of textiles correspond to the ones available in literature (Table 2.3), meaning that the method used is suitable for evaluation of dielectric properties of textile materials used in the antenna design.

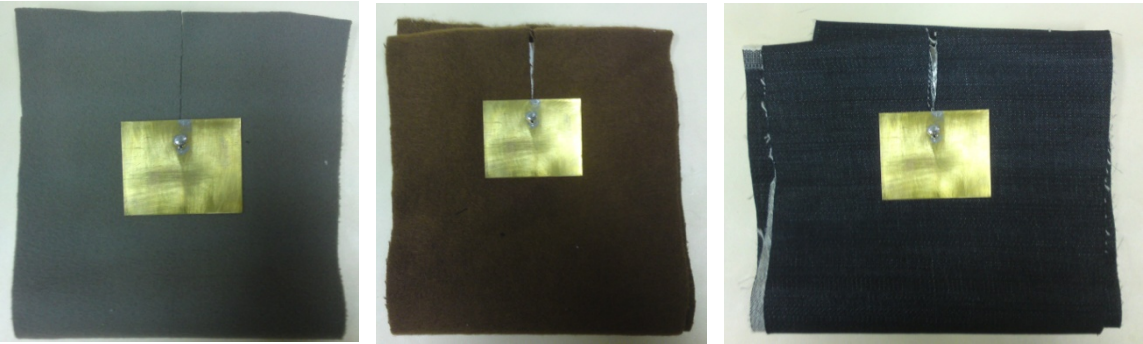


Figure 6.5 Microstrip antenna filled with various textile substrates. From left to the right: fleece, wool, denim

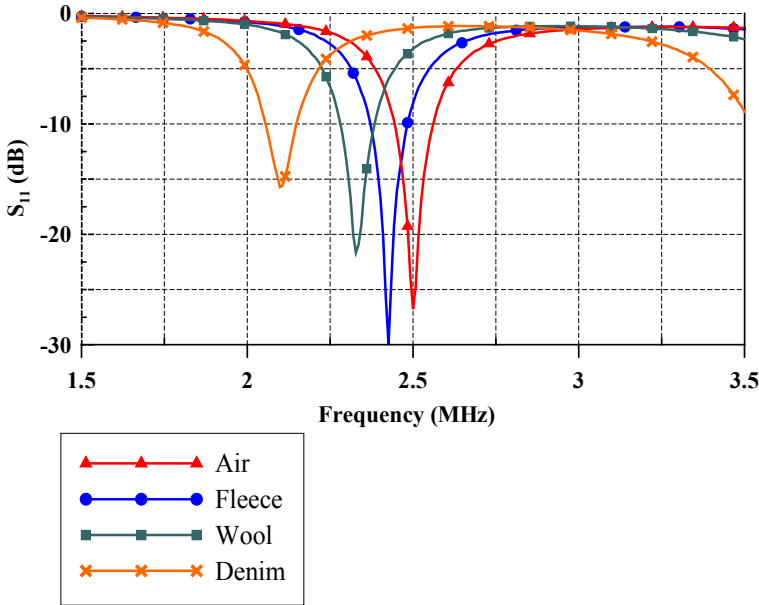


Figure 6.6 Measured magnitude of input reflection coefficient (S_{11}) for various textile substrates

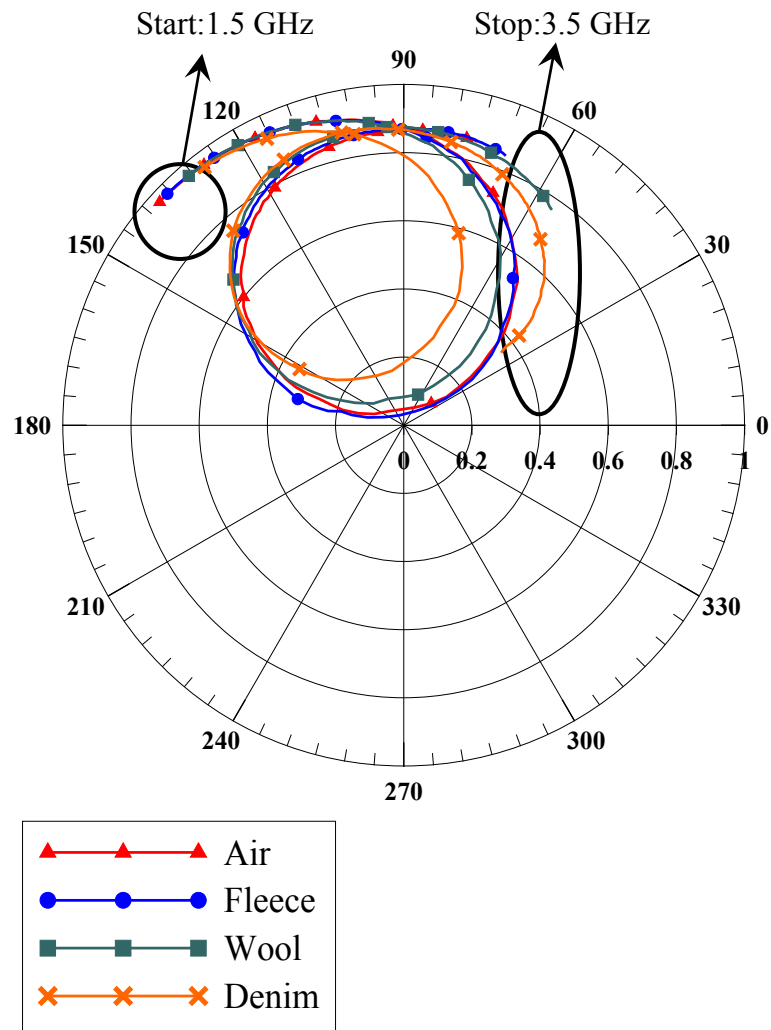


Figure 6.7 The measured input reflection coefficient (S_{11}) for various textile substrates – polar diagram (referent impedance: 50Ω , marker step: 0.09 GHz)

Table 6.2 The measured effective permittivities of textile materials in the ISM 2.4 band

Material	$f_{resonant}$ [GHz]	$\epsilon_{r,eff}$
Air	2.5	1
Fleece	2.426	1.06
Wool	2.328	1.15
Denim	2.098	1.42

6.2. Prototype of the wearable UHF 400 antenna and the influence of bending

Reflecting the research described in Chapter 4, we have designed a wearable antenna for body-centric communications in the UHF range (in particular, around 400 MHz) which would operate properly in the presence of the human body. As mentioned before, the UHF range is suitable for medium-range off-body communications, which could be useful e.g. for rescue and military teams. The typical required bandwidth for such communications is around 20 MHz (i.e. around 5% in terms of relative bandwidth). Much of this section was published by the author of the thesis in [125].

Using the commercial software “CST Microwave Studio” [99], a quarter wavelength shorted patch antenna on the air substrate, known from literature (e.g. [2]), was firstly designed. The height of the antenna was fixed to 4 mm, since this is the supposed thickness of the textile intended for later insertion as a substrate. Such low substrate thickness (the textile is typically thin) is actually the most challenging part of the design of this antenna for the intended purpose and range. In order to improve the bandwidth, the size of the ground plane was reduced from 40×40 cm to 30×15 cm, and the pi-shaped slot was introduced in the patch, as shown in Fig. 6.8. Also, the shorting wall was cut by 0.5 cm from each side. In addition, the introduction of the slot in the ground plane (which could also reduce the size of the antenna) was avoided, since it was shown that it exhibits increased radiation into the human body. The scheme of the slot in the patch is shown in Fig. 6.9 in more detail, while the respective dimensions of the slot parameters are summarized in Table 6.3.

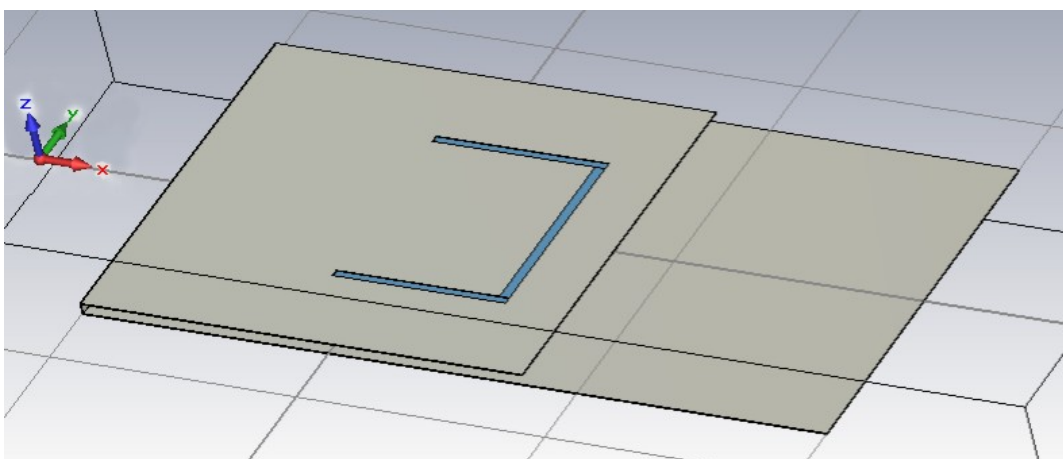


Figure 6.8 The antenna with the pi-shaped slot

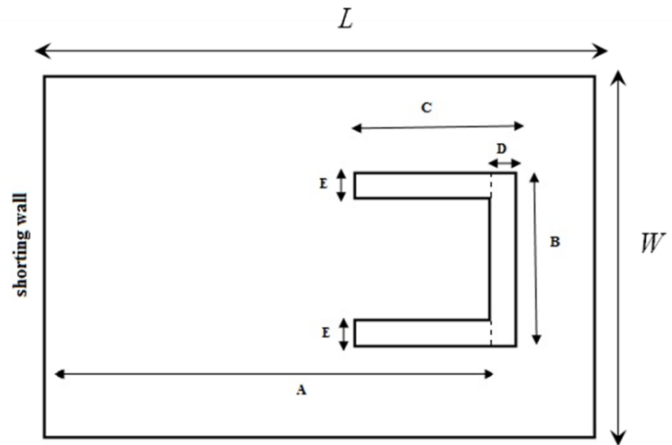


Figure 6.9 The antenna with the pi-shaped slot - scheme

Table 6.3 Slot dimensions according to Fig. 6.9

Distance from the shorting wall (A)	15 cm
Slot width (B)	8 cm
Length of slot legs (C)	7 cm
Width of slot central part (D)	0.4 cm
Width of slot legs (E)	0.3 cm

The final version of the antenna was obtained by inserting a 4 mm thick layer of fleece, with a permittivity of 1.1, as a substrate in the simulations. The resonance at 400 MHz with the fleece substrate was obtained by setting the length (L) to 17.4 cm. The patch width (W) was 15 cm. The calculated relative bandwidth was around 4.3%, which can be deemed satisfactory for the intended use. In addition, the calculated gain, when lossless case was assumed, was 4.07 dBi.

Since the antenna is supposed to be worn on the body, its performance in the vicinity of the human body was examined and compared to its performance in free-space. A rectangular lossy dielectric box (45 cm \times 40 cm \times 18 cm) was used as a simplified numerical body phantom. The relative permittivity and conductivity were taken to correspond to the muscle tissue at 400 MHz and amounted to $\epsilon_r = 57.129$ and $\sigma = 0.8$ S/m, respectively (loss tangent turns out to be 0.626) [92]. Such a model corresponds to the trunk of the body, and the antenna was placed in the middle of its largest face (corresponding to e.g. the chest), as shown in Fig. 6.10.

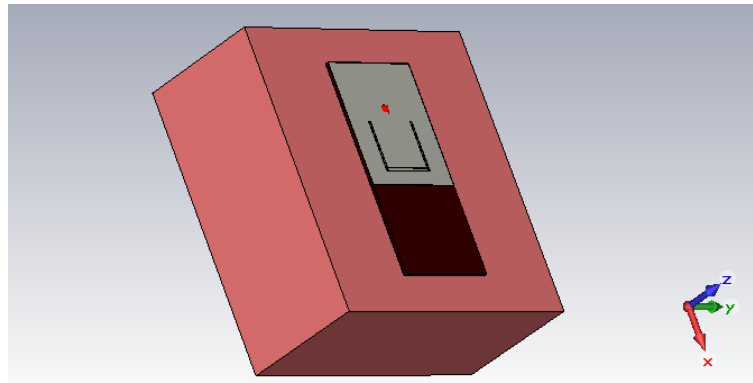


Figure 6.10 The antenna placed on the body model – illustration from CST

In the presence of the human body model, the impedance was higher, which resulted in the detuning of the input impedance matching. The new matching point was calculated at the distance of 4.2 cm from the shorting wall (previously it was 6.5 cm). With the new matching position, the relative bandwidth was reduced to only 1.8%. In addition, the calculated radiation efficiency was -4.237 dB, which led to the gain of -0.45 dBi. Such low values of gain are quite common for antennas in the vicinity of the human body [35], and are nevertheless quite an improvement when compared to the antenna with the slot in the ground plane analysed in Chapter 4 (although at the expense of bandwidth when placed on the body). The comparison between the calculated magnitudes of the input reflection coefficient for the relevant cases is given in Fig. 6.11.

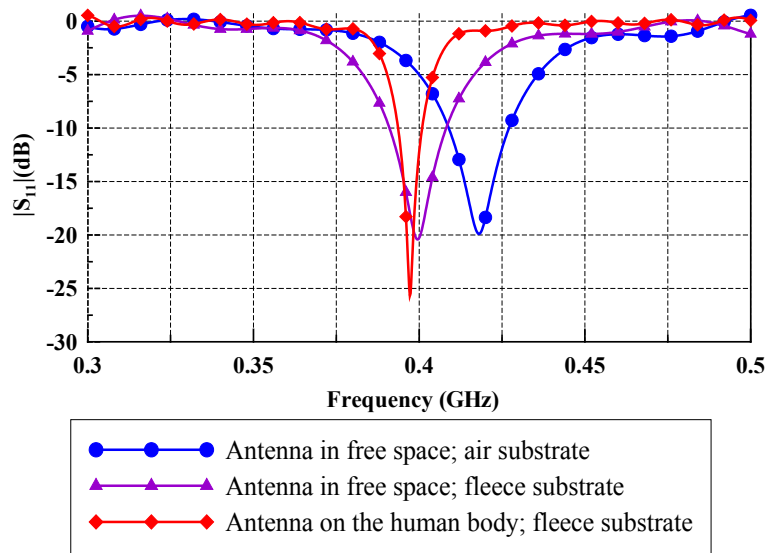


Figure 6.11 The calculated magnitudes of the input reflection coefficient (S_{11}) for the final antenna design

6.2.1. Measurements on the prototype

After performing the simulations, the prototype of the antenna was fabricated (Fig. 6.12). The characteristics of the antenna in free space were verified by measurements using the R&S ZVA 40 vector network analyser.



Figure 6.12 The prototype of the patch antenna with a pi-shaped slot on an air substrate

The comparison between the calculated and measured reflection coefficient for the antenna on an air substrate is given in Fig. 6.13.

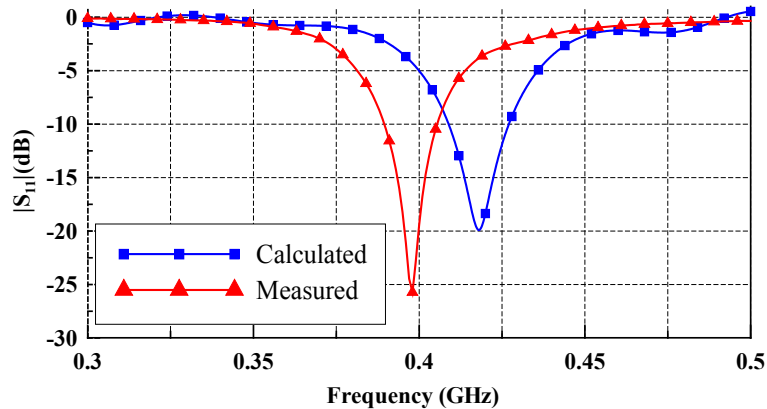


Figure 6.13 Calculated and measured magnitude of the input reflection coefficient (S_{11}) for the antenna on an air substrate

The measured resonant frequency is around 4.5% lower than the calculated one. Such a discrepancy between calculated and measured results arises due to manufacturing imperfections.

The measured co-polarization radiation patterns in the E - and H - plane for the antenna in free space at the frequency of 400 MHz are given in Fig. 6.14. The measured values are normalized to the value at 0° direction, and are in accordance with the simulated ones. The

cross-polarization levels in broadside direction were around 10 dB below the co-polarization ones, meaning that satisfactory polarization purity was obtained.

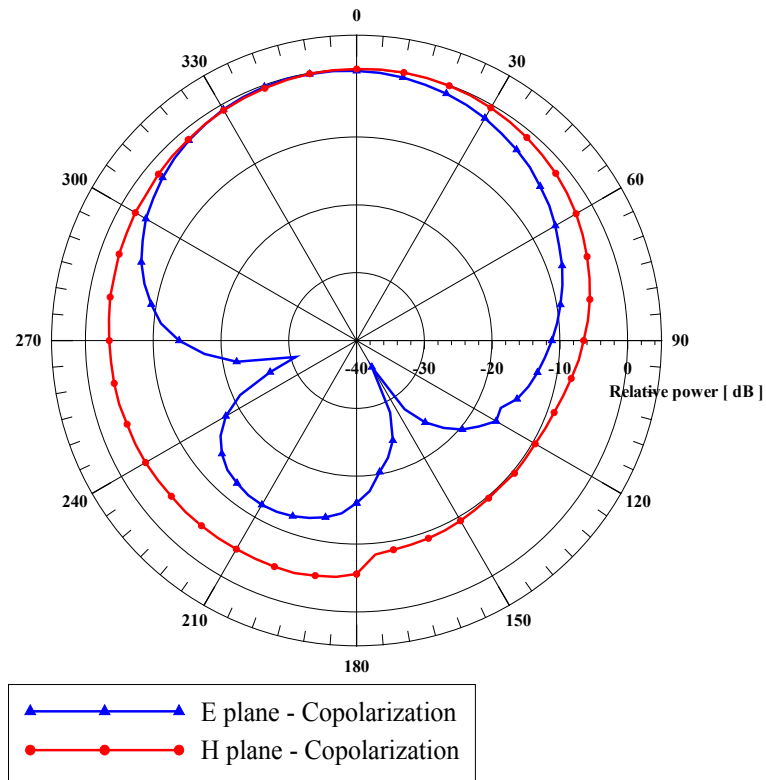


Figure 6.14 Measured co-polarization radiation pattern of the antenna in free space ($f=400$ MHz)

The measured broadside gain in free space is shown in Fig. 6.15. The maximum gain is around the resonant frequency, and is close to the values obtained by simulations in free space.

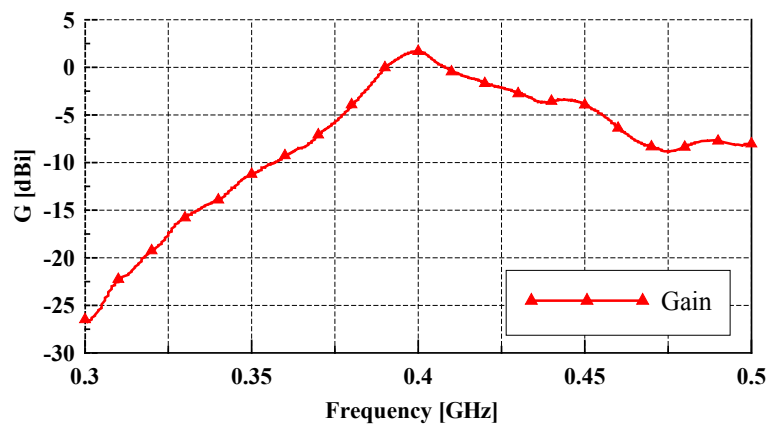


Figure 6.15 Measured gain of the antenna in free space

After measuring the performance of the antenna on an air substrate, a few commercially available textiles were inserted as substrates (Fig. 6.16), and the input reflection coefficient was measured for each case, as shown in Fig. 6.17. This method for measuring the relative permittivity of textile substrates has already been introduced in section 6.1 for the ISM 2.4 band, so using this antenna, it was merely extended to the UHF band. The effective permittivities of the antennas with textile substrates were obtained from the changes in the resonant frequency compared to the antenna on an air substrate (Table 6.4), and they mainly correspond to the measurements in the ISM 2.4 band. The slight differences in the obtained values can be explained by the mechanical role of the textile substrates that the inserted materials had in the case of the UHF antenna – namely, for the microstrip antenna in section 6.1, the patch was a stand-alone structure and the materials were just inserted. In the case of the UHF antenna, the textile also served to mechanically support the patch above the ground plane (in the case of the air substrate, that role was played by a small piece of Styrofoam). In that way, any tolerance in the substrate thickness, as well as the pressure from the patch onto the textile (since the textile is soft), actually slightly altered the patch height, thereby introducing some small uncertainties in the antenna dimensions. Nevertheless, the measured permittivities can be considered as a good estimation for further design. We also note that, although the relative permittivities of most substrates are low, the knowledge of the permittivity of the respective substrate is required for the precise antenna design, especially for the case of narrow-band (resonant) antennas.

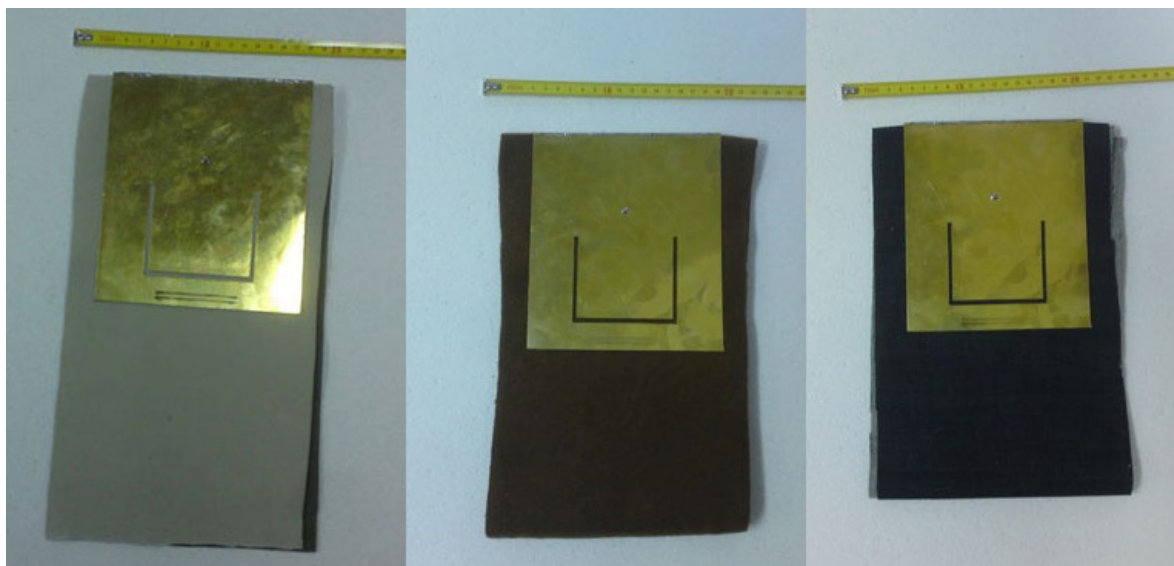


Figure 6.16 Antenna prototype filled with various textile substrates. From left to right: fleece, wool, denim

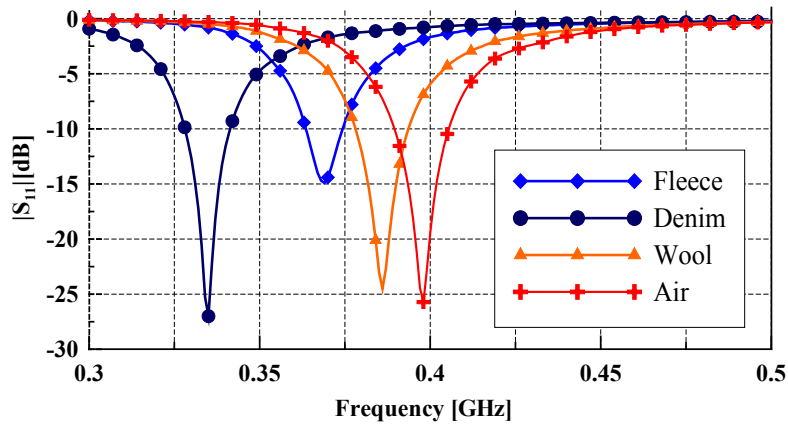


Figure 6.17 Measured magnitude of the input reflection coefficient (S_{11}) for various textile substrates

Table 6.4 Measured effective permittivities of textile materials in the UHF 400 band

Material	$f_{resonant}$ [GHz]	$\epsilon_{r,eff}$
Air	0.398	1
Fleece	0.369	1.16
Wool	0.386	1.06
Denim	0.335	1.41

6.2.2. Antenna bending

In the real environment, the antenna worn on-body is prone to mechanical deformations such as bending. Therefore, the influence of antenna bending both in the E - and the H -plane was examined. For that purpose, the flexible antenna on a wool substrate was manufactured using copper tape as a conductive material. The flexible antenna (Fig. 6.18) was attached to two empty PET bottles of different radii in order to obtain the desired bending. The bending was examined for the two radii – 10 cm and 5.5 cm, which are values that can be found in reality (e.g. when placing the antenna on the human body torso or arm, respectively). The measurement setup for bending conditions is given in Fig. 6.19.



Figure 6.18 Prototype of the flexible antenna (copper tape on wool substrate)

The measured reflection coefficients for the examined bending conditions are given in Fig. 6.20. The change in resonant frequency was more pronounced for the smaller bending radius, as expected, while the measurement added some more uncertainties (e.g. the bottle used for measuring the larger bending radius was not perfectly round), so the influences of bending in the E -plane and the H -plane cannot be conclusively distinguished at this stage.



Figure 6.19 Antenna bending in the E -plane (top) and the H -plane (bottom); radius 10 cm (left), radius 5.5 cm (right)

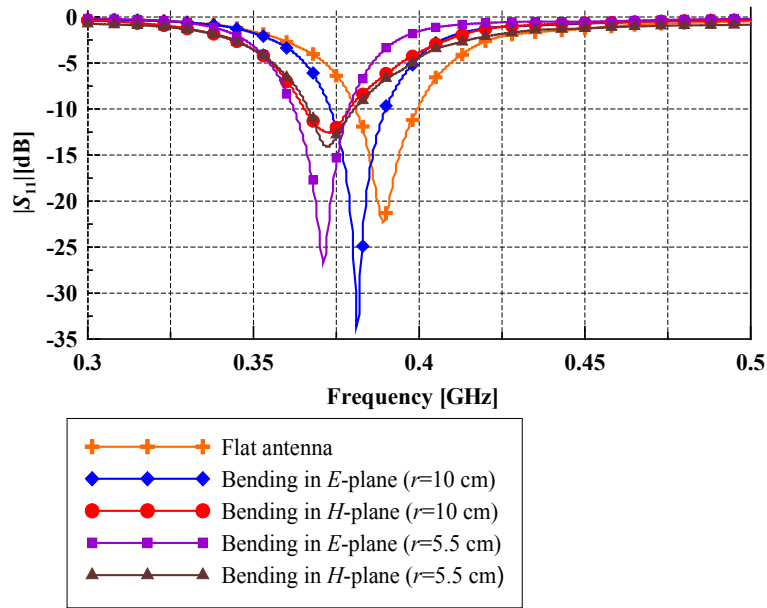


Figure 6.20 Measured magnitudes of the input reflection coefficient (S_{11}) for various bending scenarios

6.2.3. Antenna in the presence of the human body

In the next measurement, the antenna was attached to the body of a volunteer (Fig. 6.21), and its input reflection coefficient was measured. In Fig. 6.22, the comparison between the measured magnitude of the input reflection coefficient for the antenna in free space and on the human body is given (only the case of a flat antenna, i.e. without bending, was considered).



Figure 6.21 Antenna on the human body

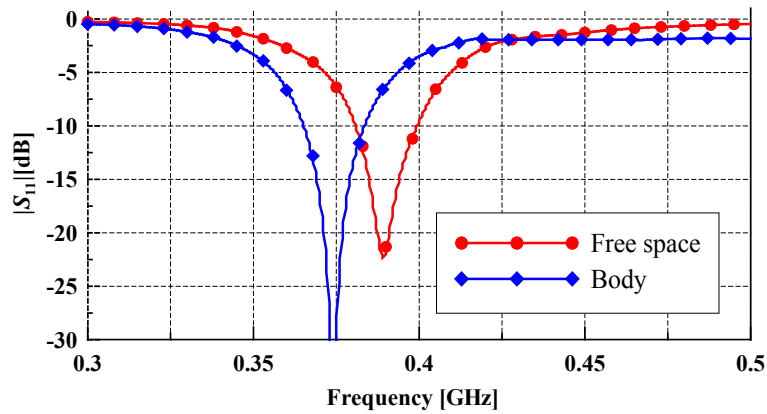


Figure 6.22 Comparison of the measured magnitude of the input reflection coefficient (S_{11}) for the flat antenna in free space and on the human body

As predicted by the simulations, the resonant frequency in the presence of the human body was around 3.9% lower; however, the matching bandwidth did not deteriorate as predicted by the simulations. Such a discrepancy between simulated and measured results is assumed to arise due to the clothing layer between the antenna and the human body, which was not included in the simulations.

6.2.4. Remarks on the UHF antenna

The example of the microstrip textile antenna with a pi-shaped slot described above outlines some of the first practical issues which arise in the design and characterization of antennas intended to be worn on the body. These issues are addressed in the following sections in order to characterize the performance of the antenna in the real environment in more detail, as well as to make a more general strategy for the design of wearable antennas.

First, one needs to know the permittivity of the textile substrate which will be used, especially when the antenna is narrow-band. The permittivity can also vary with the environmental conditions, thereby further affecting the radiation properties of the antenna.

Furthermore, to be comfortable for wear and unobtrusive to the user, the antenna needs to be flexible, which gives rise to the question of which material to use. Although flexible copper tape is satisfactory for laboratory testing, in its natural form it has limited practical value, since the antenna needs to be integrated into clothes and worn daily, thereby being exposed to various mechanical deformations (for which copper tape lacks durability and elasticity), while it also needs to remain aesthetically acceptable. Thus research into conductive textiles which could serve both as part of clothes and a part of the antenna needs to be conducted to obtain a final product suitable for use in real applications.

Due to the intended application of the antenna, as well as its flexibility, the antenna cannot be regarded as if it is to remain flat, so the influence of bending as a typical mechanical deformation was studied both in the *E*- and the *H*- planes. The procedure of measuring the effect of bending also needs to be refined to include more typical bending radii, and distinguish the influence of bending onto the antenna performance in each respective plane. Although matching and bandwidth remained stable, the resonant frequency went down by up to 7% due to bending, so an antenna with a broader bandwidth should be considered, if possible.

Another issue is the evaluation of the influence of the presence of the human body on the antenna properties. The most critical influence arises when the antenna is placed on the skin; however, in real applications there will be one or more clothing layers in between, the influence of which needs to be considered. Moreover, the placement of the antenna on the human body needs to be explored – the antenna should be placed so as to be exposed to minimal deformations caused by body movement in order to retain a stable signal. Therefore, further measurements for various body positions need to be conducted.

The coaxial feeding from the ground plane (i.e. from the bottom of the antenna) is also rather impractical in terms of conforming the wires to the surface of the human body, so other feeding arrangements need to be considered as well.

Finally, the choice of the frequency range also has an effect on the obtainable radiation properties of the antenna. For the described microstrip antenna with a pi-shaped slot, the calculated radiation efficiency was around 40%, which can be considered acceptable, but at the expense of bandwidth, which was too narrow to keep up with the changes in the resonant frequency in bending conditions, or in the presence of the human body. Note that, to design a small antenna in the lower frequency ranges (such as UHF), one in fact always needs to accept some compromises (as elaborated in section 4.1), so it can be considered as a challenge by itself, even for a conventional flat design in free space. Moving to higher frequencies can relax some demands on the antenna design, and generally lead to antennas which perform better (in terms of bandwidth), at least in the prototype stage, while the case of UHF antennas can be considered as the worst case scenario in the wearable antenna design.

6.3. Prototypes of the quarter-wavelength antenna for the ISM 2.4 band and a phenomenological evaluation of the influence of moisture

In accordance to the remarks made in the previous section, we have performed a part of the research in the the ISM 2.4 band (2.4 ÷ 2.48 GHz) to relax the demands imposed on the size of the antennas in the UHF band and compromises regarding radiation efficiency that affect the antenna design. The compromises mentioned blur the evaluation of other influences which are specific for antennas for body-centric systems (human body, mechanical deformations, environmental conditions, the materials used etc.). By moving towards the higher frequencies, one variable (antenna size) can be loosened, which makes it possible to make the antenna that operates properly in free space, and compare its performance with the one in the body-centric environment. The issues that arise in the observed environment are in principle not limited to one frequency range. Furthermore, the ISM band (together with nearby bands) possesses a larger bandwidth (admitting higher data rates) and is widely used by the general public due to its broad range of applications (e.g. WLAN, Bluetooth, GPS, UMTS), so ISM antennas arguably possess an additional practical value.

To reduce the size of the microstrip antenna from section 6.1, we have introduced a shorting wall into the microstrip antenna, thus obtaining the quarter-wavelength patch. The outline dimensions of the antenna are summarized in Fig. 6.23 and Table 6.5.

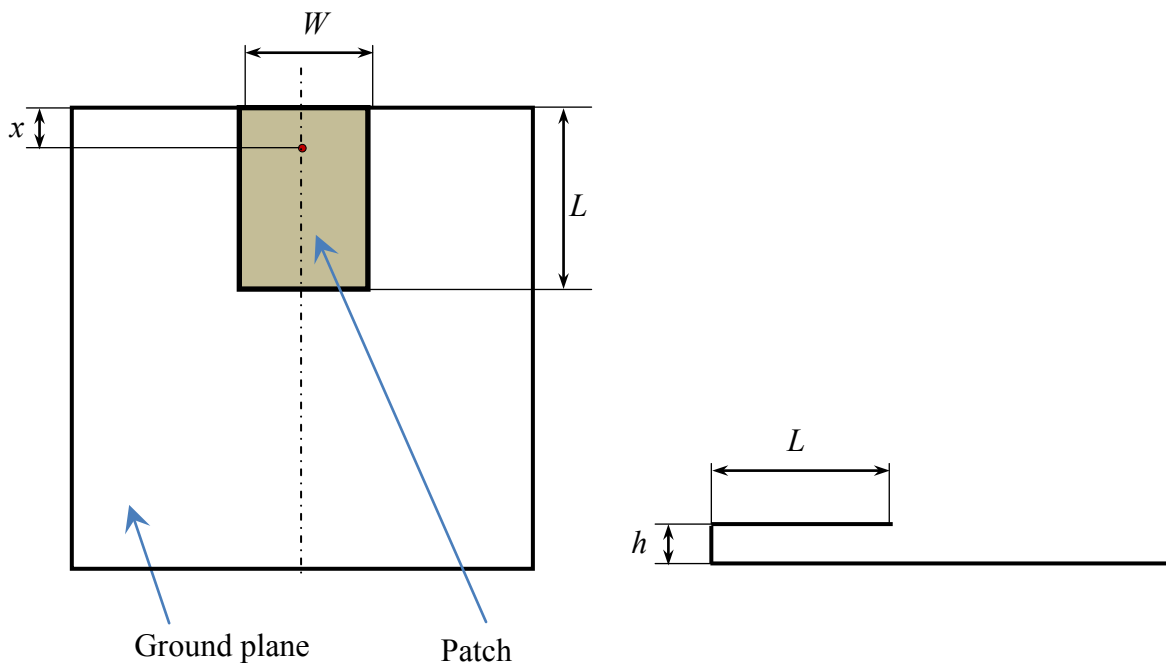


Figure 6.23 Top and side view of considered $\lambda/4$ microstrip antenna

Table 6.5 Dimensions of $\lambda/4$ microstrip antenna

Parameter	Dimensions [mm]
Length (L)	24
Width (W)	17
Substrate height (h)	4
Ground plane dimensions	61×61
Feeding point distance from the radiating edge (x)	5

The prototype was realized using solid conductive material (copper plate). while fleece was subsequently inserted as a substrate. The comparison between calculated and measured results is given in Fig. 6.24. Although the realized antenna does not exactly target the desired ISM 2.4 band, it is still suitable for evaluating the influence of moisture on the antenna properties.

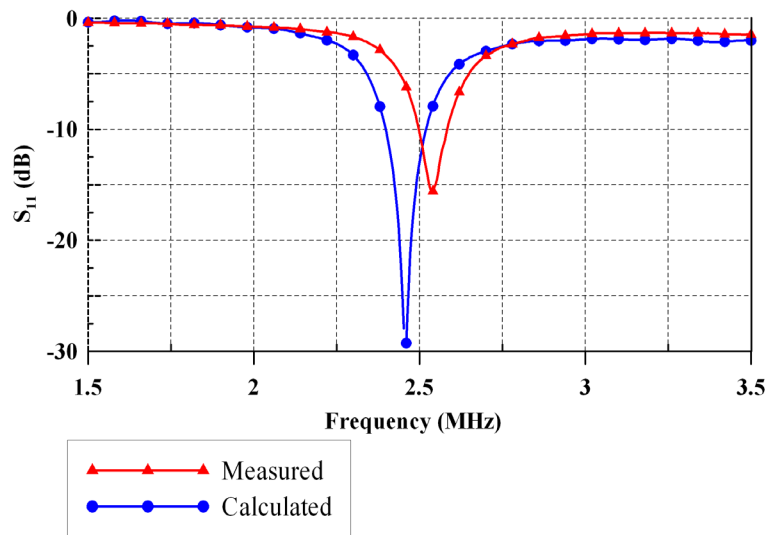


Figure 6.24 Comparison of calculated and measured magnitudes of the input reflection coefficient for the $\lambda/4$ microstrip ISM 2.4 antenna in Fig. 6.23

Using the obtained rigid antenna, the first rough evaluation of the influence of moisture in the fleece substrate was performed. The antenna was completely soaked into water (Fig. 6.25), and the input reflection coefficient subsequently measured. In Fig 6.26, the resonant frequency of the antenna was measured in intervals of 15 minutes, while in the meantime, the antenna was left to dry naturally (according to the setup in Fig. 6.25). It can be seen that the resonant frequency was lowered to 1.46 GHz, and that the resonant frequency shifted upwards almost linearly for each time interval due to the reduction of the amount of water in the

substrate. It can be seen that even after 6 hours, the resonant frequency did not return to the value of the dry antenna. Extrapolating the trend of the antenna drying (Fig. 6.26), it turns out that 5 more hours are needed for the antenna to restore its original resonant frequency. We also note intuitively that the fleece appeared relatively dry when touched by hand after only an hour, which suggests that even low humidity levels significantly affect the antenna properties.



Figure 6.25 Left: Applying water to the antenna; right: measurement setup for wet antenna

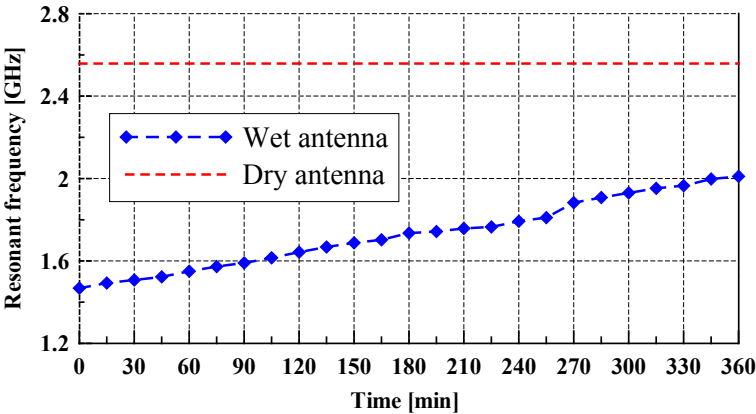


Figure 6.26 Time variation of the resonant frequency of the antenna when the antenna was left to dry naturally

In the next measurement campaign, the water was again applied to the antenna, and the magnitude of transmission parameter (S_{21}) of the wireless link (distance: 1.4 m) with the calibrated horn antenna was measured. To speed up the proces, based on previous experience, a hairdryer was used (Fig. 6.27), while the transmission parameter was measured every 5 minutes. After around 95 min, the fleece was completely dry. The results are shown in Fig. 6.28 for the three typical frequencies in the ISM 2.4 band.



Figure 6.27 Use of a hairdryer as a tool to speed up the measurements

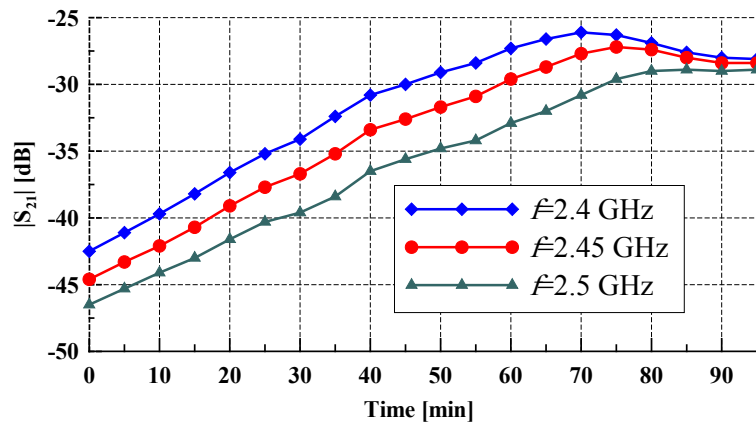


Figure 6.28 Time variation of the transmission parameter for the wireless link with the examined antenna used. The antenna was dried using a hairdryer.

At this stage, we have noted that the presence of moisture has a significant influence on the antenna performance. Therefore, the substrate reduces the performance of the antenna for a long period when exposed to environmental conditions (e.g. rain, snow). The solution to that problem could be to cover the antenna with a thin waterproof superstrate of low permittivity, or to use hydrophobic substrates such as Goretex[®] [1]. As for the measurement method, apart from the phenomenological evaluation, the influence of moisture also needs to be quantified. The improvement of the measurement method is done in section 6.4.3.

6.3.1. Improving the antenna design for the ISM 2.4 band

To improve the ISM antenna design from the previous section, we have first considered reducing the dimensions of the antenna and the ground plane, as well as extending the bandwidth to obtain good signal coverage in the whole ISM 2.4 band (2.4÷2.48 GHz). In addition we sought to replace the feeding from the bottom with feeding from the edge of the antenna, in order to more feasibly conform the antenna and connect the wires and the other electronics to the body.

After optimization in the CST Microwave Studio, a new PIFA antenna design for the ISM 2.4 band was proposed, and two prototypes were manufactured (Fig. 6.29). The antenna dimensions are summarized in Table 6.6 and Fig. 6.30.

The measured magnitude of the input reflection coefficient (S_{11}) is given in Fig. 6.31 for the cases of the antenna in free space and the antenna placed on the human body. Both proposed PIFA antenna prototypes exhibit similar frequency characteristics of input impedance, which means that the chosen design, apart from being straightforward and simple, is robust to construction tolerances. Both antennas are shown to operate adequately in the ISM 2.4 band, both in free space and when placed on the human body. This means that the ground plane is sufficiently large to reduce the influence of the human body on input impedance matching.



Figure 6.29 The prototypes of PIFA antennas for the ISM 2.4 band

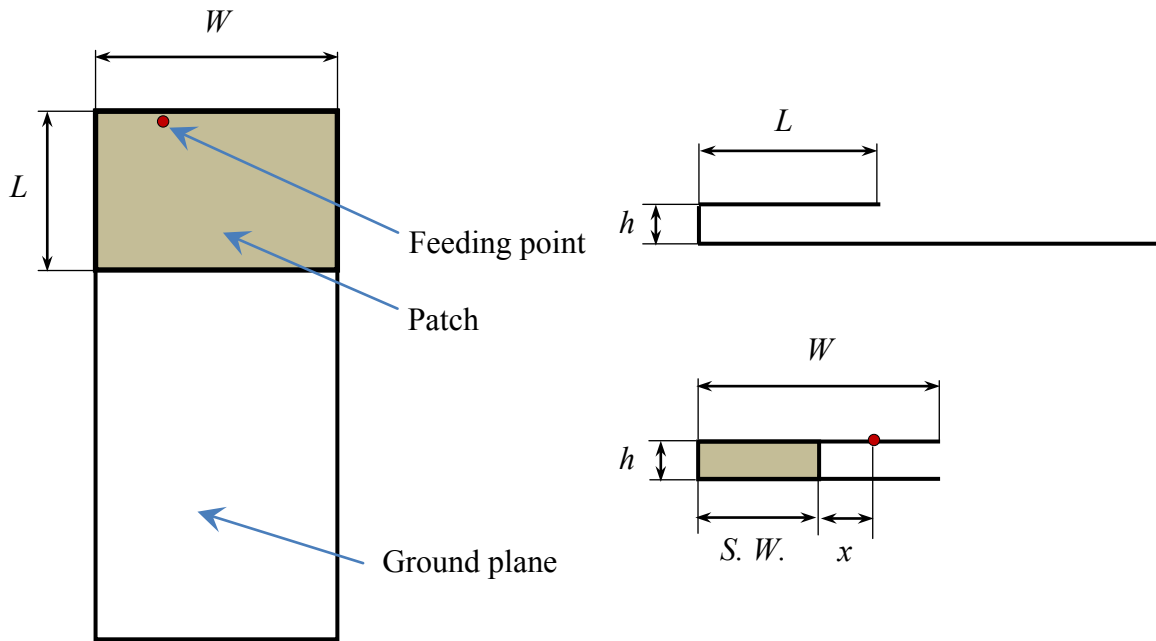


Figure 6.30 Top, bottom and rear view of the proposed PIFA from Fig. 6.29

Table 6.6 Dimensions of PIFA antenna for the ISM 2.4 band

Parameter	Dimensions [mm]
Ground plane size	70×32
Patch dimensions* ($L \times W$)	21×32
Substrate height (h)	4
Shorting wall (S.W.) length	16
Feeding distance from the S.W. (x)	7
* For the realizations with fleece substrate the patch length L was 20 mm	

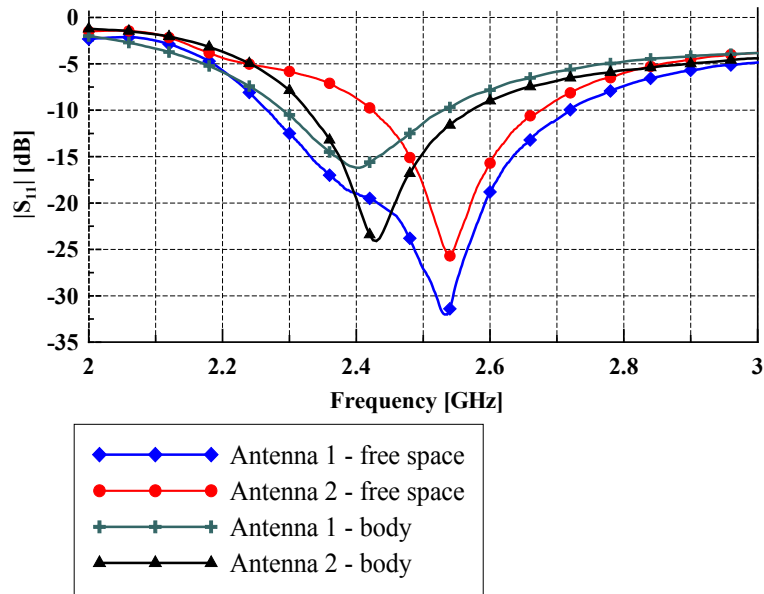


Figure 6.31 Measured magnitude of the input reflection coefficient for the PIFA antenna from Fig. 6.29

The proposed PIFA prototypes were used for measurements of the on-body propagation channel, as described in Chapter 5. They were also used in later sections as prototypes for the full-textile antenna, due to their geometrical simplicity, small dimensions, fair performance and reduced radiation into the body (due to the presence of the ground plane). In the first mentioned application, an air substrate was used, while for the second application, a fleece substrate was considered, and patch length (L) was reduced by 1 mm.

Another concept which was explored in the ISM 2.4 band is the wideband antenna. The idea is to cover a wider band than required, so that the influence of the body and other environmental conditions do not affect its performance. The planar monocone wideband antenna is proposed and characterized in section 3.4.1, where the properties of the human body phantom were studied. It proved to be a promising concept for further investigation, in terms of extending the bandwidth and isolating the antenna (which does not possess a ground plane) from the body using e.g. artificial surfaces, or placing the antenna at a larger distance from the body (e.g. on the outer part of the shirt or jacket).

6.4. Design and characterization of the textile microstrip antenna for the ISM 2.4 band

To systematically evaluate the influence of the presence of the human body and the environmental conditions (mechanical deformations, moisture) in the ISM band, a flexible

microstrip antenna with a reduced ground plane (for improving the bandwidth) was designed and optimized for operation in free space, using CST Microwave Studio. Part of this section was also published in [126].

In the manufactured prototype, the flexible conductive part was obtained using conductive tape, while fleece material (thickness of 4 mm, $\epsilon_r = 1.17$) was used as a substrate. The antenna prototype is shown in Fig. 6.32, while its length and width amount to 54 mm and 50 mm, respectively. The ground plane dimensions are 54 mm by 35 mm. R&S ZVA 40 vector network analyzer was used for the measurements.

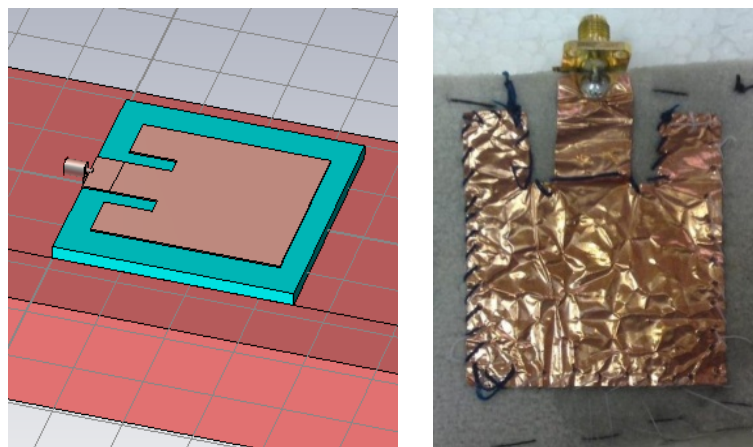


Figure 6.32 The proposed antenna prototype

6.4.1. *The influence of the body*

As a physical model of the human body, the liquid muscle-equivalent phantom already developed in section 3.4 was used. The input reflection coefficient of the antenna was measured in free space and on the body phantom, as well as on the human body of the volunteer (on the clothes and on the skin) in two cases, as shown in Fig. 6.33. The measured magnitudes of the input reflection coefficient are shown in Fig. 6.34. When placed on the body skin, the resonant frequency shifted downwards by 1.9%, which resulted in covering the desired ISM band even better. It can be seen that the results on the human body skin and the phantom correspond very well, while putting the antenna even at a distance as small as the thickness of the clothes already reduces the effect of the body on the antenna. This means that the antenna placed on the skin can be considered as the worst case scenario, so it is useful to exploit it for testing in terms of antenna performance compared to free space, but also in terms

of radiation into the human body, while, in reality (when placed on the clothes), the influence of the body can be even less pronounced.

In another test, the influence of the clothing layers on the antenna performance was investigated. Since the antenna is supposed to be worn e.g. on a T-shirt, it is useful to observe the antenna properties when an additional layer of clothes is put over the antenna. In Fig. 6.35 the comparison of measured antenna gain when the antenna is placed on the T-shirt alone, and when the subject was wearing a thick winter jacket over the T-shirt, is given (a calibrated horn antenna was used for measuring the gain). For the latter case, the gain was reduced by around $1\div 2$ dB. In addition, the case when the antenna was mounted directly on the jacket was also analyzed. It can be seen that the gain in that case improved up to values comparable to free space due to the increased distance from the body. This once again confirms that the antenna should be placed as far from the body as possible, since the influence of the body can thereby be considerably reduced.

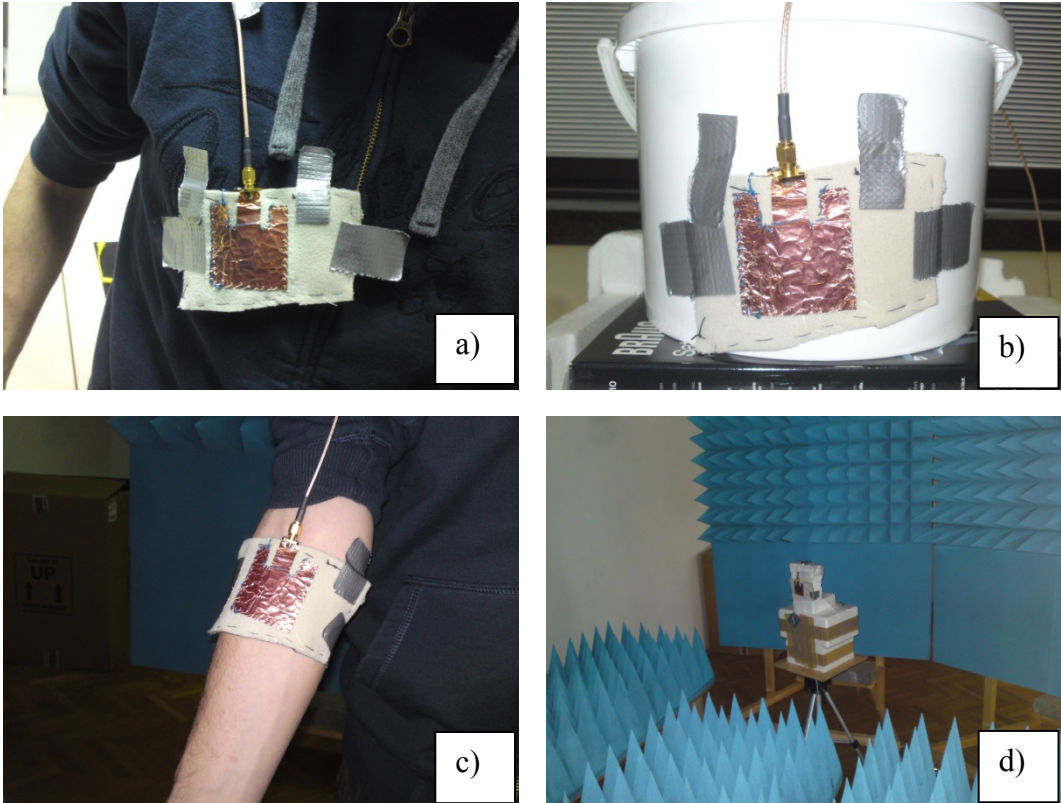


Figure 6.33 Comparing the antenna performance: (a) On the clothes, (b) On the phantom; (c) On the skin; (d) In free space

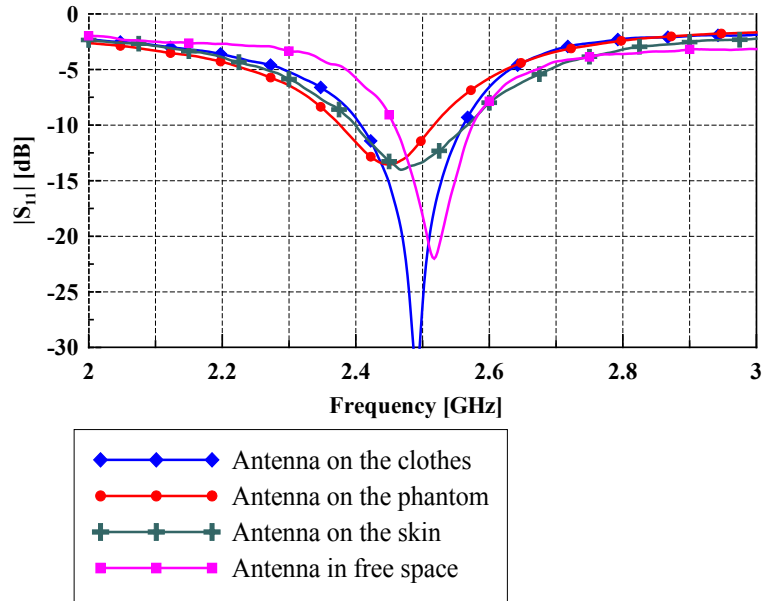


Figure 6.34 Measured magnitudes of the input reflection coefficient

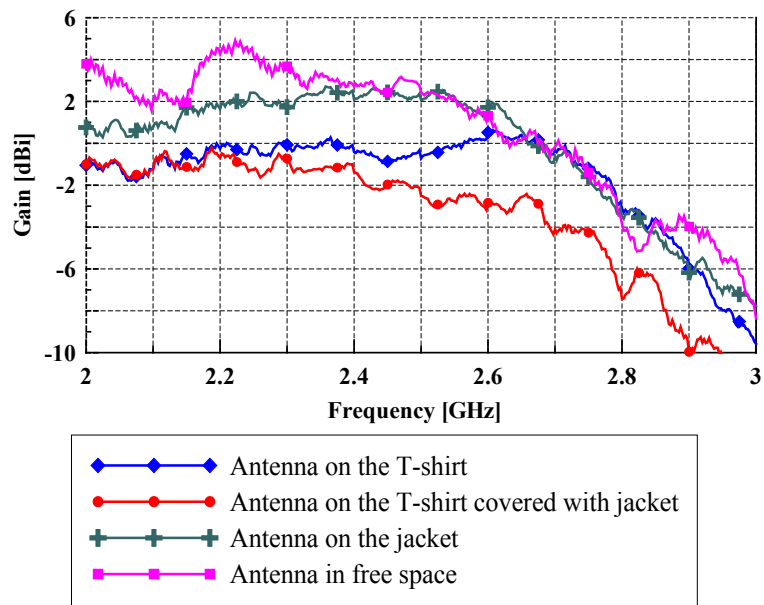


Figure 6.35 Influence of the additional clothing layers on the antenna performance

6.4.2. The influence of bending

When the antenna is mounted on the body, it usually does not remain flat, since the body is a curved shape and, depending on its placement on the body, the antenna is typically bent by some degree. Furthermore, the human body shape is time-varying due to the changes in its positions over time, thus affecting the shape of the antenna on a flexible substrate such as textile. Therefore, the effect of mechanical deformations needs to be checked for the prototype, while bending can be regarded as the most dominant one, and it is hence

established as a standard test, used by the other authors as well [75 – 77]. For measuring the effect of bending, a paperboard cylinder was created, while the radius of cylinder was changed from 2 cm to 6 cm with 1 cm steps. The said range of bending radii is usually encountered when placing the antenna on the human body (e.g. hand or chest). The measurement procedure is basically similar to the one already performed in section 6.2.2, while a slight refinement was made for controlling the bending radius. The examples of setup for measurements of bending in the E - and the H - plane are given in Fig. 6.36.

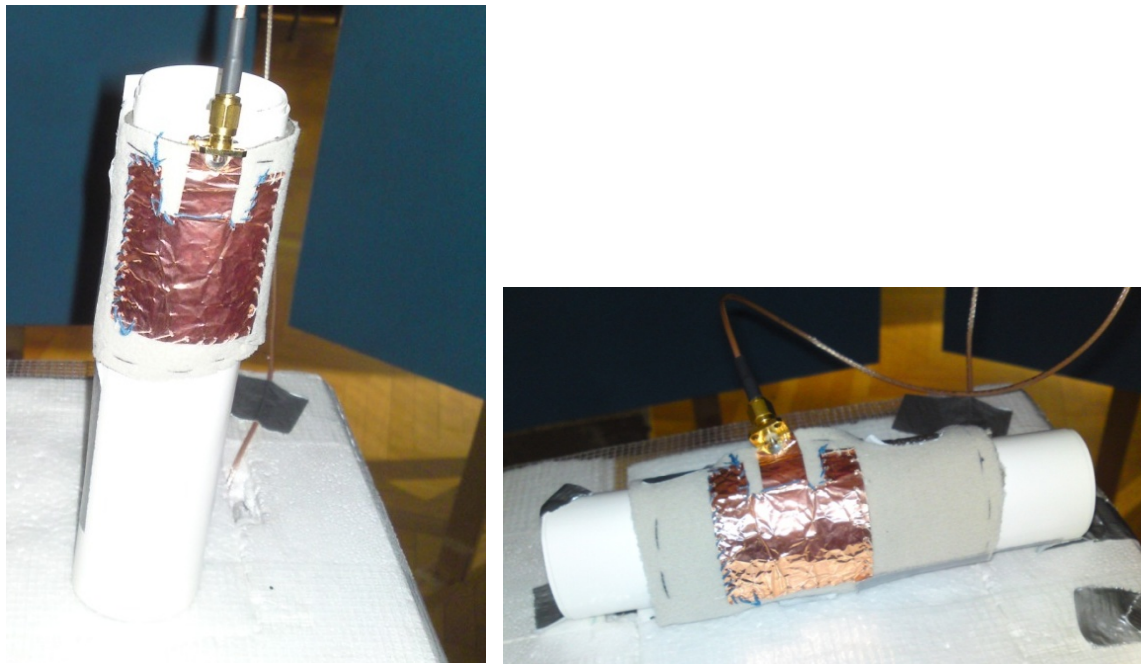


Figure 6.36 Setup for measuring the bending effect in the H -plane (left) and the E -plane (right)

In Figs. 6.37 and 6.38, the measured magnitudes of the input reflection coefficient are shown for different bending radii in the E - and the H - plane. It can be seen that in the H -plane the change in characteristics is barely noticeable for all the considered bending radii, while in the E -plane, the resonant frequency shifted upwards by up to around 4%.

In Fig. 6.39, the measured antenna gain for respective bending radii of 2 cm and 6 cm (the smallest and largest considered radius) is given. Again, it can be seen that the bending in the E -plane has a larger influence on the antenna performance compared to bending in the H -plane, so the placement on the body should be chosen to minimize the probability of bending in the E -plane. The larger effect of bending in the E -plane was also confirmed by other authors (e.g. [75]), and is explained by the changes in the path of the dominant currents.

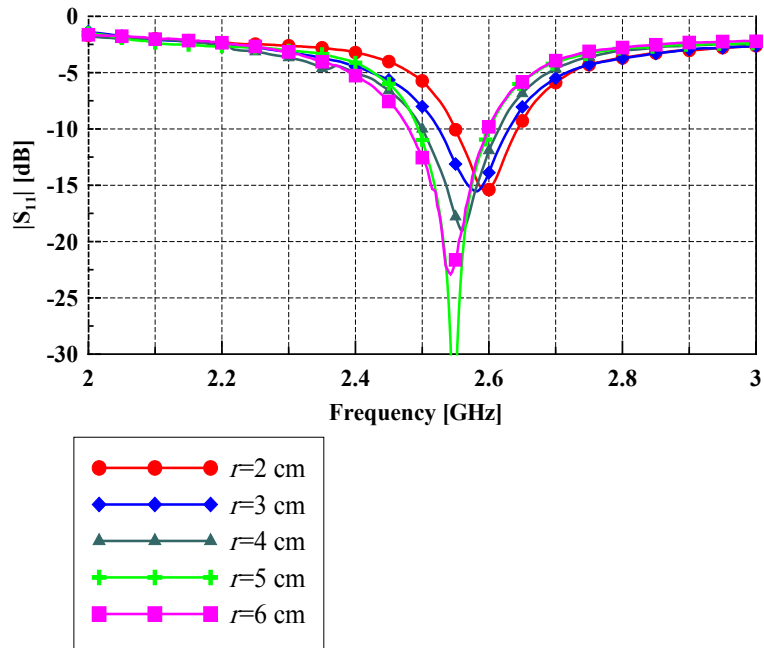


Figure 6.37 Measured magnitudes of the input reflection coefficient (S_{11}) for various bending radii in the E -plane

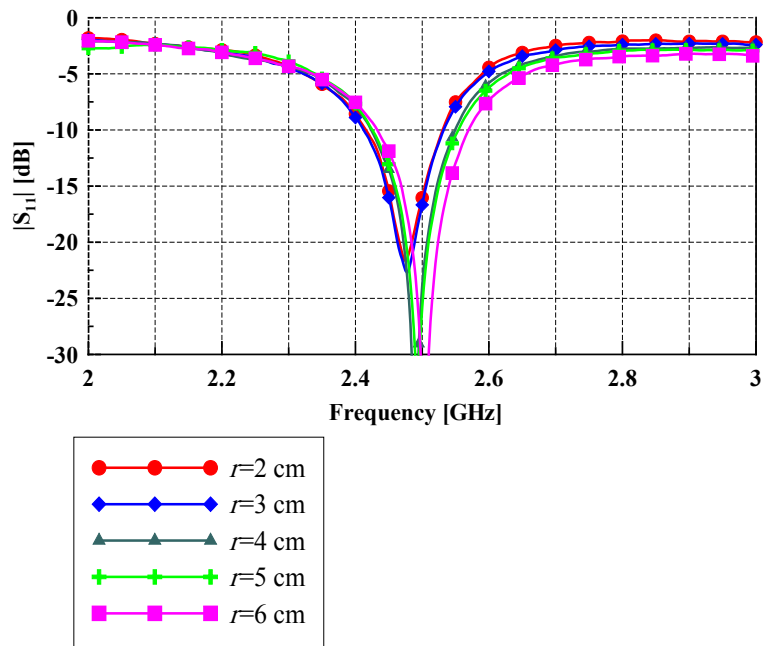


Figure 6.38 Measured magnitudes of the input reflection coefficient (S_{11}) for various bending radii in the H -plane

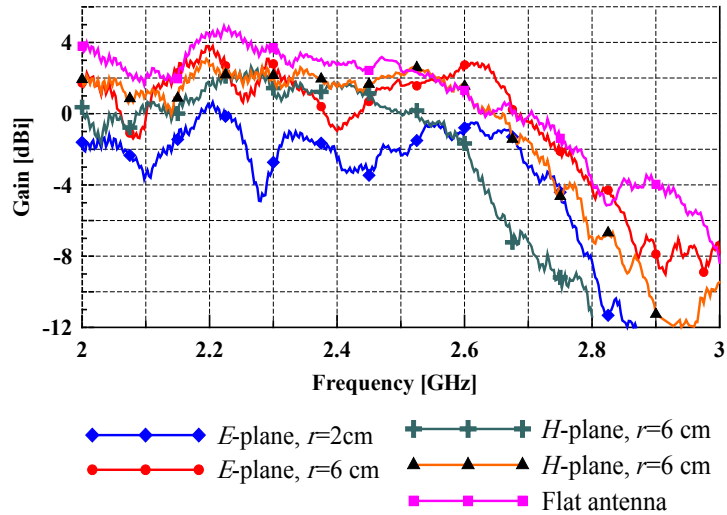


Figure 6.39 Influence of bending on the antenna gain

6.4.3. The influence of the environmental conditions

Apart from the influence of body, the antenna needs to be tested for environmental conditions, such as moisture in the textile substrate. To quantify the influence of moisture, relative humidity as a percentage of water in the total mass of the antenna has been determined. The mass of the antenna was measured using a technical balance with a resolution of 0.01g. The procedure is illustrated in Fig. 6.40, and can be considered a refinement of the procedure described in section 6.3 in terms of providing a quantitative base for the influence of moisture.



Figure 6.40 Measuring the effect of moisture. From left to the right: applying water using a sprinkler; measuring the mass of the wet antenna; drying the antenna with a hairdryer

Firstly, water was applied to the antenna using a sprinkler to achieve a relative humidity of around 50%, which corresponds to the mass of water equal to the mass of the antenna. In continuation of the procedure, the antenna was gradually dried with a hairdryer to speed up the drying process. After each minute of drying, the input reflection coefficient and the transmission parameter of the wireless link between the considered antenna and a calibrated UWB horn (distance: 2m) were measured. The relative humidity was also measured at each “check-point”.

In Fig. 6.41, the magnitude of the input reflection coefficient is given for a few illustrative relative quantities of water. It can be seen that, when the relative humidity is 50% (i.e. the mass of water equals the mass of the antenna), the second-order resonant mode already appears in the observed ISM band. This means that, for some large quantities of water, it is theoretically possible to recover the proper matching in the desired band. Nevertheless, in terms of signal transmission, a larger quantity of water introduces larger losses, so any possible improvement in matching is overridden by losses, and the effect of second-order modes is negligible. For instance, in Fig. 6.42, it can be seen that the transmission in the ISM band is somewhat better for high humidity (50%); however, it is still around 20 dB lower than with the dry antenna.

By analyzing the input impedance matching for various relative humidities, it was also found that the relative humidity in the textile substrate of only around 10% significantly reduces the antenna performance by shifting its resonant frequency downwards, as shown in Fig. 6.43. Thus, the influence of moisture is significant, which means that, for practical uses, the antenna needs to be protected (e.g. by coating with a waterproof superstrate or using hydrophobic textiles such as Goretex[®] instead of nonwoven fabric such as fleece) to be usable in tough weather conditions (e.g. rain, storm) as well.

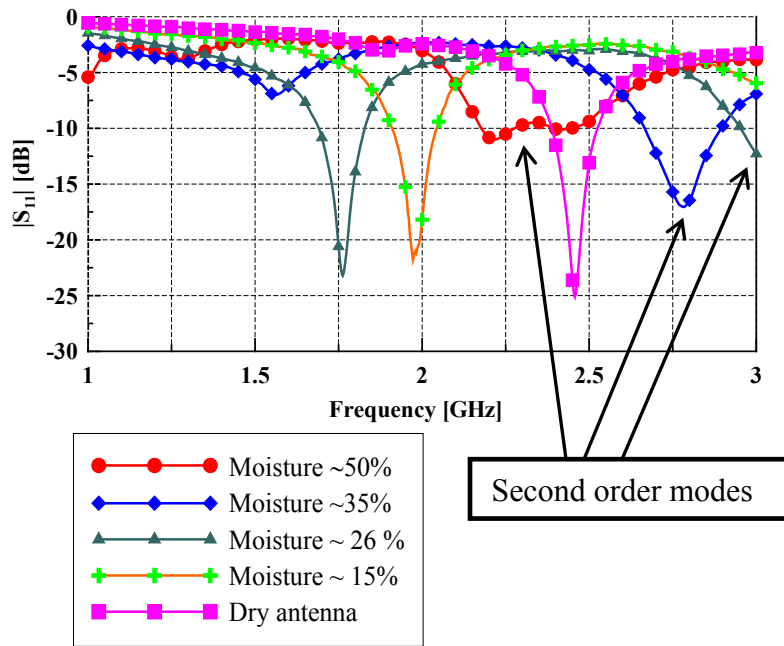


Figure 6.41 Measured magnitude of input reflection coefficient for different moisture contents

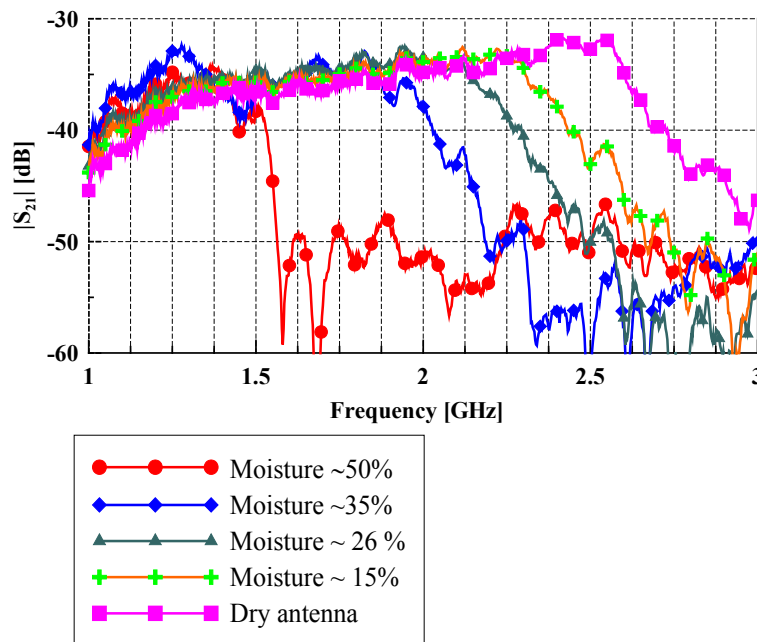


Figure 6.42 Measured magnitude of input transmission coefficient of the wireless link employing the antenna for different moisture contents

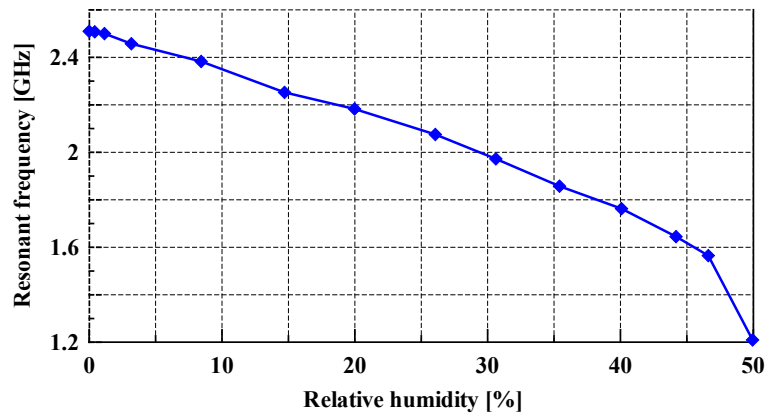


Figure 6.43 Influence of the relative humidity on the resonant frequency of the first-order mode

6.4.4. Antenna under extreme conditions - freezing

To further evaluate the influence of the environmental conditions, we have tested the antenna performance and issues that arise when antenna is put under extreme environmental conditions such as freezing. Such situation can be expected when the antenna is used by rescue teams which operate in harsh environments and needs to be taken into account by which the requirements of the receiver can be specified. The freezing test was inspired by [11], while in the Fig. 6.44 the characteristic moments of the considered procedure are illustrated. The antenna was covered with nylon superstrate to avoid moisturing the substrate and subsequently immersed into the pot with water and frozen. After measuring its parameters the antenna was put in the pot with boiling water for around two minutes, by which part of the ice surrounding the antenna was removed (i.e. the half-frozen antenna was obtained).

The results of measurements are given in Figs. 6.45 and 6.46. It can be seen that the presence of ice resulted in deterioration of the antenna impedance matching while the transmission in the considered ISM band was reduced by 15÷20 dB. When the antenna was completely unfrozen it was observed that water had penetrated into the antenna despite the nylon used as a superstrate (presumably the nylon was not entirely sealed or some holes appeared in the boiling water). The measured relative humidity of the unfrozen antenna was around 50% and the parameters correspond to the ones observed in Figs. 6.41 and 6.42. The performed test nevertheless confirms that the realistic environment can significantly alter the antenna properties while even the protection from moisture itself also needs to be tested in reality and improved if needed.

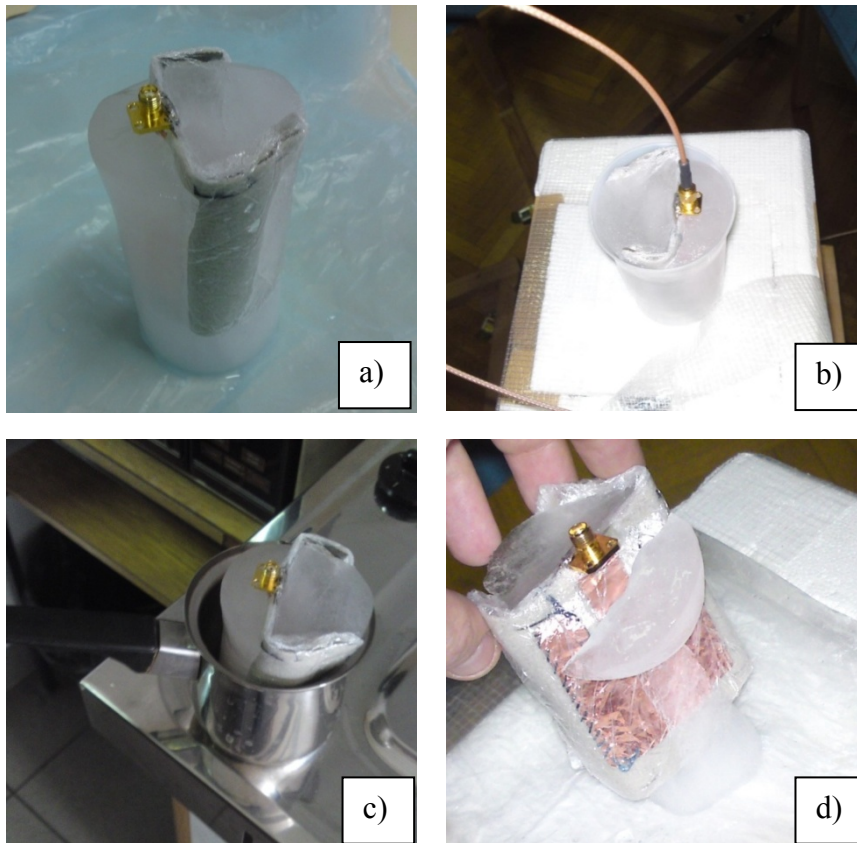


Figure 6.44 (a) Frozen antenna; (b) Measurements on frozen antenna; (c) Thawing the antenna; (d) Half-frozen antenna

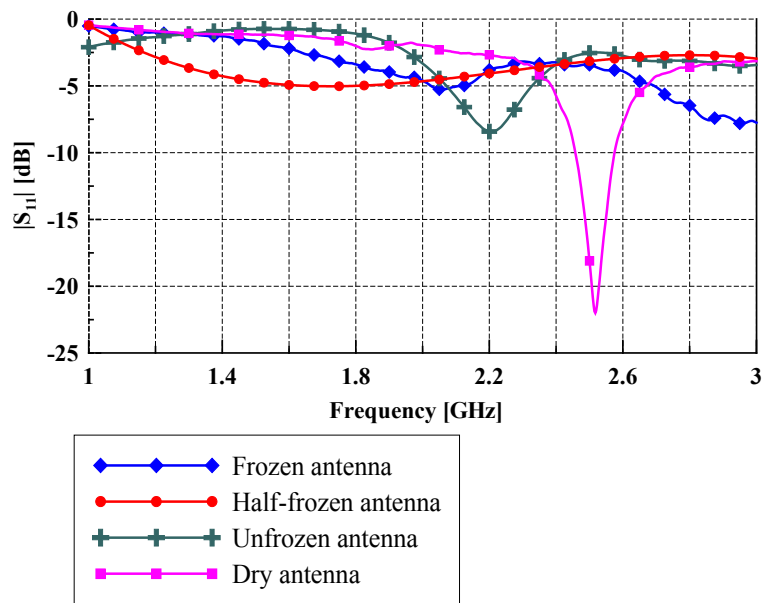


Figure 6.45 Measured magnitude of input reflection coefficient for different freezing levels

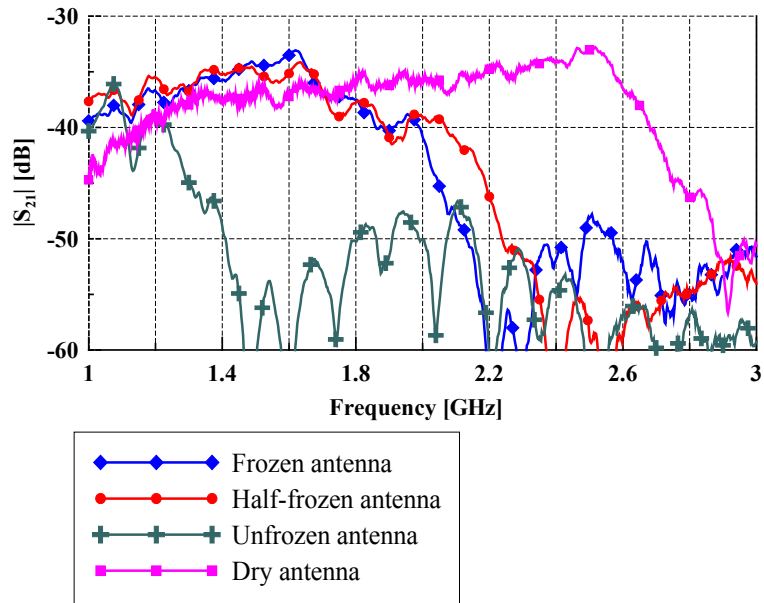


Figure 6.46 Measured magnitude of input transmission coefficient of the wireless link employing the considered antenna for different freezing levels

6.4.5. Comments on the antenna placement on the body

When the influence of various parameters on the antenna properties was evaluated, the antenna was found to perform well in the ISM 2.4 band, and its characteristics remained relatively stable, except from in the conditions of moisture (for which adding a waterproof layer can be considered). Another test consisted of mounting the antenna at three various positions (chest, back, arm) on the human subject, as shown in Fig. 6.47. For each case, the subject (volunteer) was allowed to walk freely outside the anechoic chamber, while the calibrated UWB horn antenna was used to establish a wireless link, thus simulating an off-body realistic link in the multipath environment (the subject was, however, required to remain roughly in the range of the measuring horn antenna to avoid trivial path loss due to the horn).

Similar to the measurements performed in section 5.6, the magnitude of the transmission parameter S_{21} was measured at different times in the process of walking for each off-body wireless link. The time points of measurements were chosen with no particular rule (mostly 30 ÷ 60 s between two measurements) because the process of walking is in itself a random one, so regular time steps would not make any difference. The results are given in Fig. 6.48 for 20 time points, together with the time average of the transmission parameter. The largest average path loss and somewhat smaller variations around the average were observed when the antenna was placed on the back, since it is generally less prone to changing its shape when

a human is walking. Therefore, it can be said that the placement of the antenna on the body also plays a role depending on the desired application.



Figure 6.47 Off-body wireless link for three different positions of the antenna. From left to right: antenna on the chest; antenna on the back; antenna on the arm

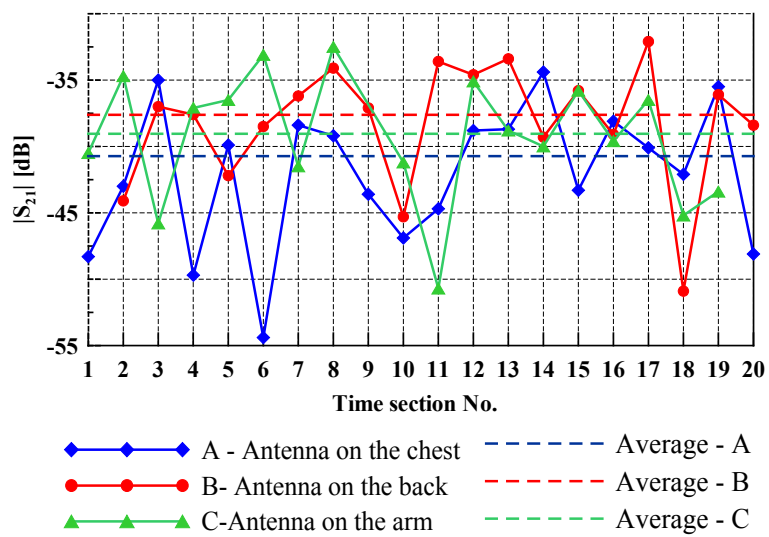


Figure 6.48 Time variation of the three typical off-body links with regard to walking in the room

6.5. Full-textile antennas

The transition to full-textile antennas can be regarded as the next step in the antenna design. By applying textile materials to make the conductive parts, total integration of the antenna into clothes can be achieved. The application of conductive textile fabrics possesses a twofold effect [69]:

- finite conductivity of the textile material
- mixing the conductive and non-conductive threads

The latter is recommended in order to keep the price of the conductive textile lower, but also to keep the “good” mechanical properties of the textile and the functionality of the clothes themselves.

6.5.1. *The preliminary measurements on the textile samples*

In the first stage, we have analyzed the performance of the samples of textile fabrics:

- no-name fabric (industrially made)
- thin metal wire mesh
- composite fabric metal + polyester
- composite fabric metal+cotton
- composite fabric conductive thread +cotton

The considered textile materials are shown in Fig. 6.49, while the data are given in Table 6.7. For the industrial no-name fabric which was also analyzed, there was no data available.

Using the textile materials, the flexible PIFA antennas for ISM 2.4 have been manufactured on a fleece substrate (the design of the PIFA antenna itself is described in section 6.3.1). This antenna has already been used for on-body propagation measurements (Chapter 5). Compared to other prototypes of realized antennas for the ISM 2.4 band described in previous sections, this antenna has the advantage of geometrical simplicity, small dimensions and good overall performance. Thus, it was considered as a benchmark for the full-textile antenna analysis.

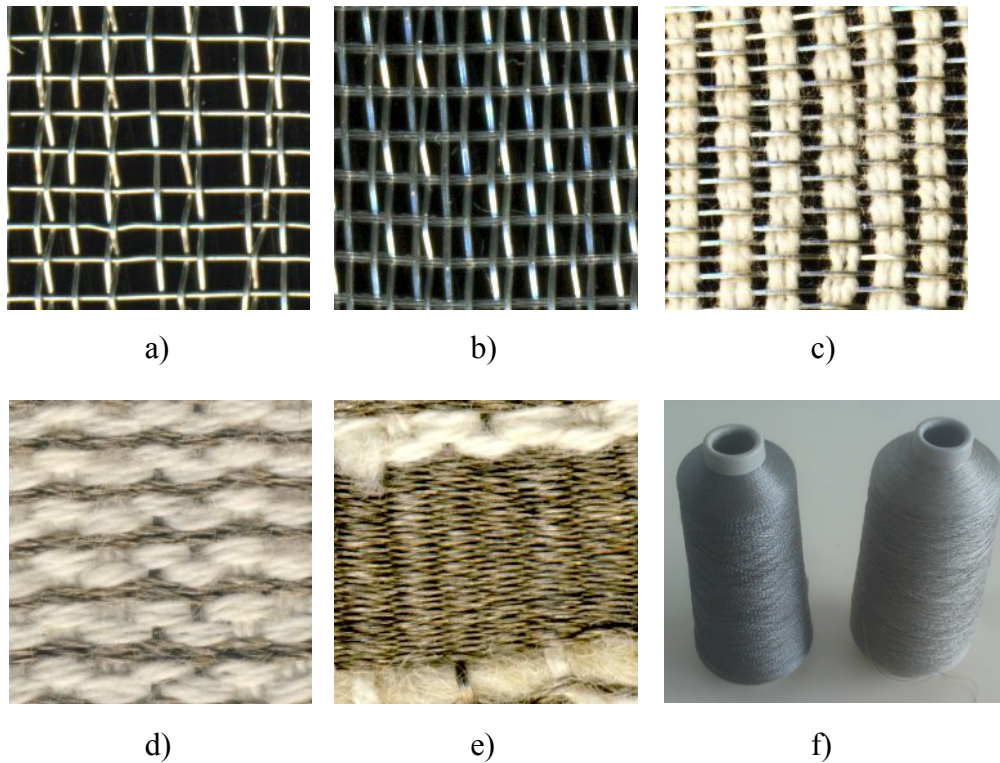


Figure 6.49 The considered textile materials. (a) metal mesh; (b) metal + polyester; (c) metal + cotton; (d) conductive thread+cotton – part 1; (e) conductive thread+cotton – part 2; (f) examples of cones containing conductive threads (i.e. conductive yarns [81])

Table 6.7 Data about the studied textile materials

Material	Warp	Weft	Thread density (fibers/cm)	Capability of direct soldering
Metal mesh	Nickel plated copper	Nickel plated copper	12 (warp); 8 (weft)	Yes
Metal+polyester	Nickel plated copper	Polyester	15 (warp); 8 (weft)	Yes
Metal+cotton	Cotton	Nickel plated copper	6 (warp); 19 (weft)	No
Conductive thread - 1	Periodic- 7 cotton fibers + 1 conductive yarn	Periodic- 4 cotton fibers + 8 conductive yarn	12 (warp); 24 (weft)	No
Conductive thread - 2	Periodic- 7 cotton fibers + 1 conductive yarn	Conductive yarn	12 (warp); 32(weft)	No

The realizations of the full-textile PIFA antennas are shown in Fig. 6.50. Compared to the prototype made of metal plate, the inserted fleece substrate accounted for a reduction in resonant length of 1 mm for the antennas made using textile materials. The feeding was applied by direct soldering where possible, while a small piece of copper tape (mostly around 1 cm × 1 cm) was placed over the textile at the feeding point to enable soldering where direct soldering was not possible. The use of conductive epoxy was also considered; however, it was dismissed in favor of soldering mostly for practical reasons (speed of process and possibility of fast retuning of the feeding point if needed). In addition, the use of conductive epoxy is considered inferior to soldering due to the finite conductivity of the epoxy, and durability in the real environment [18].

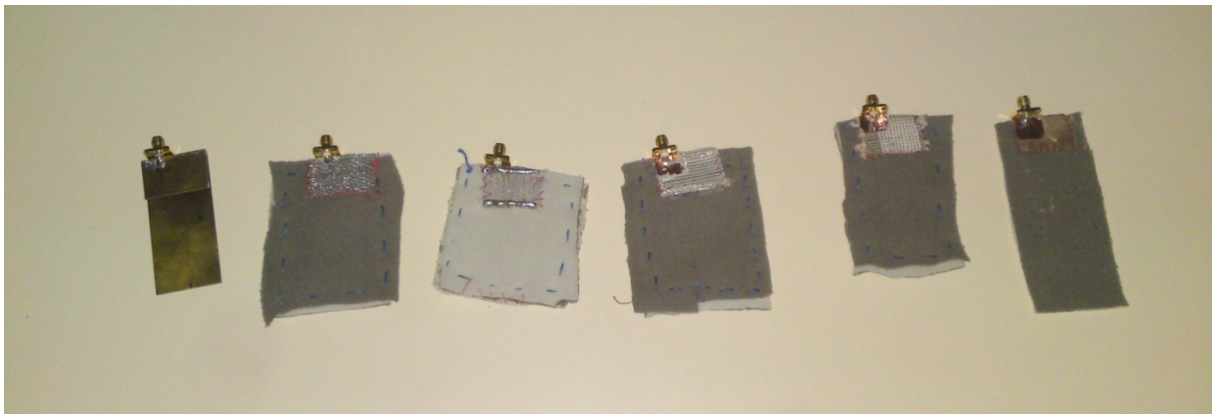


Figure 6.50 The textile PIFA antennas. From left to the right: Prototype, metal mesh, metal+polyester, metal+cotton, conductive thread, conductive fabric

It should be noted that the composite materials metal+polyester and metal+cotton had conductive fibers only across one direction (the orthogonal fibers were made of dielectric). The original antenna realizations using those materials exhibited poor performance, so by soldering and applying the conductive epoxy, the orthogonal conductive direction was artificially created to enable the current flow, as shown in Fig. 6.51. This means that it is not enough to have conductive wires that allow current flow in only one direction (even if they are densely placed), since it closes some current paths in the antenna, thereby deteriorating its radiation properties. After “opening” the orthogonal direction of the current flow, the antennas obtained from both materials in question performed well, as will be shown in the subsequent figures.

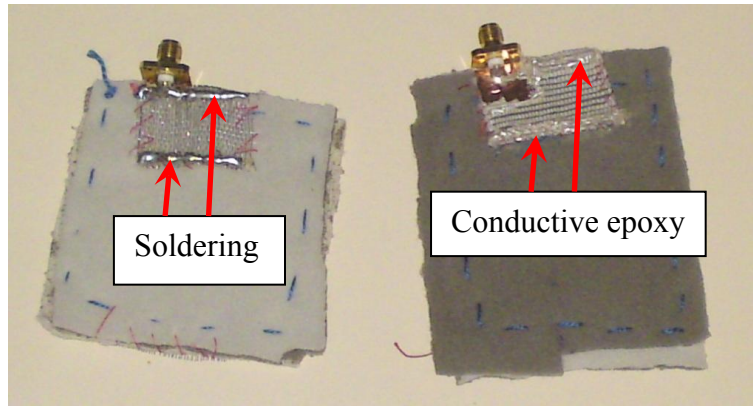


Figure 6.51 Use of soldering and conductive epoxy to enable the additional orthogonal path of the current flow. Left: antenna made of metal+polyester; right: antenna made of metal+cotton

The performance of the obtained antennas in terms of input impedance matching and the transmission parameter for the wireless link with the calibrated UWB horn (distance of 2 meters) is given in Figs. 6.52 and 6.53, respectively. The comparison with the prototype made of metal plate from section 6.3.1 is also given. It can be seen that, except for the no-name fabric, the magnitude of the transmission coefficient (S_{21}) is within 5 dB in the ISM band, compared to the full-metal prototype, which can be considered acceptable for use.

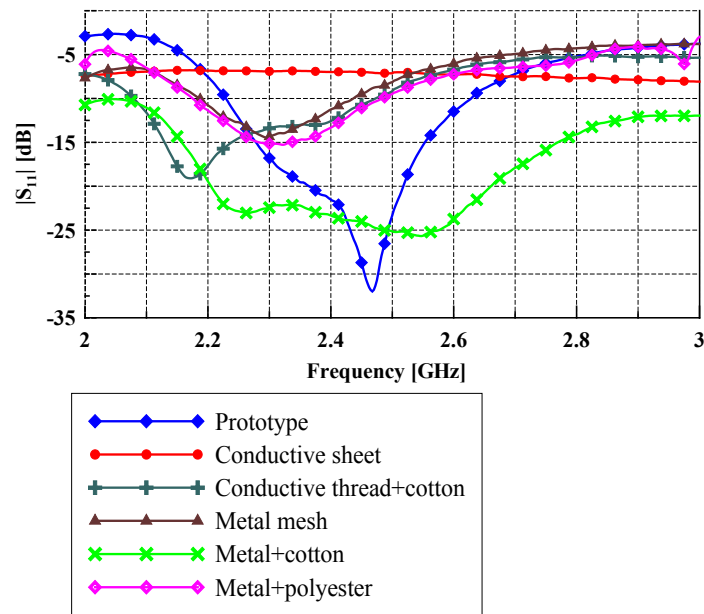


Figure 6.52 Measured magnitudes of the reflection coefficient for various PIFA realizations from Fig. 6.50

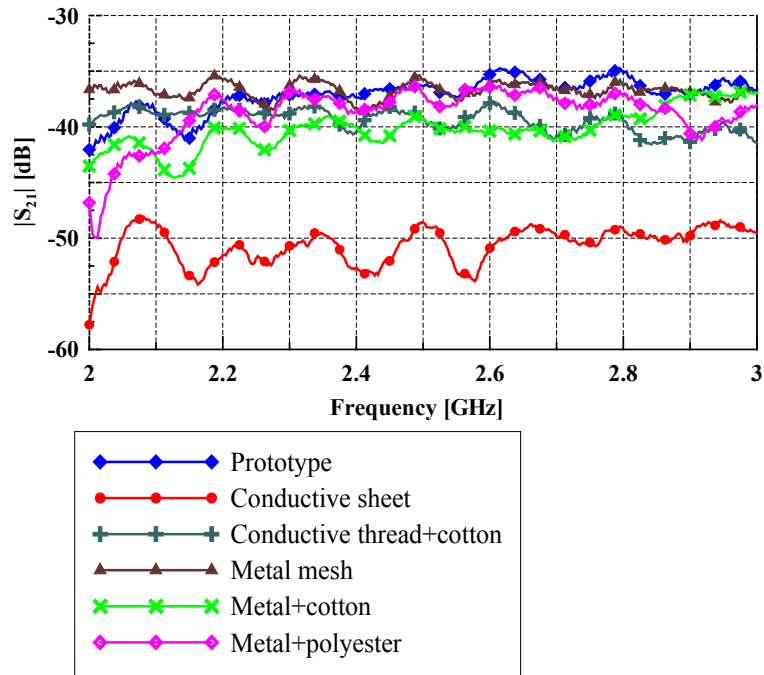


Figure 6.53 Measured transmission parameter between the calibrated UWB horn and various PIFA realizations from Fig. 6.50 at a distance of 2 m

6.5.2. Creating the conductive mesh

From the analysis of the conductive textile materials in the previous section, it was observed that:

- it is possible to obtain a good communication link using the antenna made of conductive threads
- the conductive material needs to be applied both in the horizontal and the vertical direction to ensure the proper current flow in the antenna

These findings gave rise to two questions:

- is it possible to embroider the conductive thread (yarn) into some existing conventional fabric, thus obtaining the mesh that would mimic the conventional conductive material?
- what would be the density of such a mesh which would ensure the proper current flow and antenna operation?

Using embroidering instead of weaving possesses an advantage regarding the simplicity of the process, as well as the retention of the “good” properties of clothes, as already discussed in section 2.5.2.

For evaluating the properties of the conductive textile in CST Microwave Studio, a 10 cm section of the matched microstrip transmission line was drawn from a rectangular mesh of artificially created conductive materials (Fig. 6.54). This mesh represents the conductive threads inserted into some conventional fabric (the permittivity of the fabric was not examined at this point, since it is generally low). The transmission parameter S_{21} was calculated for several conductivity orders of magnitudes (typical for conductive yarns [81]), as well as for different mesh densities.

The simulation results are given in Figs. 6.56 and 6.57. It can be seen that, for the chosen length of microstrip, performance similar to the perfect electric conductor is obtained for the case of full plate for a conductivity of 10^5 S/m. For the conductivity of the order of 10^4 S/m, it can be seen that the mesh densities up to $3\text{ mm} \times 3\text{ mm}$ exhibit path losses within 1 dB, which is considered acceptable for use. In addition, the use of inhomogeneous mesh in two orthogonal directions was also analyzed. As expected, it was shown that the density of the mesh in the direction of the current flow has a larger influence on the transmission (Fig. 6.58). Although the use of inhomogeneous mesh could somewhat reduce the amount of required conductive yarn (and thereby the price), it is still less universal and limited to the structures with the current flow in one dominant direction. Therefore, in this stage, the homogeneous conductive meshes of $2\text{ mm} \times 2\text{ mm}$ and $3\text{ mm} \times 3\text{ mm}$ are chosen for further research as a good compromise between mesh complexity, price and ability to mimic the conventional conductive material.

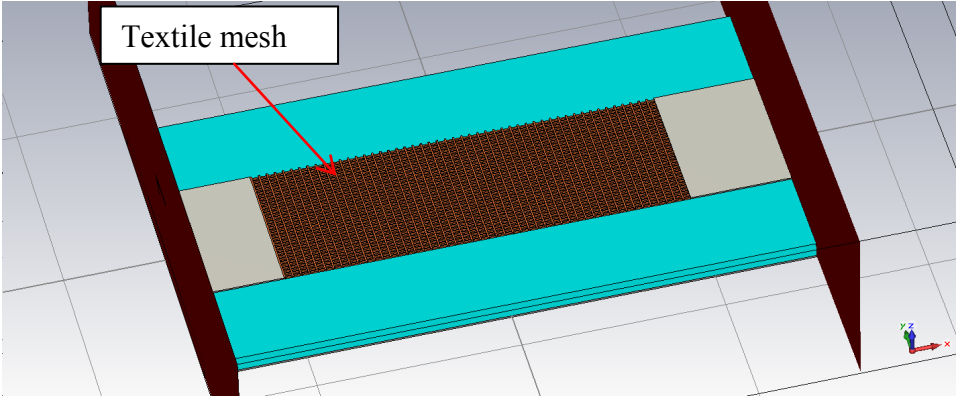


Figure 6.54 Microstrip antenna made of textile mesh (the simulation setup)

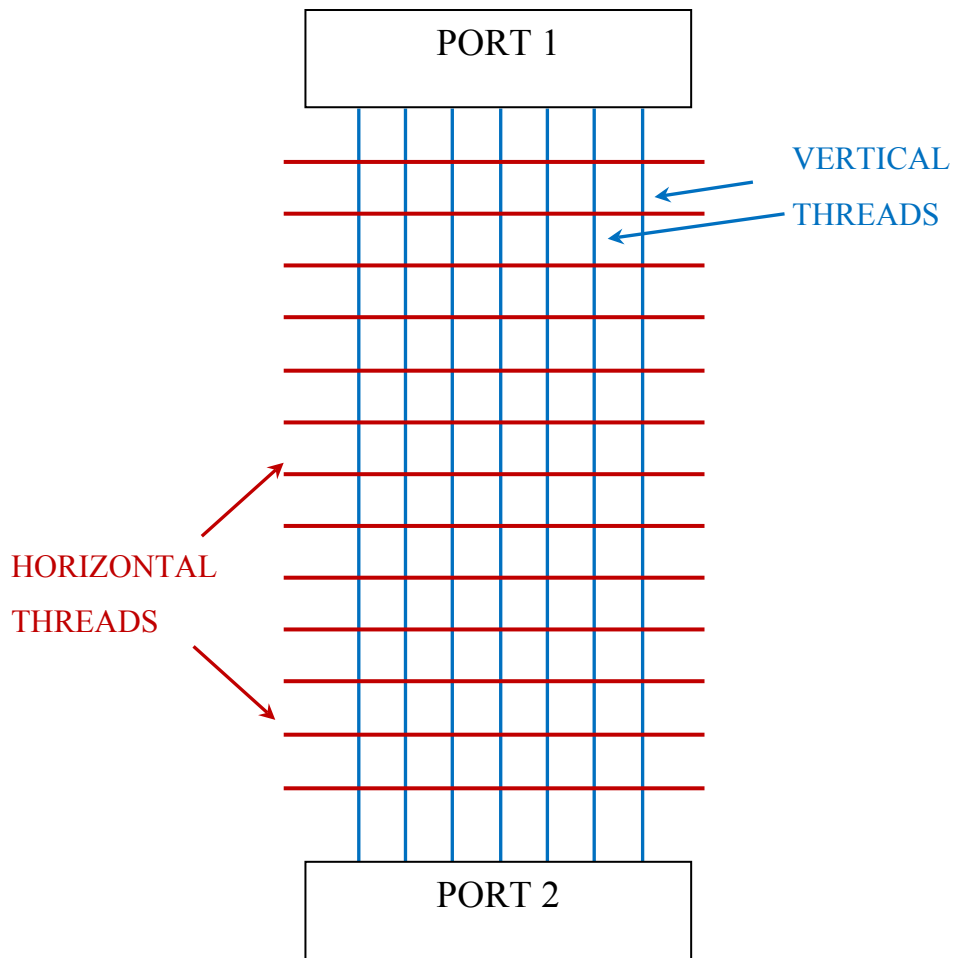


Figure 6.55 Principal scheme of the simulation of conductive mesh

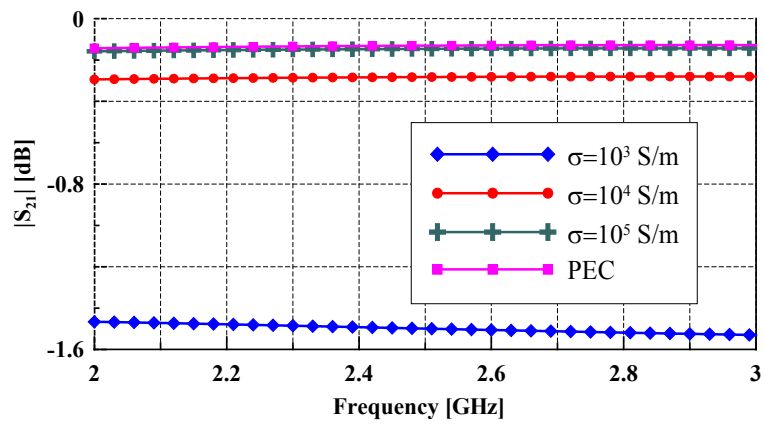


Figure 6.56 Calculated transmission parameter for various conductivities (full plate)

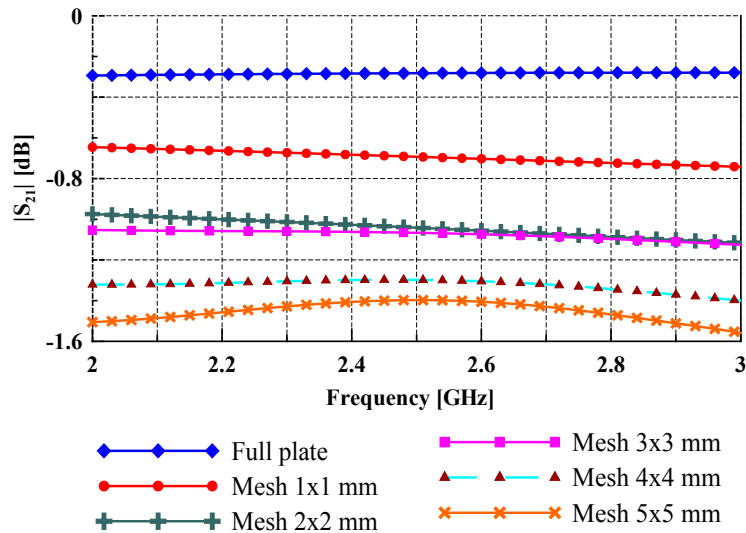


Figure 6.57 Calculated transmission parameter vs. thread mesh densities ($\sigma=10^4$ S/m)

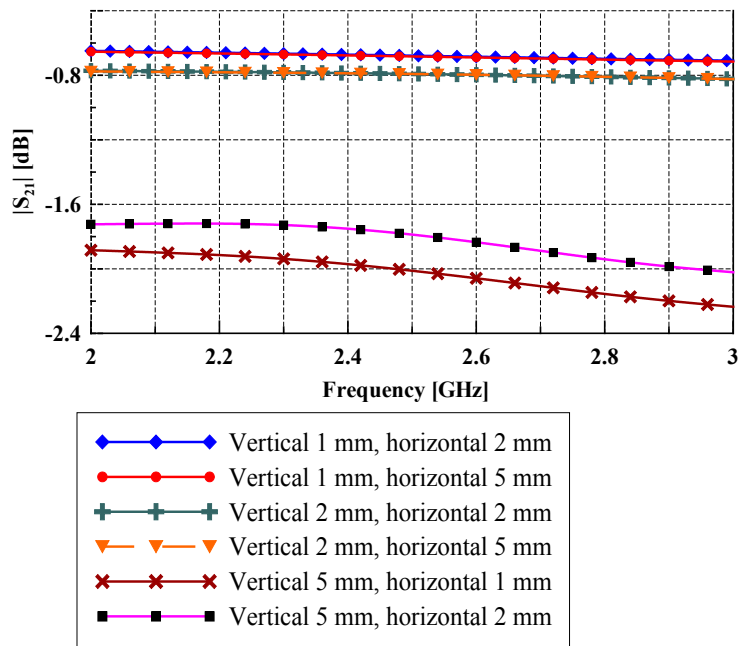


Figure 6.58 Calculated transmission parameter for inhomogeneous mesh (i.e. different distances of threads in two orthogonal directions). The vertical and horizontal direction as defined in Fig. 6.55 ($\sigma=10^4$ S/m).

6.5.3. Realizations of PIFA antennas using embroidered conductive textile mesh

Using a conductive yarn which consisted of silver-plated polyamide ($\sigma \approx 10^4$ S/m) produced by Statex GmbH [81], we have manufactured a 3 mm×3 mm conductive mesh embroidered into cotton, and used it to build a PIFA antenna (of the type described in section 6.3.1). The feed was soldered by applying a small piece of copper tape (dimensions of around 1 cm×1 cm

and 1 cm×3 cm, from the upper and bottom side) over the portion of textile close to the feeding (Fig. 6.59). The copper tape-textile contact was later reinforced by conductive adhesive. The measured input reflection coefficient is shown in Fig. 6.60 at two stages of production. It can be seen that the resonant frequency shifted downwards (compared to the metal plate prototype), so the antenna was cut in length by around 2 mm and retuned again to obtain matching in the ISM 2.4 band. Although the antenna seems to work properly, it needs to be noted that some better arrangements for applying the feeding on textile antenna than copper tape also need to be considered to make the characteristics more stable and the antenna feasible for wear in practice.



Figure 6.59 PIFA antenna from conductive threads of a density of 3 mm × 3 mm – top and bottom view

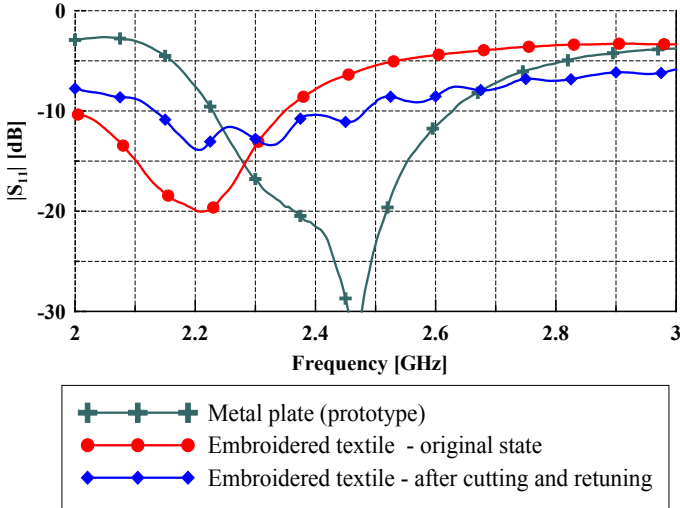


Figure 6.60 Comparison of measured magnitudes of the input reflection coefficient for the metal-plate prototype and considered full-textile PIFA antenna from Fig. 6.59 (two cases)

In Fig. 6.61, two more realizations of PIFA antennas using conductive textile meshes of a density of 2 mm ×2 mm are given, together with the magnitude of the input reflection coefficient (Figure 6.62). The meshes were professionally embroidered into felt (material 1) and cotton (material 2). Note that the cotton was additionally lined from the inner side, so, in effect, the thickness of both textiles was actually similar.

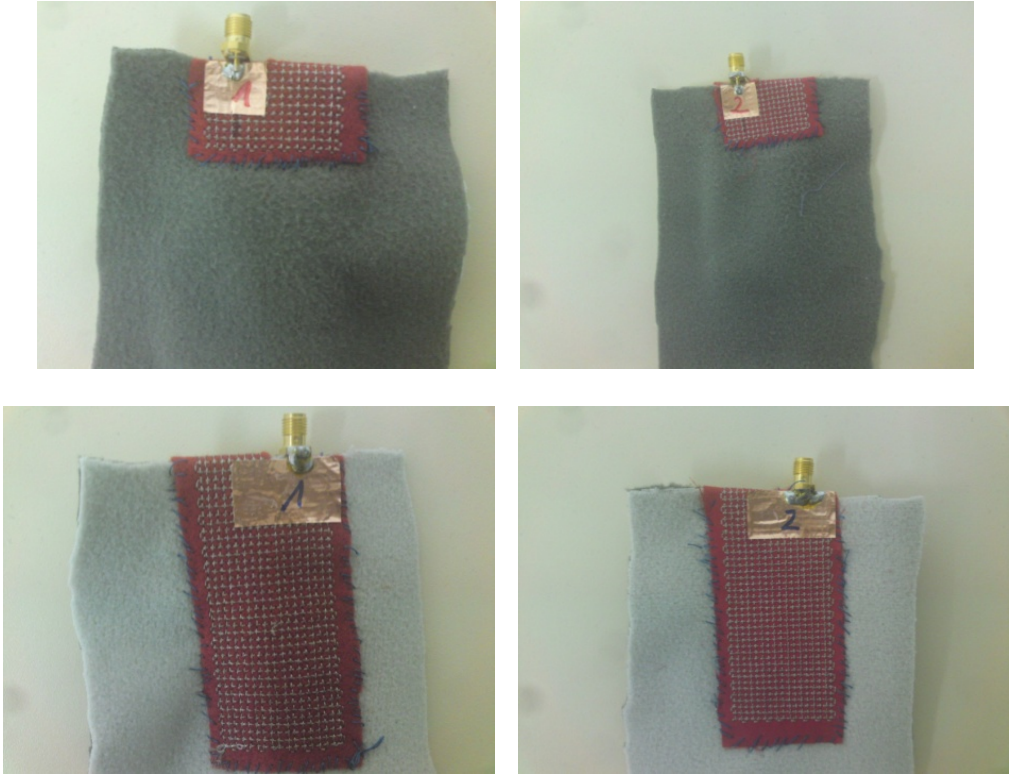


Figure 6.61 Two PIFA antennas created from conductive threads of a density of 2 mm×2 mm – top and bottom view (left: material 1 - felt; right: material 2 – cotton+inner lining)

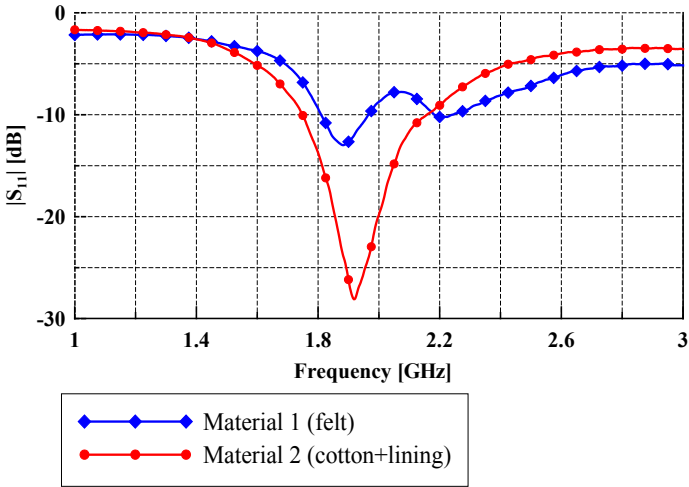


Figure 6.62 Measured magnitudes of the input reflection coefficient for the PIFA antennas of a mesh density of 2 mm×2 mm

6.5.4. Effect of the conductive yarn

From Figs. 6.60 and 6.62, it can be seen that the resonant frequency was lower than the one expected and confirmed by the prototype. For mesh embroidered in cotton, the resonant frequency (with the original dimensions of the PIFA) was around 2.2 GHz, while for mesh embroidered in felt and cotton reinforced by lining, the resonant frequency shifted to 1.9 GHz. To explain such a systematic shift in the resonant frequency for the antenna originally designed for the ISM 2.4 band (the shift was also observed at a smaller scale for the antenna realizations in Fig. 6.52), first we have evaluated the influence of the fabric the conductive threads were embroidered into. In Fig. 6.63, the calculated influence of permittivity of the supporting textile on the resonant frequency is given. For calculations, the PIFA antenna created using a conductive mesh in question was simulated in CST. It can be seen that such influence is rather minor, and that the permittivity of the textile should be around 10 and more to accommodate that shift (which is, of course, unrealistic, since permittivities of textiles at microwave frequencies are usually low, according to the results from section 6.1 and Table 2.3).

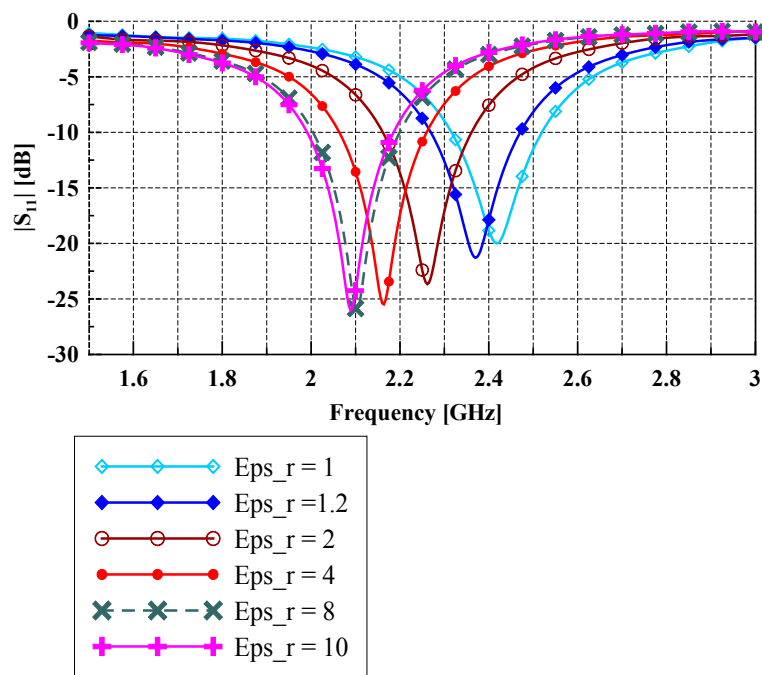


Figure 6.63 Influence of the permittivity of the host fabric for embroidered mesh onto the antenna resonant frequency

Another mechanism which could possibly explain the shift in frequency is the effective length of the yarn itself. Namely, when embroidered into fabric, the yarn does not follow a straight

line, but the actual path is of the “zig-zag” type, one actually needs to take more yarn in the embroidering process in order to obtain a desired length of a line on the surface. This could extend the current path and make the antenna appear larger.

To study the influence of cotton, we have embroidered a few lines of different lengths into the used felt material and denim (which possesses similar thickness as cotton) using a similar sewing pattern to the one used on the antennas. In that way, we have measured the actual length of the yarn which needs to be used to obtain the desired length on the surface of the fabric. The results for the two materials used are given in Tables 6.8 and 6.9. It can be seen that the length of yarn used is around 10% and 15 % higher for the cases of denim and felt, respectively. This way, the dominant mechanism causing the downshift in the antenna resonant frequency when the embroidered conductive yarn was used could be explained.

Table 6.8 Statistics – felt (thickness: ≈ 1.1 mm)

Length of line on felt surface[cm]	Length of used yarn [cm]	Extension of length [cm]	Extension of length [%]
3.6	4.1	0.5	13.89
5	6	1	20.00
5.7	6.6	0.9	15.79
6	6.8	0.8	13.33
6.5	7.5	1	15.38
7	8.1	1.1	15.71
8	9.2	1.2	15.00
9	10.4	1.4	15.56
11.5	12.8	1.3	11.30
Average extension: 15.11 %			

Table 6.9 Statistics – denim (thickness: ≈ 0.85 mm)

Length of line on denim surface[cm]	Length of used yarn [cm]	Extension of length [cm]	Extension of length [%]
5	5.5	0.5	10.00
5.7	6.4	0.7	12.28
6	6.5	0.5	8.33
7	7.8	0.8	11.43
8	8.6	0.6	7.50
Average extension: 9.91 %			

6.5.5. The feeding issue

The antenna, of course, needs to be connected to the outer circuit. Since direct soldering of the textile is impossible for most textile materials, other feeding arrangements have been considered so far, such as applying conductive epoxy or using a small piece of copper tape. To obtain a more realistic and stable transition from the coaxial cable to the antenna, the idea of using metal parts of clothes, such as buttons or rivets, has arisen. To explore the possible additional influence of a button onto the antenna resonant properties, we have manufactured three sections of a microstrip line and measured the input reflection coefficient (S_{11}) and transmission parameter (S_{21}). The microstrip lines were made on a fleece substrate with a thickness of around 4 mm. The length and width of each line amounted to 9.2 cm and 2 cm, respectively. The considered cases are:

- a microstrip line section with a classic soldered feeding
- a microstrip line section with the feeding soldered via a metallic button
- a microstrip line section on a conductive textile mesh of a density of $3 \text{ mm} \times 3 \text{ mm}$ embroidered in denim, where the feeding was soldered via a metallic button (the button itself was hand-sewn into the denim using conductive thread)

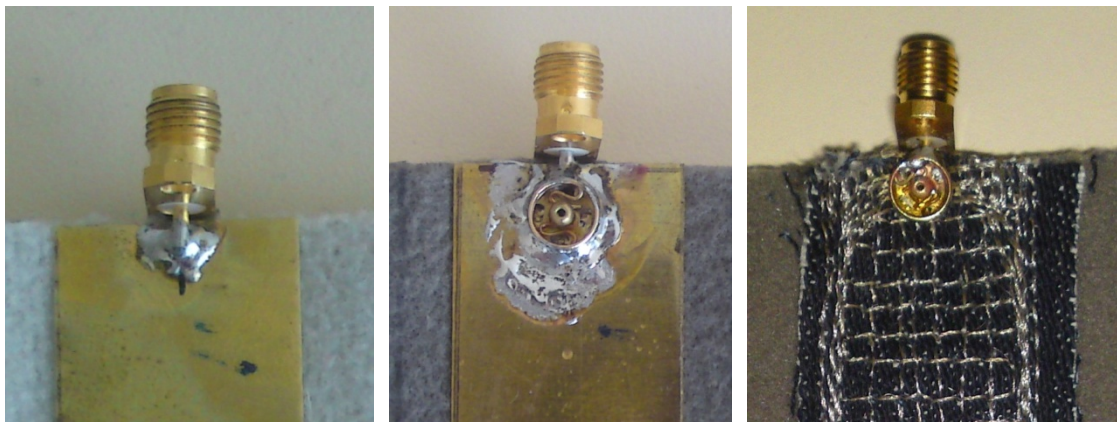


Figure 6.64 The considered microstrip line sections used for evaluating the influence of the button in the feeding. From left to the right: full plate-no button; full plate-with button; textile mesh – with button

The measured scattering parameters are shown in Figs 6.65 – 6.68. It can be seen that the presence of the button exerts only a little influence on the reflection and transmission, both in terms of magnitude and phase. In addition, it was demonstrated that, when the feeding was applied that way onto the textile, the magnitude of the transmission parameter across the line is acceptable and in accordance with the results predicted for such a mesh density (Figure

6.57). This means that the button serves as a good mediator between the coaxial feeding and the textile. In addition, the use of a button possesses esthetical value as well, since it is usually found on regular clothes and, as such, can be made unobtrusive.

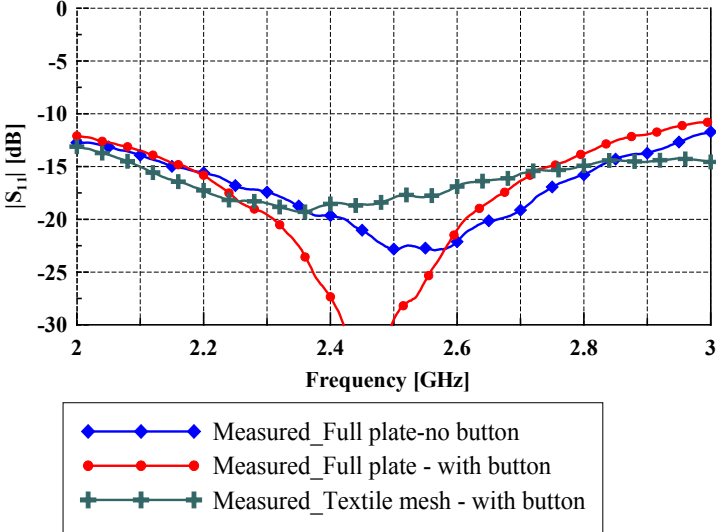


Figure 6.65 Comparison of the performance of the considered microstrip line sections – magnitude of the input reflection coefficient

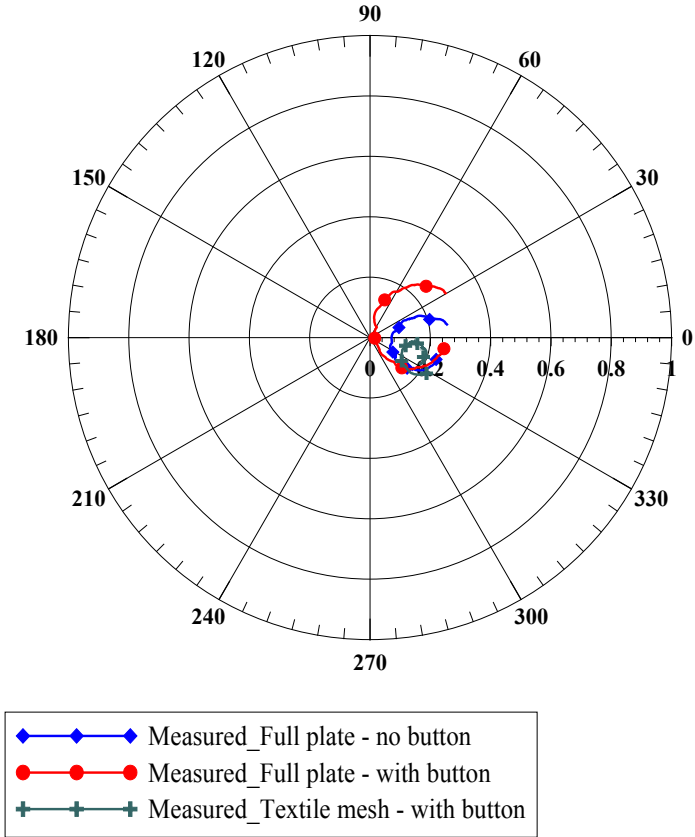


Figure 6.66 Comparison of the performance of the considered microstrip line sections – polar plot of the input reflection coefficient

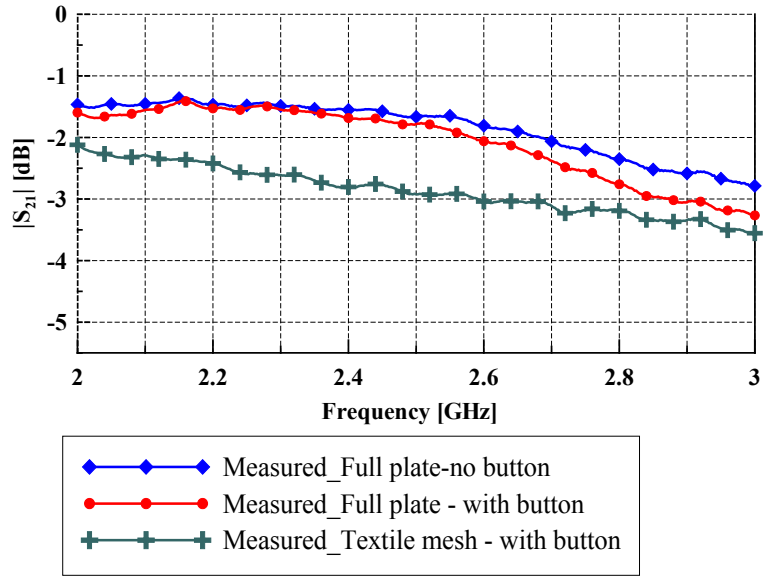


Figure 6.67 Comparison of the performance of the considered microstrip line sections – magnitude of the transmission coefficient

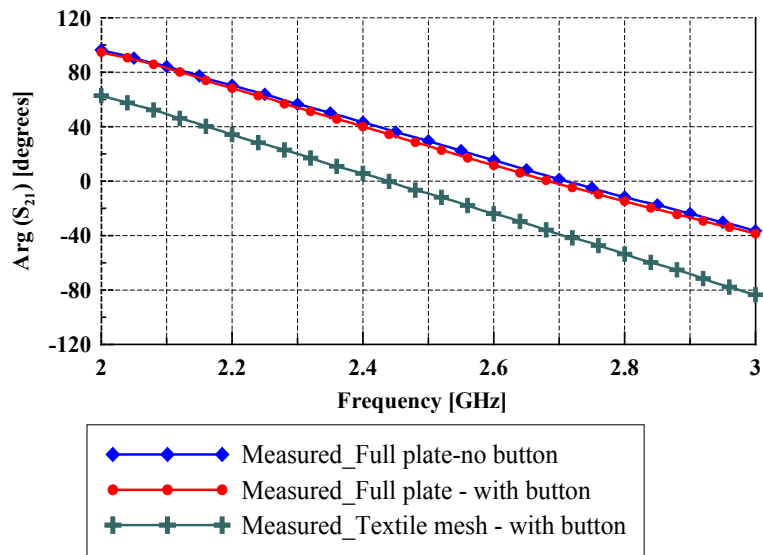


Figure 6.68 Comparison of the performance of the considered microstrip line sections – phase of the transmission coefficient

6.6. A practical strategy for the wearable antenna design

In this section, we apply the findings of the previous sections and chapters in order to design and characterize a full-textile PIFA antenna for the ISM 2.4 band. In the flowchart given in Fig. 6.69, the observed issues and the proposed process of the antenna design for wearable applications is outlined. This strategy is based on the research and analysis of several prototypes, and the analysis of the common issues, i.e. the behaviour of the antenna when the

human body is present, the influence of the supposed environment, and the peculiarity of the suitable materials. In that sense, the addressed issues are rather general, and can be used as a strategy in the design of wearable antennas. Here are some remarks regarding the strategy given in Fig. 6.69:

- Using free space for the initial design considerably reduces the computation time [32], enables better comparison between simulated and measured results, excluding the interference of the human body (which is a dynamic medium that is modeled using approximations), and does not extend the bandwidth by radiation into the human body.
- The obtained prototype should possess adequate input impedance matching, both in free space and when placed on the human body. The modifications in the original design should also account for the properties of the used textile substrate.
- The most critical influence of the human body on the antenna appears when the antenna is placed directly on the skin. When layers of clothes are present, this effect is less pronounced. Furthermore, the use of the ground plane of adequate size is in most cases sufficient for reducing the interaction between the antenna and the human body.
- The influence of bending can be reduced by using more rigid textile substrates. Nevertheless, a compromise should be made since too rigid substrates are uncomfortable for wear. The placement of the antenna on the body can also have an effect on the bending influence (as discussed in section 6.4.2).
- Another way of reducing the effect of the human body is to extend the bandwidth of the antenna beyond what is desired, so that the central frequency of the antenna has some “freedom” to move without affecting the desired bandwidth.
- Using conductive textiles in antennas, instead of conventional conductive materials (copper plate or copper tape), adds another layer of uncertainty (finite conductivity, anisotropy, effective yarn length) to the design, so the original prototype should be modified in accordance to the properties of the textile material used.

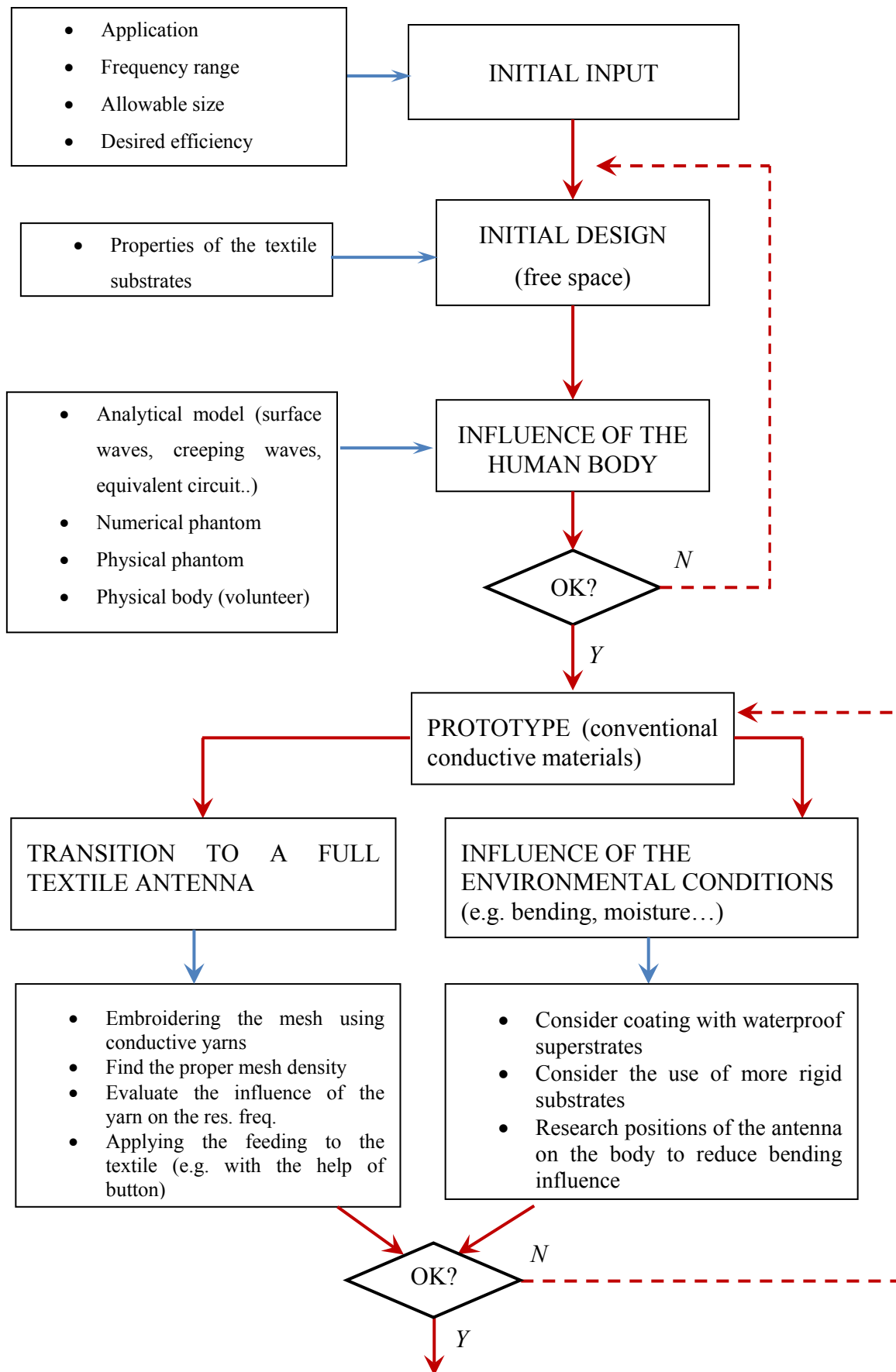


Figure 6.69 The proposed strategy for the design of wearable textile antenna

According to the observed issues in the transition to a full textile antenna, we have designed a full-textile PIFA antenna for the ISM 2.4 band. The prototype of the antenna was proposed in section 6.3.1, while several realizations of the same antenna have been manufactured during the search for a simple and aesthetically acceptable textile structure that could both serve as part of clothes, and retain a large enough conductivity to enable the good radiation properties of the antenna.

As already mentioned, the PIFA prototype was first built on an air substrate and characterized in section 6.3.1. To account for the influence of the fleece substrate, the patch length was reduced by 1 mm. For the construction of the conductive part of the antenna, different textile materials, obtained by the process of weaving and embroidering, were researched. Embroidering the mesh using conductive threads (yarns) into an existing fabric was found to be the most appealing solution which could mimic the homogeneous conductive material at microwave frequencies. In addition, other practical issues have been researched:

- the extension of the current path since the yarn does not follow a straight line when embroidered into textile
- the transition between textile material and coaxial feeding that would operate properly and remain aesthetically acceptable. As a possible solution, the use of a metallic part of clothes, such as buttons, was explored, and demonstrated to operate properly.

In Fig. 6.70, the proposed full-textile version of the PIFA antenna is shown. The antenna was built on a fleece substrate, while the conductive mesh of a density of $3 \text{ mm} \times 3 \text{ mm}$ was sewn onto a denim host using a sewing machine. The mesh was reinforced at the edges by sewing additional layers of yarn (to enable more current paths in that area, since the dominant current densities reside on the edges). The metallic button (radius: 3 mm; height: 2.5 mm) was sewn by hand onto the denim host at the supposed place of the feeding point using conductive thread. The SMA coaxial adapter was subsequently soldered onto the button. The dimensions of the realized PIFA are given in section 6.3.1 (Table 6.6) – the only alteration compared to the prototype is the reduction in patch length of 1 mm to account for the fleece substrate.

As already suggested in sections 6.5.3 and 6.5.4, the resonant frequency of the PIFA antenna with the original dimensions of the patch ($20 \text{ mm} \times 32 \text{ mm}$) shifted downwards to around 2.1 GHz (instead of 2.4 GHz, for which the prototype dimensions were optimized), as shown in Fig. 6.71. Therefore, the dimensions of the patch (supposed to be the dominant part regarding antenna resonance) needed to be reduced. The reduction was done fully experimentally, by a cut-and-try method (i.e. one by one layer of yarn was ripped off), and with the general idea

that the currents on the patch flow both in the horizontal and vertical directions. To reduce the current path (and thereby raise the resonant frequency), the yarn was iteratively removed in each direction until the ISM 2.4 band coverage was measured on the network analyzer. The mesh was again reinforced at the edges by hand-sewing additional yarn. Note also that, to reduce fluctuations and instability in the measured input reflection coefficient, the denim needs to be firmly sewn onto the fleece.

The comparison between old and new dimensions is given in Table 6.10. The simulations were performed in CST Microwave Studio for the full-plate PIFA of the original and new dimensions of the patch obtained by experiment. According to simulations, for the full plate antenna with reduced dimensions, the resonant frequency would have shifted above the desired ISM 2.4 band. The comparison between the measured and calculated magnitudes of the input reflection coefficient for all the relevant cases is given in Fig. 6.71.



Figure 6.70 The full-textile PIFA antenna (original size). Left: top view (patch); Right: bottom view (ground plane)

Table 6.10 Comparison of patch dimensions before and after tuning (ripping off the yarn)

	Original dimensions [mm]	Dimensions after tuning [mm]
Patch length (L)	20	16
Patch width (W)	32	30

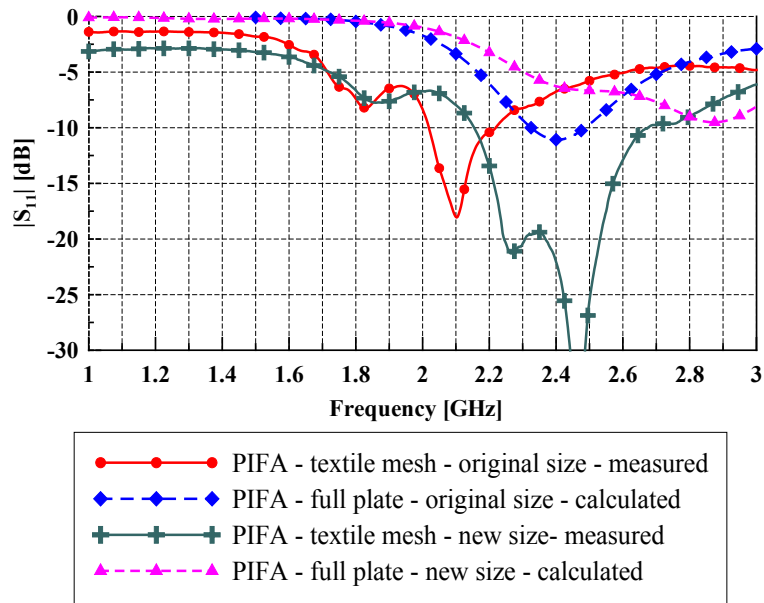


Figure 6.71 Comparison of simulated and measured magnitudes of input reflection coefficient for PIFA antenna before and after changing the dimensions of the patch

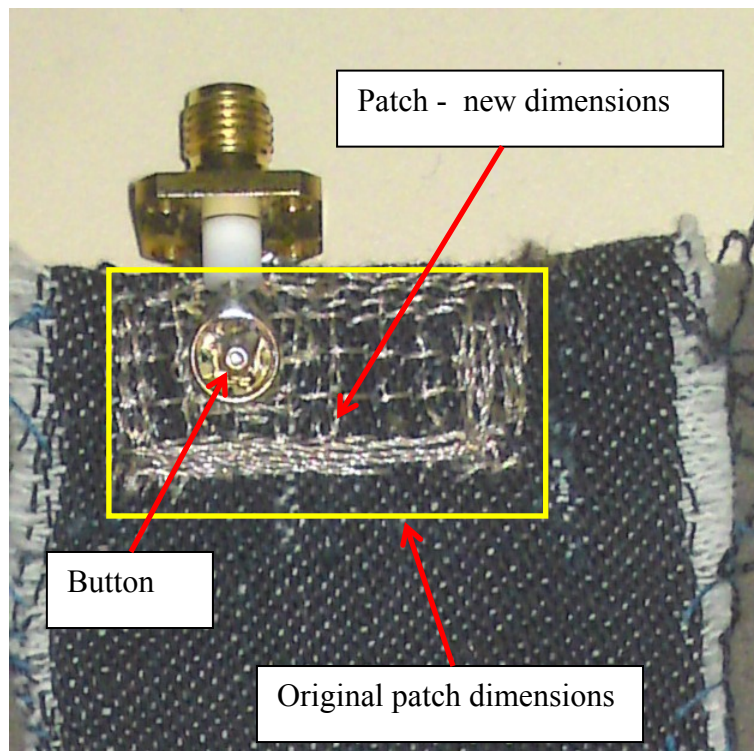


Figure 6.72 The patch after tuning to raise the resonant frequency

6.6.1. Comments on the current density and the effective length of yarn

To analyze the reduction in the size of the patch that was obtained experimentally (Fig. 6.72), we have plotted the current density distributions, calculated in CST Microwave Studio, on the patch (made of metallic plate). The textile mesh is required to mimic the current distribution on the homogeneous plate. From Figs 6.73 and 6.74, it can be seen that the dominant currents flow along both edges (hence the additional yarn added on the edges), leading to the resultant diagonal direction which determines the resonant length.

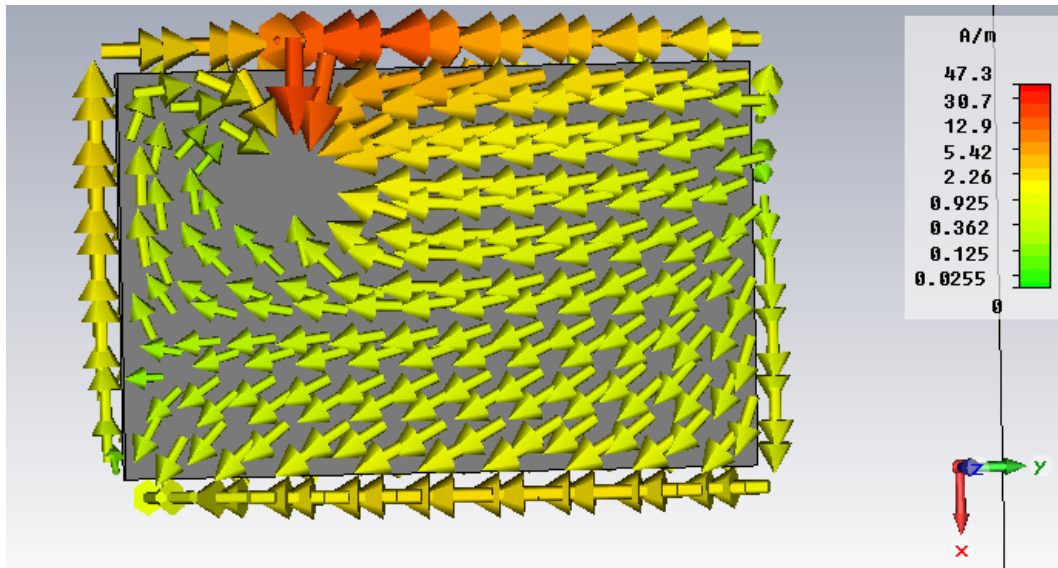


Figure 6.73 Current density distribution on the patch – phase of 0 degrees

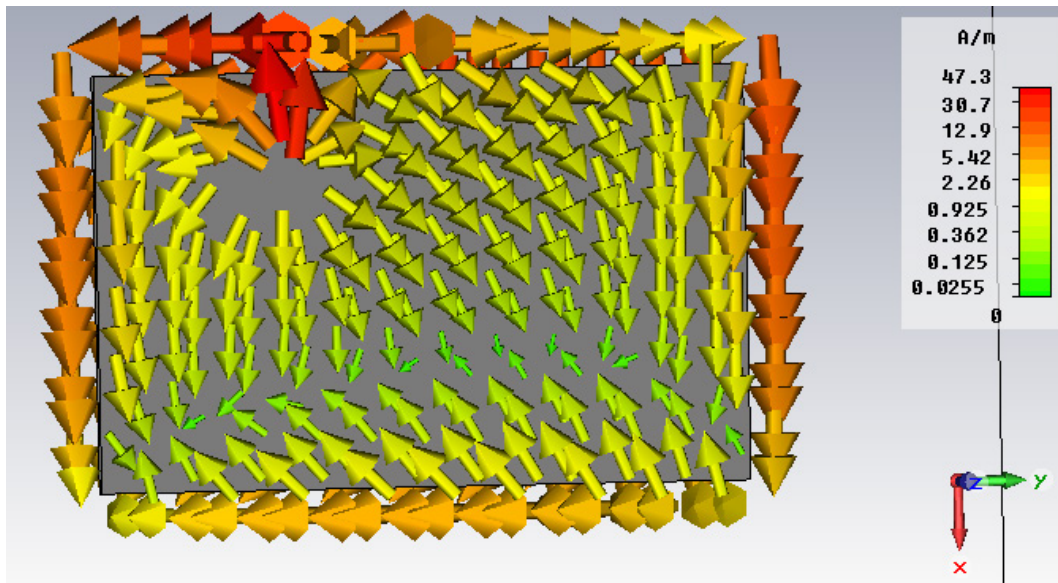


Figure 6.74 Current density distribution on the patch – phase of 90 degrees

In Table 6.11, the length of the diagonal for the original and reduced patch dimension is given. The reduction in diagonal length is 9.88%, while from Table 6.9, the average effective extension in length of the used yarn (since it does not follow a straight line when embroidered in denim) is 9.91%. This similarity in numbers suggests that the extension of the current path due to effective yarn length (discussed in section 6.5.4) could have been compensated by reducing the diagonal of the patch, which in turn led to a shift in resonant frequency of around 14% (towards the ISM 2.4 band).

To check whether the dominant resultant current flow is in the diagonal direction, we have analyzed the transmission parameter between the calibrated UWB horn antenna and the observed textile antenna. The UWB horn was vertically polarized, and the antenna placed in a way that patch symmetral is placed vertically as well. The patch symmetral was tilted by angles in steps of 10 degrees, and the magnitude of the transmission parameter subsequently measured. The results are given in Fig. 6.75, while the typical measurement setup is illustrated in Fig. 6.76. It can be seen that a slight rise of around 30° in the magnitude of the transmission parameter was obtained, which suggests that the antenna is linearly polarized along the diagonal of the patch (meaning that the patch diagonal roughly determines resonant length), as predicted by simulations (Figs 6.73 and 6.74).

Table 6.11 Length of the patch diagonal

	Diagonal length [mm]
Original dimensions (20 mm × 32 mm)	37.73
Dimensions after ripping off the yarn (16 mm × 30 mm)	34
Reduction in diagonal length: 9.88 %	

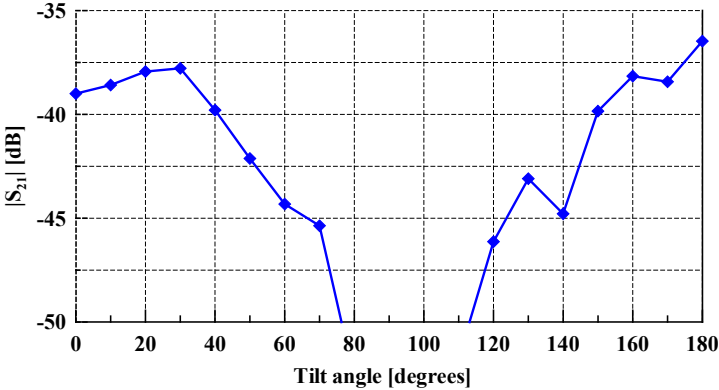


Figure 6.75 Measured magnitude of the transmission parameter for various tilt angles of the full-textile PIFA antenna with respect to the vertical axis



Figure 6.76 Tilting the antenna with respect to the vertical axis

6.6.2. Characterization of the full-textile PIFA antenna

In the final measurement campaign, we have characterized the obtained full-textile PIFA antenna in terms of input reflection coefficient, gain, and the radiation pattern. The characterization was performed both in free space and when the antenna was placed on the body phantom (developed in section 3.4).

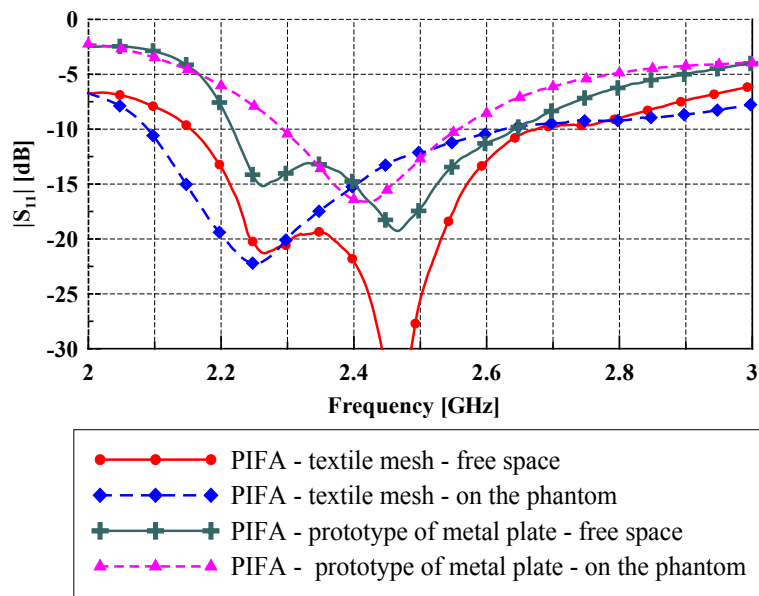


Figure 6.77 Measured magnitude of the input reflection coefficient for the full-textile and metallic prototype PIFA antenna in free space and on the body phantom.

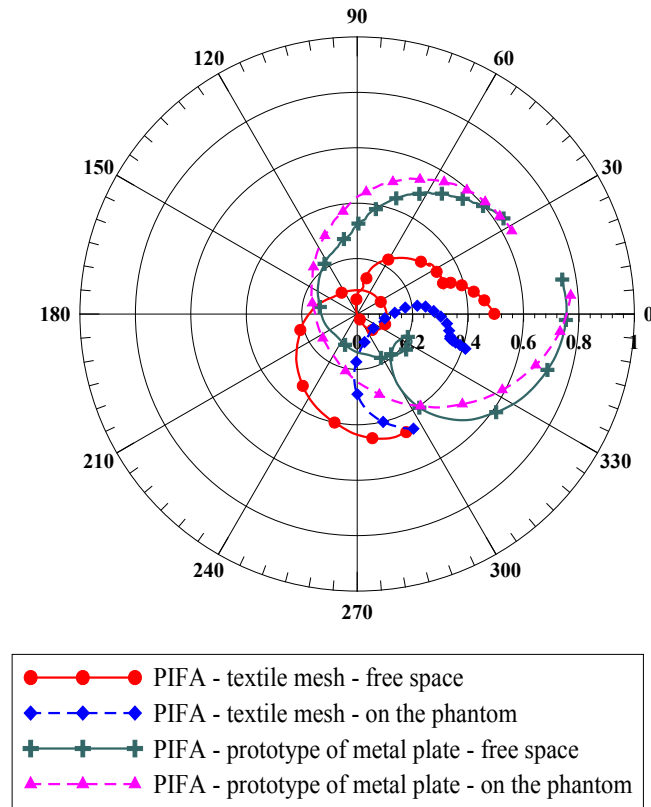


Figure 6.78 Polar plot of the measured input reflection coefficient for the full-textile and metallic prototype PIFA antenna in free space and on the body phantom (start: 2 GHz; stop: 3 GHz; step: 0.05 GHz).

In Figs. 6.77 and 6.78, the input reflection coefficient is shown and compared to the prototype made of metal plate. The full-textile antenna with reduced patch dimensions exhibits similar input impedance behaviour as the metal prototype of the original dimensions, while for both antennas, suitable impedance coverage in the ISM 2.4 band is obtained for free space and in the presence of the body phantom, meaning that the ground plane provides enough isolation of the antenna and the human body.

In terms of gain, for the case of a textile antenna, realization gain in the ISM band is reduced by around 2 dB in free space compared to the metal prototype, which is caused by the finite conductivity of the textile threads. As expected, an additional reduction in gain of around 2 dB is obtained for the antenna placed on the phantom for both antenna realizations.

It needs to be noted that the liquid phantom used is contained in a plastic shell, so it does not correspond to placing the antenna on the skin (but rather on a clothing layer), meaning that, for the worst case of the antenna on the skin, the reduction in gain could be somewhat higher. It was already observed in section 6.4.1 that the thin dielectric layer between the phantom and

antenna could reduce (in combination with the ground plane) the interaction between the antenna and the human body.

The radiation pattern was measured both for the antenna in free space and the antenna placed on the phantom. The used coordinate system is given in Fig. 6.80, and the measurement setup is shown in Fig. 6.81. The radiation patterns are measured at typical frequencies along the ISM 2.4 band for two respective polarizations of the calibrated UWB horn (which was used for measurements). They are given in Figs. 6.82 - 6.87, and are normalized to the broadside value in the copolarization direction. It can be seen that the copolarization patterns in both considered principal planes are rather similar, which would again confirm that the antenna is linearly polarized by some angle with respect to the principal plane. In addition, at the broadside direction, crosspolarization levels are around 10 dB lower than the copolarization ones. The transmitted power in the broadside direction is around 1÷2 dB lower when the phantom is present, which is expected, and accounts for losses in the antenna gain due to absorption of the power in the human body.

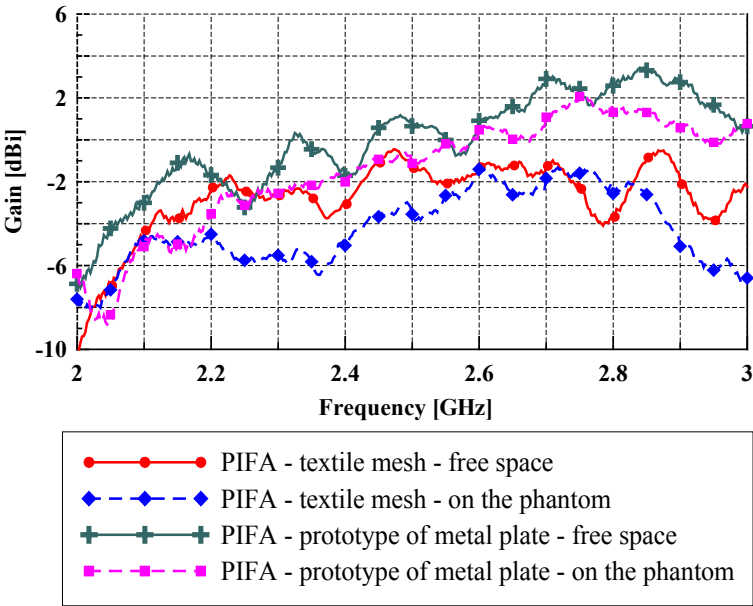


Figure 6.79 Measured gain in broadside direction for the full-textile and metallic prototype PIFA antenna in free space and on the body phantom

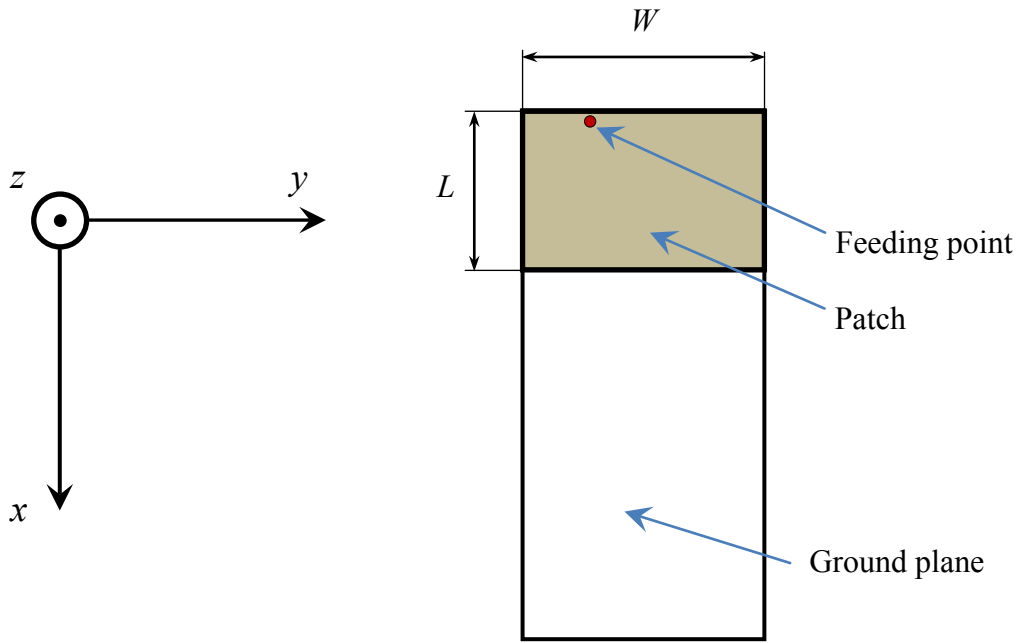


Figure 6.80 Coordinate system used in measurements of the radiation pattern



Figure 6.81 Measurement setup for measuring the radiation pattern. Left: antenna in free space (attached to Styrofoam); Right: Antenna attached on the phantom

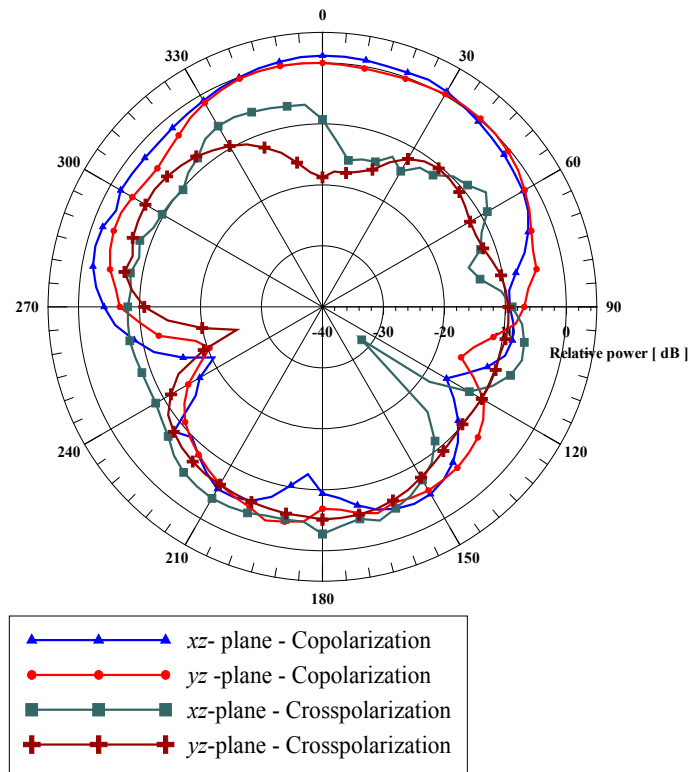


Figure 6.82 Measured radiation pattern for full-textile PIFA antenna in free space ($f=2.4$ GHz)

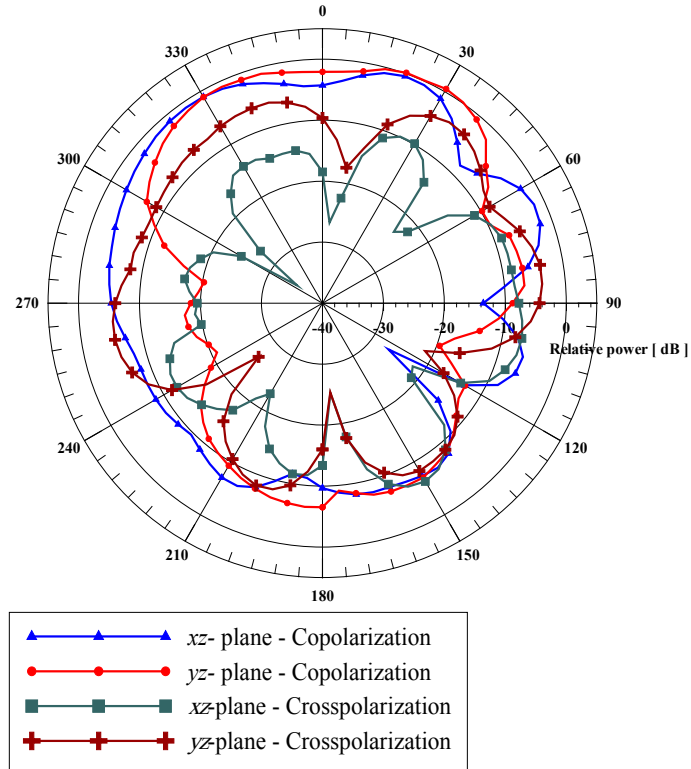


Figure 6.83 Measured radiation pattern for full-textile PIFA antenna placed on the phantom ($f=2.4$ GHz)

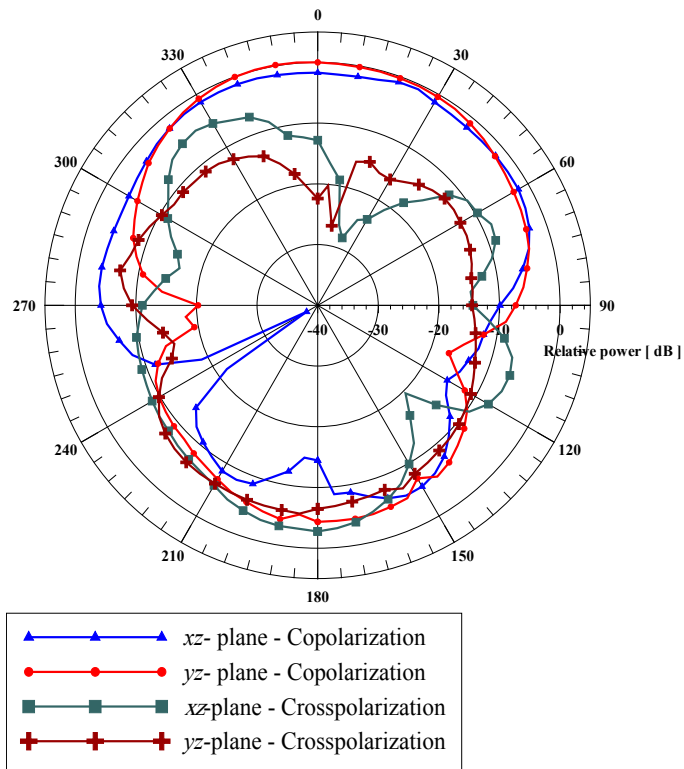


Figure 6.84 Measured radiation pattern for full-textile PIFA antenna in free space ($f=2.45$ GHz)

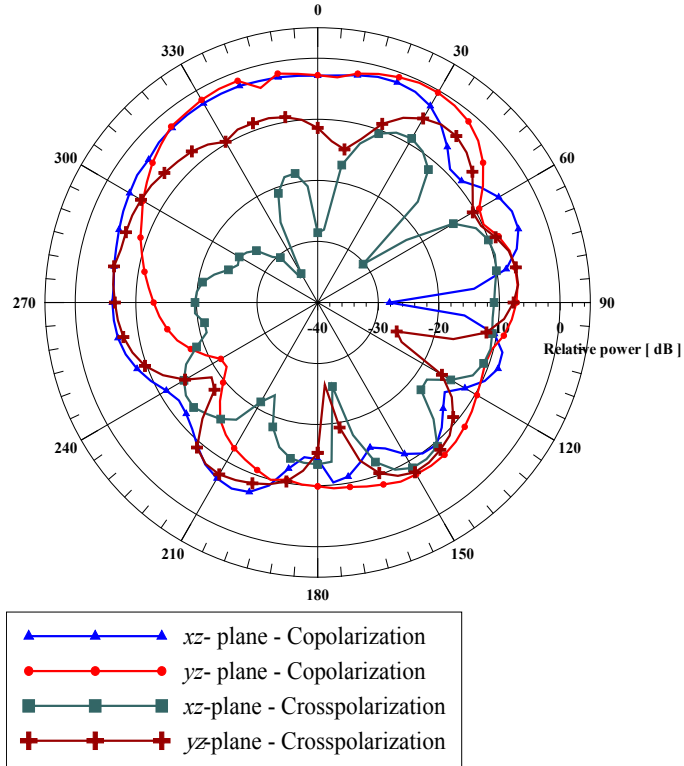


Figure 6.85 Measured radiation pattern for full-textile PIFA antenna placed on the phantom ($f=2.45$ GHz)

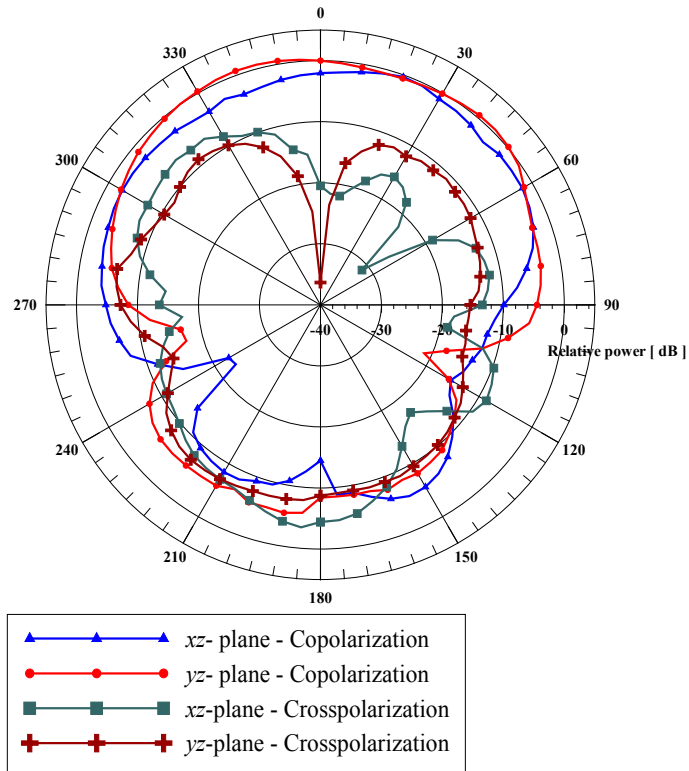


Figure 6.86 Measured radiation pattern for full-textile PIFA antenna in free space ($f=2.5$ GHz)

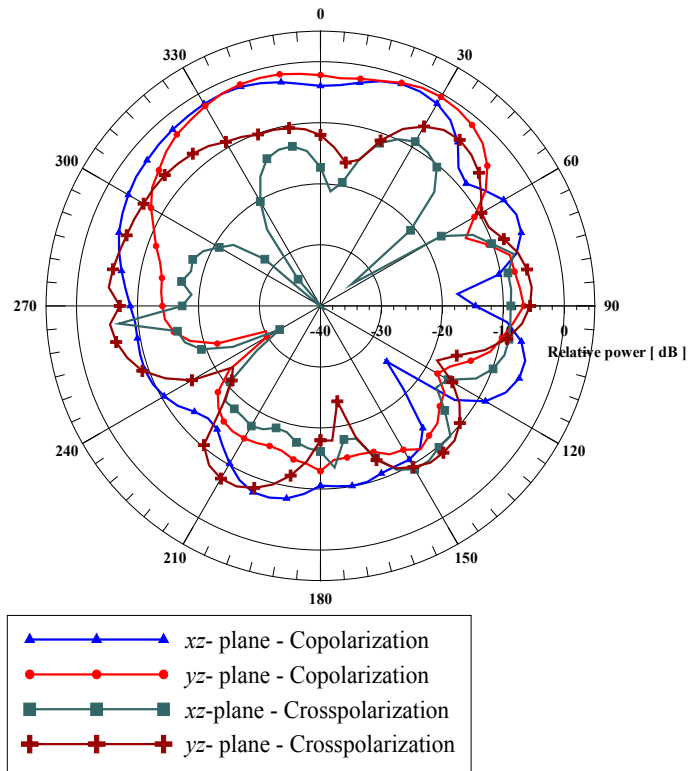


Figure 6.87 Measured radiation pattern for full-textile PIFA antenna placed on the phantom ($f=2.5$ GHz)

7. CONCLUSION

In this thesis, we have dealt with the specific characteristics of body-centric communication systems, and have analyzed them from the point of view of the antenna engineer. This means that the focus of the research was on the design of antennas suitable to be worn on the body, and their characterization in the vicinity of the human body. The aspects of concern in the thesis were on-body and off-body communications in the UHF and ISM 2.4 bands. To conform with user demands (unobtrusiveness and aesthetical acceptability), planar antennas on textile substrates were taken as a logical choice for the analysis and design.

In the course of the research for this thesis and the evaluation of the specific characteristics of the body-centric environment, several antenna prototypes have been proposed and measured in free space, on the human body phantom and the body of a human volunteer. The issues that have received particular attention throughout this thesis are as follows:

- *A model of the influence of the human body on the wearable antenna and the on-body communication system.* Using a cylindrical approximation of the human body, the analysis of the creeping wave portion of the radiated wave spectrum was performed. The Green's function in the spectral domain was calculated for a vertical dipole in the vicinity of a circular cylinder, while the contribution from the waves flowing only around the curved surface (i.e. creeping waves) was evaluated using Watson's transformation. To reduce the problem to 2D, a cylinder of infinite height was assumed. In the two measurement campaigns, it was shown that the slope of path loss corresponds with the predicted one only at the beginning of the transition to the shadow region, while a path loss of a smaller extent than predicted was measured in the shadow region. This means that the finiteness of the considered cylinder height (i.e. the human body) also plays a role, and that the waves flowing in the vertical direction diffract around the body adding to creeping waves in the shadow region, thereby reducing the path loss. Therefore, such a model can be considered as a worst case scenario in designing an on-body communication system, arguably more accurate at higher frequencies such as the 60 GHz range, where the human body is even larger electrically. In reality, the reflection and scattering from nearby objects (i.e. the multipath) can also improve the situation.

In another approach, the influence of the ground plane on the antenna radiation properties was studied. For this purpose, a PIFA antenna with a slot in the ground plane was first numerically designed using common methods for antenna size reduction. While the

antenna was shown to operate properly in free space, in the presence of the numerical phantom (i.e. the standard muscle equivalent box), its gain in the worst case fell below acceptable levels for on-body and off-body systems. In addition, it was found that, with the slot in the ground plane, the resonant frequency of the antenna is increased when the body model is present. This was explained by deriving an equivalent circuit of the PIFA antenna and the slot, where the slot in the presence of human body acts as a capacitance. Reflecting this research, a PIFA antenna of somewhat larger dimensions was made without the slot in the ground plane and the gain was improved to acceptable values, meaning that a sufficient ground plane provides fair isolation between the antenna and the human body.

- *Evaluating the influence of moisture in the textile substrate on the radiation properties of antennas.* Measurements of a planar antenna with wet textile substrates of various levels of humidity have been performed. The considered substrate was fleece, the fibers of which are known not to absorb water, which makes it appear dry (to touch) rather soon after applying water, compared to other fabrics used in clothes (such as denim or cotton). It was shown that even small levels of moisture significantly affect the antenna radiation properties by reducing its resonant frequency (due to increased effective permittivity of the substrate) and gain (due to absorption from water), and that, when left to dry naturally, it takes several hours for the antenna to recover its original properties.
- *Evaluating the influence of mechanical deformations on the radiation properties of the antenna.* When the antenna is mounted on the body, it does not generally remain flat (due to the curved surface of the body and changes of body posture). Therefore, the influence of bending, as the most dominant deformation, has been researched. The antenna was bent around cylinders of different radii of curvature which are actually found on the body (e.g. when the antenna is placed on the arm or on the chest). It was found that bending in the *E*-plane exerts a stronger influence on the antenna radiation properties, and can reduce the obtained gain and cause impedance mismatch at the desired frequency range for smaller bending radii. In the *H*-plane, this effect was found to be less pronounced (for bending in the *E*-plane, the current path is more altered than in the *H*-plane).
- *A strategy for the design of wearable antennas with reduced radiation on human body.* Based on the issues observed above, a general strategy for the design of wearable antennas has been proposed. The obtained prototype needs to operate both in free space and when

placed on the human body (placing it on the human skin is the worst case scenario). In general, for on-body and off-body communications, it is advised, if possible (due to users demands), to use the proper ground plane and place the antenna on the outer part of clothes. It is also advised to extend the bandwidth of the antenna in free space to make it larger than desired, so that the influence of the body and bending does not put the antenna out of resonance. Using hydrophobic substrates, or covering the antenna with a waterproof layer could help alleviate the influence of moisture. The obtained prototype should be tested both for bending and environmental conditions, so that the antenna design and the requirements of communication systems utilizing such an antenna can be modified if needed. In the course of several simulation and measurement campaigns, it was shown that the presence of the human body in the near field of the antenna affects the antenna input impedance matching and the realized gain due to the power absorbed in the body. It was also shown that the worst case occurs when the antenna is placed directly on the skin—when a layer of clothes is placed between the antenna and the body, the antenna gain is improved. This means that the antenna should be placed on an outer layer of clothes or in/on a jacket.

After the prototype with adequate characteristics was obtained, the next step was taken to design a full-textile antenna – the design of conductive parts of the antenna using conductive textile fibers instead of common conductive materials. Based on findings from the analysis of conductive threads in several woven fabrics, the procedure of creating conductive textiles was simplified by embroidering the conductive threads into some existing fabrics (for which only a sewing machine is required). It was found that conductive threads in both orthogonal directions (i.e. a mesh-like structure) can mimic the conventional conductive materials. Various densities of such a mesh were researched. It was also found that, since the the conductive fibers (yarn) sewn into the fabric do not follow a straight line, they extend the current path and allow some size reduction.

Finally, methods of applying the feeding onto the conductive textile were researched, and it was found that the use of a metallic button sewn on the conductive textile can serve as a good mediator between the soldered coaxial feeding and the textile. This is a good compromise between the aesthetical and engineering points of view. Based on this strategy, a full-textile PIFA antenna was designed and shown to operate properly in the ISM 2.4 band.

The findings of the thesis can serve as a basis for future work, with the following directions:

- *Refining the model of on-body communication.* Investigating communication via surface waves for antennas placed on the same side of the body (e.g. on the chest).
- *Tests of durability.* The obtained antenna and conductive textile realizations need to be tested for durability due to other issues that arise in the real world (e.g. washing, scratching, freezing etc.)
- *Improvements in the antenna design.* Based on the findings of the thesis and the obtained strategy, the research could move towards other frequency ranges such as UWB antennas.
- *Utilizing other textile substrates.* The use of advanced artificial substrates in the antenna design, instead of common ones, could reduce the influence of moisture (using hydrophobic substrates) or bending (using less flexible substrates). However, at that stage, the final price of the product, as well as the comfort when worn on the body, need to be taken into account.

Appendix A. SPHERICAL HARMONICS

Vector eigenvectors

When solving a differential equation such as e.g. a wave equation, one of the common methods is to find an appropriate set of linearly independent functions (eigenfunctions) in terms of which it is possible to express any solution (function). By applying such a method, to obtain a particular solution (due to source terms or boundary conditions), one only needs to find the coefficients corresponding to each term of the eigenfunction, i.e. the differential equation could be, in principle, reduced to an algebraic one. Spherical harmonics are a useful tool for analyzing the fundamental limitations of the antennas, while they were also used by the author of the thesis in [127], where spherical electromagnetic cloaks were analyzed.

In this section we will show how to construct eigenfunctions for a vector wave equation that is satisfied by the electric and magnetic field. Let $\mathbf{C} \equiv \mathbf{C}(\mathbf{r})$ be a vector field that satisfies the homogeneous vector Helmholtz equation (it represents e.g. the electric or magnetic field or vector potential in the absence of sources):

$$\nabla^2 \mathbf{C} + k^2 \mathbf{C} = 0, \quad (\text{A.1})$$

where k is called the wavenumber (in general it is a complex number).

As mentioned above, the idea is to find a complete set of vectors in terms of which it is possible to expand any vector \mathbf{C} that satisfies (A.1). As a basis for such an expansion, we first find the scalar function ψ which satisfies the scalar Helmholtz equation (subject to some boundary conditions):

$$\nabla^2 \psi + k^2 \psi = 0. \quad (\text{A.2})$$

Using the scalar function ψ and defining a constant vector \mathbf{a} , it is possible to derive three sets of mutually linearly independent vector functions [128], each of which individually satisfies (A.1):

$$\begin{aligned} \mathbf{L} &= \nabla \psi, \\ \mathbf{M} &= \nabla \times \mathbf{a} \psi, \\ \mathbf{N} &= \frac{1}{k} \cdot (\nabla \times \nabla \times \mathbf{a} \psi) = \frac{1}{k} \cdot (\nabla \times \mathbf{M}). \end{aligned} \quad (\text{A.3})$$

The \mathbf{L} , \mathbf{M} and \mathbf{N} vectors also have the following properties, which arise due to their definition:

- a) \mathbf{L} is irrotational, i.e. $(\nabla \times \mathbf{L}) = 0$
- b) \mathbf{M} and \mathbf{N} are solenoidal, i.e. $\nabla \cdot \mathbf{M} = \nabla \cdot \mathbf{N} = 0$
- c) Since \mathbf{a} is presumed constant, vector \mathbf{M} could also be written as:

$$\mathbf{M} = \mathbf{L} \times \mathbf{a} = \frac{1}{k} \cdot (\nabla \times \mathbf{N})$$

- d) Vector \mathbf{M} is perpendicular to \mathbf{L} , i.e. $\mathbf{L} \cdot \mathbf{M} = 0$. Also, \mathbf{M} is perpendicular to \mathbf{a} .

If by solving (A.2) we find a set of scalar functions $\{\psi_n\}$ which form a complete set in the Hilbert space, it can be shown that any vector field \mathbf{C} that satisfies (A.1) could be represented by a linear combination of \mathbf{L} , \mathbf{M} and \mathbf{N} vectors that correspond to each scalar ψ_n in the set, i.e.

$$\mathbf{C} = \sum_n (a_n \mathbf{M}_n + b_n \mathbf{N}_n + c_n \mathbf{L}_n), \quad (\text{A.4})$$

where a_n , b_n and c_n are coefficients to be determined for a specific configuration.

Now, we turn our attention to the electric and magnetic fields in a region without sources, where they are described by the following equations (the time-harmonic case and isotropic medium are assumed):

$$\begin{aligned} \nabla \times \mathbf{E} &= -j\omega\mu\mathbf{H}, \\ \nabla \times \mathbf{H} &= j\omega\varepsilon\mathbf{E}, \\ \nabla \cdot \mathbf{E} &= \nabla \cdot \mathbf{H} = 0. \end{aligned} \quad (\text{A.5})$$

Since the divergence of the electric and magnetic field in source free regions is zero, it is possible to write them as a curl of another vector (divergence of the curl is always zero). If we define vectors \mathbf{A} and \mathbf{F} so that:

$$\begin{aligned} \mathbf{H} &= \frac{1}{\mu} \nabla \times \mathbf{A}, \\ \mathbf{E} &= -\frac{1}{\varepsilon} \nabla \times \mathbf{F}. \end{aligned} \quad (\text{A.6})$$

for each vector we can derive an independent solution for both the electric and magnetic field, by inserting them into Maxwell's equations and applying the Lorenz condition. Physically, vectors \mathbf{A} and \mathbf{F} represent potentials that arise due to electric and magnetic sources, respectively. The total field in the region without sources turns out to be the superposition of the fields that arise from \mathbf{A} and \mathbf{F} :

$$\begin{aligned}\mathbf{E} &= \mathbf{E}_A + \mathbf{E}_F = \frac{1}{j\omega\mu\epsilon} \nabla \times \nabla \times \mathbf{A} - \frac{1}{\epsilon} \nabla \times \mathbf{F}, \\ \mathbf{H} &= \mathbf{H}_A + \mathbf{H}_F = \frac{1}{\mu} \nabla \times \mathbf{A} - \frac{1}{j\omega\mu\epsilon} \nabla \times \nabla \times \mathbf{F}.\end{aligned}\tag{A.7}$$

Now, we make a particular choice for \mathbf{A} and \mathbf{F} :

$$\begin{aligned}\mathbf{A} &= \psi_{TM} \cdot \mathbf{a}, \\ \mathbf{F} &= \psi_{TE} \cdot \mathbf{a},\end{aligned}\tag{A.8}$$

where ψ_{TM} and ψ_{TE} are scalar functions that both satisfy the Helmholtz equation (A.2), and \mathbf{a} is a constant vector. The expression (A.7) could now be rewritten as:

$$\begin{aligned}\mathbf{E} &= \frac{1}{j\omega\mu\epsilon} \nabla \times \nabla \times (\psi_{TM} \cdot \mathbf{a}) - \frac{1}{\epsilon} \nabla \times (\psi_{TE} \cdot \mathbf{a}), \\ \mathbf{H} &= \frac{1}{\mu} \nabla \times (\psi_{TM} \cdot \mathbf{a}) - \frac{1}{j\omega\mu\epsilon} \nabla \times \nabla \times (\psi_{TE} \cdot \mathbf{a}).\end{aligned}\tag{A.9}$$

Comparing the equation (A.9) with (A.3), we immediately find that it is possible to define equivalent vector functions e.g. $\mathbf{M}_{TE} = \nabla \times (\psi_{TE} \cdot \mathbf{a})$ and $\mathbf{N}_{TM} = \nabla \times \nabla \times (\psi_{TM} \cdot \mathbf{a})$ in terms of which it is possible to expand the electric and magnetic field in the way as described in (A.4). Such expansion is of the form:

$$\begin{aligned}\mathbf{E} &= \sum_n (a_n \mathbf{M}_{TE,n} + b_n \mathbf{N}_{TM,n}) = \mathbf{E}_{TE} + \mathbf{E}_{TM}, \\ \mathbf{H} &= -\frac{k}{j\omega\mu} \sum_n (a_n \mathbf{N}_{TE,n} + b_n \mathbf{M}_{TM,n}) = \mathbf{H}_{TE} + \mathbf{H}_{TM}.\end{aligned}\tag{A.10}$$

We also note that:

- a) the expansion (A.10) is a bit more general than (A.4), in the sense that two generating scalar functions (ψ_{TM} and ψ_{TE}) are actually needed (however, they only differ to a specific multiplier)
- b) in such an expansion, the terms in vector \mathbf{L} are zero, which is expected since the divergence of \mathbf{L} is not, by definition, generally zero, unlike the divergence of the electric and magnetic field.
- c) Since vector \mathbf{M} is perpendicular to the constant vector \mathbf{a} , we denote the respective terms of the field expansion in \mathbf{M} (and accordingly their \mathbf{N} counterparts) as transverse electric (TE) or transverse magnetic (TM) to \mathbf{a} . This means that each field is decomposed into the TE part and TM part (generated by ψ_{TE} and ψ_{TM} , respectively).

To summarize the above mentioned considerations, we note that the procedure of solving for electric and magnetic fields can be formulated as:

- i. fixing the appropriate constant vector \mathbf{a}
- ii. finding the complete sets of scalar functions ψ_{TE} and ψ_{TM} by solving the homogeneous scalar Helmholtz equation of the type (A.2)
- iii. expanding the field in TE and TM parts (so-called magnetic and electric multipoles, respectively) and determining coefficients such as a_n and b_n by applying the given boundary conditions or expanding the given source functions.

Expansion in spherical coordinates

The scalar functions ψ in the expansion of the fields (A.10), as well as suitable choices of vector \mathbf{a} , depend on the choice of the coordinate system. In this section, we describe the procedure for the spherical coordinate system (r, φ, θ) and seek the expansion of the fields in free space in terms of spherical eigenfunctions, i.e. spherical harmonics. The procedure described above requires finding a fixed vector \mathbf{a} . Although any vector \mathbf{a} can be chosen in principle, in the spherical coordinate system it is not possible to find such a vector that would a priori generate independent vectors \mathbf{M} and \mathbf{N} across the whole surface of the sphere – if e.g. we use the radial unit vector $\hat{\mathbf{r}}$, we find that it is not constant across the sphere. Similar issues also arise in more general coordinate systems.

Nevertheless, for spherical coordinate systems in particular it can be found that, from the radial vector, it is actually still possible to construct the appropriate vectors \mathbf{M} and \mathbf{N} that are independent across the spherical surface. We try to construct the vector \mathbf{M} tangential to the sphere (which is proportional to e.g. the electric or magnetic field) of the following form:

$$\mathbf{M} = \nabla \times \hat{\mathbf{r}}u(r)\psi, \quad (\text{A.11})$$

i.e. we have chosen a non-constant vector of the form $\mathbf{a} = u(r) \cdot \hat{\mathbf{r}}$, where $u(r)$ is some radial function, yet undetermined. After some derivation, it can be shown that, with selection $u(r) = r$, the function ψ satisfies the scalar Helmholtz differential equation of the type (A.2) [108, 128].

Now, we need to find the complete set of functions ψ that satisfy the scalar Helmholtz equation (A.2) in spherical coordinates. The typical procedure is the method of separation of

variables. We assume that the function $\psi \equiv \psi(\mathbf{r})$ can be written as a product of three functions of r -, θ - and φ - coordinates, respectively:

$$\psi = f(r) \cdot g(\theta) \cdot h(\varphi). \quad (\text{A.12})$$

This form of ψ is then inserted in the Helmholtz equation in spherical coordinates, and after some manipulations, one obtains three independent equations for functions f , g and h :

a) 1D Helmholtz equation

$$\frac{\partial^2 h}{\partial \varphi^2} + m^2 h = 0 \quad (\text{A.13})$$

b) Legendre differential equation

$$\frac{1}{\sin \theta} \frac{\partial}{\partial \theta} \left[\sin \theta \frac{\partial g}{\partial \theta} \right] + \left[n(n+1) - \left(\frac{m}{\sin \theta} \right)^2 \right] g = 0 \quad (\text{A.14})$$

c) Spherical Bessel differential equation

$$\frac{\partial^2 f}{\partial r^2} + \frac{2}{r} \frac{\partial f}{\partial r} + \left[k^2 - \frac{n(n+1)}{r^2} \right] f = 0. \quad (\text{A.15})$$

Here, m^2 and $n(n+1)$ are separation constants, while m, n are integers. The solutions of (A.13) are harmonic functions $h(\varphi) = e^{-jm\varphi}$, while the solutions of (A.14) are Legendre functions of the first and second kind $g(\theta) = P_n^m(\cos \theta)$ and $g(\theta) = Q_n^m(\cos \theta)$ (the latter ones give a non-physical solution due to singularity at $\theta = 0^\circ$ and $\theta = 180^\circ$). Finally, the solutions of (A.15) are spherical Bessel and Hankel functions of the first and second kind $f(r) = h_n^{(1)}(kr)$ and $f(r) = h_n^{(2)}(kr)$. We choose the solutions in accordance to the physical reality of the problem in question (outgoing wave in free space, no singularities on the spherical surface) and write the normalized solution for ψ as:

$$\psi_{mn} = f(r) \cdot g(\theta) \cdot h(\varphi) = h_n^{(2)}(kr) \cdot P_n^m(\cos \theta) \cdot e^{-jm\varphi}. \quad (\text{A.16})$$

Note that the actual solution is actually a multiple of ψ_{mn} . If one needs to take into account standing waves in a spherical layer, then spherical Bessel functions $j_n(kr)$ should also be considered.

Spherical vector eigenfunctions **L**, **M** and **N** can now be constructed from each ψ_{mn} , i.e. by inserting (A.16) into (A.11) and (A.3). Therefore, we have by now obtained a proper

mathematical tool to expand any vector function in spherical coordinates as a sum of vector eigenfunctions. The remaining task is to apply the developed tool to potential and field equations and to obtain the required field expressions in terms of vector eigenfunctions.

In accordance with the discussions described above, we expand the potentials \mathbf{A} and \mathbf{F} as:

$$\begin{aligned}\mathbf{A} &= \psi_{TM} \cdot \mathbf{r} = \sum_{m,n} B_{mn} \psi_{mn} \cdot r \hat{\mathbf{r}}, \\ \mathbf{F} &= \psi_{TE} \cdot \mathbf{r} = \sum_{m,n} A_{mn} \psi_{mn} \cdot r \hat{\mathbf{r}},\end{aligned}\tag{A.17}$$

where A_{mn} and B_{mn} are coefficients to be determined for a specific configuration.

We note that the potentials contain only the radial component. The final expansion of the electric and magnetic field is then obtained by inserting (A.17) into (A.9), which is the expression for the electric and magnetic field in terms of radial components of potentials that provide decomposition to the TE and TM (to r -coordinate) parts. The expression is of the form (A.10) only, with double index mn . The coefficients in the expansion are then obtained by applying boundary conditions or by expanding the (known) source terms in the spherical harmonics and finding the field coefficients that correspond to each source term (i.e. the differential equation is then reduced to an algebraic one).

As a final remark, note that the radial dependence in (A.16) is often incorporated in the modified form of spherical Hankel functions (so-called Schelkunoff form):

$$\hat{H}_n^{(2)}(kr) = kr \cdot h_n^{(2)}(kr).\tag{A.18}$$

The connection between spherical Hankel functions in Schelkunoff and ordinary form $\hat{H}_n^{(2)}$ and $h_n^{(2)}$ with the regular (cylindrical) functions $H_n^{(2)}$ is given by:

$$\hat{H}_n^{(2)}(kr) = kr \cdot h_n^{(2)}(kr) = kr \cdot \sqrt{\frac{\pi}{2kr}} H_{n+\frac{1}{2}}^{(2)}(kr) = \sqrt{\frac{kr\pi}{2}} H_{n+\frac{1}{2}}^{(2)}(kr).\tag{A.19}$$

The same relation as (A.19) holds also for other types of Bessel/Hankel functions. The Bessel/Hankel functions of the Schelkunoff form are solutions to the slightly modified equation compared to (A.15):

$$\frac{\partial^2 f}{\partial r^2} + \left[k^2 - \frac{n(n+1)}{r^2} \right] f = 0.\tag{A.20}$$

Note that the expansions of the type (A.17) are only slightly changed by employing the Schelkunoff form of Hankel functions instead of the ordinary ones (only the coefficients such as A_{mn} or B_{mn} are different, and r is incorporated into Hankel functions).

Appendix B. SURFACE WAVE - PROTOTYPE SOLUTION

Plane wave incidence – parallel polarization

The study of surface waves starts by examining the planar interface between the air and a lossless dielectric. Such an interface has been investigated from the early 20th century [90], and is associated with the Brewster angle of incidence at which total transmission across the interface occurs. This is, in fact, the special case of fast waves when there is no standing wave in the x -direction. To derive the equivalent scheme, we start with the parallel polarized plane wave incident from the air with an angle of θ_i to the surface normal, as given in Fig. B-1. Such a wave has components E_x , E_z and H_y , i.e. the electric field lays entirely in the plane of incidence (xz -plane), hence the name parallel polarization [89, 90].

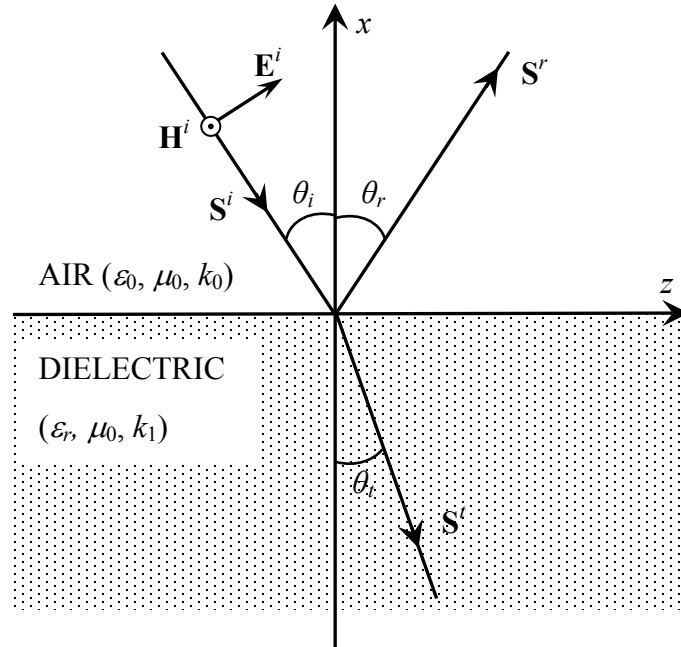


Figure B-1 Parallel polarized plane wave incidence

The configuration consists of the incident, reflected and transmitted fields. The incident electric field is given from Fig. B-1 as:

$$\mathbf{E}^i = \mathbf{E}_0^i e^{-jk_x x} = (E_x^i \hat{\mathbf{x}} + E_z^i \hat{\mathbf{z}}) e^{-j(k_x \hat{\mathbf{x}} + k_z \hat{\mathbf{z}})(x\hat{\mathbf{x}} + z\hat{\mathbf{z}})} = E_0^i (\sin \theta_i \hat{\mathbf{x}} + \cos \theta_i \hat{\mathbf{z}}) e^{-jk_x x} e^{-jk_z z}, \quad (\text{B.1})$$

where $k_x = -k_0 \cos \theta_i$; $k_z = k_0 \sin \theta_i$ and k_0 is the wavenumber in the air. The minus sign of k_x denotes the propagation of the incident wave in the negative x -direction, as also seen in Fig. B-1. Of course, along with the air, the discussion is valid for any planar interface between two dielectrics.

Inserting (B.1) into Maxwell's equations the incident magnetic field is obtained as:

$$\mathbf{H}^i = -\frac{1}{j\omega\mu}(\nabla \times \mathbf{E}^i) = \frac{E_0^i}{\eta_0} e^{-jk_x x} e^{-jk_z z} \hat{\mathbf{y}} \quad (\text{B.2})$$

where $\eta_0=377 \Omega$ is the characteristic impedance of free space. The reflected and transmitted fields could be written as:

$$\begin{aligned} \mathbf{E}^r &= \mathbf{E}_0^r e^{-jk_r \mathbf{r}}, \\ \mathbf{E}^t &= \mathbf{E}_0^t e^{-jk_t \mathbf{r}}. \end{aligned} \quad (\text{B.3})$$

Using the boundary conditions, we derive the reflected and transmitted fields from the given incident field. The tangential component of the electric field must be continuous on both sides of the interface ($x=0$), so we can write:

$$\begin{aligned} \mathbf{E}_{\text{tan}}^{\text{air}} &= \mathbf{E}_{\text{tan}}^{\text{dielectric}}, \text{ i.e.} \\ (\mathbf{E}_0^i e^{-jk_r \mathbf{r}} + \mathbf{E}_0^r e^{-jk_r \mathbf{r}})_{\text{tan}} &= (\mathbf{E}_0^t e^{-jk_t \mathbf{r}})_{\text{tan}}. \end{aligned} \quad (\text{B.4})$$

The same consideration holds for tangential magnetic fields, since no sources are present on the surface.

Since these boundary conditions need to be satisfied for all the points in the interface, the spatial variation of the fields needs to be the same for all points z at the interface; thus, for $x=0$, we can write (so-called *phase-matching* [114]):

$$\mathbf{k}_i \mathbf{r} = \mathbf{k}_r \mathbf{r} = \mathbf{k}_t \mathbf{r} \quad (\text{B.5})$$

By inserting $x=0$, we obtain the relation:

$$k_{z,\text{incident}} = k_{z,\text{reflected}} = k_{z,\text{transmitted}}. \quad (\text{B.6})$$

From Fig. B-1, it can be seen that $\theta_i = \theta_r$ and that $k_0 \sin \theta_i = k_1 \sin \theta_t$, which are the *Snell's laws* for reflection and refraction, respectively. In addition, we can arbitrarily choose the default direction of reflected electric field as long as it is perpendicular to the direction of \mathbf{k}_r (in particular, by convention we assume that the tangential reflected field component has the same default direction as the tangential incident field [89]). Using these relations, all the field components can be written:

$$\mathbf{E}^r = E_0^r (-\sin \theta_i \hat{\mathbf{x}} + \cos \theta_i \hat{\mathbf{z}}) e^{+jk_x x} e^{-jk_z z},$$

$$\mathbf{E}^t = E_0^t (-\sin \theta_i \hat{\mathbf{x}} + \cos \theta_i \hat{\mathbf{z}}) e^{-jk_{x1}x} e^{-jk_{z1}z},$$

$$\mathbf{H}^r = -\frac{1}{j\omega\mu} (\nabla \times \mathbf{E}^r) = -\frac{E_0^r}{\eta_0} e^{+jk_x x} e^{-jk_z z} \hat{\mathbf{y}},$$

$$\mathbf{H}^t = -\frac{1}{j\omega\mu} (\nabla \times \mathbf{E}^t) = \frac{E_0^t}{\eta_1} e^{-jk_{x1}x} e^{-jk_{z1}z} \hat{\mathbf{y}}, \quad (\text{B.7})$$

where $k_{x1} = k_x \sqrt{\epsilon_r}$ and $k_{z1} = k_1 \sin \theta_i = k_z$.

Equivalent scheme – plane wave incidence

To derive the equivalent transmission-line scheme, we need to reduce the problem to 1D. Thus, we take a look at the power that flows in the vertical ($\pm x$ -) direction, i.e. the direction where the structure is inhomogeneous. This is the power that flows into the dielectric. The total incident power density is given as:

$$\mathbf{S}^i = \frac{1}{2} \text{Re}(\mathbf{E}^i \times \mathbf{H}^{i*}) = \frac{1}{2} \text{Re}((\mathbf{E}_x^i + \mathbf{E}_z^i) \times \mathbf{H}^{i*}) = \frac{(E_0^i)^2}{2\eta_0} (\sin \theta_i \hat{\mathbf{z}} - \cos \theta_i \hat{\mathbf{x}}). \quad (\text{B.8})$$

Therefore, the incident power density in the (negative) x - direction is:

$$\mathbf{S}_x^i = \frac{1}{2} \text{Re}(\mathbf{E}_z^i \times \mathbf{H}^{i*}) = \frac{(E_0^i)^2}{2\eta_0} \cos \theta_i (-\hat{\mathbf{x}}), \quad (\text{B.9})$$

which can be rewritten as:

$$\mathbf{S}_x^i = \frac{(E_0^i)^2}{2\eta_0} \cos \theta_i \cdot \frac{\cos \theta_i}{\cos \theta_i} (-\hat{\mathbf{x}}) = \frac{(E_z^i)^2}{2\eta_0 \cos \theta_i} (-\hat{\mathbf{x}}) = \frac{(E_z^i)^2}{2Z_{w0}} (-\hat{\mathbf{x}}). \quad (\text{B.10})$$

Here, Z_{w0} is introduced as the *wave impedance* in the x -direction for parallel polarized waves in the air. It is defined as the ratio of magnitudes of the electric and magnetic field, which contribute to a power flow in a specific direction [89, 90, 114]. In the considered case, it is given as:

$$Z_{w0} = \frac{E_z^i}{H_y^i} = \eta_0 \cos \theta_i. \quad (\text{B.11})$$

The reflected and transmitted power flows in the x -direction are then obtained in the same way as the incident power flow:

$$\mathbf{S}_x^r = \frac{(E_z^r)^2}{2Z_{w0}} \hat{\mathbf{x}},$$

$$\mathbf{S}_x^t = \frac{(E_z^t)^2}{2Z_{w1}} (-\hat{\mathbf{x}}), \quad (\text{B.12})$$

where $Z_{w1} = \eta_1 \cos \theta_t = \frac{\eta_0}{\sqrt{\epsilon_r}} \cos \theta_t$ is the wave impedance in the dielectric.

We also note that

$$\mathbf{S}_x^t + \mathbf{S}_x^r = \mathbf{S}_x^i, \quad (\text{B.13})$$

since all the incident power in the (negative) x -direction is either reflected or transmitted.

We then define the field reflection and transmission coefficients with respect to tangential electric field (i.e. z - directed) components:

$$\Gamma = \frac{E_z^r}{E_z^i},$$

$$T = \frac{E_z^t}{E_z^i}. \quad (\text{B.14})$$

With the coefficient introduced in this way, from (B.4) and (B.7) one gets the following set of equations:

$$1 + \Gamma = T,$$

$$\frac{1 - \Gamma}{Z_{w0}} = \frac{T}{Z_{w1}}. \quad (\text{B.15})$$

By solving the system of equations we get:

$$\Gamma = \frac{Z_{w1} - Z_{w0}}{Z_{w1} + Z_{w0}},$$

$$T = \frac{2Z_{w1}}{Z_{w1} + Z_{w0}}. \quad (\text{B.16})$$

From (B.13) we have:

$$\mathbf{S}_x^r = |\Gamma|^2 \mathbf{S}_x^i,$$

$$\mathbf{S}_x^t = \mathbf{S}_x^i (1 - |\Gamma|^2). \quad (\text{B.17})$$

The expressions (B.14) - (B.17) are analogous to the ones found on a transmission line, i.e. the tangential electric and magnetic fields act as voltage and current on a transmission line. The characteristic impedance of each equivalent line is equal to the x -directed wave impedance in the air and dielectric, respectively. Such a transmission line is given in Fig. B-2, and represents the power flow into the dielectric.

In addition, as suggested in Fig. B-2, the quantity Z_{w1} in this case can also be regarded as the input impedance into the surface of the dielectric, leading to the concept of so-called *surface impedance* Z_S [89, 90]), which describes how the electromagnetic wave in the air “sees” the half-space below the surface ($x < 0$). The surface impedance is defined as the ratio of total tangential electric and magnetic field components in the air taken just at the surface of the dielectric, i.e.

$$Z_S = \frac{|\mathbf{E}_{\text{tan}}^{\text{air}}|}{|\mathbf{H}_{\text{tan}}^{\text{air}}|_{x=0^+}}. \quad (\text{B.18})$$

In general, when the dielectric is inhomogeneous or multilayered in the direction of the surface normal (x -axis), surface impedance is not equal to the wave impedance in the dielectric.

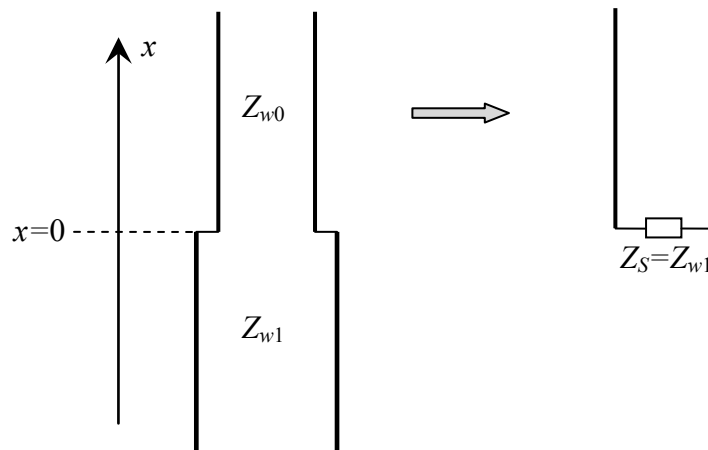


Figure B-2 Equivalent transmission lines for parallel polarized wave incidence

The total transmission occurs when the reflection coefficient vanishes, i.e. when the wave impedance in the air is matched to the surface impedance. Therefore:

$$\Gamma = \frac{Z_{w1} - Z_{w0}}{Z_{w1} + Z_{w0}} = \frac{\frac{\eta_0}{\sqrt{\epsilon_r}} \cos \theta_t - \eta_0 \cos \theta_i}{\frac{\eta_0}{\sqrt{\epsilon_r}} \cos \theta_t + \eta_0 \cos \theta_i} = \frac{\cos \theta_t - \sqrt{\epsilon_r} \cos \theta_i}{\cos \theta_t + \sqrt{\epsilon_r} \cos \theta_i}. \quad (\text{B.19})$$

To get $\Gamma=0$ (and therefore $T=1$), we need to solve the equation:

$$\cos \theta_t - \sqrt{\epsilon_r} \cos \theta_i = 0. \quad (\text{B.20})$$

By using Snell's law of refraction, we get the solution for θ_i , also called the *Brewster angle*:

$$\sin \theta_i = \sqrt{\frac{\epsilon_r}{\epsilon_r + 1}}. \quad (\text{B.21})$$

When the angle of incidence is equal to the Brewster angle, the reflected fields vanish. Inserting (B.21) into (B.7), the magnetic field components in the air and the dielectric are given as:

$$\begin{aligned} \mathbf{H}^i &= \frac{E_z^i}{Z_{w0}} e^{+jk_0 \frac{1}{\sqrt{\epsilon_r+1}} x} e^{-jk_0 \frac{\sqrt{\epsilon_r}}{\sqrt{\epsilon_r+1}} z} \hat{\mathbf{y}} \dots x > 0, \\ \mathbf{H}^t &= \frac{E_z^i}{Z_{w0}} e^{+jk_0 \frac{\epsilon_r}{\sqrt{\epsilon_r+1}} x} e^{-jk_0 \frac{\sqrt{\epsilon_r}}{\sqrt{\epsilon_r+1}} z} \hat{\mathbf{y}} \dots x < 0. \end{aligned} \quad (\text{B.22})$$

The relevant electric fields can be recovered using Maxwell's equations. The solution above is the prototype solution for surface waves guided by a plane interface [90]. Since the magnetic field does not have a component in the assumed direction of propagation along the surface (z -direction), this wave is commonly classified as a TM_z surface wave or hard-polarized wave [89, 90]. Furthermore, for dual polarization (perpendicular) of the incident wave, the Brewster angle does not exist, unless the media possess different magnetic permeabilities, which means that the lossless nonmagnetic dielectric cannot support TE_z waves. Although the above-considered case of plane wave incidence is only a special case of fast waves, and not a true surface wave, other surfaces could be analyzed and characterized using the same methodology, with respect to their surface impedance Z_S and wavenumbers k_x and k_z which support surface wave.

Appendix C. EQUIVALENT SCHEMES OF THE SURFACE WAVEGUIDING STRUCTURES

Surface impedance

Here we extend the discussions from section 5.2 and Appendix B to some more general conductive surfaces which could be characterized by surface impedance:

$$Z_S = R_S + jX_S. \quad (\text{C.1})$$

The surface wave solution occurs when surface impedance equals wave impedance in the air (ratio of the “incident” fields). Therefore, we can make a generalization of (B.11) via Maxwell’s equations, and that way obtain surface impedance. Thus, for TM_z fields in the air:

$$E_z^i = \frac{1}{j\omega\epsilon} \frac{\partial H_y^i}{\partial x} = \frac{-jk_x}{j\omega\epsilon} H_y^i = -\frac{k_x}{k_0} \eta_0 H_y^i = Z_{w0} H_y^i, \quad (\text{C.2})$$

which leads to the more general expression for surface impedance:

$$Z_S = Z_{w0} = -\frac{k_x}{k_0} \eta_0. \quad (\text{C.3})$$

The real part of surface impedance accounts for power loss in the surface, while the reactive part supports surface waves, which can be shown by writing wavenumbers k_x and k_z in the air (5.15) in terms of surface impedance (C.3):

$$k_x = \beta_x - j\alpha_x = -\frac{1}{\eta_0} k_0 Z_S = -\frac{1}{\eta_0} k_0 R_S - j\frac{1}{\eta_0} k_0 X_S,$$

$$k_z = \beta_z - j\alpha_z = \sqrt{k_0^2 - k_x^2} = \frac{k_0}{\eta_0} \sqrt{\eta_0^2 - R_S^2 + X_S^2 + j2R_S X_S}. \quad (\text{C.4})$$

Note that in this nomenclature $\alpha_x > 0$, which ensures the exponential decay in the air away from the surface. This means that for TM_z waves, the surface reactance turns to be inductive. The wave would be more closely bound to the surface (larger α_x) when X_S is large, while small attenuation occurs when the product $R_S X_S$ is small; hence, to obtain long-distance surface wave transmission, the surface needs to have small losses R_S and large inductive reactance X_S [90].

The phase velocity of the wave along the surface in the z -direction is given as:

$$v_{p,z} = \frac{\omega}{\beta_z} \approx \frac{\omega}{k_0} \sqrt{\frac{\eta_0^2}{\eta_0^2 + X_S^2}}. \quad (\text{C.5})$$

When the surface reactance X_S is large, the phase velocity along the surface can become considerably smaller than light, hence the name *slow wave*, which is sometimes used for surface waves [115]. Note that in metal at microwave frequencies, R_S and X_S are in fact both small, which means that although fields do not penetrate (and thereby dissipate) deeply into the metal, in the air (x -direction) the field amplitude does not decrease to a negligible value up to several thousand wavelengths away from metal, since the imaginary part of k_x from (5.15) is very small. Therefore, the wave on the metal itself is too loosely bound to the surface to be of much use in practical surface-wave transmitting systems. The same is also valid for a lossy dielectric. To obtain a practical waveguiding surface, one needs to introduce modifications to the metal, such as covering it with a dielectric (Fig. C-1), or using artificially created periodic structures [46].

The analogous analysis could be provided for TE_z surface waves, which is the dual case to the TM_z case considered above. By duality, the required surface impedance is given as [90]:

$$Z_{S,TE} = \frac{k_0}{k_x} \eta_0. \quad (\text{C.6})$$

Since $\alpha_x > 0$, surface impedance for TE_z waves turns out to be capacitive. Although one-layered surfaces which occur in nature (such as metals or lossy dielectrics) do not themselves possess capacitive surface reactance, surfaces which would support TE_z waves (i.e. capacitive surfaces) can still be easily composed e.g. by covering the metal with a dielectric, which enables the tuning of the surface reactance to the capacitive value.

In Fig. C-1, the metallic ground plane covered with a dielectric, together with its equivalent scheme, are shown. In most cases, the surface impedance of metal (Z_S) is negligible, so metal can often be approximated as a short circuit (PEC). The dielectric acts as an impedance transformer, so by varying the dielectric thickness, the required surface reactance could be obtained. The surface impedance as seen from the air is given as:

$$Z_S' = Z_{w1} \frac{Z_S + jZ_{w1} \tan k_{x1}t}{Z_{w1} + jZ_S \tan k_{x1}t}, \quad (\text{C.7})$$

where Z_S is the surface impedance of metal (which is usually assumed zero in practice), k_{x1} is the x -directed wavenumber in the dielectric, and t is the thickness of the dielectric.

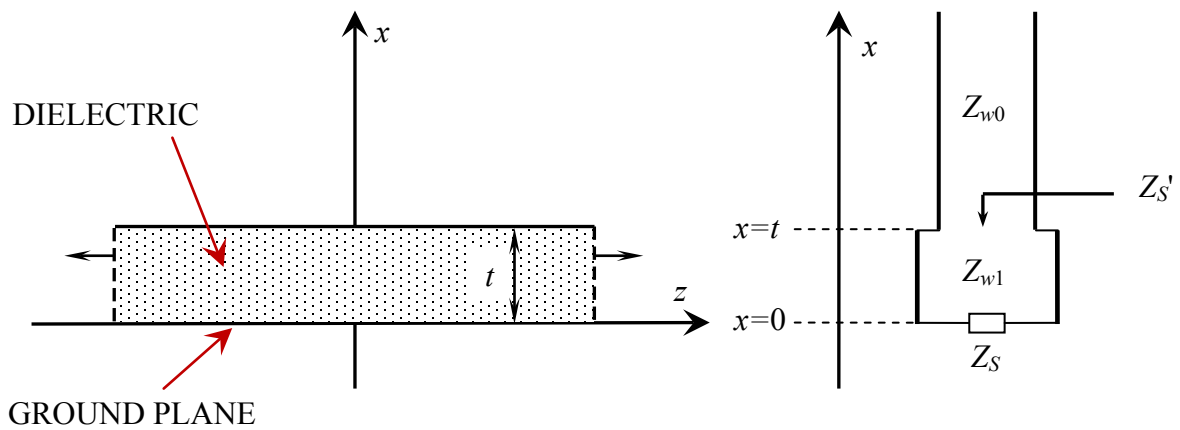


Figure C-1 Dielectric-covered ground plane and its equivalent scheme

Dielectric slab

Although the equivalent transmission line scheme (Fig. C-1) is simple to comprehend, for surfaces which are inhomogeneous in the x -direction, and whose thickness is of the order of the wavelength, there is more than one combination of k_x , k_{x1} and k_z that enable surface wave propagation, and finding them becomes a more complicated task. Here, the principle of full-wave analysis is illustrated for a dielectric slab. It will be shown that only the discrete combinations of k_x , k_{x1} and k_z are allowed to support surface waves.

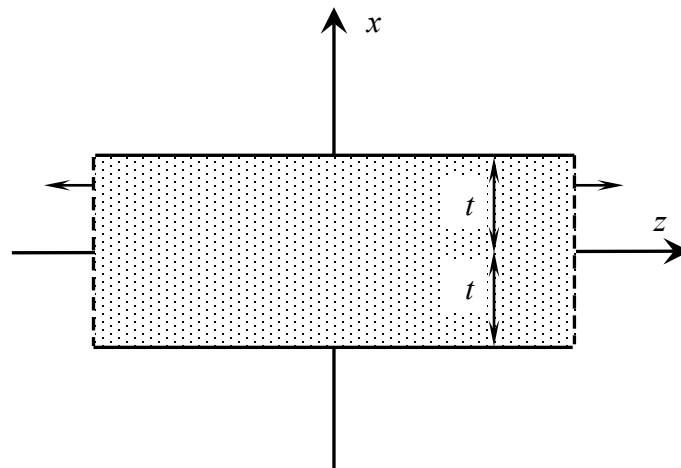


Figure C-2 Dielectric slab

In Fig. C-2, a dielectric slab of the thickness $2t$ is given. It is assumed to extend to infinity in the z - and y - directions, so there is again only one direction of inhomogeneity (x -). It can be shown that the dielectric slab supports both TM_z and TE_z waves. The TM_z fields can be derived starting from the magnetic vector potential $A_z \hat{z}$ and enforcing the boundary conditions

of field continuity at $x=\pm t$ [89]. It turns out that the field components in question are E_x , E_z and H_y , which is in accordance with previous discussions. The magnetic field has only one component in that case, so it is more convenient to start with. In the air ($|x|>t$), it is given as:

$$H_y = A e^{-j(k_x(|x|-t))} e^{-jk_z z}. \quad (C.8)$$

In the dielectric ($|x|<t$), it is given as:

$$H_y = (B \cos k_{x1} x + C \sin k_{x1} x) e^{-jk_z z}, \quad (C.9)$$

where k_{x1} is assumed to be real.

The tangential electric field (E_z) is obtained from

$$E_z = \frac{1}{j\omega\epsilon} \frac{\partial H_y}{\partial x}. \quad (C.10)$$

We separate (C.9) into parts with cosine (even) and with sine (odd), each of which are analysed separately, giving even and odd modes. For the even part, the continuity of magnetic fields at the boundary gives the first equation:

$$A = B \cos k_{x1} t. \quad (C.11)$$

Applying the continuity of the electric field (E_z) on the interface gives the second equation:

$$jk_x \epsilon_r A = k_{x1} B \sin k_{x1} t. \quad (C.12)$$

By dividing (C.11) with (C.12), one gets the transcendental equation for wavenumbers k_x and k_{x1} [89, 90]:

$$jk_x \epsilon_r = k_{x1} \tan k_{x1} t, \quad (C.13)$$

together with the usual requirement for k_z :

$$k_z^2 = k_0^2 - k_x^2 = k_0^2 \epsilon_r - k_{x1}^2. \quad (C.14)$$

These two equations can be solved graphically, as follows. If we wish to obtain the surface wave that decays in the x -direction (the air), the real part of k_x must be zero, so we substitute $k_x = -j\alpha_x$, which leads to decay in the air proportional to $e^{-\alpha_x x}$. Now, (C.13) and (C.14) can be rewritten as:

$$\varepsilon_r (\alpha_x t) = k_{x1} t \tan k_{x1} t,$$

$$(k_{x1} t)^2 + (\alpha_x t)^2 = (k_0 t)^2 (\varepsilon_r - 1). \quad (\text{C.15})$$

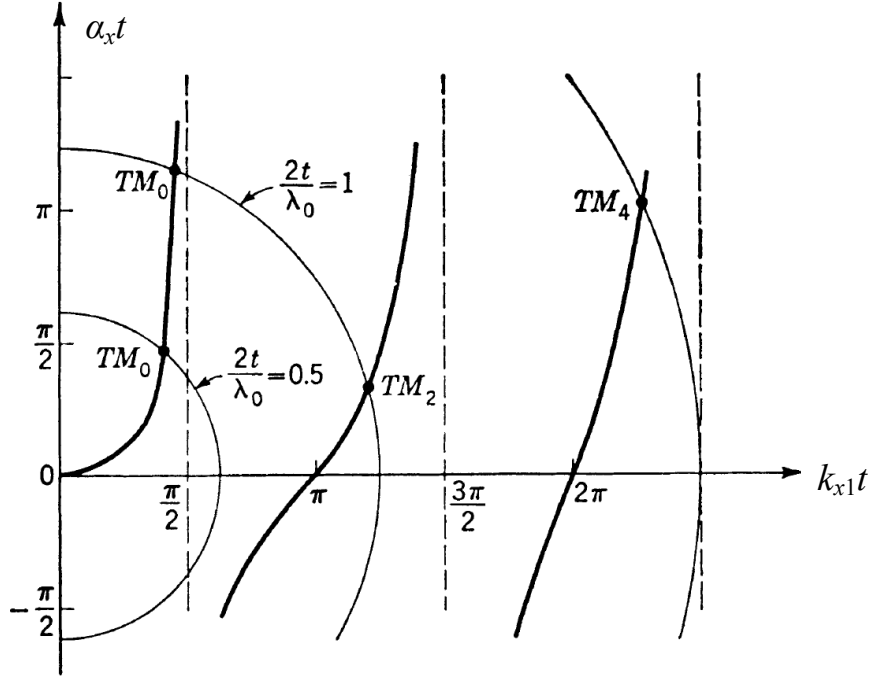


Figure C-3 Example of the graphical solution of the equation for even TM_z surface wavenumbers [90]

The intersection of the two curves gives the possible combinations of wavenumbers $k_x = -j\alpha_x$ and k_{x1} which lead to the surface wave, which is illustrated in Fig. C-3 for $\varepsilon_r = 2.56$ [90]. The first curve is proportional to the tangent, and contains poles at $k_{x1} t = (2n+1)\pi/2$, while the second curve is the circle of the radius $k_0 t \sqrt{\varepsilon_r - 1}$ and with the centre at the origin. Only those intersections of the two curves which lie in the first quadrant (where $\alpha_x > 0$) correspond to proper surface waves, which is equivalent to the requirement:

$$n \cdot \pi \leq k_{x1} t \leq n\pi + \frac{\pi}{2}, \quad (\text{C.16})$$

where n is an integer, and $2n$ by convention gives the name of the considered even mode (i.e. TM_z^0 , TM_z^2 etc.). Two circles are given in Fig. C-3 for the two different slab thicknesses ($2t = \lambda/2$ and $2t = \lambda$). Obviously, by increasing the slab thickness, more and more surface-wave modes can propagate. The so-called cutoff values of k_{x1} occur when $k_z = k_0$ which from (C.14) and (C.13) means that $\tan k_{x1} t = 0$ (i.e. $k_{x1} t = n\pi$), so the cutoff (lowest) frequency of the n -th mode is given as [89, 90]:

$$f = \frac{c}{t} \frac{n}{2\sqrt{\epsilon_r - 1}}, \quad (\text{C.17})$$

where c is the velocity of light in free space. Note that the dominant mode (TM_z^0) has no cutoff frequency, hence it can always propagate, no matter what the dielectric thickness is (it can also be seen in the graphic representation in Fig. C-3 – every circle intersects the tangent curve corresponding to the TM_z^0 mode, regardless of its radius). In a similar manner, the odd TM_z modes, as well as TE_z modes, can be derived.

The equation for surface wave modes for the dielectric slab such as (C.13) can be simply derived in terms of the equivalent transmission line model. Since the dielectric slab is assumed symmetric around $x=0$, the plane of symmetry is replaced with a perfect electric or perfect magnetic conductor, thereby readily obtaining equations for even and odd modes, respectively. Thus, the equation for even TM_z modes can be derived from (C.7) by inserting $Z_S=0$:

$$Z_S' = jZ_{w1} \tan k_{x1}t. \quad (\text{C.18})$$

By inserting the requirement $Z_S' = Z_{w0}$ and using (C.3), one arrives at (C.13) immediately. Similarly, for the odd modes, one inserts $Z_S=\infty$. To derive TE_z modes, the equation (C.6) should be used for Z_{w0} (and of course, the corresponding Z_{w1}). The equivalent circuits for even and odd modes are given in Fig. C-4, while the transcendental equations for both TM_z and TE_z modes are summarized in Table Table C-1.

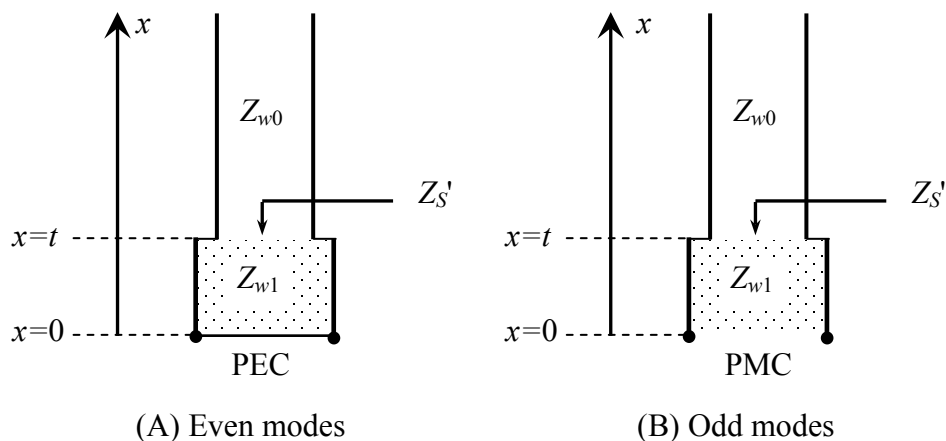


Figure C-4 Equivalent circuits for even and odd modes in the dielectric slab

Table C-1 Modes in the dielectric slab

Mode	Characteristic equation	Z_{w0}	Boundary condition
TM _z even	$jk_x \varepsilon_r = k_{x1} \tan k_{x1} t$	$-\frac{k_x}{k_0} \eta_0$	PEC
TM _z odd	$-jk_x \varepsilon_r = k_{x1} \cot k_{x1} t$	$-\frac{k_x}{k_0} \eta_0$	PMC
TE _z even	$jk_x = k_{x1} \tan k_{x1} t$	$\frac{k_0}{k_x} \eta_0$	PEC
TE _z odd	$-jk_x = k_{x1} \cot k_{x1} t$	$\frac{k_0}{k_x} \eta_0$	PMC

Surface waves in the wave spectrum

As described in the discussions above, surface waves are specific solutions to the wave equation which exist only for discrete combinations of wavenumbers. In addition, there is only a finite number of surface-wave modes for some particular structure. When the source is present, it excites many waves, only few of them being surface waves. To put things into perspective, as an example we consider dielectric-covered ground plane (assumed lossless) and the incident parallel-polarized plane wave excitation. This is the case already illustrated in Fig. C-4 (A), so the solution is analogous to the even TM_z modes in the dielectric slab. Here we analyze this problem from another point of view, in order to identify the possible waves (and thus their wavenumbers) which can exist in the considered configuration. In particular, we consider the plane wave incidence (Fig. C-5) for both real and complex angles.

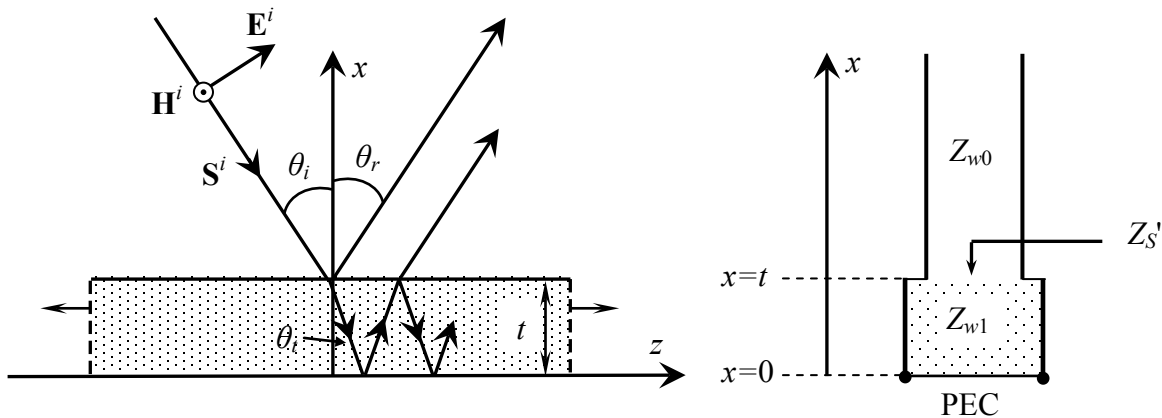


Figure C-5 Dielectric-covered ground plane excited by parallel-polarized plane wave

The wave impedances for TM_z modes are given as:

$$Z_{w0} = -\frac{k_x}{k_0} \eta_0,$$

$$Z_{w1} = -\frac{k_{x1}}{k_1} \eta_1 = -\frac{k_{x1}}{k_0 \epsilon_r} \eta_0. \quad (C.19)$$

The surface impedance at $x=t$ is given as:

$$Z_S' = jZ_{w1} \tan k_{x1}t = j\frac{k_{x1}}{k_0} \frac{\eta_0}{\epsilon_r} \tan(k_{x1}t), \quad (C.20)$$

which leads to the input reflection coefficient:

$$\Gamma = \frac{Z_S' - Z_{w0}}{Z_S' + Z_{w0}} = \frac{k_{x1} \tan(k_{x1}t) + jk_x \epsilon_r}{k_{x1} \tan(k_{x1}t) - jk_x \epsilon_r}. \quad (C.21)$$

We rewrite the relevant wavenumbers in terms of the incident angle θ_i , as in Appendix B; however, here we allow the angle to be both real and complex:

$$k_x = -k_0 \cos \theta_i = \beta_x - j\alpha_x,$$

$$k_z = k_0 \sin \theta_i = \beta_z - j\alpha_z,$$

$$k_{x1} = -k_1 \cos \theta_i = -k_0 \sqrt{\epsilon_r - \sin^2 \theta_i} = \beta_{x1} - j\alpha_{x1}, \quad (C.22)$$

where Snell's law was used to express θ_i . In addition, k_x , k_{x1} and k_z are interdependent as:

$$k_z^2 = k_0^2 - k_x^2 = k_0^2 \epsilon_r - k_{x1}^2. \quad (C.23)$$

Now, we take a look at possible combinations of wavenumbers k_x and k_z . For real angles of incidence, $0 \leq \theta_i \leq \pi/2$ the reflection exists and the modulus of Γ is 1 (meaning that for TM_z , incidence magnetic energy is stored in the dielectric), which gives rise to *fast waves*. In this case k_x and k_z both need to be real, so the corresponding values are:

$$0 \leq \beta_z \leq k_0,$$

$$0 \leq |\beta_x| \leq k_0. \quad (C.24)$$

Note that in eq. (C.24), the modulus of quantity β_x is considered, since both directions of propagation in x -direction need to be taken into account due to the existence of standing waves in that case. The spectrum of values of β_x and β_z is continuous in the given range [129].

The next case occurs when $|\beta_x| > k_0$ which leads to imaginary k_z , i.e. $k_z^2 = -\alpha_z^2$. Here standing waves also occur; however, there is no propagation in the z -direction. These modes are called *evanescent* modes and also form a continuous spectrum:

$$\begin{aligned} k_0 < |\beta_x| \leq \infty, \\ 0 \leq \alpha_z \leq \infty. \end{aligned} \tag{C.25}$$

Finally, there is the case where $\beta_z > k_0$, where k_x is imaginary, i.e. $k_x^2 = -\alpha_x^2$. These are *trapped surface waves*. Note that they are discrete in number and hence form a discrete spectrum, since they also need to satisfy the transcendental equation (C.13). This equation also has solutions with $\alpha_x < 0$, which are the *improper* (“leaky”) waves since they violate the radiation condition by increasing away from the surface. They usually appear in the evaluation of the integral representation of the electric field; however, they need to be treated with caution.

The arbitrary source radiates a spectrum of wavenumbers which in theory contribute to all of the mentioned types of fields [129]. The mentioned cases are shown principally in the complex k_x and k_z planes in Fig. C-6. The surface waves occur for $k_0 < \beta_z < k_1$ which corresponds to $\alpha_x > 0$ and $\alpha_{x1} < 0$, which ensures exponential decay both above and below the surface. Improper waves occur for $\beta_z > k_1$. Furthermore, note that if the dielectric was lossy, then the wavenumbers k_x and k_z would become general complex numbers and the whole complex plane would be exploited [130].

Taking a closer look at (C.21), one can see that the transcendental equation (C.13) for surface waves is contained in the denominator of the reflection coefficient. Therefore, surface waves can be said to occur when the reflection coefficient Γ is infinite, i.e. at the pole of Γ . This means that the “incident” field vanishes, and that only the “reflected” field exists in the air. The same results would, however, be obtained by taking zero of the reflection coefficient, since the sign of k_x (i.e. the sign of wave impedance) would change accordingly. This “zero Γ ” approach was actually taken in studying the Brewster angle in Appendix B, when the field in the air was associated with the “incident” one. Although both approaches are arguably correct and lead to the same results, the association of surface wave with the pole in the reflection coefficient turns out to be more convenient in the further evaluation of the total field excited by the source [90, 131].

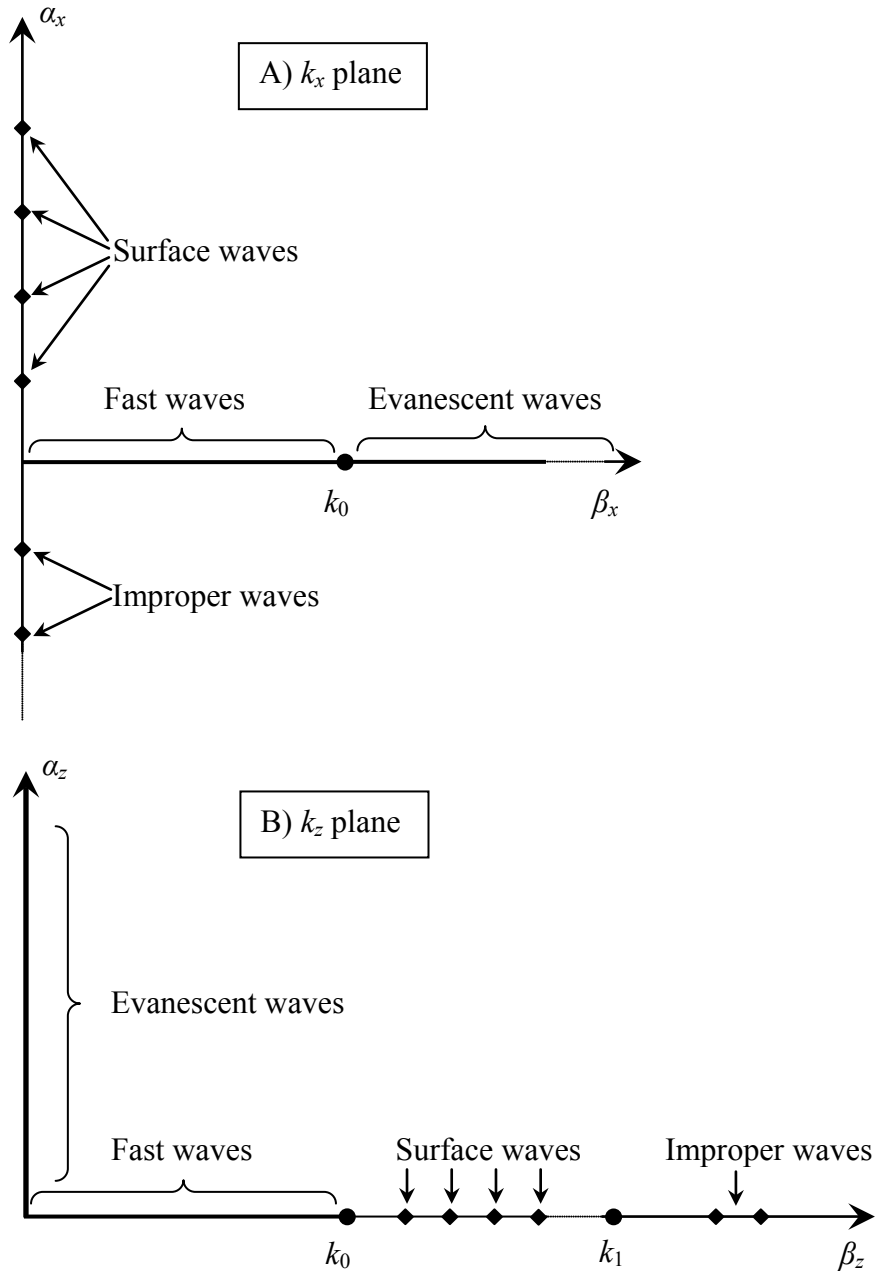


Figure C-6 Principal positions of various wave types of the dielectric-covered ground plane in the k_x and k_z plane (for the case of the lossless dielectric)

REFERENCES

- [1] P. S. Hall and Y. Hao (eds), “Antennas and propagation for body-centric wireless communications”, Artech house, 2006
- [2] A. K. Skrivervik, J. F. Zürcher, O. Staub, J.R. Mosig, “PCS antenna design: The challenge of miniaturization”, IEEE Antennas and Propagation Magazine, Vol. 43, No. 4, pp. 12-26, August 2001.
- [3] (2012) T. Starner, “The cyborgs are coming or the real personal computer”, technical report [Online]. Available: <http://hd.media.mit.edu/tech-reports/TR-318-ABSTRACT.html>
- [4] O. Amft, P. Lukowicz, “From backpacks to smartphones: past, present, and future of wearable computers”, IEEE Pervasive Computing, Vol. 8, No. 3, pp.8-13, 2009
- [5] T. Starner, “The challenges of wearable computing: Part 1”, IEEE Micro, Vol. 21, No. 4, pp. 44-52, 2001
- [6] (2012) Augmented reality and wearable computer research [Online]. Available: www.tinmith.net
- [7] (2012) [Online]. Available: <http://www.eurotech.com/en/products/devices>
- [8] B.H. Thomas, “Have we achieved the ultimate wearable computer?”, in Proceedings of 16th International Symposium on Wearable Computers, pp.104-107, Newcastle (UK), 2012
- [9] (2012) [Online]. Available: <http://www.apple.com/ipod/nike/>
- [10] (2012) [Online]. Available: <http://sensewear.bodymedia.com/>
- [11] T. Kaija, J. Lilja, and P. Salonen, “Exposing textile antennas for harsh environment”, in Proceedings of Milcom 2010, pp. 737-742, San Jose (USA), 2010.
- [12] R. W. Adler, D. S. Gibbs, J. E. Lebaric, S.S. Schwarz, “Helmet mounted UHF antenna for mobile user objective system (MUOS)”, in Proceedings of Milcom 2002, , pp. 311-315, Anaheim (USA), 2002.
- [13] J. S. Roh,, “Embroidered wearable multiresonant folded dipole antenna for fm reception”, IEEE Antennas and Wireless Propagation Letters, Vol. 9, pp.803-806, 2010
- [14] D. Psychoudakis, G-Y. Lee, C-C Chen, and J. L. Volakis, “Military UHF body-worn antennas for armored vests”, in Proceedings of EuCAP 2010, pp. 1-4, Barcelona (Spain), 2010

- [15] G.Y. Lee, D. Psychoudakis, C.C. Chen, and J.L. Volakis, "Omni-directional vest-mounted body-worn antenna system for UHF operation", *IEEE Antennas and Wireless Propagation Letters*, pp. 581-583, 2011
- [16] J. E. Lebaric, R. W. Adler, M. E. Limbert, "Ultra-wideband, zero visual signature RF vest antenna for man-portable radios", in *Proceedings of Milcom 2001*, , pp. 1291-1294, Vienna, Virginia (USA), 2001
- [17] T. Kellomaki, J. Heikkinen, M. Kivikoski, "Wearable antennas for FM reception", in *Proceedings of EuCAP 2006*, pp. 1-6, Nice (France), 2006
- [18] J. C. G. Matthews, G. Pettit, "Development of flexible, wearable antennas", in *Proceedings of EuCAP 2009*, pp. 273-277, Berlin (Germany), 2009
- [19] C. Hertleer, H. Rogier, L. Valozzi, L. Van Langenhove, "A textile antenna for off-body communication integrated into protective clothing for firefighters", *IEEE Transactions on Antennas and Propagation*, Vol. 57, No. 4, pp. 919-925, 2009
- [20] L.Vallozzi, P. Van Torre, C. Hertleer, H. Rogier, M. Moeneclaey, J. Verhaevert, "Wireless communication for firefighters using dual-polarized textile antennas integrated in their garment", *IEEE Transactions on Antennas and Propagation*, Vol. 58, No. 4, pp. 1357-1368, 2010
- [21] L. Vallozzi, W. Vandendriessche, Hendrik Rogier, C. Hertleer, M. L. Scarpello, "Wearable textile GPS antenna for integration in protective garments", in *Proceedings of EuCAP 2010*, pp.1-4, Barcelona (Spain), 2010
- [22] T. F. Kennedy, P.W. Fink, A.W. Chu, G.F. Studor, "Potential space applications for body-centric wireless and e-textile antennas", in *Proceedings of IET Seminar on Antennas and Propagation for Body-Centric Wireless Communications*, pp. 77-83, London (UK), 2007
- [23] T. F. Kennedy et al, "Body-worn e-textile antennas: the good, the low-mass, and the conformal", *IEEE Transactions on Antennas and Propagation*, Vol. 57, No. 4, pp. 910-918, 2009
- [24] A. Kiourti, K. S. Nikita, "A review of implantable patch antennas for biomedical telemetry: challenges and solutions", *IEEE Antennas and Propagation Magazine*, Vol. 54, No. 3, pp. 210-228, 2012
- [25] H. S. Savci et al, "MICS transceivers: regulatory standards and applications", in *Proceedings of IEEE SoutheastCon 2005*, pp. 179-182, Fort Lauderdale (Florida, USA), 2005

- [26] H. Higgins, "Body implant communication-making it possible", in Proceedings of EuCAP 2007, pp. 1-4, Edinburgh (UK), 2007
- [27] H. Higgins, "Implant communication – out of the lab, into patients", in Proceedings of IET Seminar on Antennas and Propagation for Body-Centric Wireless Communications, pp. 1-5, London (UK), 2009
- [28] T. Karacolak, R. Cooper, E. Topsakal, "Electrical properties of rat skin and design of implantable antennas for medical wireless telemetry", IEEE Transactions on Antennas and Propagation, Vol. 57, No. 9, pp. 2806-2812, 2009
- [29] T. Karacolak, R. Cooper, J. Butler, S. Fisher, and E. Topsakal, "In vivo verification of implantable antennas using rats as model animals," IEEE Antennas and Wireless Propagation Letters, Vol. 9, pp. 334-337, 2010
- [30] J. Abadia, F. Merli, J. F. Zurcher, J. R. Mosig, A. K. Skrivervik, "3D-spiral small antenna design and realization for biomedical telemetry in the MICS band", Radioengineering, Vol. 18, No. 4, pp. 359-367, 2009
- [31] F. Merli et al, "Design, realization and measurements of a miniature antenna for implantable wireless communication systems", IEEE Transactions on Antennas and Propagation, Vol. 59, No. 10, pp. 3544-3555, 2011
- [32] A. K. Skrivervik, F. Merli, "Design strategies for implantable antennas", in Proceedings of Antennas and Propagation Conference (LAPC), pp. 1-5, Loughborough (UK), 2011
- [33] T. Alves et al., "Analytical propagation modelling of BAN channels based on the creeping wave theory", in Proceedings of EuCAP 2010, pp. 1-5, Barcelona (Spain), 2010
- [34] A. Fort et al., "A body area propagation model derived from fundamental principles: analytical analysis and comparison with measurements", IEEE Transactions on Antennas and Propagation, Vol. 28, pp. 503-514, 2010
- [35] N. H. M. Rais et al., "A review of wearable antenna", in Proceedings of Antennas and propagation conference (LAPC) 2009, pp. 225-228, Loughborough (UK), 2009
- [36] T. G. Zimmerman, "Personal area networks: Near-field intra-body communication", IBM Systems Journal, Vol. 35, No.3&4, pp.609-617, 1996
- [37] K. Fujii, M. Takahashi, and K. Ito, "Electric field distributions of wearable devices using the human body as a transmission channel," IEEE Transactions on Antennas and Propagation, Vol. 55, No. 7, pp. 2080-2087, 2007

- [38] P. S. Hall and Y. Hao, "Antennas and propagation for body-centric communications", in Proceedings of EuCAP 2006, pp. 1-7, Nice (France), 2006
- [39] K. Ito, "Basics of antennas for body-centric wireless communications and human-body phantoms", European School of Antennas: Body-centric wireless communications, London (UK), 2011
- [40] P. Salonen, Y. Fan, Y. Rahmat-Samii, M. Kivikoski "WEBGA - wearable electromagnetic band-gap antenna", Antennas and Propagation Society International Symposium (ISAP), Vol. 1, pp. 451-454, Sendai (Japan), 2004
- [41] Z. Duan, D. Linton, W. Scanlon, G. Conway, "Improving wearable slot antenna performance with EBG structures", in Proceedings of Antennas and Propagation Conference (LAPC), pp. 173-176, Loughborough (UK), 2008
- [42] S. Zhu, R. Langley, "Dual-band wearable textile antenna on an EBG substrate", IEEE Transactions on Antennas and Propagation, Vol. 57, No. 4, pp. 926-935, 2009
- [43] N. Chahat, M. Zhadobov, R. Sauleau, K. Mahdjoubi, "Improvement of the on-body performance of a dual-band textile antenna using an EBG structure", in Proceedings of Antennas and Propagation Conference (LAPC) 2010, pp. 465-468, Loughborough (UK), 2010
- [44] P. S. Kildal, A. A. Kishk, S. Maci, "Special issue on artificial magnetic conductors, soft/hard surfaces, and other complex surfaces", IEEE Transactions on Antennas and Propagation, Vol. 53, No. 1, pp. 2-7, 2005
- [45] Y. Rahmat-Samii, H. Mosallei, "Electromagnetic band-gap structures: classification, characterization, and applications", in Proceedings of 2001 International Conference on Antennas and Propagation (ICAP), Vol. 2, pp.560-564 , Manchester (UK), 2001
- [46] D. Sievenpiper et al., "High-impedance electromagnetic surfaces with a forbidden frequency band", IEEE Transactions on Microwave Technology and Techniques, Vol. 47, No.11, pp. 2059-2074, 1999
- [47] G. A. Conway, W. S. Scanlon, "Antennas for over-body-surface communication at 2.45 GHz", IEEE Transactions on Antennas and Propagation, Vol. 57, No. 4, pp. 844-855, 2009
- [48] P. S. Hall, Y. Hao and S. L. Cotton, "Advances in antennas and propagation for body-centric wireless communications", in Proceedings of EuCAP 2010, pp. 1-7, Barcelona (Spain), 2010

- [49] R. Khouri, P. Ratajczak, P. Brachat, R. Staraj, "A thin surface-wave antenna using a via-less EBG structure for 2.45 GHz on-body communication systems", in Proceedings of EuCAP 2010, pp. 1-4, Barcelona (Spain), 2010
- [50] J. Kelly, L. Ford, R. Langley, "Slotline structure for on/off-body communications at 2.45 GHz", in Proceedings of EuCAP 2011, pp. 525-529, Rome (Italy), 2011
- [51] R. Langley, K. L. Ford, H. J. Lee, "Switchable on/off-body communication at 2.45GHz using textile microstrip patch antenna on stripline", in Proceedings of EuCAP 2012, pp. 728 - 731, Prague (Czech Republic), 2012
- [52] I. Khan, P. S. Hall, "Experimental evaluation of MIMO capacity and correlation for narrowband body-centric wireless channels", IEEE Transactions on Antennas and Propagation, Vol. 58, pp.195-202,2010
- [53] G. Adamiuk, T. Zwick, W. Wiesbeck, "UWB antennas for communication systems", in Proceedings of the IEEE, Vol. 100, No. 7, pp. 2308-2321, 2012
- [54] W. Wiesbeck, G. Adamiuk, C. Sturm, "Basic properties and design principles of UWB antennas", Proceedings of the IEEE, Vol. 97, No. 2, pp. 372-385, 2009
- [55] N. Chahat, M. Zhadobov, R. Sauleau, K. Ito, "Design and characterization of an UWB wearable antenna", in Proceedings of Antennas and propagation conference (LAPC) 2010, pp. 461-464, Loughborough (UK), 2010
- [56] N. Chahat, M. Zhadobov, R. Sauleau, K. Ito, "A compact planar UWB antenna for on-body communications", in Proceedings of EuCAP 2011, pp. 728-731, Rome (Italy), 2011
- [57] A. Alomainy, A. Sani, A. Rahman, J. G. Santas, Y. Hao, "Transient characteristics of wearable antennas and radio propagation channels for ultrawideband body-centric wireless communications", IEEE Transactions on Antennas and Propagation, Vol. 57, pp.875-884, 2009
- [58] N. Chahat, M. Zhadobov, L. Le Coq, S. I. Alekseev, R. Sauleau, "Characterization of the interactions between a 60-GHz antenna and the human body in an off-body scenario", IEEE Transactions on Antennas and Propagation, Vol. 60, No. 12, pp. 5958-5965, 2012
- [59] N. Chahat, M. Zhadobov, L. Le Coq, R. Sauleau, "Wearable endfire textile antenna for on-body communications at 60 GHz", IEEE Antennas and Wireless Propagation Letters, Vol. 11, pp. 799-802, 2012

- [60] N. Chahat, M. Zhadobov, S. A. Muhammad, L. Le Coq, R. Sauleau, “ 60-GHz textile antenna array for body-centric communications ”, IEEE Transactions on Antennas and Propagation, accepted for publication, 2012
- [61] P. F. M. Smulders, “Statistical characterization of 60-GHz indoor radio channels”, IEEE Transactions on Antennas and Propagation, Vol. 57, No. 10, pp. 2820-2829, 2009
- [62] S. L. Cotton, W. G. Scanlon, B. K. Madahar, “Simulation of millimetre-wave channels for short-range body to body communications”, in Proceedings of EuCAP 2010, pp. 1-5, Barcelona (Spain), 2010
- [63] M. Gallo et al., “Simulation and measurement of dynamic on-body communication channels”, IEEE Transactions on Antennas and Propagation, Vol. 59, No. 2, pp. 629-629, 2011
- [64] J. A. Nanzer, P.T. Callahan, M. L. Dennis, T. R. Clark Jr., “Photonic signal generation for millimeter- wave communications”, Johns Hopkins APL Technical Digest, Vol. 30, No. 4, pp. 299-308, 2012
- [65] C. Park, T. S. Rappaport, “Short-range wireless communications for next-generation networks: UWB, 60 GHz, millimeter-wave WPAN, and ZigBee”, IEEE Wireless Communications, Vol. 14, No. 4, pp. 70-78, 2007
- [66] B. Sanz-Izquierdo, J.C. Batchelor, “WLAN jacket mounted antenna”, in Proceedings of 2007 International Workshop on Antenna Technology: Small and Smart Antennas Metamaterials and Applications (IWAT), pp. 57-60, Cambridge (UK), 2007
- [67] B. Sanz-Izquierdo, J. C. Batchelor, M. I. Sobhy, “Button antenna on textiles for wireless local area network on body applications”, IET Microwaves, Antennas and Propagation, Vol. 5, No. 11, pp. 1980-1987 , 2010
- [68] M. Mantash, A. C. Tarot , S. Collardey, K. Mahdjoubi, “Zip based monopole antenna for wearable communication systems”, in Proceedings of EuCAP 2012, pp. 762-764, Prague (Czech Republic), 2012
- [69] K. Karlsson, J. Carlsson, “Wideband characterization of fabrics for textile antennas”, in Proceedings of EuCAP 2012, pp. 1358-1361, Prague (Czech Republic), 2012
- [70] D. L. Paul, H. Giddens, M. G. Paterson, G. S. Hilton, J. P. McGeehan, “Impact of body and clothing on a wearable textile dual band antenna at digital television and wireless communications bands”, IEEE Transactions on Antennas and Propagation, accepted for publication, 2012

- [71] J. Lilja, P. Salonen, "Textile material characterization for SoftWear antennas", in Proceedings of Milcom 2009, pp.1-7, Boston (USA), 2009
- [72] J. Trajkovikj, B. Fuchs, A. K. Skrivervik, "Study of wearable (body-worn) antennas - Intermediate report I.: State of the art and study scenarios", technical report, EPFL, 2011
- [73] Y. Ouyang, W. J. Chappell, "High frequency properties of electro-textiles for wearable antenna applications", IEEE Transactions on Antennas and Propagation, Vol. 56, No. 2, pp. 381-389, 2008
- [74] P. Salonen, Y. Rahmat-Samii, M. Schafth, M. Kivikoski, "Effect of textile materials on wearable antenna performance: a case study of GPS antennas", in Proceedings of IEEE International Symposium on Antennas and Propagation (ISAP), Sendai (Japan), Vol. 1, pp. 459-462, 2004
- [75] P. Salonen, Y. Rahmat-Samii, "Textile Antennas: effects of antenna bending on input matching and impedance bandwidth", in Proceedings of EuCAP 2006, pp. 1-5, Nice (France)
- [76] P. Salonen, Y. Rahmat-Samii, "Textile antennas: effects of antenna bending on input matching and impedance bandwidth", IEEE Aerospace and Electronic Systems Magazine, Vol. 22, No. 3, pp. 10-14, 2007
- [77] Q. Bai, R. Langley, "Crumpling of PIFA textile antenna", IEEE Transactions on Antennas and Propagation, Vol. 60, No. 1, pp. 63-70, 2012
- [78] H. R. Khaleel, H. M. Al-Rizzo, Y. A. Rahmatallah, D. G. Rucker, S. Mohan, "An investigation on the effect of bending on UC-PBG structures", in Proceedings of 2011 IEEE International Symposium on Antennas and Propagation (APSURSI), pp. 1796-1799, Spokane (USA), 2011
- [79] I. Locher, M. Klemm, T. Kirstein, G. Tröster, "Design and characterization of purely textile patch antennas", IEEE Transactions on Advanced Packaging, Vol. 29, No. 4, pp. 777-788, 2006
- [80] A. Chauraya et al., "Addressing the challenges of fabricating microwave antennas using conductive threads", in Proceedings of EuCAP 2012, pp. 1365-1367, Prague (Czech Republic), 2012
- [81] (2012) [Online]. Available: <http://www.shieldextrading.net>
- [82] J. C. G. Matthew, B. Pirollo, A. Tyler, G. Pettitt, "Body wearable antennas for UHF/VHF", in Proceedings of Antennas and Propagation Conference (LAPC), pp. 357- 360, Loughborough (UK), 2008

- [83] J. S. Roh, Y. S. Chi, T. J. Kang, "Wearable textile antennas", *International Journal of Fashion Design, Technology and Education*, Vol. 3, No. 3, pp.135-153, 2010
- [84] K. Ito, "Human body phantoms for evaluation of radiation of wearable antennas", in *Proceedings of EuCAP 2007*, pp. 1-6, Edinburgh (UK), 2007
- [85] The INTERPHONE Study Group, "Brain tumours risk in relation to mobile telephone use: results of the INTERPHONE international case-control study", *International Journal of Epidemiology*, Vol. 39, pp. 675-694, June 2010
- [86] R. Walsh. (2010) Cell Phones and Cancer: A Study's Muddled Findings.[Online]. Available: <http://www.time.com/time/health/article/0,8599,1989740,00.html>
- [87] ICNIRP Guidelines; Guidelines for limiting exposure to time-varying electric, magnetic, and electromagnetic fields (up to 300 GHz), *Health Physics*, Vol. 74, No. 4, pp. 494-552, April 1998
- [88] F. Merli, "Implantable antennas for biomedical applications", PhD Thesis, EPFL, 2011
- [89] C. A. Balanis, "Advanced engineering electromagnetics", John Wiley&Sons, 1989
- [90] R. E. Collin, "Field theory of guided waves", 2nd Ed., John Wiley&Sons, 1991
- [91] E. J. Rothwell, M. J. Cloud, "Electromagnetics", CRC Press, 2001
- [92] (2012) An Internet resource for calculation of dielectric parameters of body tissues. [Online]. Available: <http://niremf.ifac.cnr.it/tissprop/>
- [93] (2012). European Commission-Scientific Committee on Consumer Products, "Opinion on diethylene glycol monobutyl ether" [Online]. Available: http://ec.europa.eu/health/ph_risk/committees/04_sccp/docs/sccp_o_081.pdf
- [94] K. Fukunaga, S. Watanabe, Y. Yamanaka, "Dielectric properties of tissue-equivalent liquids and their effects on specific absorption rate", *IEEE Transactions on Electromagnetic Compatibility*, Vol. 46, No. 1, pp. 126-129, 2004
- [95] M. Y. Kanda, M. Ballen, S. Salins, C.K. Chou, Q. Balzano, "Formulation and characterization of tissue equivalent liquids used for RF densitometry and dosimetry measurements", *IEEE Transactions on Microwave Theory and Techniques*, Vol. 52, No. 8, pp. 2046-2056, 2004
- [96] N. Chahat, M. Zhadobov, R. Sauleau, "Broadband tissue-equivalent phantom for BAN applications at millimeter waves", *IEEE Transactions on Microwave Theory and Techniques*, Vol. 60, No. 7, pp. 2259-2266, 2012
- [97] T. Kobayashi, T. Nojima, K. Yamada, S. Uebayashi, "Dry phantom composed of ceramics and its application to SAR estimation", *IEEE Transactions on Microwave Theory and Techniques*, Vol. 41, No. 1, pp. 136-140, 1993

- [98] (2012) Schmid&Partner Engineering AG homepage. [Online]. Available: <http://www.speag.com/>
- [99] (2012) The CST website. [Online]. Available: <http://www.cst.com/>
- [100] J. Bešlić, “Širokopojasne tekstilne antene u blizini modela ljudskog tijela”, Master thesis No. 441, University of Zagreb, FER, 2012 (In Croatian)
- [101] J. Bartolić, Z. Šipuš, S. Škokić, T. Debožović, D. Crnogorac, “EM radiation analysis of electrical dipole in close vicinity of dissipative object”, in Proceedings on IEEE International Conference on Portable Information Devices (PORTABLE 2007), pp. 1-5, Orlando (USA), 2007
- [102] B. Ivšić, D. Bonefačić, J. Bartolić, A. Skrivervik, J. Trajkovikj, “Design and analysis of planar UHF wearable antenna”, in Proceedings of CARE Workshop at EuCAP 2012, pp. 1-4, Prague (Czech Republic), 2012
- [103] B. Ivšić, D. Bonefačić, J. Bartolić, “Reconfigurable pico-cell antenna array for indoor coverage in GSM 900 band.”, Radioengineering 18, No.4, pp. 388-394, 2009
- [104] B. Ivšić, D. Bonefačić, J. Bartolić, “Simple electromagnetic sensor for simultaneous measurement of three orthogonal linear polarizations”, in Proceedings of EuCAP 2010, pp. 1-5, Barcelona (Spain), 2010.
- [105] R. C. Hansen, R. E. Collin, “Small antenna handbook”, John Wiley&Sons, 2011
- [106] O. Staub, “Electrically small antennas”, PhD Thesis, EPFL, 2001
- [107] M. Abramowitz, I. A. Stegun (eds), “Handbook of mathematical functions”, Dover Publications, 1965
- [108] R. F. Harrington, “Time-harmonic electromagnetic fields”, IEEE Press - Reissue, John Wiley&Sons, 2001
- [109] M. Cabedo-Fabres, E. Antonino-Daviu, A. Valero-Nogueira, M. F. Bataller, “The theory of characteristic modes revisited: A contribution to design of antennas for modern applications”, IEEE Antennas and Propagation Magazine, Vol. 49, No. 5, pp. 52-68, 2007
- [110] A. G. Derneryd, “Linearly polarized microstrip antennas”, IEEE Transactions on Antennas and Propagation, Vol. 24, No. 6, pp. 846-850, 1976
- [111] J. Bartolić, “Mikrovalna elektronika”, Graphis, 2012. (in Croatian)
- [112] C. A. Balanis, “Antenna theory: Analysis and design”, 3rd Ed., John Wiley&Sons, 2005
- [113] N. Chahat, G. Valerio, M. Zhadobov, R. Sauleau, “On-body propagation at 60 GHz”, IEEE Transactions on Antennas and Propagation, accepted for publication, 2013

- [114] A. Ishimaru, "Electromagnetic wave propagation, radiation and scattering", Prentice Hall, 1991
- [115] J. D. Joannopoulos et al., "Photonic crystals: molding the flow of light", 2nd Ed., Princeton University Press, 2008
- [116] J. Wait, "Electromagnetic radiation from cylindrical structures", Peter Peregrinus Ltd., 1988
- [117] J. Wait, "The ancient and modern history of EM ground-wave propagation", IEEE Antennas and Propagation Magazine, Vol. 40, No. 5, pp. 7-24, 2008
- [118] A. Lea, P. Hui, J. Ollikainen, R. G. Vaughan, "Propagation between on-body antennas", IEEE Transactions on Antennas and Propagation, Vol. 57, No. 11, pp. 3619-3627, 2009
- [119] B. Ivšić, Z. Šipuš, S. Hrabar, "Analysis of uniaxial multilayer cylinders used for invisible cloak realization", IEEE Transactions on Antennas and Propagation, Vol. 57, No. 5, 1521-1527, 2009
- [120] S. Maci et al, "Advanced mathematic for antenna analysis", ESoA Coursebook, 2008
- [121] R. Harrington, "Time-harmonic electromagnetic fields", IEEE Press, 2001
- [122] Z. Sipus, "Analysis of planar and circular cylindrical multilayers structures with application to soft and hard surfaces", PhD Thesis, Chalmers University of Technology, Gothenburg, 1997
- [123] R. Paknys, "Evaluation of Hankel functions with complex argument and complex order", IEEE Transactions on Antennas and Propagation, Vol. 40, No. 5, pp. 569-578, 1992
- [124] B. Ivsic, I. Vujica, D. Bonefačić, J. Bartolić, Z. Šipuš, "On-body wireless link investigation", in Proceedings of EuCAP 2013, pp. 1-4, Gothenburg (Sweden), 2013
- [125] I. Bubalo; B. Ivšić, D. Bonefačić, "Wearable Pi-Slot Microstrip Antenna for Applications in UHF Band", in Proceedings of Radioelektronika 2012, pp. 175-178, Brno (Czech Republic), 2012
- [126] G. Golemac, "Tekstilna mikrotrakasta antena", Master thesis No. 464, University of Zagreb, FER, 2013 (In Croatian)
- [127] B. Ivšić, Z. Šipuš, S. Hrabar, "Performance of uniaxial multilayer cylinders and spheres used for invisible cloak realization", in Proceedings of EuCAP 2010, pp. 1092-1096, Rome (Italy), 2010.
- [128] J. A. Stratton, *Electromagnetic Theory*, IEEE Press - Reissue, John Wiley&Sons, 2007

- [129] J. Brown, "The types of waves that may exist near a guiding surface", Proceedings of IEE- Part III: Radio and Communication Engineering, Vol. 100, No.68, pp. 363-364, 1953
- [130] M. J. Neve, R. Paknys, "A technique for approximating the location of surface- and leaky-wave poles for a lossy dielectric slab", IEEE Transactions on Antennas and Propagation, Vol. 54, No.1, pp. 115-120, 2006
- [131] O. Balosso, J. Sokoloff, Sylvain Bolioli, "Brief overview about surface wave theory and applications", in Proceedings of ANTEM 2012, pp. 1-7, Toulouse (France), 2012

ABOUT THE AUTHOR

Branimir Ivšić was born in 1982 in Zagreb, Croatia, where he completed his primary and secondary school. In the year 2001 he began his graduate study in the University of Zagreb, Faculty of Electrical Engineering and Computing and in 2003, after completing the fundamental part of study he attended the program "Wireless communications and professional electronic". He graduated in November 2006, defending the graduate thesis "Electromagnetic wave polarization in optical fiber communication and sensor systems", under the supervision of Prof. Zvonimir Šipuš.

In the year 2007 he began postgraduate study in the University of Zagreb, Faculty of Electrical Engineering and Computing. In July 2007 he started to work in the same faculty as a research assistant in the Department of Wireless Communications, within the scientific project "Multifunctional antennas in communication and radar systems" coordinated by Professor Juraj Bartolić and funded by financed by the Ministry of Science, Education and Sports of the Republic of Croatia. As a doctoral supervisor Professor Davor Bonefačić was appointed. During his postgraduate study he has participated in research in the area of electromagnetic scattering and small antennas, as well as in the area of body-centric communication systems which are his current research topics. He is an author or coauthor of several scientific papers within his area of research, that are published in scientific journals and presented at international conferences. He attended several courses within the program European School of Antennas while 2011 he was in secondment to Ecole Polytechnique Federale de Lausanne (EPFL), Lausanne, Switzerland, where he has participated in research in wearable antennas.

He also deals a bit with music, having finished courses in playing violin and double bass. He speaks English fluently. He is a member of IEEE society.

AUTHOR'S PUBLICATIONS

A) Journal papers

1. B. Ivšić, Z. Šipuš, S. Hrabar, "Analysis of uniaxial multilayer cylinders used for invisible cloak realization", IEEE Transactions on Antennas and Propagation, Vol. 57, No. 5, 1521-1527, 2009
2. B. Ivšić, T. Komljenović, Z. Šipuš, "Optimization of uniaxial multilayer cylinders used for invisible cloak realization", IEEE Transactions on Antennas and Propagation, Vol. 58, No. 10, 3397-3401, 2010
3. B. Ivšić, D. Bonefačić, J. Bartolić, "Reconfigurable pico-cell antenna array for indoor coverage in GSM 900 band.", Radioengineering 18, No.4, pp. 388-394, 2009

B) Conference papers

1. B. Ivšić, Z. Šipuš, "Analysis of uniaxial multilayer cylinders used for invisible cloak realization", in Proceedings of 19th International Conference on Applied Electromagnetics and Communications (ICECOM), pp. 193-196, Dubrovnik (Croatia), 2007
2. B. Ivšić, Z. Šipuš, J. Bartolić, "Bandwidth of invisible cloak realized with split ring resonators", in Proceedings of the 14th Conference on Microwave Techniques (COMITE), pp.279-282, Prague (Czech Republic), 2008
3. B. Ivšić, D. Bonefačić, J. Bartolić, "New stacked patch antenna for polarisation and radiation pattern diversity", in Proceedings of EuCAP 2009, pp. 2664-2664, Berlin (Germany), 2009
4. B. Ivšić, D. Bonefačić, J. Bartolić, "3D electromagnetic sensor based on shorted stacked patches", in Proceedings of ELMAR 2009, pp. 321-325, Zadar (Croatia), 2009
5. M. Banožić, J. Bartolić, B. Ivšić, T. Debogović, "Dual band planar folded monopole", in Proceedings of 2010 International Workshop on Antenna Technology: Small Antennas, Innovative Structures and Materials (IWAT), pp. 1-4, Lisabon (Portugal), 2010

6. B. Ivšić, D. Bonefačić, J. Bartolić, "Simple electromagnetic sensor for simultaneous measurement of three orthogonal linear polarizations", in Proceedings of EuCAP 2010, pp. 1-5, Barcelona (Spain), 2010
7. B. Ivšić, T. Komljenović, Z. Šipuš, "Time and frequency domain analysis of uniaxial multilayer cylinders used for invisible cloak realization", in Proceedings of 20th International Conference on Applied Electromagnetics and Communications (ICECOM), pp. 1-4, Dubrovnik (Croatia), 2010
8. B. Ivšić, T. Komljenović, Z. Šipuš, "Performance of uniaxial multilayer cylinders and spheres used for invisible cloak realization", in Proceedings of EuCAP 2011, pp. 1092-1096, Rome (Italy), 2011
9. B. Ivšić, D. Bonefačić, J. Bartolić, "Performance of electromagnetic sensor based on shorted stacked patches", in Proceedings of EuCAP 2011, pp. 452-455, Rome (Italy), 2011
10. Z. Šipuš, B. Ivšić, T. Komljenović, S. Hrabar, "Feasibility study of uniaxial structures used for invisible cloak design", in Proceedings of 2011 IEEE International Symposium on Antennas and Propagation (APSURSI), pp. 2869-2871, Spokane (USA), 2011
11. B. Ivšić, D. Bonefačić, J. Bartolić, A. Skrivervik, J. Trajković, "Design and analysis of planar UHF wearable antenna", in Proceedings of CARE Workshop at EuCAP 2012, pp. 1-4, Prague (Czech Republic), 2012
12. D. Bojanjac, B. Ivšić, T. Komljenović, Z. Šipuš, "Performance of uniaxial multilayer cylinders used for invisible cloak realization", in Proceedings of EuCAP 2012, pp. 2664-2668, Prague (Czech Republic), 2012
13. I. Bubalo, B. Ivšić, D. Bonefačić, "Wearable pi-slot microstrip antenna for applications in UHF band", in Proceedings of Radioelektronika 2012, pp. 175-178, Brno (Czech Republic), 2012
14. Z. Sriča, B. Ivšić, D. Bonefačić, "Dual-band microstrip antenna for GSM applications", in Proceedings of ELMAR 2012, pp. 293-298, Zadar (Croatia), 2012
15. B. Ivšić, I. Vujica, D. Bonefačić, J. Bartolić, Z. Šipuš, "On-body wireless link investigation", in Proceedings of EuCAP 2013, pp. 1-4, Gothenburg (Sweden), 2013

C) Abstracts

1. S. Hrabar, I. Krois, B. Ivšić, D. Zaluški, G. Pavlaković, “Active dispersionless ‘plasmonic’ metamaterial – a step towards broadband cloaking”, in Proceedings of the 2008 IEEE AP-S International Symposium and USNC/URSI National Radio Science Meeting, pp.243, San Diego (USA), 2008
2. B. Ivšić, Z. Šipuš, S. Hrabar, J. Bartolić, “Analysis of uniaxial multilayer cylinders used for invisible cloak realization”, in Proceedings of the 2008 IEEE AP-S International Symposium and USNC/URSI National Radio Science Meeting, pp.26, San Diego (USA), 2008

O AUTORU

Branimir Ivšić rođen je 30. travnja 1982. godine u Zagrebu, gdje je završio osnovnu i srednju školu. Godine 2001. upisao je Fakultet elektrotehnike i računarstva Sveučilišta u Zagrebu, a 2003. završetkom temeljnog dijela studija, opredijelio se za smjer radiokomunikacije i profesionalna elektronika. Diplomirao je u studenom 2006. godine na temu “Polarizacija elektromagnetskog vala u svjetlovodnim komunikacijskim i senzorskim sustavima”, pod mentorstvom prof.dr.sc. Zvonimira Šipuša.

Godine 2007. upisuje poslijediplomski studij na Fakultetu elektrotehnike i računarstva te se zapošljava kao znanstveni novak na Zavodu za radiokomunikacije, na projektu Ministarstva znanosti, obrazovanja i sporta “Višefunkcijske antene u komunikacijskim i radarskim sustavima” pod vodstvom prof. dr. sc. Jurja Bartolića. Kao mentor doktorskog rada određen je prof. dr. sc. Davor Bonefačić. Autor je odnosno koautor više radova na međunarodnim skupovima i časopisima iz područja elektromagnetskog raspršenja, malih antenna kao i iz područja komunikacijskih sustava na ljudskom tijelu. Sudjelovao je na više stručnih seminara u inozemstvu u sklopu programa European school of antennas a godine 2011. stručno je boravio 2 mjeseca u Ecole Polytechnique Federale de Lausanne (EPFL), Lausanne, Švicarska, gdje je sudjelovao u istraživanju antenna prikladnih za nošenje na odjeći.

Uz redovno obrazovanje završio je i srednju glazbenu školu kao glazbenik violinist i kontrabasist. Aktivno se služi engleskim jezikom. Član je strukovne udruge IEEE.

ERRATA

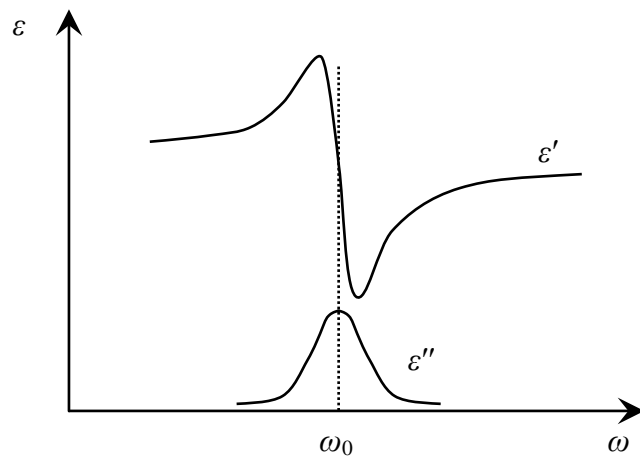


Figure 3.3 Lorentz frequency characteristics of complex permittivity